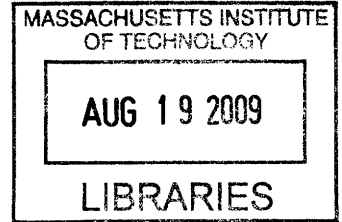# Spontaneous Brillouin Scattering Quench
Diagnostics for Large Superconducting Magnets

by
Scott Brian Mahar
B.S., Chemical Engineering Theory (2003),
B.S., Nuclear Engineering (2005),
M.S., Nuclear Engineering (2005),
Massachusetts Institute of Technology
Submitted to the Department of Nuclear Science & Engineering
in partial fulfillment of the requirements for the degree of
Doctor of Philosophy in Nuclear Science & Engineering
at the
MASSACHUSETTS INSTITUTE OF TECHNOLOGY
September 2008

Author ....
Department of Nuclear Science & Engineering
August 26, 2008

Certified by......................
Joseph V. Minervini
Division Head and Senior Research Engineer
Thesis Supervisor

Certified by......................
Joel H. Schultz
Principal Research Engineer and Group Leader
Thesis Supervisor

Certified by.............
Jeffrey P. Freidberg
Professor, Nuclear Science & Engineering Department
Thesis Reader

Accepted by ....
Prof. Jacquelyn C. Yanch
Professor of Nuclear Science & Engineering
Chair, Department Committee on Graduate Students

Spontaneous Brillouin Scattering Quench Diagnostics for Large Superconducting Magnets

by

Scott Brian Mahar

Abstract

Large superconducting magnets used in fusion reactors, as well as other applications, need a diagnostic that can non-invasively measure the temperature and strain throughout the magnet in real-time. A new fiber optic sensor has been developed for these long-length superconducting magnets that simultaneously measures the temperature and strain based on spontaneous Brillouin scattering in an optical fiber. Using an extremely narrow (200 Hz) linewidth Brillouin laser with very low noise as a frequency shifted local oscillator, the frequency shift of spontaneous Brillouin scattered light was measured using heterodyne detection. A pulsed laser was used to probe the fiber using Optical Time Domain Reflectometry (OTDR) to define the spatial resolution. The spontaneous Brillouin frequency shift and linewidth as a function of temperature agree well with previous literature of stimulated Brillouin data from room temperature down to 4 K. Analyzing the frequency spectrum of the scattered light after an FFT gives the Brillouin frequency shift, linewidth, and intensity. For the first time, these parameters as a function of strain have been calibrated down to 4 K. Measuring these three parameters allow for simultaneously determining the temperature and strain in real-time throughout a fiber with a spatial resolution on the order of several meters. The accuracy of the temperature and strain measurements vary over temperature-strain space, but an accuracy of better than $\pm$ 2 K and $\pm$ 100 $\mu\varepsilon$ are possible throughout most of the calibrated temperature-strain space (4-298 K and 0-3500 $\mu\varepsilon$). In the area of interest for low-temperature superconducting magnets (4-25 K), the temperature accuracy is better than $\pm$ 1 degree. This temperature accuracy, along with the sub-second measurement time, allows this system to be used not only as a quench detection system, but also as a quench propagation diagnostic. The sensing fiber can also simultaneously provide the first ever spatially resolved strain measurement in an operating magnet.

Thesis Supervisor: Joseph V. Minervini
Title: Division Head and Senior Research Engineer

Thesis Supervisor: Joel H. Schultz
Title: Principal Research Engineer and Group Leader

Thesis Supervisor: Jeffrey P. Freidberg
Title: Professor, Nuclear Science & Engineering Department

Acknowledgments

There are many people, and several organizations, who have helped to make this thesis successful, and I am forever grateful to all of them. I would first like to thank my advisors, Drs. Joseph Minervini and Joel Schultz, who have been there since day one with invaluable advice and support. Their knowledge about everything even remotely pertaining to the field of superconducting magnets, as well as their experimental engineering expertise made this thesis successful.

The experiments performed in this thesis would also not have been possible without the collaboration with NP Photonics. I would like to thank Shibin Jiang for his help in winning a Phase I SIBR grant which covered a large portion of the experimental costs. I am especially thankful to Jihong Geng for all of his work on the spontaneous Brillouin scattering system which we modified and used for our experiments. Jihong also saved us several days work by coming in during the evening to help us get the system operational for the second set of experiments, even though he is no longer with NP Photonics. His dedication to this thesis is greatly appreciated. I would also like to thank Wenyan Tian and Arturo Chavez-Pirson for their help with the strain experiment. I also want to thank Dennis Ryan for having all of the equipment and cryogens available and ready to go when I arrived in Tucson, as well as dragging me out of the lab a couple of times during the long 16-hour setup days to get some good food and fresh air.

I would like to thank my thesis reader, Professor Jeffrey Freidberg for his efforts in improving both the initial experimental plans, and the actual writing in this thesis. I would like acknowledge the other members of my thesis committee, Professors Ian Hutchinson, Ronald Parker, and Dennis Whyte. I would also like to especially thank Peter Titus for his help in the stress calculations and design for the strain probe, which worked exactly as planned. In addition to those mentioned above I would like to thank all of the scientists, technicians, and administrators that make up the Fusion Technology and Engineering Group at the Plasma Science and Fusion Center, especially Makoto Takayasu, Chen-yu Gung, Philip Michael, Peter Stahle, Leslie

Contents

List of Figures

12

14

15

List of Tables

Chapter 1

Introduction

Consistently increasing energy consumption, coupled with dwindling reserves of natural resources, magnifies the need for alternative energy sources. Renewable energy such as hydroelectric, wind, and solar power can help supplement the power generation, but they all have limitations and challenges associated with when, where, and how much power they can generate. On the other hand, nuclear power has the potential to supply the worldwide energy demand for orders of magnitude longer than the current energy sources, as shown in Table 1.1 [6].

Table 1.1: Energy reserves for several selected resources and the length of time that they could power the world, assuming that the total usage is 500 quads/year (from Reference [6]).

	Energy Reserves (Quads)	Usage Length (Years)
Coal	10^5	200
Oil	10^4	20
Natural Gas	10^4	20
Nuclear Fission (standard)	10^4	20
Nuclear Fission (breeder)	10^7	20,000
Nuclear Fusion (D-T)	10^7	20,000
Nuclear Fusion (D-D)	10^{12}	2,000,000,000

Coal, oil, and natural gas are all fossil fuels that will eventually be depleted and prohibitively expensive to extract. Standard nuclear fission reactors use Uranium-235 at a non-sustainable pace. Breeder reactors that use Uranium-238 or Thorium could
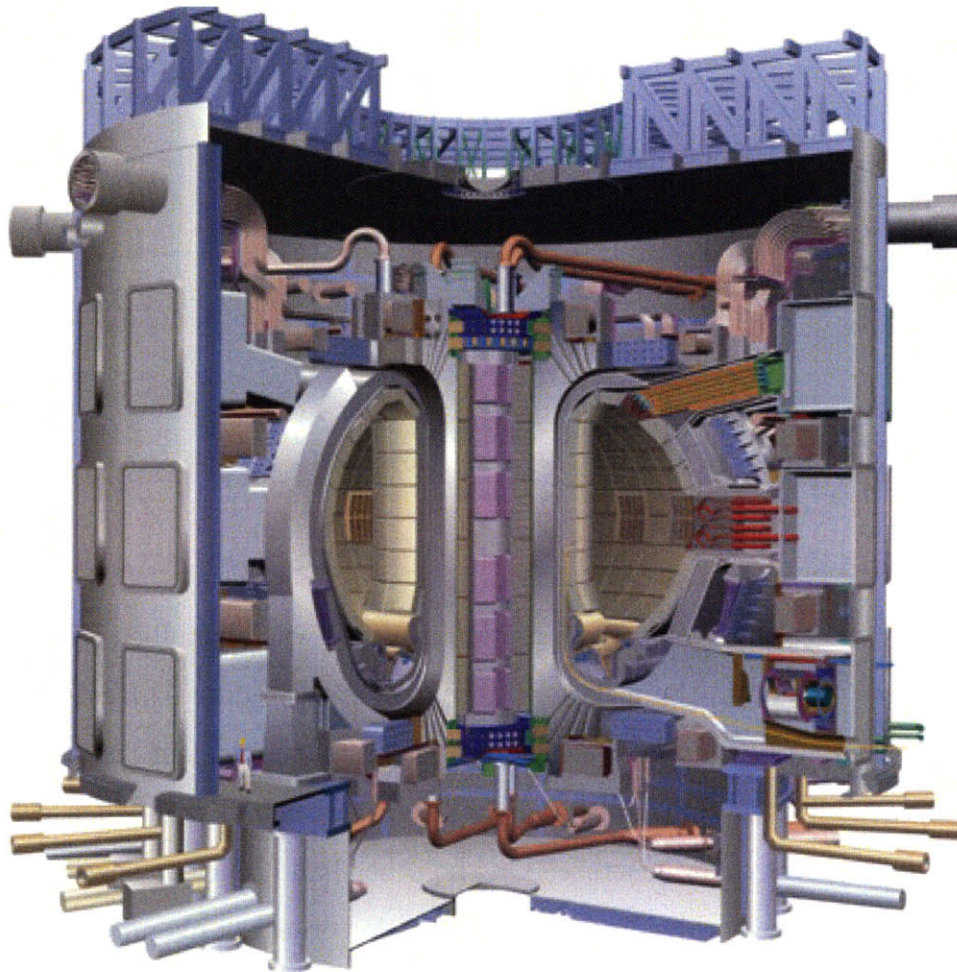
Figure 1-1: Diagram of the International Thermonuclear Fusion Experimental Reactor (ITER).

power the world for another 20,000 years, but have limited public acceptance, because of concerns about proliferation and high-level waste.

Nuclear fusion reactors have the potential to provide energy for orders of magnitude longer than any of these options. Although the first electricity producing fusion reactor is still decades away, extremely productive experimental reactors are providing the needed information to design the first fusion based power plant. The International Thermonuclear Experimental Reactor (ITER) is a joint project to build the first power plant size fusion reactor, capable of generating 500 MW of fusion power, as seen in Figure 1-1 [9].

The massive size of ITER is seen by the inclusion of a person in the bottom left of Figure 1-1. Engineering a system of this size is difficult, not to mention the

extremely complex systems that are needed to run and control a fusion reactor. In particular, ITER's magnet system is an extremely complex system on the leading edge of superconducting magnet capabilities, and will be discussed later in this chapter.

1.1   Fusion Energy

Nuclear fusion reactors are composed of complicated systems that demand both leading edge physics and engineering. Over the last several decades, plasma physics research has brought the idea of a fusion-based power plant from small-scale laboratory experiments to the production of megawatts of fusion power.

Fusion reactors will most likely use some combination of hydrogen isotopes as the fuel. Deuterium is hydrogen with an extra neutron, and tritium is hydrogen with two extra neutrons. The three most likely nuclear fusion reactions for a reactor are deuterium-deuterium, deuterium-helium, and deuterium-tritium, as described by Equations 1.1 - 1.4, where Equations 1.1 and 1.2 happen with equal likelihood for a reactor operating with deuterium-deuterium fuel.

$$_1D^2 +_1 D^2 \rightarrow_2 He^3 +_0 n^1 + 3.27 MeV \tag{1.1}$$

$$_1D^2 +_1 D^2 \rightarrow_1 T^3 +_1 p^1 + 4.03 MeV \tag{1.2}$$

$$_1D^2 +_2 He^3 \rightarrow_2 He^4 +_1 p^1 + 18.3 MeV \tag{1.3}$$

$$_1D^2 +_1 T^3 \rightarrow_2 He^4 +_0 n^1 + 17.6 MeV \tag{1.4}$$
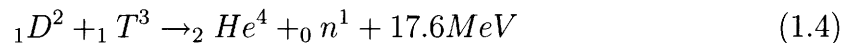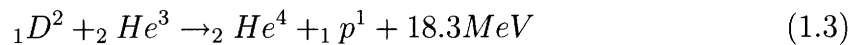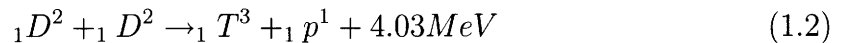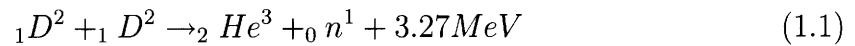
The energy released in a fusion reaction comes from the mass difference between the sum of the products and the sum of the initial nuclei according to Equation 1.5.

$$E = mc^2 \tag{1.5}$$

For example, the deuterium and tritium nuclei weigh 3.14×10^{-29} kg more than the alpha particle and neutron. Plugging that mass loss into Equation 1.5, a value of 17.6 MeV is calculated [10]. Deuterium is naturally occurring in ocean water, about 1 part in 6700; however, there is no naturally occurring tritium, since its half-life is only twelve years [6]. Luckily, bombarding a lithium blanket with neutrons will breed tritium according to Equations 1.6 and 1.7.

$$_3Li^6 +_0 n^1 (slow) \rightarrow_2 He^4 +_1 T^3 + 4.8 MeV \qquad (1.6)$$

$$_3Li^7 +_0 n^1 (fast) \rightarrow_2 He^4 +_1 T^3 +_0 n^1 - 2.5 MeV \qquad (1.7)$$
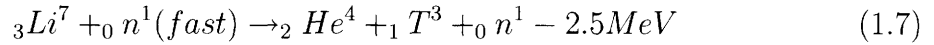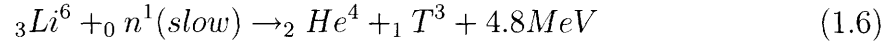
Because of the positive charge of all nuclei on the left sides of Equations 1.1 - 1.4, the atoms must be at a high enough energy to overcome Coulombic repulsion. This means that their energies need to be in the KeV range or higher. Another important parameter is the density. In order for collisions to occur regularly, the plasma must have a density on the order of 10^{20} atoms per cubic meter. A third important parameter is the energy confinement time, τ_E, which varies from reactor to reactor based on many parameters such as size, magnetic field strength, particle transport, etc. The fusion triple product is calculated by multiplying these three parameters.

Along with the fusion triple product, $n\tau T$, another common parameter used to compare reactors is the gain of the plasma, Q. The gain of the plasma is defined as the power output divided by the power input. Important values include $Q = 1$, which corresponds to break-even, and $Q = \infty$ which corresponds to ignition, when the plasma heats itself enough that no input power is necessary. A fusion reactor would ideally operate at some finite value of Q, e.g. $Q = 25$, since ignited plasmas are thermally unstable. Figure 1-2 shows a triple product of $5 \times 10^{21} m^{-3} s KeV$, which is the value needed for ignition of a deuterium-tritium plasma. In terms of the three parameters, this corresponds to a temperature on the order of 10 KeV, a density on the order of 10^{20} atoms per cubic meter, and an energy confinement time around 1

second. As seen in Figure 1-2, ITER is designed to operate slightly below this value, where Q is finite, but plasma heating is dominated by the internal heating of fusion alpha particles.
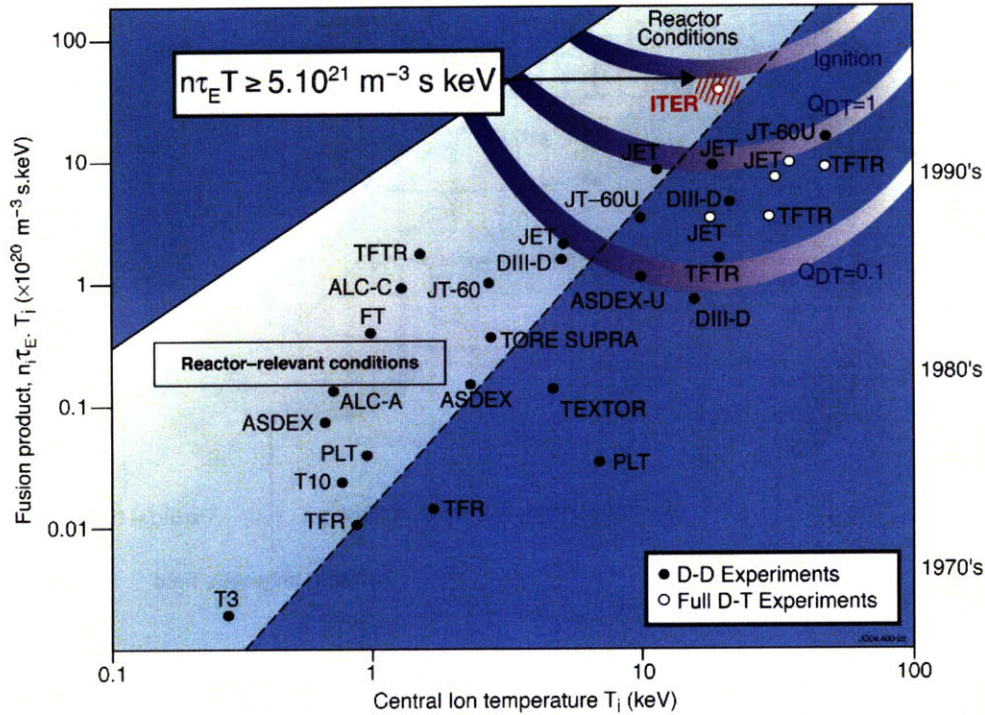
Figure 1-2: Comparison of the fusion triple product of many research tokamaks, as well as the projected ITER parameter for comparison. (Figure from Reference [1]).

One of the main plasma physics demonstrations is that the confinement time, τ_E, of the plasma in a fusion reactor increases with increasing size of the reactor. Throughout the world, there are many fusion reactors; however, ITER will have twice the diameter of the largest current reactor, which gives it a plasma volume ten times as large [11]. One of the many engineering issues associated with nuclear fusion reactors is the magnet system. Since the plasma needs to be heated to millions of degrees, fusion reactors rely on magnet systems to confine the plasma within its vacuum vessel so that it does not destroy the walls. The poloidal and toroidal magnetic fields are used to hold the plasma in place as well as to position and shape the plasma as seen in Figure 1-3. A central solenoid magnet is also used to drive current in the plasma, which helps to stabilize the plasma. (For a much more comprehensive discussion on fusion reactors see References [6, 10]).
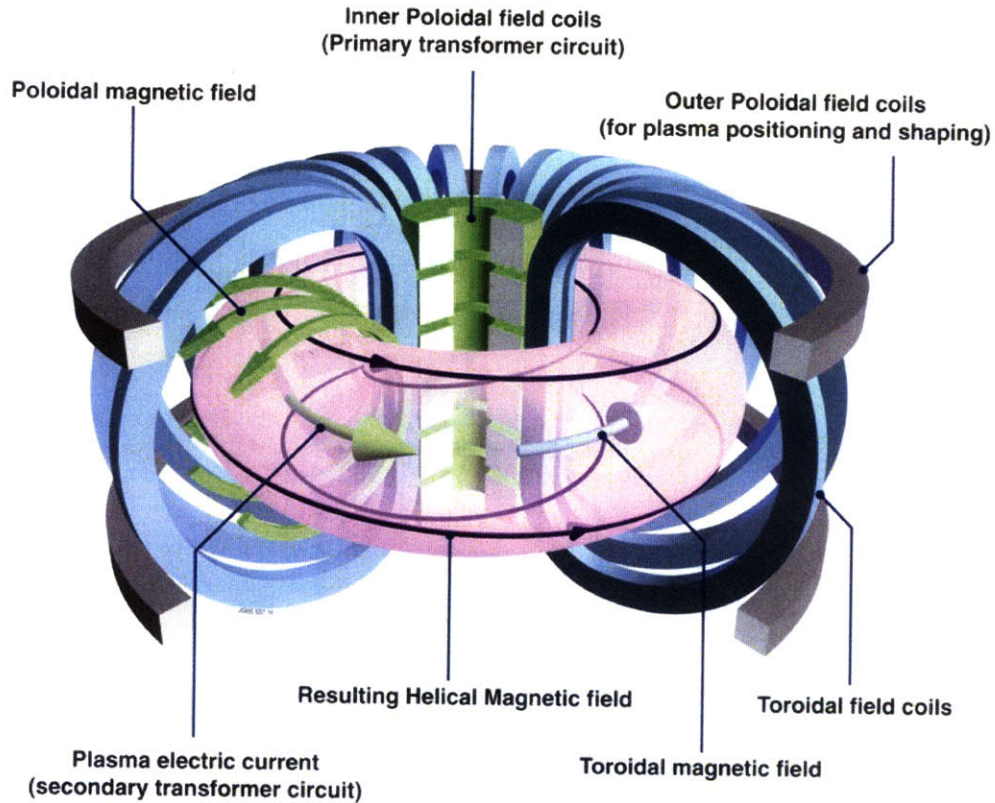
Figure 1-3: Schematic diagram of the magnet layout of standard tokamak fusion reactor. (Figure from Reference [1]).

For ITER to achieve steady state operation using high magnetic field strengths, and to simultaneously demonstrate satisfactory fusion energy gain, these magnet systems need to be superconducting. Not only do the specifications of the ITER superconducting magnets approach the present limits of superconducting capabilities, but the total stored energy in the magnet set is close to 100 GJ. It is extremely important to have a fast and reliable system to detect an unstable magnet so the magnet's stored energy can be properly discharged. It is equally important that the detection system can distinguish the magnet signal from background noise in the complicated fusion reactor environment, as will be discussed in the following sections.

1.2 Superconducting Magnets

Outside of fusion reactors, superconducting magnets are used in a variety of fields, including health care and physics research, as well as being proposed for electrical power and transportation. Magnetic Resonance Imaging (MRI), and Nuclear Magnetic Resonance (NMR) machines use both low and high temperature superconducting magnets. The proton-antiproton collider at Fermilab was the first collider to use superconducting magnets, and the most recent collider, the Large Hadron Collider at CERN, is also being constructed with superconducting magnets. Electric generators, fault current limiters, and motors using superconductors are being implemented since they are more efficient and compact than conventional electrical equipment made with copper wires. Superconducting transmission lines are currently under development to eliminate the large losses in long distance high power cables, and to increase capacity in existing conduits. Magnetically levitated trains (MAGLEV) have been developed that float above a guide-way due to magnetic repulsion, while a second set of superconducting magnets serves as the linear synchronous "motor" in the guide-way. In order to incorporate superconducting magnets into existing and developing technologies, the fundamental physics and limitations of the magnets must be understood.

1.2.1 Background and Basics

Superconductivity was discovered by Kammerlingh Onnes in 1911 as a result of his joint studies in helium liquefaction and the conductivity of metals [12]. Onnes measured the resistivity of distilled, purified mercury as he cooled his sample down to 4 Kelvin, as shown in Figure 1-4. In his experiment, Onnes discovered that the critical temperature, T_c, of mercury is about 4.2 K [13].

Onnes continued his experiments with mercury, and also investigated lead and tin. His hopes of using superconductive metals to make large and powerful electromagnets were crushed when he discovered that his samples had not only a critical temperature, but also a low critical magnetic field, B_c. Using his samples of mercury, lead, and tin, Onnes determined that the critical magnetic field is only about 0.05 Tesla [12].
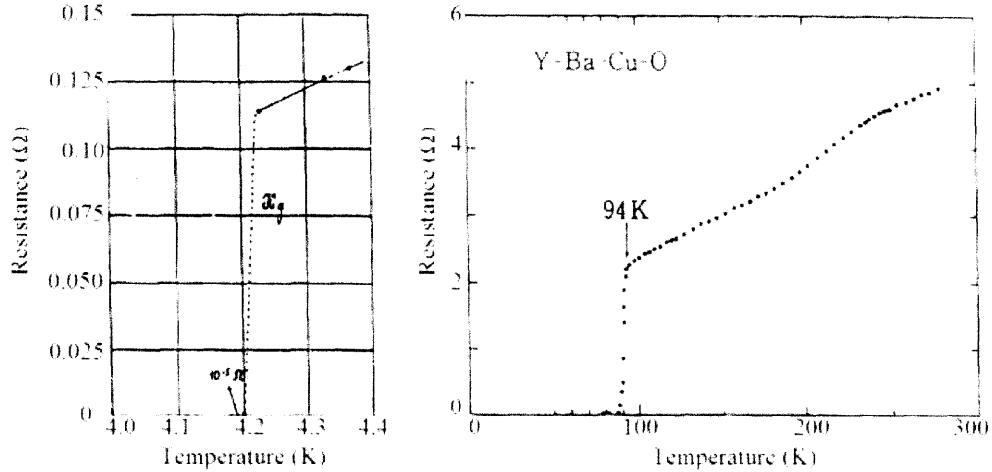
Figure 1-4: Kammerlingh Onnes' plot of resistance as a function of temperature for mercury (left), and a similar plot for a high temperature superconductor (right).

The materials that Onnes studied are now called "Type I", or "soft" superconductors and are not used in magnets because of their low critical magnetic field. The first "Type II" or "hard" superconductor, a lead-bismuth alloy, was discovered by Haas and Voogd in 1930 [3]. Type II superconductors are normally alloys including part Type I superconductor material, and part normal conducting material. These alloys have critical magnetic fields much higher than the 0.05 Tesla of the Type I superconductors, which allow these alloys to be used to make the large and powerful electromagnets Onnes envisioned.

The superconductivity of a material is not only constrained by a critical temperature and a critical magnetic field, but also by a critical current density, J_c. When a critical surface is plotted in temperature, magnetic field, current density space, the material is superconducting anywhere under the curve shown in Figure 1-5.

Niobium titanium, NbTi, has a critical temperature of 9.3 K, where the surface would cross the temperature axis in Figure 1-5. Although NbTi is superconducting at 9.3 K, it is not useful at that temperature since any magnetic field or current would make it non-superconducting, or "normal". Most low temperature superconductors operate at 4.2 K, since that is the boiling point of liquid helium under atmospheric pressure. Assuming that a NbTi or Nb_3Sn magnet is at 4.2 K, its critical current densities and critical magnetic fields are shown in Figure 1-6.
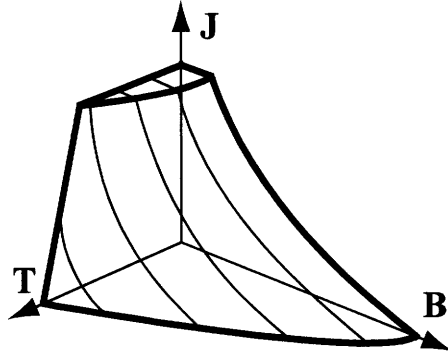
Figure 1-5: The general shape of a critical temperature, magnetic field, and current density surface for niobium titanium.

To put the numbers in this plot in perspective, normal household wires are rated to about 10^7 A m^{-2}, and fuses blow at about 10^8 A m^{-2}. Also shown in Figure 1-6 is the range where conventional iron-cored electromagnets operate. Since iron saturates at about 2 T, that is the upper limit on the possible magnetic field for a conventional iron-cored electromagnet [12].

All low temperature superconducting magnets use a composite wire, part Type II superconductor and part normal conductor, where the normal conductor is called "stabilizer" since it improves stability against perturbations in the case of a quench. There are several different ways that composite superconducting wires are made. Most methods involve a large cylinder with the appropriate dimensions, which eventually is drawn down to wire size. Different companies use different layouts, but in general all superconducting wires are designed to have a matrix of superconducting filaments embedded in a stabilizer. Depending on the type of superconductor, the wire may also need to be heat treated to form superconducting filaments. For example, the niobium and tin are separate during the drawing of the wire, and do not join together to make Nb$_3$Sn until the wires undergo a heat treatment ranging from tens to hundreds of hours. While the magnet is operating in a superconducting state, the current flows exclusively through the superconducting filaments; however, when a magnet quenches, current is transferred to the stabilizer. Figure 1-7 shows the cross section of an ITER cable and of a wire, along with the general sub-wire layout before being drawn down and heat treated.
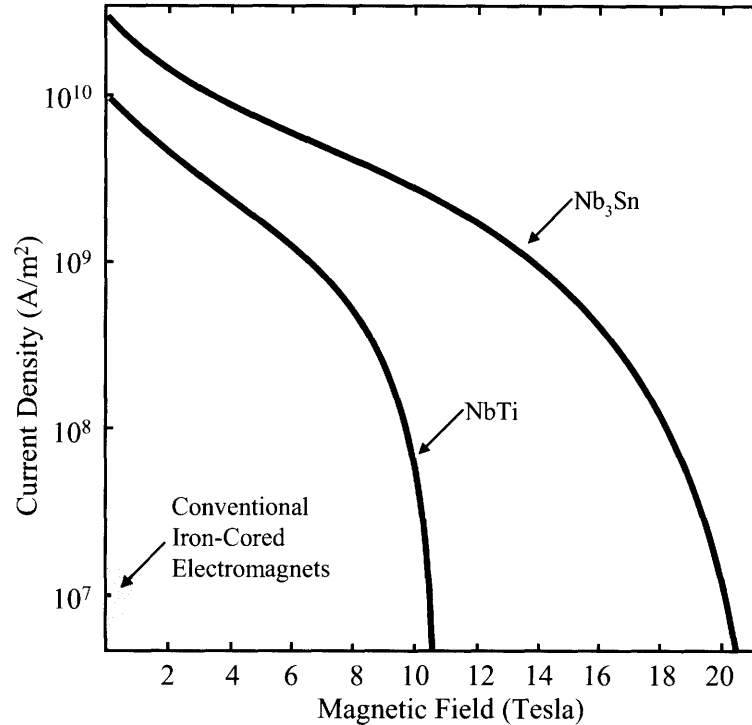
Figure 1-6: Critical curves at 4.2 K for niobium titanium and niobium tin compared to the critical region for conventional iron-cored electromagnets.

Since most low temperature superconducting magnets are operated at around 4 K, they need to be continually cooled using cryogens. The oldest method is pool boiling He I cooling, which uses saturated helium at atmospheric pressure and at a temperature of 4.25 K [13]. The helium will boil off, so it will have to be replaced periodically or continuously. These cryostable pool boiling magnets tend to have low current density, which means that they need to be large and expensive [14].

In 1974, Hoenig developed a new method for cooling the superconducting filaments called a Cable in Conduit Conductor, or CICC [15]. This design incorporates a strong jacket, usually a steel alloy, surrounding the superconducting wires. The jacket not only protects the filaments, but it also provides a channel that helium can be pumped through as a coolant. CICC magnets today, including the magnets being designed for ITER, are normally cooled by pumping supercritical helium through the conduit. Helium in the supercritical state has low viscosity and extremely large thermal conductivity, making it an ideal coolant for CICCs. The phase diagram showing the characteristics of supercritical helium is shown in Figure 1-8. As seen in

CICC

50 mm

Single Strand

0.8 mm

Sub-Strand

Nb
Cu
Sn

0.12 mm

Filament

50 μm
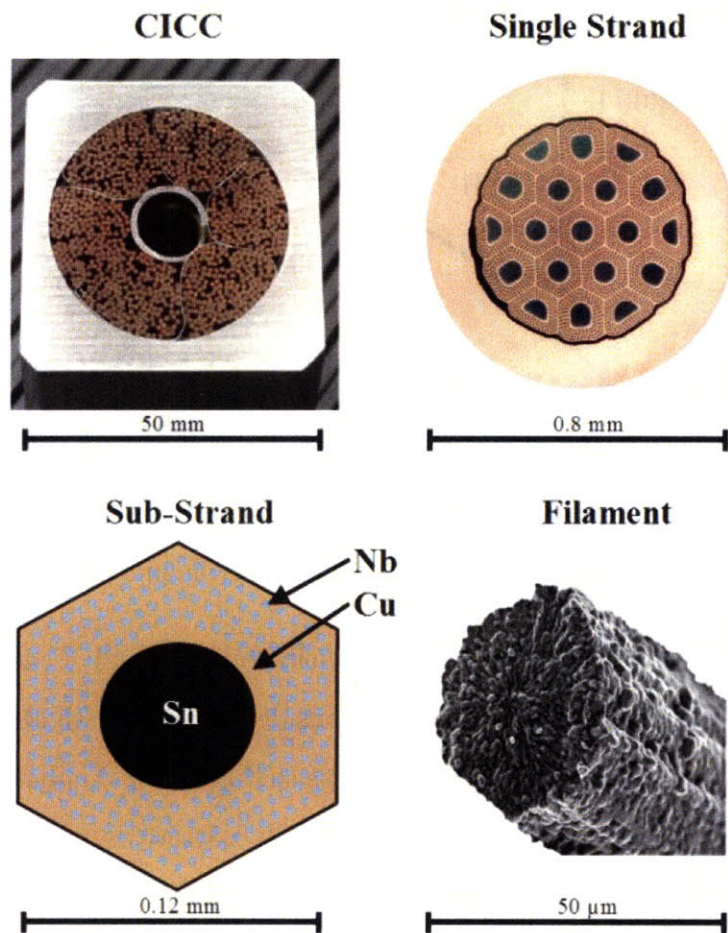
Figure 1-7: Cross sections of: an ITER cable in conduit conductor (top left), a single strand in the CICC (top right), a diagram of the sub-components of part of a strand (bot. left), and a superconducting filament (bot. right).

33

Figure 1-7, there is a central cooling channel as well as space between the wires for the helium to flow; typically the void fraction between the wires is about 28-40 % [14].
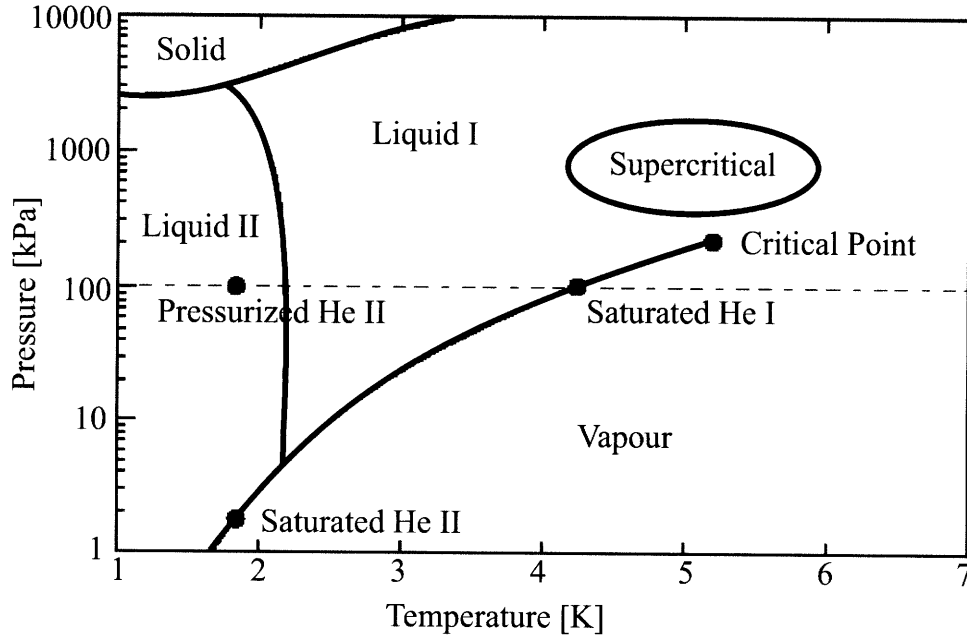
Figure 1-8: Phase diagram of helium at cryogenic temperatures [2].

The ITER central solenoid and toroidal field coils use a CICC design with roughly 1100 wires, each about 0.7 mm in diameter, inside a conduit with about a 4 cm diameter channel. These wires are not randomly packed into the channel, but are carefully cabled in a strategic pattern. The exact ITER pattern is still being determined; however, the Quench of Long Length (QUELL) magnet, which was built to simulate conditions in the ITER magnets, used a subsized conductor with a $3 \times 3 \times 4 \times 6$ cabling pattern. Groups of three wires are cabled together, then three of those groups are cabled together. Next, four of those groups are cabled together, producing six large groups which are ultimately cabled around the central cooling channel. Once the cabling is done, the wires are pulled into the conduit and it is compacted to achieve the desired void fraction. Figure 1-9 shows a similar cabling pattern in a short length of unwound wires.

Each of the six ITER central solenoid coils, shown as light purple in the middle of the reactor in Figure 1-1, are made up of approximately 6 km of CICC. The conduit is

34
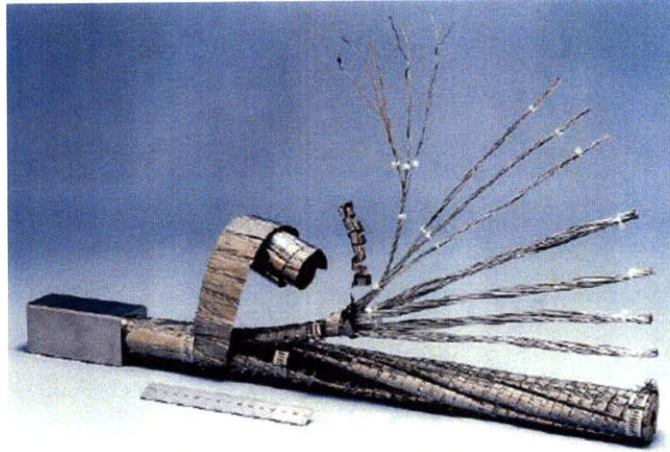
Figure 1-9: CICC partially uncabled to show the cabling pattern of the wires.

bent into shape and "pancake wound", meaning it is wound from the outside spiraling inward to the inner radius, and then moves up a level and spirals back out, as shown in Figure 1-10.
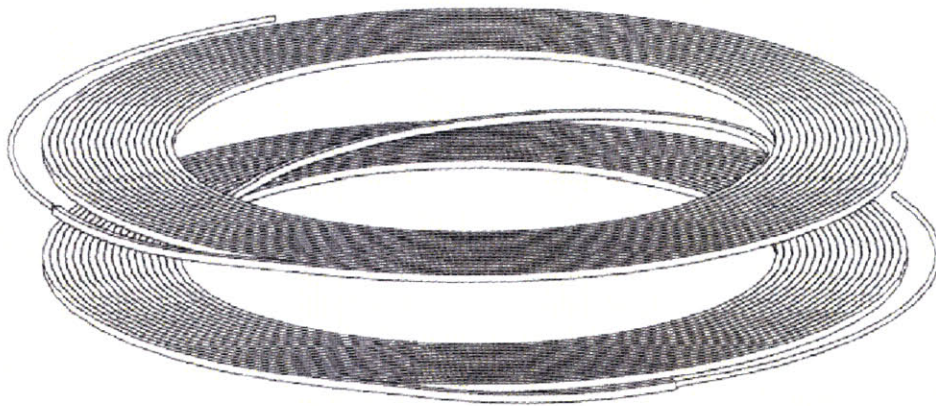
Figure 1-10: Schematic diagram of a "pancake" winding (cover of Reference [3]).

This winding continues until the magnet has the designed dimensions. The conduit is wrapped in insulation composed of fiberglass and kapton tape, which is eventually impregnated with epoxy once the magnet is in its final form. The central solenoid model coil made for ITER testing in 1999 is shown in Figure 1-11.
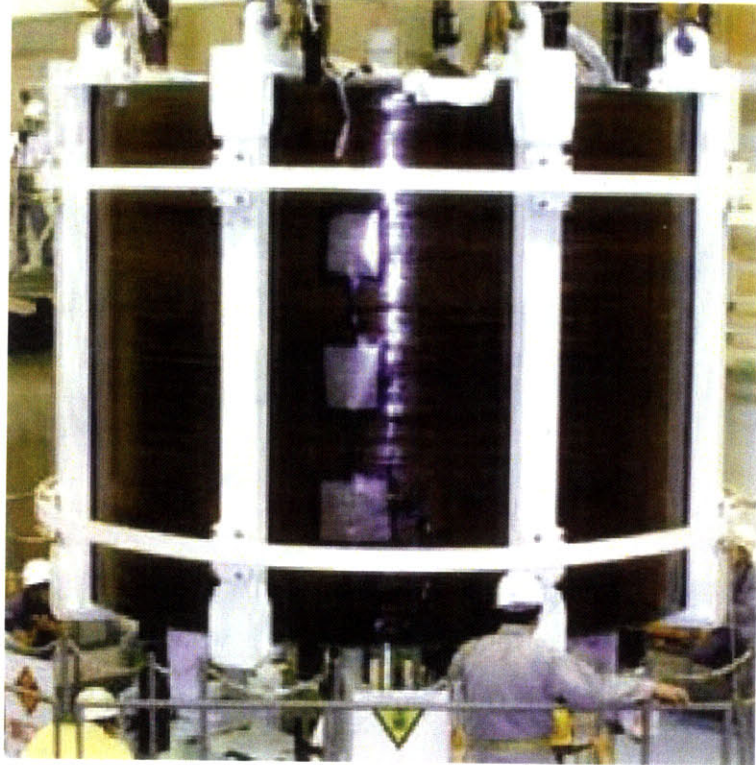
Figure 1-11: The ITER CS model coil achieved a maximum field of 13.5 T, with a maximum current of 46 kA, and a stored energy of 640 MJ.

1.2.2 Quench Detection

The most important aspect of superconducting magnet protection is the detection of a thermal instability called a quench. Quenches are caused when one or more of the critical values are exceeded and the magnet moves out from under the curve in Figure 1-5. Since quenches are the irreversible loss of superconductivity somewhere in the magnet, the stored energy in the magnet must be eliminated before it damages the magnet. Most quenches begin locally, and immediately begin to spread throughout the magnet at a speed known as the quench propagation velocity. As a quench propagates, the temperature increase also propagates, causing more of the magnet to lose its superconductivity, or "go normal".

Once a magnet has begun to quench, it rarely continues to operate at constant current since the "normal" zones are now resistive. The current and the stored energy in the magnet need to be eliminated by either absorbing the energy throughout the magnet, or by dumping the current and energy externally. During a quench, the cur-

rent is transferred from the superconducting filaments to the stabilizer wires, since the stabilizer wires are designed to have lower resistance than the normal superconducting filaments. Some magnets are designed to have enough enthalpy in their stabilizers and other passive components to absorb the energy without unacceptable temperature or pressure rises [7]. This is only acceptable if the peak-to-average ratio of temperature and pressure rise is held to a moderate level. A magnet can be designed to have a moderate peak-to-average temperature and pressure ratio by incorporating internal resistive or inductive heaters to quench the whole magnet at the same time. Most MRI and NMR magnets are designed to be passively protected by shunt diodes and resistors across the magnets [3]. Another way to obtain a moderate ratio is to rapidly dump the helium coolant in a pool-boiling magnet, so the quench zone will spread to a much larger fraction of the magnet quickly. As mentioned previously, the alternative to designing a passively protected magnet is to dump the current, and therefore the energy, into external dump circuits that can either be at room temperature or cryogenically cooled.

Any active quench detection method, such as dumping the current into dump circuits, requires rapid detection of a quench. Most magnets detect a quench electromagnetically: either by using voltage taps to detect a resistive voltage, or by detecting a loss of superconducting diamagnetism. This works well for the small, DC magnets used in MRI and NMR machines; however, electromagnetic detection is not ideal for magnets in electromagnetically noisy environments, like fusion reactors. Pulsed coils and multi-coil systems also introduce new challenges when trying to implement electromagnetic quench detection. When a magnet is operating near its stability limits, as is the case for most high temperature superconducting magnets and large fusion magnets, it will have a slow quench propagation velocity, which leads to small resistive voltage signals [7]. These are the magnets that are in need of new, innovative quench detection systems.

1.2.3 Quench Diagnostics

While the quench detection system of a superconducting magnet is the most important system in terms of protection, it is usually not very informative of what happened inside the magnet. From a standard voltage tap, we can not tell where a quench originated, why it originated, or exactly how it spread through the magnet. Standard temperature and strain diagnostics cannot be implemented to investigate these interesting properties of superconducting magnets because they can only measure conditions on the surface of the magnet. First of all, to locate where the quench originated and how it spread, the magnet would need to have hundreds (if not thousands) of thermocouples and voltage taps covering different regions of the magnet, which is not realistic. Even if it was possible, the holes and pathways for these voltage taps and thermocouples would modify the heat transfer within the magnet.

Although actual quench location and propagation diagnostics do not exist, several theoretical computer simulations have been developed. The ITER QUELL experiment compared its results with several computer simulations, including GANDALF and QUENCHER [16]. GANDALF is a one-dimensional model that consists of three parts: the helium, the conductors, and the jacket. The helium is modeled by two flows, one through the conductors and one through the central cooling channel. GANDALF derives a numerical solution using adaptive meshing and time steps [17]. QUENCHER is a simulation that relies on the conservation of helium mass, helium momentum, helium/conductor energy, and conduit wall energy [18].

Minor uncertainties of input data into GANDALF can lead the numerical solutions far from the actual data. Also, a simplified 2-flow model overestimates quench propagation at the beginning and underestimates it at the end. During the QUELL study there were initially problems with QUENCHER since it assumed an infinite heat transfer coefficient between the cable and the hole space; however, it was modified to QUENCHER2, which fixed that problem and achieved very accurate simulations of the measured data [16].

Other simulation codes, such as SOLXPT3D [19], simulate the development of

temperature, pressure, and thermal diffusion in cable-in-conduit superconductors. SOLXPT3D also models the quench signal and voltage noise on voltage taps and co-wound internal voltage sensors, which is very important in determining the type of quench detector a magnet should use. Several commercial quench simulation codes are now being developed, such as QUENCH by Vector Fields. The interest of companies in developing quench codes shows that this is a difficult problem that many people are interested in trying to solve.

1.3 Thesis Outline and Overview

Chapter 2 begins by describing standard quench detection diagnostics for superconducting magnets. Fiber optic basics and sensor capabilities are then discussed, followed by several more advanced fiber optic sensing systems.

Spontaneous Brillouin scattering is explained in detail in Chapter 3, including derivations of the key parameters, and temperature effects on these parameters. The theoretical capabilities of a spontaneous Brillouin scattering system are also compared with common superconducting diagnostics.

Chapter 4 describes the spontaneous Brillouin scattering system used in this thesis, as well as the experiments that were run and the results that were obtained. The chapter concludes with a description of how to use this data to calculate the distributed temperature and strain.

The tradeoffs of key measurement parameters, such as measurement time and spatial resolution, are discussed in Chapter 5. This chapter also derives the accuracy of the measurements and calculations made in Chapter 4.

The major engineering issues that need to be solved before this system is implemented in an actual magnet are explained in Chapter 6, followed by conclusions and suggestions for future work in Chapter 7.

Chapter 2

Superconducting Magnet Diagnostics and Fiber Optic Sensors

2.1 Quench Detection

As discussed in the previous chapter, quench detection is the most important system of an actively protected magnet. If a magnet is passively protected, as most MRI and NMR magnets are, the detection of a quench is not as important because nothing is actively changed.

Most superconducting magnets use a relatively simple voltage tap system to detect quenches. Others use changes in temperature, pressure, and flow of the cryogenic coolant to detect a quench; however, these methods are inadequate in strongly pulsed magnetic fields [7]. Noise in the voltage tap systems is only made worse by the growing size of fusion magnets.

Although voltage taps have been the easy and reliable solution in the past, superconducting magnet systems with high terminal voltages and large unpredictable voltage transients demand other solutions. The QUench Experiment on Long Length (QUELL) was designed and run with the sole purpose of figuring out the best quench

41

protection system for the large ITER magnets. Several new quench detection methods were tested in this experiment, including fiber optic, pressure, mass flow, density, and acoustic systems. These new systems, as well as internally wound voltage taps, were tested and compared to the standard voltage tap, in order to determine the best system to protect the extremely expensive ITER superconducting magnets.

2.1.1   Voltage Taps

Compared to all of the complicated engineering and design work that goes into making a superconducting magnet, using a voltage tap to protect it is relatively simple. To measure the voltage across a coil, or a section of a coil, wires penetrate the insulation to the outer surface of the conductor. The locations of the two tap points are normally as close as possible in order to avoid high inductance in the circuit. Even though the basic idea behind a voltage tap seems straightforward: superconducting magnets do not have any resistance when they are superconducting, but when they become normal the voltage drop due to the resistance can be measured by the voltage taps.

While the basic idea is simple enough, there are some subtleties that one has to consider when using voltage taps. One may expect that during a quench the voltage measured across the terminals of the coil will be large and increasing, due to the increasing resistance in the magnet; however, this is not necessarily the case. Most of the voltage drop is located in the coil, where the resistive and inductive voltages oppose each other [12]. The only voltage measured across the terminals is that of the current supply, which is turned off soon after a quench is detected, as illustrated in Figure 2-1. Also, the supply only provides a few volts, compared to the hundreds or even thousands of volts produced in the resistive quenching part of the magnet [12].

When a superconducting coil, like the ITER central solenoid, is being designed to operate with alternating current, the inductance will render a simple voltage tap useless. (This also pertains to the ramping up and down of direct current magnets). The voltage across a simple voltage tap in this case is described in Equation 2.1.
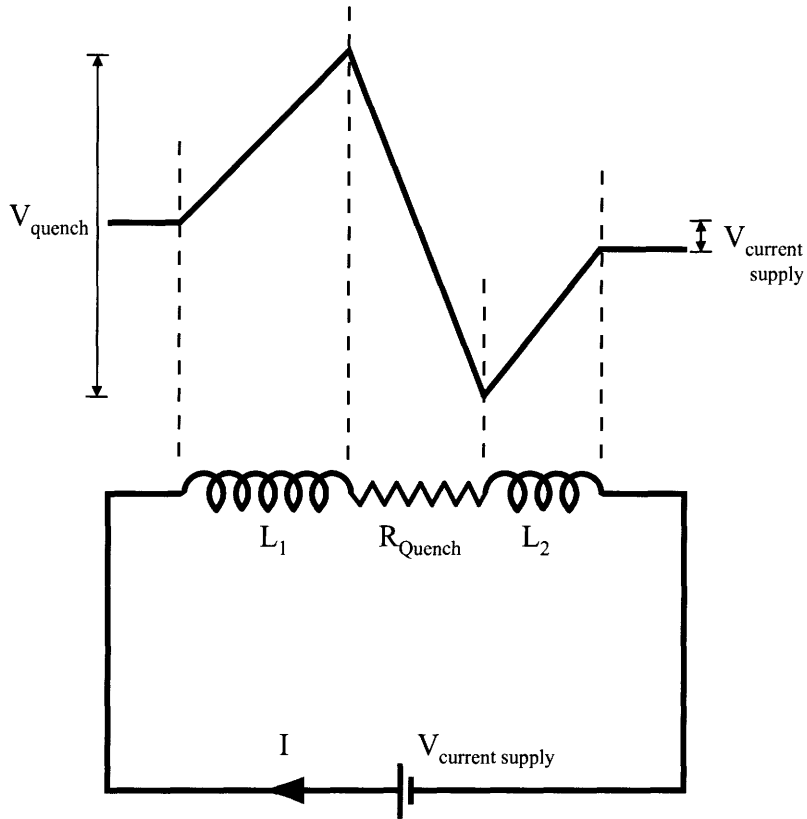
Figure 2-1: The resistive voltage due to a quench is opposed by the magnet's inductive voltages.

$$V = IR + L\frac{dI}{dt} \tag{2.1}$$

The inductance term, $L\frac{dI}{dt}$, in Equation 2.1 is normally much larger than the resistive term, even at relatively low currents.

In order to measure the resistive voltage between voltage taps in an AC, or charging DC magnet, the inductance term needs to be canceled. The most common way to cancel the inductive voltage is to use a bridge circuit. By putting two equal inductive signals, normally two adjacent double pancakes, into the two arms of a bridge circuit the inductive voltages will cancel each other out [7]. The use of a bridge circuit to cancel the inductances can also be used by a hybrid magnet, with the two magnets as the two arms of the bridge [3]. In Figure 2-2, L_1 and L_2 are the self inductances of two coils connected in series, which can be two adjacent double pancakes, the two

coils of a hybrid magnet, or even one coil divided into two.
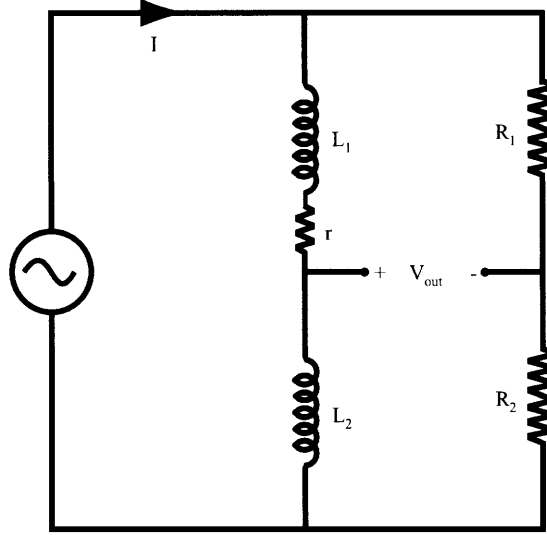
Figure 2-2: Standard bridge circuit for quench detection using voltage taps.

Since the two coils are connected in series, the mutual inductance can be included in the self inductances [3]. Using L_1 and L_2 as the inductances of coils 1 and 2 respectively, R_1 and R_2 as the bridge circuit resistors, r as a normal zone resistance in coil 1, and V_{out} as the bridge circuit output, we can write Equations 2.2 - 2.4 [3].

$$V_{cl}(t) = L_1 \frac{dI(t)}{dt} + rI(t) + L_2 \frac{dI(t)}{dt} \tag{2.2}$$

$$i_R(t) = \frac{V_{cl}(t)}{R_1 + R_2} \tag{2.3}$$

$$V_{out}(t) = L_1 \frac{dI(t)}{dt} + rI(t) - R_1 i_R(t) \tag{2.4}$$

Combining these equations gives an equation for V_{out}, expressed in Equation 2.5.

$$V_{out}(t) = \left(\frac{R_2}{R_1 + R_2} \right) L_1 \frac{dI(t)}{dt} - \left(\frac{R_1}{R_1 + R_2} \right) L_2 \frac{dI(t)}{dt} + \left(\frac{R_2}{R_1 + R_2} \right) rI(t) \tag{2.5}$$

When $R_2 L_1 = R_1 L_2$, the first two terms on the right hand side of Equation 2.5 cancel each other out and V_{out} becomes a function of the normal zone resistance and

44

current, as shown in Equation 2.6.

$$V_{out}(t) = \left(\frac{R_2}{R_1 + R_2}\right) r I(t) \qquad (2.6)$$

Another way to eliminate the inductive term in Equation 2.1 is to co-wind the voltage tap with the superconducting cable. If the voltage tap travels along the same path as the conductor, it will experience the same inductive effects as the magnet, and the signal will simply be the resistive voltage. The location of the co-wound voltage tap is also important in canceling the inductive voltage. The best location for the voltage tap is to have it cabled into the windings as a part of a triplet as if it was a superconducting wire; however, the second best place, which is in the center of the final stage of the cable winding, is easier to cable [7]. QUELL tested co-wound voltage taps inside the conduit and showed an inductive voltage rejection 500 times better than the normal voltage taps [7]. The location of the co-wound voltage taps were studied in the Tokamak Physics Experiment, TPX, and determined that depending on the location of the sensor in a cable, the noise rejection can be up to 60,000 times that of a standard voltage tap [20]. Using signal processing methods to use a volt-second threshold instead of an absolute voltage threshold has been shown to give an additional noise rejection factor of 20 [7].

The ITER superconducting coils will use a combination of conventional and co-wound voltage taps as their method of quench detection. While this system may work adequately as a quench detector, it will not give any additional information such as quench location and quench propagation. By using a certain number of internally terminated co-wound voltage taps, a degree of spatial resolution can be achieved equal to the total length of the coil divided by the number of voltage taps used. Since the only job of the co-wound voltage taps in the ITER magnets is to detect quenches, a lack of spatial resolution is not a problem; however, a spatially resolved measurement that can locate and track a quench in real time would be a significant improvement.

2.1.2   Other Quench Detection Methods

Voltage is the most common quench detection signal; however, there are a lot of other changes in a quenching magnet that can be measured, leading to many other quench detection methods. These other quench detection methods include pickup coils to detect a change in diamagnetism, pressure sensors to detect the rising pressure in a warming conduit, mass flow measurements to monitor the helium flow, helium flow density measurements, and acoustic sensors to listen for internal changes in flow.

Aside from voltage taps, pickup coils are the next most common quench detection diagnostics. One major advantage that pickup coils have over voltage taps is that they do not interfere with the structural integrity of the actual magnet, i.e. they do not penetrate through the insulation and conduit as voltage taps do. By connecting a pickup coil to a low transient impedance circuit, it can detect a quench by sensing a change in overall current [7]. When a superconducting magnet is quenching, the super-currents are suppressed faster than the overall current causing a rapid decrease in diamagnetism, which is detected by the pickup coils [7]. A pickup coil array is used to protect the Fermi National Accelerator Laboratory's Tevatron magnet [21]. Placing an array of higher-order pickup coils around a superconducting magnet will act as a multi-pole antenna which will detect the rapid change in diamagnetism of a quenching magnet. An eight coil array is used on the Relativistic Heavy Ion Collider, RHIC, at Brookhaven National Laboratory and operates in excellent agreement with the voltage taps [22].

When a superconducting magnet quenches, the helium is violently heated and expelled from the original quench zone [14]. This is what propagates the temperature increase longitudinally, as well as causing a significant increase in pressure. Pressure sensors installed in the QUELL experiments saw a pressure rise of 0.6 - 14.5 bars [23]. Initially the pressure will rise due to the increase in temperature. This is followed by the expulsion of helium at the cable ends, which will allow the density to drop, followed by a drop in the pressure. In 1980 Miller conducted an experiment to study the pressure rise due to a quenching magnet. Using a dummy CICC, he compared

experimental data with a theoretical derivation of the maximum pressure achieved during a quench, Equation 2.7 [24].

$$P_{max} = 0.65 \left(\frac{fQ^2 \left(\frac{L}{2} \right)^3}{D_h} \right)^{0.36} \left(1 - \frac{p_o}{p_{max}} \right)^{-0.36} \tag{2.7}$$

In Equation 2.7, f is the space and time averaged friction factor, Q is the heating rate per unit helium (which is assumed to be a constant), L is the length of the conduit, D_h is the hydraulic diameter, and p_o is the initial pressure. Normally, the initial pressure is much less than the maximum pressure, allowing Equation 2.7 to be simplified to Equation 2.8, which was in excellent agreement with Miller's experimental data [24].

$$P_{max} = 0.65 \left(\frac{fQ^2 \left(\frac{L}{2} \right)^3}{D_h} \right)^{0.36} \tag{2.8}$$

Pressure sensors were part of the QUELL experimental diagnostics, and although they had reproducible sensitivities of only ± 0.5 %, the experiment determined that they should not be used in ITER magnets due to the slow propagation time of the pressure wave through the conduit. QUELL experiments measured this speed to be about 100 m/s, meaning it would take on the order of seconds for the pressure from a quench in the middle of a coil to reach the ends, as well as another few seconds for it to reach the threshold pressure [23].

As mentioned above, there is a change in the helium flow rate in the conduit during a quench. Dresner derived a theoretical expulsion velocity, Equation 2.9, for the ends of a completely normal-conducting cable [25].

$$v \approx 0.952 \left(\frac{Q\beta c_o}{\rho C_p} \right)^{\frac{2}{3}} \left(\frac{D_h}{f} t \right)^{\frac{1}{3}} \tag{2.9}$$

β is the thermal expansion coefficient of helium in a constant pressure process, c is the isentropic speed of sound, ρ is the helium density, C_p is the specific heat at constant pressure, and t is the time since the quench began. Equation 2.9 was derived

47

assuming frictional heating was small compared to Joule heating, as well as assuming constant helium properties, which means that it can only be used as a first-order approximation. Even so, at early values of t, it agrees relatively well with the data from Miller's experiment [7].

Computer simulations predicted that the flow rate of helium would increase from 10 g/s to 50 g/s during a quench in the QUELL sample [26]. Flow meters were also installed on QUELL, but since the flow measurement is a function of pressure it ran into the same delay problems as the pressure sensors [23].

Another quench diagnostic that was tested in QUELL was a fiber optic interferometer [16]. The general idea behind using a fiber optic probe is that it is immune to electromagnetic fields and fluctuations; and therefore is not affected by an AC magnet like most electromagnetic sensors. This fiber optic interferometer, as well as many other fiber optic sensors, will be discussed further in the following sections.

2.2 Fiber Optics

Channeling light through a long narrow dialectic was first accomplished in 1870 when John Tyndall showed that light could be guided along a thin stream of water due to total internal reflection [27]. This idea was developed using glass fibers in the 1920s, but it was not until the 1950s, with the addition of cladding around the glass fibers, that the potential of fiber optics was realized [28]. The early fiber optics in the 1960s had losses of more than 1000 dB per kilometer; however, in 1970 the losses were reduced to below 20 dB per kilometer. Further processing developments led to fibers with losses of 0.2 dB per kilometer in 1979 in the 1.55 μm range, which is limited by the Rayleigh scattering losses [28].

2.2.1 Fiber Optic Basics

In order to understand light propagation in a fiber optic cable, we look at the interaction of an electromagnetic wave at a boundary (the surface of the core and cladding layers in a fiber), shown in Figure 2-3.
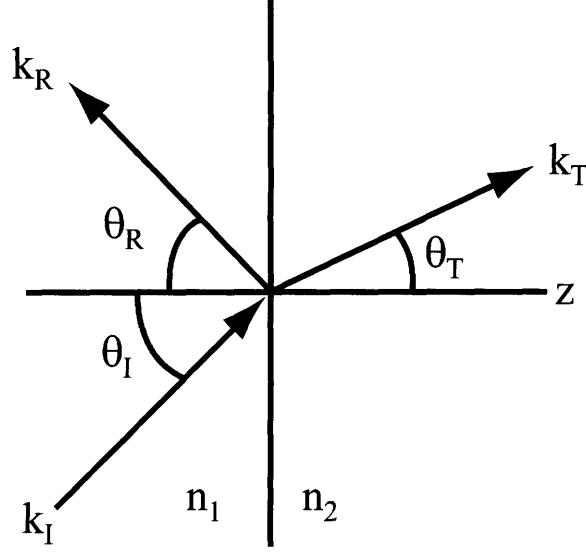
Figure 2-3: Diagram of a plane wave being reflected and refracted at the boundary between two media.

Taking an incident monochromatic plane wave, Equation 2.10, we write the equations for the reflected wave, Equation 2.11, and the transmitted wave, Equation 2.12.

$$\tilde{\mathbf{E}}_I(\mathbf{r}, t) = \tilde{\mathbf{E}}_{oI} e^{i(\mathbf{k}_I \cdot \mathbf{r} - \omega t)}, \, \tilde{B}_I(\mathbf{r}, t) = \frac{1}{v_1} \left(\hat{\mathbf{k}}_I \times \tilde{\mathbf{E}}_I \right) \tag{2.10}$$

$$\tilde{\mathbf{E}}_R(\mathbf{r}, t) = \tilde{\mathbf{E}}_{oR} e^{i(\mathbf{k}_R \cdot \mathbf{r} - \omega t)}, \, \tilde{B}_R(\mathbf{r}, t) = \frac{1}{v_1} \left(\hat{\mathbf{k}}_R \times \tilde{\mathbf{E}}_R \right) \tag{2.11}$$

$$\tilde{\mathbf{E}}_T(\mathbf{r}, t) = \tilde{\mathbf{E}}_{oT} e^{i(\mathbf{k}_T \cdot \mathbf{r} - \omega t)}, \, \tilde{B}_T(\mathbf{r}, t) = \frac{1}{v_2} \left(\hat{\mathbf{k}}_T \times \tilde{\mathbf{E}}_T \right) \tag{2.12}$$

In Equations 2.10, 2.11, and 2.12, v_1 and v_2 are the wave propagation velocities in the two media. The subscripts I, R, and T stand for the incident, reflected, and transmitted components respectively. Since the boundary conditions must hold at all points along the interface and at all times, the exponential parts of the equations must be equal at the interface [29]. Normal convention orients the axes such that k_I lies in the x-z plane and the interference surface is located at $z = 0$. The spatial terms in the exponential parts of Equations 2.10-2.12 lead to Equation 2.13.

$$\mathbf{k}_I \cdot \mathbf{r} = \mathbf{k}_R \cdot \mathbf{r} = \mathbf{k}_T \cdot \mathbf{r}|_{z=0} \qquad (2.13)$$

Equation 2.13 only holds when all of the components are separately equal, which leads to the first fundamental law of geometrical optics: the incident, reflected, and transmitted waves form a plane, called the plane of incidence [29]. Equation 2.13 implies Equation 2.14.

$$k_I \sin \theta_I = k_R \sin \theta_R = k_T \sin \theta_T \qquad (2.14)$$

Since the wave numbers are related by Equation 2.15, Equation 2.14 gives us the second fundamental law, or the law of reflection: the angle of incidence equals the angle of reflection, expressed in Equation 2.16.

$$k_I v_1 = k_R v_1 = k_T v_2 = \omega \qquad (2.15)$$

$$\theta_I = \theta_R \qquad (2.16)$$

The third fundamental law of geometrical optics, also known as the law of refraction, or Snell's law, is shown in Equation 2.17.

$$\frac{\sin \theta_T}{\sin \theta_I} = \frac{n_1}{n_2} \qquad (2.17)$$

In a fiber designed for total internal reflection, we do not want any light transmitted through the core to the cladding. Referring to Figure 2-3, when the angle of incidence increases to a certain critical angle, θ_c, all of the light will be reflected. At the critical angle, the angle between the refracted ray and the line normal to the surface will be 90°. Using this information with Snell's law, Equation 2.17, we derive Equation 2.18.

$$\sin \theta_c = \frac{n_2}{n_1} \qquad (2.18)$$

In a fiber, n_1 is the core index of refraction, and n_2 is the cladding index. If light travels in the core of a fiber with an angle of incidence greater than the critical angle, it will be completely reflected, and will continue through the fiber. However, if the light travels with an angle of incidence less than the critical angle, it will be transmitted out of the core to the cladding, and will not propagate down the fiber, as illustrated in Figure 2-4.
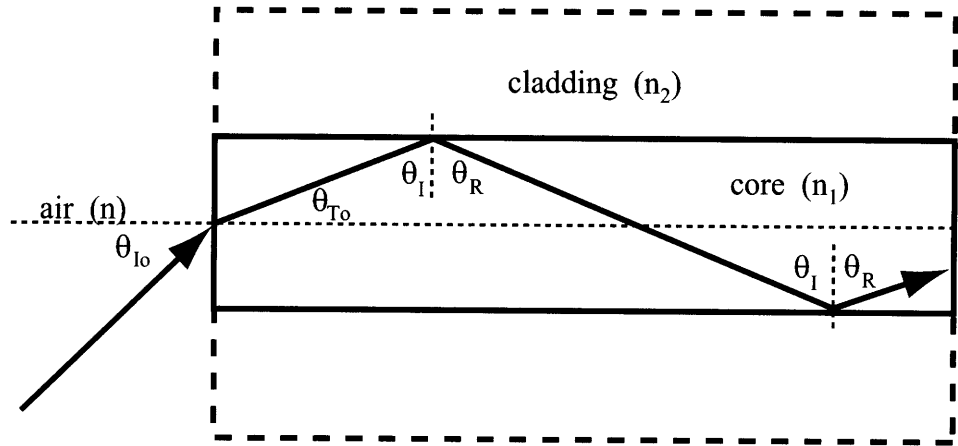
Figure 2-4: Ray entering a fiber and reflecting down the core.

The numerical aperture, N.A., of a fiber is a measure of the light acceptance capability of a fiber, and can be derived as shown in Equation 2.19 [30].

$$n \sin \theta = n_1 \sin \theta_1 = n_1 \sin \left(\frac{\pi}{2} - \theta_c \right) = n_1 \sqrt{1 - \left(\frac{n_2}{n_1} \right)^2} = \sqrt{n_1^2 - n_2^2} = N.A. \quad (2.19)$$

There are four main types of fiber optic cables: multi-mode, single-mode, graded index, and polarization maintaining. The major differences are in the density cross-sections of the fibers, leading to different propagation properties of the fibers. Figure 2-5 shows the four different types of fibers, along with their cross-sections as a function of their indices of refraction.

The multi-mode and single-mode fibers are both step index fibers, where there is an abrupt change from the core to the cladding. However, the multi-mode fiber's core is significantly larger than that of the single-mode fiber. This allows the propagation

51
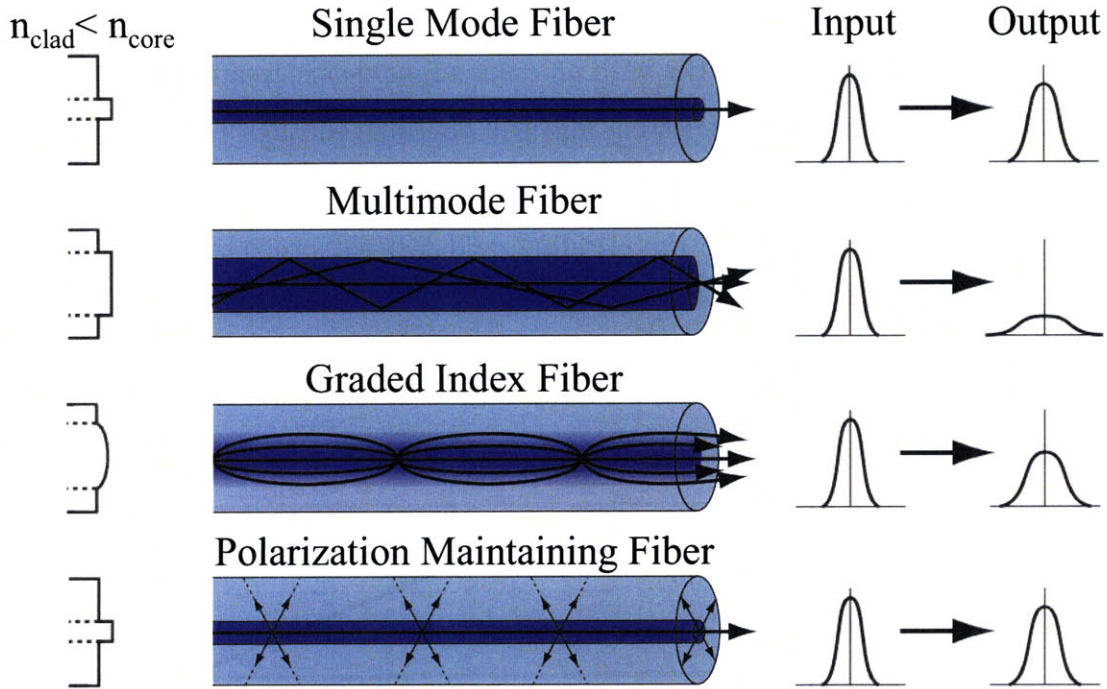
Figure 2-5: Profile of the index of refraction of four different types of fibers, and the dispersion of the input signal (in both time and frequency space).

of many modes of light, as well as many different wavelengths. The graded index fiber has a gradual change from the core to the cladding, which bends the light instead of reflecting it right at the boundary of the core and cladding, as is the case in step indexed fibers. Polarization maintaining fiber is also a single-mode, step index fiber, but it also has some sort of stress rods in the fiber, which separate the propagation paths in the core into a "fast" and a "slow" axis. Each axis only propagates linearly polarized light, and can be viewed as two separate paths in the same fiber. Applications of polarization maintaining fibers will be discussed later.

As shown in Figure 2-5, the single-mode fiber has a much smaller diameter core than the multimode fiber, which leads to the cutoff of other modes. In order to understand the physics behind the cutoffs for certain modes in a fiber, we start with Maxwell's equations, Equations 2.20-2.23.

$$\nabla \times \mathbf{E} = -\frac{\partial \mathbf{B}}{\partial T} \qquad (2.20)$$

$$\nabla \times \mathbf{H} = \mathbf{J} + \frac{\partial \mathbf{D}}{\partial T} \qquad (2.21)$$

$$\nabla \cdot \mathbf{D} = \rho \qquad (2.22)$$

$$\nabla \cdot \mathbf{B} = 0 \qquad (2.23)$$

In Equations 2.20 through 2.23, E is the electric field, H is the magnetic field, D is the electric flux density, and B is the magnetic flux density. The current density, J, and the charge density, ρ, are both equal to zero in an optical fiber since there are no free charges [28]. The relations of D and E, as well as B and H are shown in Equations 2.24 and 2.25.

$$\mathbf{D} = \varepsilon_o \mathbf{E} + \mathbf{P} \qquad (2.24)$$

$$\mathbf{B} = \mu_o \mathbf{H} + \mathbf{M} \qquad (2.25)$$

In Equations 2.24 and 2.25, μ_o and ε_o are the vacuum permeability and permittivity respectively. P and M are the induced electric and magnetic polarizations. Since optical fibers are nonmagnetic, $M = 0$ [28]. Equation 2.26 can be obtained by taking the curl of Equation 2.20, and using Maxwell's other equations.

$$\nabla \times \nabla \times \mathbf{E} = -\frac{1}{c^2} \frac{\partial^2 \mathbf{E}}{\partial t^2} - \mu_o \frac{\partial^2 \mathbf{P}}{\partial t^2} \qquad (2.26)$$

Determining the relationship between the induced polarization and the electric field is usually done quantum mechanically. However, in the 0.5-2 μm range commonly used in optical fibers, the third order nonlinear effects are the dominant component of the induced polarization [28]. Using only the third order effects, and assuming that the fibers are low loss and spatially uniform, Equation 2.26 can be simplified to Equation 2.27 (A more detailed derivation is available in Reference [28]).

53

$$\nabla^2 \tilde{\mathbf{E}} + n^2(\omega)\frac{\omega^2}{c^2}\tilde{\mathbf{E}} = 0 \tag{2.27}$$

In Equation 2.27, $\tilde{E}$ is the Fourier transform of the electric field, defined by Equation 2.28.

$$\tilde{\mathbf{E}}(\mathbf{r}, \omega) = \int_{-\infty}^{\infty} \mathbf{E}(\mathbf{r}, t)e^{i\omega t}dt \tag{2.28}$$

Since fibers are cylindrical, it makes sense to write Equation 2.27 in cylindrical coordinates, as is done in Equation 2.29.

$$\frac{\partial^2 \tilde{\mathbf{E}}}{\partial \rho^2} + \frac{1}{\rho}\frac{\partial \tilde{\mathbf{E}}}{\partial \rho} + \frac{1}{\rho^2}\frac{\partial^2 \tilde{\mathbf{E}}}{\partial \phi^2} + \frac{\partial^2 \tilde{\mathbf{E}}}{\partial z^2} + n^2 k_o^2 \tilde{\mathbf{E}} = 0 \tag{2.29}$$

Equation 2.29 uses $k_o = \frac{\omega}{c} = \frac{2\pi}{\lambda}$. Since E and H satisfy Maxwell's equations, only two of the six components are independent. Conventionally, $\tilde{E}_z$ and $\tilde{H}_z$ are chosen as the independent variables, and using the method of separation of variables, the wave equation for $\tilde{E}_z$ can be solved in the form shown in Equation 2.30 [28].

$$\tilde{E}_z(r, \omega) = A(\omega)F(\rho)e^{\pm im\phi}e^{i\beta z} \tag{2.30}$$

In Equation 2.30, A is a normalization constant, β is the propagation constant, m is an integer, and $F(\rho)$ is the solution of the differential equation for Bessel functions expressed in Equation 2.31.

$$\frac{d^2 F}{d\rho^2} + \frac{1}{\rho}\frac{dF}{d\rho} + \left(n^2 k_o^2 - \beta^2 - \frac{m^2}{\rho^2}\right)F = 0 \tag{2.31}$$

The index of refraction, n, in Equation 2.31 is the core index of refraction for $\rho \leq a$, and the cladding index of refraction for $\rho > a$. Using boundary conditions, and looking for physically meaningful solutions, the general solutions can be expressed as in Equations 2.32 and 2.33 [28].

$$F(\rho) = J_m(\kappa\rho), \kappa = \left(n_1^2 k_o^2 - \beta^2\right)^{\frac{1}{2}} \tag{2.32}$$

$$F(\rho) = K_m(\gamma\rho), \gamma = \left(\beta^2 - n_2^2 k_o^2\right)^{\frac{1}{2}} \qquad (2.33)$$

Solving the eigenvalue equation, we obtain an important relationship, Equation 2.34 [28].

$$\kappa^2 + \gamma^2 = \left(n_1^2 - n_2^2\right) k_o^2 \qquad (2.34)$$

Fiber design parameters, such as the core diameter, a, as well as the indexes of refraction for the core and cladding will determine what modes of a given wavelength are supported in that fiber. The cutoff frequency of a fiber is determined by solving Equation 2.34 when $\gamma = 0$ [28]. A common parameter associated with the cutoff frequency is the normalized frequency, V, as expressed in Equation 2.35.

$$V = \kappa_c a = k_o a \left(n_1^2 - n_2^2\right)^{\frac{1}{2}} \qquad (2.35)$$

A single mode fiber, by definition, supports only one mode, the HE_{11} mode which is also known as the fundamental mode. When the normalized frequency is less than the critical normalized frequency of $V_c \approx 2.405$, determined by the smallest solution to the Bessel function, all other modes are cut off, and the fiber is a single-mode fiber as seen in Figure 2-6. Since the micro-bending losses increase with decreasing $\frac{V}{V_c}$, single mode fibers are generally designed with V close to V_c [28]. In order to determine the cutoff wavelength for a fiber, $k_o = \frac{2\pi}{\lambda_c}$ can be substituted into Equation 2.35, using $V = 2.405$.

Energy is not only carried in the core of the fiber, but also in the cladding. This energy carried in the cladding is due to evanescent wave phenomena, and exponentially decreases with distance into the cladding as described by Equations 2.36 and 2.37 [30].

$$E = E_o e^{-\beta r} \qquad (2.36)$$
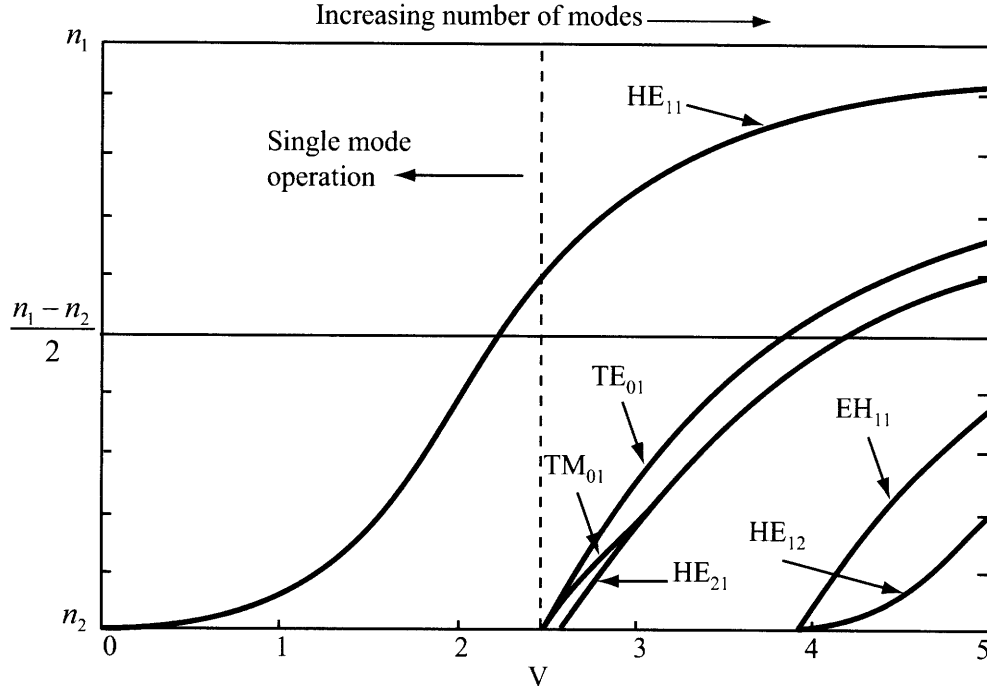
Figure 2-6: Mode formation as a function of the normalized frequency parameter, V.

$$\beta = k_o\sqrt{n_1^2\sin^2\phi - n_2^2} \qquad (2.37)$$

The penetration distance can be solved by using Maxwell's equations at the interface, as is done in Equation 2.37 [31].

$$d_p = \frac{\lambda}{2\pi\sqrt{n_1^2\sin^2\phi - n_2^2}} \qquad (2.38)$$

Although the penetration depth is expressed in Equation 2.38, most of the power is contained in a distance of 1-10 λ into the cladding. Figure 2-7 shows the basic layout of a fiber optic cable, along with some of the general dimensions.

There are many sources of attenuation in fibers, such as absorption, scattering, micro-bending and end losses due to reflection. Attenuation in fibers is defined by Equation 2.39, where P_i is the input power, and P_o is the output power. The units of attenuation are decibels per unit length, normally dB/km.
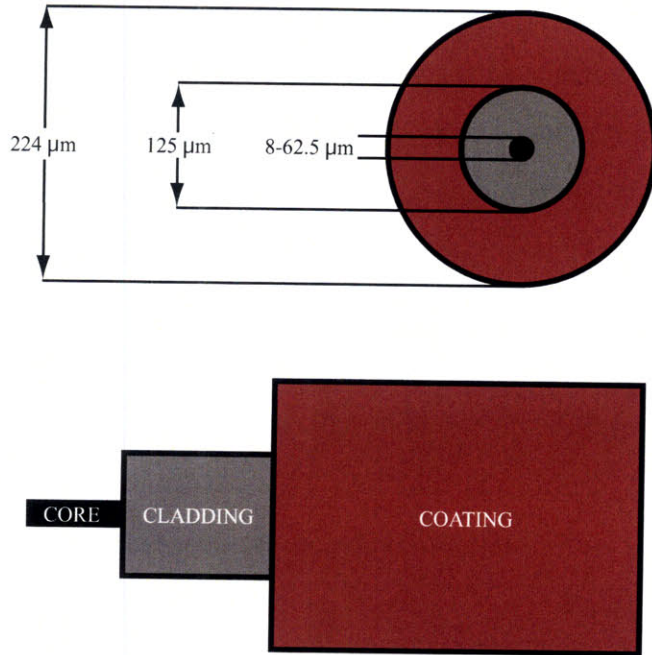
Figure 2-7: Cross-section and cut-away of a fiber with typical dimensions.

$$A = -10 \log \frac{P_i}{P_o} \tag{2.39}$$

Impurities in fibers, such as copper, chromium, iron, and hydroxyl ions absorb and scatter the light [30]. These different impurities cause losses at different wavelengths, and the sum of the losses from these impurities creates certain "pockets" where attenuation is a minimum. Rayleigh scattering is the dominant attenuation mechanism for low wavelengths since it is proportional to λ^{-4} [30]. Micro-bending losses are due to changes in the shape of the fiber, and are very useful in sensor applications. Reflection losses at the ends of the fibers are unavoidable if there is a glass-local atmosphere interface; however, it is easy to calculate using Fresnel's equations.

Another unavoidable problem with fiber optics is the dispersion of the initial signal as a function of length traveled. The most obvious source of dispersion seen in multimode fibers is the different total lengths of travel by the light. Since the core of a multi-mode fiber is quite large, a ray bouncing off of the walls a lot will travel slower than a wave traveling straight down the center, and therefore broaden the input pulse, as shown in Figure 2-5.

57

A more subtle form of dispersion is called chromatic dispersion, which is due to the frequency dependence of the index of refraction. Lasers do not produce perfect delta functions in frequency space; therefore, all laser pulses have a distribution of frequencies. The frequency dependence of the index of refraction allows the longer wavelengths to travel faster than the shorter wavelengths, which over a long fiber, will lead to broadening of the input pulse.

Polarization mode dispersion is another type of dispersion that will broaden an input pulse. Irregularities in the fiber will cause the light to travel at different speeds at different spatial locations in the fiber. This change in speed of the modes in a fiber will cause them to arrive at the detector at slightly different times, which causes the input pulse to broaden.

In order for chromatic dispersion or polarization mode dispersion to have deleterious effects on a signal, the optical path needs to be extremely long or the input pulses need to be very short. Luckily, in the field of fiber optic sensors, it is uncommon to use sensing paths long enough or pulses short enough for dispersion to be a problem.

2.2.2 Fiber Optic Diagnostics

As the field of fiber optic sensing continues its rapid development, fiber optic sensors are being implemented in many applications with better results than conventional sensors. The most obvious advantage fiber optic sensors have over conventional sensors is that fiber optics are immune to radio frequency and electromagnetic fields and fluctuations. Due to the small size and weight, fiber optic sensors can be fit into normally inaccessible spaces. Since fiber optic cables are extremely low-loss, they can be used as remote sensors. Fiber optic sensors can securely transfer data over long ranges, and can easily be interfaced with data communication systems.

Fiber optic sensors can be used to measure an extremely wide range of parameters. The most common fiber optic sensors are Fiber Bragg Gratings (FBG), which are used to measure temperature and strain; however, the temperature and strain can also be measured using many other fiber optic sensors. Pressure and flow are two common parameters measured by fiber optic sensors. Although fiber optic cables are immune

to electromagnetic fields and fluctuations, specially engineered fiber optic sensors can be used to measure magnetic fields, electric fields, and even the current in a wire. Fiber optic sensors are commonly used as radiation sensors and also chemical sensors in solutions that would destroy conventional sensors. Three dimensional motion is also routinely measured using fiber optic interferometric sensors called optical gyroscopes. Fiber optic systems are employed in buildings and bridges and can monitor the real time temperatures and strains throughout the structures.

Fiber Bragg Gratings are used routinely to measure either temperature or strain in experiments operating around room temperature. Using ultraviolet light, a grating is inscribed in the core of the fiber. The grating will reflect light with the same wavelength as the period of the inscribed grating. When the FBG is heated or strained, the physical period of the grating also changes, and therefore the grating reflects a different wavelength. The change in the reflected wavelength of a FBG is dependent on both the change in temperature and the change in strain as expressed in Equation 2.40.

$$\Delta\lambda_{FBG} = \Delta\lambda_\varepsilon + \Delta\lambda_T \tag{2.40}$$

The shifts due to temperature and strain are described in Equations 2.41 and 2.42.

$$\Delta\lambda_T = \lambda_{FBG}(\alpha + \xi)\Delta T \tag{2.41}$$

$$\Delta\lambda_\varepsilon = \lambda_{FBG}(1 - P_\varepsilon)\Delta\varepsilon \tag{2.42}$$

In Equation 2.41, α is the thermal expansion coefficient, and ξ is the thermo-optic coefficient. In Equation 2.42, P_e is the photo-elastic constant. Special FBGs known as Long Period Gratings, or LPGs, can be used together with regular FBGs to simultaneously determine temperature and strain. The length of a grating, typically about one cm, is a design variable that can be decreased to achieve better spatial resolution. However, the amount of reflected light is proportional to the length of the grating. Although FBGs are "point" sensors, one fiber can have many FBGs inscribed

59

along its length. There are two methods that are used to separate the signals from the FBGs on a fiber: time-based and time-based. The time-based method uses Optical Time Domain Reflectometry (OTDR), sending pulses of light down the fiber and mapping the position of the signal based on the time the signal is received. The frequency-based system uses gratings with different initial periods, so that they all reflect a different wavelength of light. In the experiments discussed in this thesis we used FBGs as strain gages, described in more detail in Appendix A.

Fiber optic temperature sensors use a variety of materials that change their spectral response, size, or opaqueness, such as liquid crystals, birefringent materials, semiconductor materials, and fluorescent materials [30]. One example of a fiber optic temperature sensor is shown in Figure 2-8.
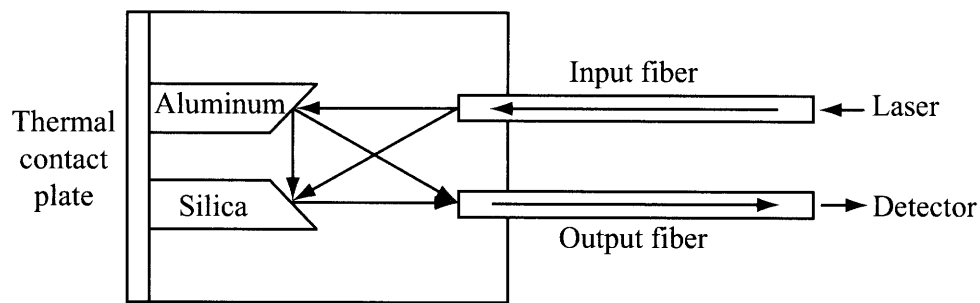
Figure 2-8: Temperature sensor using the difference in thermal expansions of aluminum and silica.

The aluminum and silica have different thermal expansion coefficients, so a temperature change will change the relative location of the mirrors; and therefore, the light coupled back into the fiber.

Another fiber optic temperature sensor relies on the absorptivity of erbium-doped glass. Erbium is mixed into the glass fiber and as the temperature changes the intensity of the light at the far end of the fiber is measured [4]. Figure 2-9 shows the temperature dependence of Erbium, which allows an erbium-doped fiber to be used as a thermometer for some cryogenic applications.

Displacement sensors are another area where fiber optic sensors are frequently used. There are two main fiber optic displacement sensors: reflective sensors, and
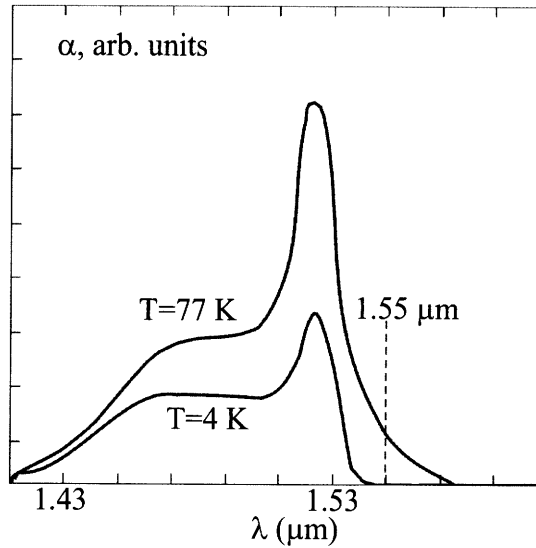
Figure 2-9: Absorption spectrum for an Erbium doped fiber at 4 K and 77 K (From reference [4].

micro-bending sensors. Reflective sensors have at least two fibers ending very close to a reflective surface. One fiber carries the source light, and the other fibers receive the reflected light. Since the angle of reflection is equal to the angle of incidence, the area of the reflected spot at the fiber tips is twice as large as the spot that hits the target originally. As the length, L, between the fiber tips and the reflective surface increases, the spot area increases proportional to L^2, and the intensity received by the sensing fibers is proportional to $\frac{1}{L^2}$ [30]. The layout is shown in Figure 2-10.

Micro-bending of a fiber causes losses due to radiated energy [32]. A simple way to think about this loss is that when a fiber is bent, the normal plane changes relative to the propagating light, so the rays propagating at close to the critical angle may get absorbed into the cladding depending on the degree of the bend. By placing a fiber in a mechanism, like the one shown in Figure 2-11, and measuring the intensity of the light at the far end of the fiber, the displacement can be measured as a loss in intensity.

Parameters like pressure and flow can be measured by fiber optics by relating the parameter to a displacement. Using a reflective surface on a diaphragm would relate the pressure to a displacement. By forcing fluid through a restriction area with reduced area causes an increase in flow rate around that point, causing a pressure

61
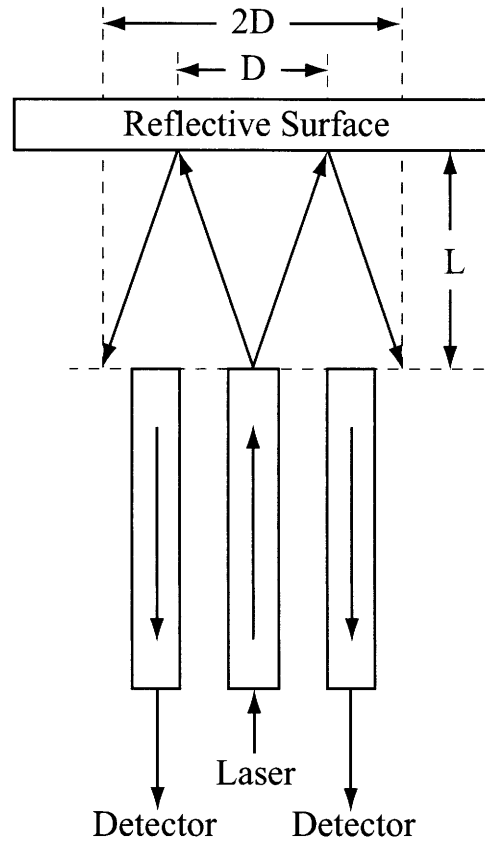
Figure 2-10: A displacement sensor with one input fiber and two fibers receiving the reflected light.

drop [30]. This pressure drop can also be related to a displacement, as described above.

Using a fiber optic sensor to detect magnetic or electric fields is similar to using fiber optics to detect pressure or flow. The most common way to detect a magnetic field is to use a magnetostrictive material, and somehow make that material cause a physical change in the fiber. Fibers can be coated with materials such as nickel alloys, cobalt-iron alloys, or certain metallic glasses [30]. A fiber can also be wound around a cylinder, or epoxied to a plate of one of these alloys. By positioning an FBG to be epoxied to the surface of the magnetostrictive material, or to be coated by one, the magnetic field is converted to a strain, which is easily measured by standard FBG methods. By positioning a magnetostrictive material in the correct location and orientation in regards to a cable, the magnetic field can be used to determine the current in the cable.
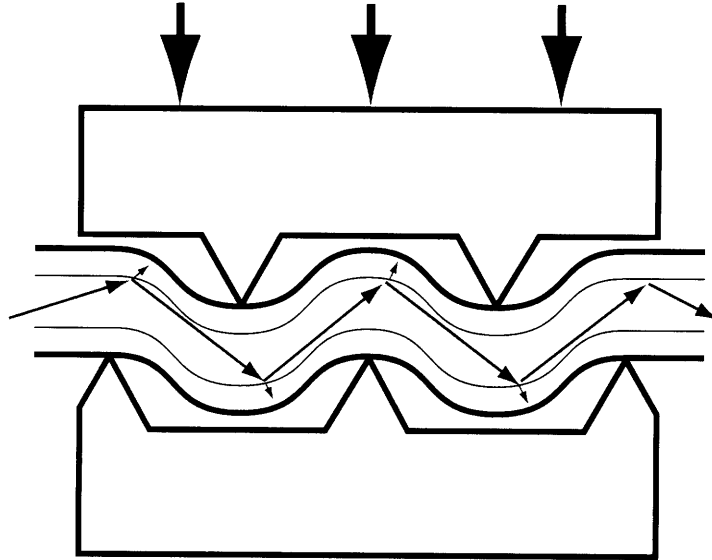
Figure 2-11: Micro-bending losses in a fiber being used as a displacement sensor.

The electric field can be measured in the same way as the magnetic field, only using an electro-optic material instead of a magnetostrictive material. Epoxying an FBG to the electro-optic material will convert the effect of the electric field into a strain that can be easily measured. Materials exhibiting the Pockels effect, a change in refractive index directly proportional to the electric field, or the Kerr effect, a change in the refractive index proportional to the square of an electric field, can also be used to measure the electric field [30]. This requires an electro-optic material to be in the light path, which normally requires lenses to couple the light out of, and back into, the fibers.

Fiber optic gyroscopes have several advantages over other mechanical devices: there are no moving parts, they are small and extremely rugged, they turn on instantly, have a long shelf-life, and are almost maintenance free [33]. The most common gyroscope uses the Sagnac effect to determine the rotation rate [30]. By using three gyroscopes to determine the rotation in all three dimensions, a system can be tracked or directed. This type of gyroscope system is used in navigational systems in planes, missiles, and satellites. As shown in Figure 2-12, the light is split into two paths, each traveling along the same circle, but in opposite directions.

This gyroscope is an interferometer, where the two legs are the paths in opposite
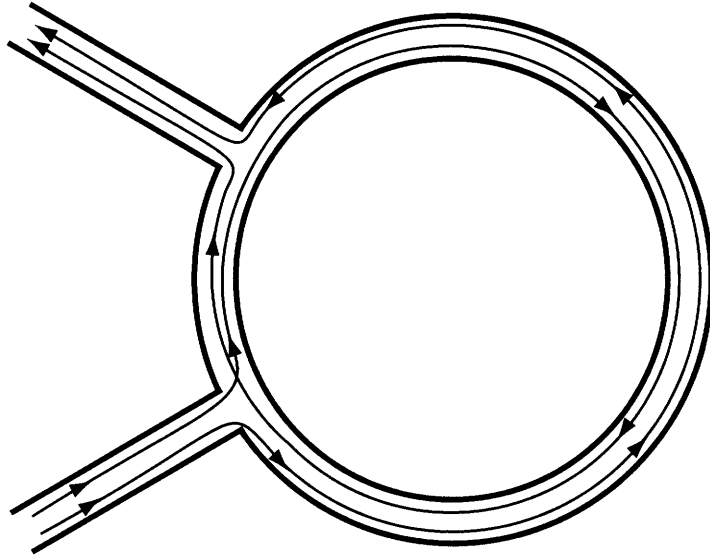
Figure 2-12: In a Sagnac interferometer, light travels in opposite directions around a circle and then is recombined to measure rotation.

directions around the circle. When the gyroscope rotates, the relative path lengths of the two directions changes, and it takes the light traveling in one direction a little longer to get to the detector than the other direction. The phase shift, $\Delta\phi$, of the interfered light is measured and can be expressed as a function of rotation rate, Ω, shown in Equation 2.43.

$$\Delta\phi = \left(\frac{2\pi LD}{\lambda_o c}\right) \Omega \tag{2.43}$$

The fiber length, L, and loop diameter, D, can also be used in an expression for the total change in path length shown in Equation 2.44.

$$\Delta L = \left(\frac{LD}{c}\right) \Omega \tag{2.44}$$

Although the previously discussed fiber optic sensors are mostly point sensors, they can be combined into systems that give some spatial resolution. Knowing the location of an array of point sensors, and being able to distinguish the signals from each of the different sensors allows a degree of spatial resolution. Fibers can also be run along pipelines, country borders, bridges, etc. to sense changes in the initial con-

64

ditions. Using the simplest techniques, a break in a fiber due to a pipeline explosion, or concrete cracking can be detected and located. More advanced systems looking at scattered light can make distributed measurements along long sensing paths, which will be described in more detail later in this chapter.

2.2.3 Interferometers

Different types of interferometers can be used to measure parameters other than rotation, including temperature and strain. If a fiber optic cable is heated, the optical path length changes due to thermal expansion, as well as due to the temperature dependence of the index of refraction, as expressed in Equation 2.45.

$$\Delta\phi = \frac{2\pi}{\lambda}(n\Delta L + \Delta nL) \tag{2.45}$$

By carefully measuring the change in the optical path length, the associated change in temperature can be derived. In order to accurately measure the change in optical path length, an interferometer is used. The two most common types of interferometers are the Mach-Zehnder and the Michelson interferometers, pictured in Figure 2-13.
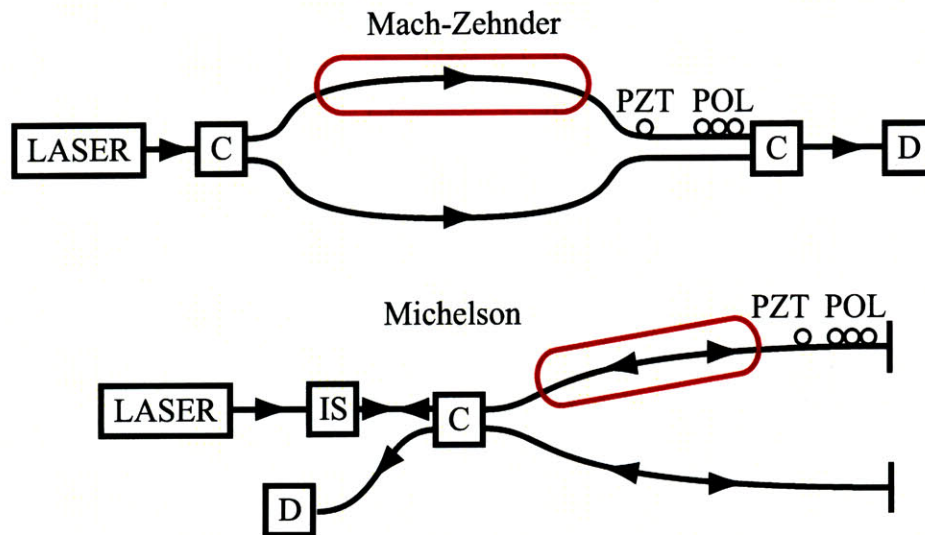
Figure 2-13: Schematic diagram of a Mach-Zehnder and Michelson interferometer.

One leg of the interferometer is subject to the change in temperature and the other leg is held at a constant temperature to serve as a reference. Laser light is coupled into both legs, and then recombined after passing through the two legs. An interference pattern is formed based on whether the two signals are constructively or destructively interfering. As the temperature in the sensing arm increases, the index of refraction increases, causing the speed of light in the fiber to decrease. This has the overall effect of lengthening the optical path length compared to the reference path length. The interference pattern shifts back and forth from constructive to destructive interference as the optical path length increases, creating an intensity pattern that oscillates from zero to some maximum value, as shown in Figure 2-14.

The reason that fiber optic interferometers are interesting for use in superconducting magnets is that the sensing path and reference arm can be any length because fibers are so low-loss. Running a fiber through the conduit in a CICC magnet, will allow the whole length of the cable to be monitored. Although the measurement is a line-integrated measurement along the length of the fiber, it will be able to pick up temperature changes at any location.

Placement of a temperature sensing fiber in a CICC is a very important decision that needs to be made based on the mechanical integrity of the fiber as well as the thermal diffusion time from the superconducting strands to the fiber. There are several regions where the fiber will be relatively safe, such as the central cooling channel and the inner or outer valleys created by the winding patterns, as shown in Figure 2-15. Regardless of the placement of the fiber, it needs to be protected from being crushed during the magnet fabrication and from Lorentz loads during a magnet pulse. One way to protect the fiber is to put it in a steel capillary tube, perhaps with a fiberglass sleeve between the fiber and the tube for further protection. This protection system, shown in Figure 2-16, was used for the fibers in the QUELL tests.

A coating for the fiber also has to be chosen carefully, since the fiber will have to survive several thermal cycles from room temperature down to cryogenic temperatures. Depending on the type of superconductor being used, it may also have to
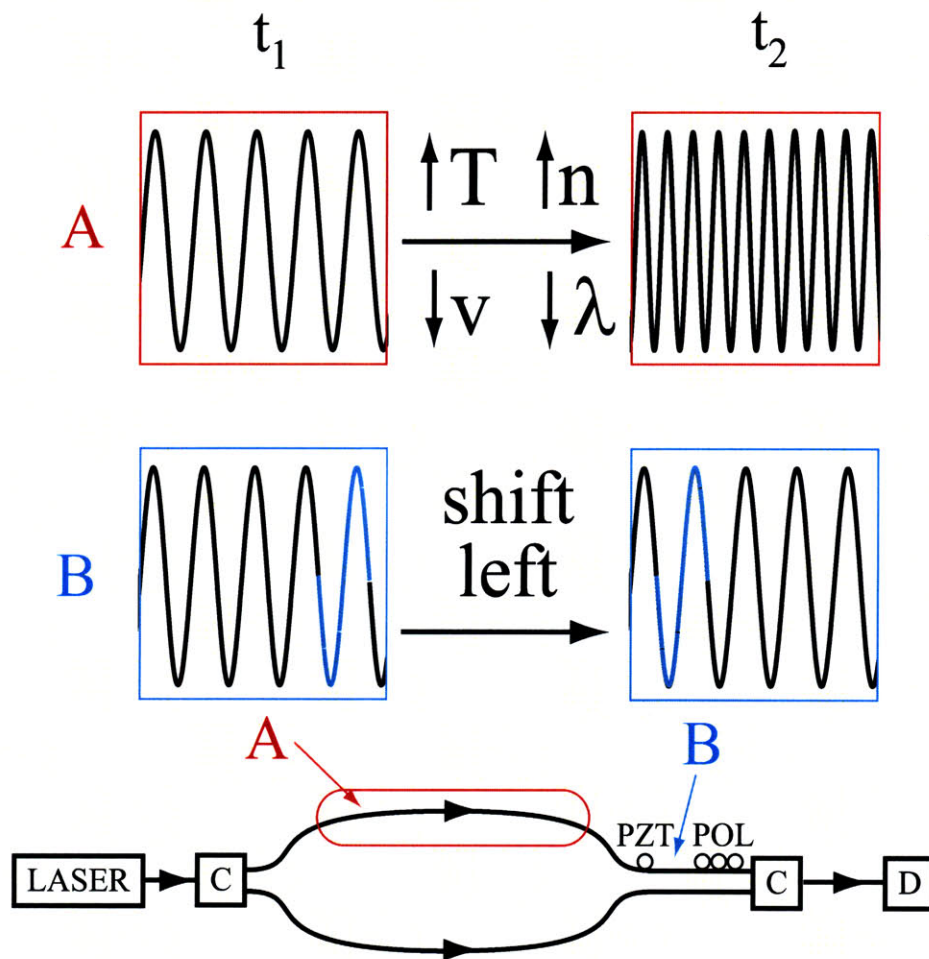
Figure 2-14: A view of the signal before (left) and after (right) the sensing arm is heated. The top view (A) is the heated fiber and the bottom (B) is the unheated fiber. The changes in the heated fiber cause the signal in the unheated fiber to effectively shift to the left. Combining this signal with the reference gives fringe shifts.

survive a heat treatment from tens to hundreds of hours at temperatures up to 700 C. At these high temperatures, the normal acrylate coating on fibers will vaporize, leaving a bare fiber. One solution is to use gold or copper coated fibers that will survive the extreme temperatures. These are typically much more expensive than commercial fibers, but still significantly less expensive than a superconducting cable.

QUELL was the first major experiment to test a fiber optic quench detection system for large magnets and compare it to other quench detection methods. A copper coated fiber arranged as a Michelson interferometer was used with the sensing arm terminated by an internal mirror in the magnet so only one extraction was needed. This

Figure 2-15: The fiber can be placed in the valleys due to the winding, in the central cooling channel, or co-wound with the superconducting wires.
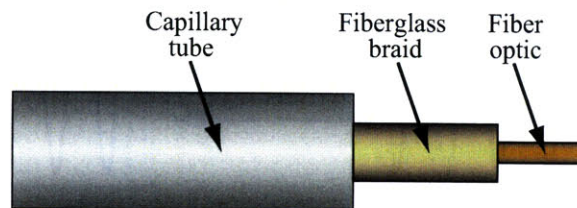
Figure 2-16: Diagram of the steel capillary tube and fiberglass protection of a fiber optic cable.

system performed very well in the QUELL tests, quickly detecting sample quenches with no false quench detections [16]. A positive feature of an interferometric quench detection system is that the temperature sensitivity of the refractive index increases with increasing cryogenic temperatures. The sensitivity is 200 times higher at 30 K than it is at 5 K [7]. This means that a disturbance that raises the magnet temperature from 5 K to 5.2 K over a 1 km length will give a much smaller signal than a temperature rise to 30 K over only 1 meter of the magnet, which is a realistic early quench stage [7].

Although the fiber optic quench detection system performed as well as the co-wound voltage taps, external co-wound voltage taps were chosen to be used on ITER with expected performance not quite as good as that of the internal co-wound taps tested by QUELL. The extraction of a fiber from a conduit is a difficult and unproven engineering task. A seal needs to be formed at the point of extraction that will not break the fiber, or leak through many thermal and pressure cycles. Several sealants,

such as Stycast, were shown to be leak-tight at a high vacuum level up to 70 atm. However, no seals tested as part of the KSTAR program were able to survive tens of thousands of pressure cycles.

Another problem facing the QUELL fiber optic quench detection system was the elimination of the strain contribution to the fringe shifts. Both a change in temperature and a change in strain of the fiber will lead to fringe shifts, and determining what shift is due to temperature and what shift is due to strain is a problem that will be discussed further in the next section.

2.2.4 Separation of Temperature and Strain

The optical path length in a fiber is a function of the actual length of the fiber and its index of refraction. Unfortunately, both a change in temperature and a change in strain will change the optical path length. If it is known that a fiber is either strain-free or at a constant temperature, an interferometer system could easily measure the other parameter. However, when the fiber can be strained and is not held at a constant temperature, determining the change in temperature becomes a more difficult problem. As seen in Equation 2.46, there is only one measured quantity, $\Delta\phi$, and there are two unknowns, ΔT and $\Delta\varepsilon$.

$$\Delta\phi = \frac{2\pi}{\lambda_o} \left[n\frac{\partial L}{\partial T}\Delta T + n\frac{\partial L}{\partial \varepsilon}\Delta\varepsilon + L\frac{\partial n}{\partial T}\Delta T + L\frac{\partial n}{\partial \varepsilon}\Delta\varepsilon \right] \qquad (2.46)$$

In order to be able to separate the temperature and strain contributions, we need another independent measurement. By using a dual-interferometer system of two frequencies or two polarizations, the temperature and strain contributions to the phase shift can be separated [34]. The layout of a dual-frequency interferometer system is shown in Figure 2-17.

This system is based on the assumption that the two fibers traveling the same path through the magnet, but carrying different frequencies of light, will experience the same temperature and strain. By measuring the two phase shifts, $\Delta\phi_1$ and $\Delta\phi_2$, we get two equations and two unknowns as described in Equations 2.47 and 2.48.
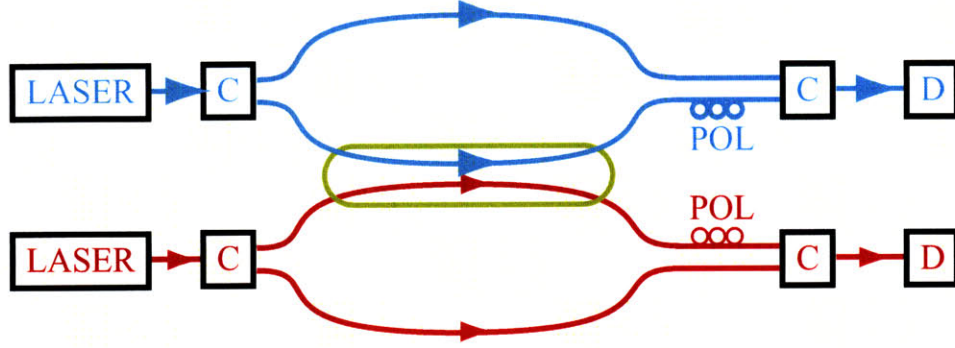
Figure 2-17: A dual-frequency Mach-Zehnder interferometer system with the common sensing path circled in green.

Assuming that $\left(\frac{\partial n}{\partial T}\right)_1$ and $\left(\frac{\partial n}{\partial T}\right)_2$ are different, which is true for certain wavelengths, we can solve this set of equations for the change in temperature and strain [35].

$$\Delta\phi = \frac{2\pi}{\lambda_o}\left[n\frac{\partial L}{\partial T}\Delta T + n\frac{\partial L}{\partial \varepsilon}\Delta\varepsilon + L\left(\frac{\partial n}{\partial T}\right)_1\Delta T + L\frac{\partial n}{\partial \varepsilon}\Delta\varepsilon\right] \qquad (2.47)$$

$$\Delta\phi = \frac{2\pi}{\lambda_o}\left[n\frac{\partial L}{\partial T}\Delta T + n\frac{\partial L}{\partial \varepsilon}\Delta\varepsilon + L\left(\frac{\partial n}{\partial T}\right)_2\Delta T + L\frac{\partial n}{\partial \varepsilon}\Delta\varepsilon\right] \qquad (2.48)$$

Another way to eliminate the strain contribution is to use a polarization maintaining fiber, and to have interferometer's two arms be the two axes in the fiber. A polarization maintaining fiber is designed so that there is a fast axis and a slow axis that can each propagate linearly polarized light independent of the other axis, as shown in Figure 2-18.
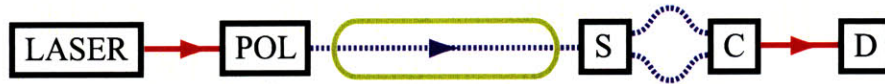
Figure 2-18: A dual-polarization interferometer with the sensing path circled in green.

Although we can assume that the two sensing fibers with different frequencies of light in the previous dual-interferometer system experience the same strain, in this system we know that both arms of the interferometer experience the same strain,

70

since they are in the same fiber. Since the change in length of the fast and slow axis is exactly the same, the first two terms in Equation 2.49 are zero.

$$\Delta\phi = \frac{2\pi}{\lambda_o}\left[n\left(\frac{\partial L_f}{\partial T} - \frac{\partial L_s}{\partial T}\right)\Delta T + n\left(\frac{\partial L_f}{\partial \varepsilon} - \frac{\partial L_s}{\partial \varepsilon}\right)\Delta\varepsilon + L\left(\frac{\partial n_f}{\partial T} - \frac{\partial n_s}{\partial T}\right)\Delta T + L\left(\frac{\partial n_f}{\partial \varepsilon} - \frac{\partial n_s}{\partial \varepsilon}\right)\Delta\varepsilon\right]$$
(2.49)

Because both arms are in the same fiber, the effect of strain on the two arms is negligible. However, there is a small difference in the propagation constants of the two axes which causes them to experience slightly different responses to changes in temperature [34]. This leaves us with Equation 2.50.

$$\Delta\phi = \frac{2\pi}{\lambda_o}\left[L\left(\frac{\partial n_f}{\partial T} - \frac{\partial n_s}{\partial T}\right)\Delta T\right]$$
(2.50)

By measuring the relative phase change between the two axes of the polarization maintaining fiber, we can calculate the change in temperature because everything else in Equation 2.50 is known.

The typical sensitivities of the dual-frequency and the dual-polarity interferometer systems are shown in Table 2.1.

Table 2.1: Sensitivities of dual-interferometers to temperature and strain (from Reference [7]).

Method	Temperature Sensitivity (radians / m K)	Strain Sensitivity (radians / m ε)
Dual-Frequency	0.1	500
Dual-Polarity	1.2	5000

2.3   Fiber Optic Scattering System

While a dual-interferometer system is able to cancel the strain contribution to the phase shift, and therefore provide a reliable temperature measurement, it can still only provide a line-integrated measurement. By using several Michelson interferometers of different lengths which monitor different parts of the magnet, one could get

some spatial resolution, proportional to the channel length divided by the number of interferometers. In order to achieve better spatial resolution, scattering measurements need to be used. The three main scattering processes in optical fibers are Rayleigh, Raman, and Brillouin scattering, and their relative frequency shifts are shown in Figure 2-19.
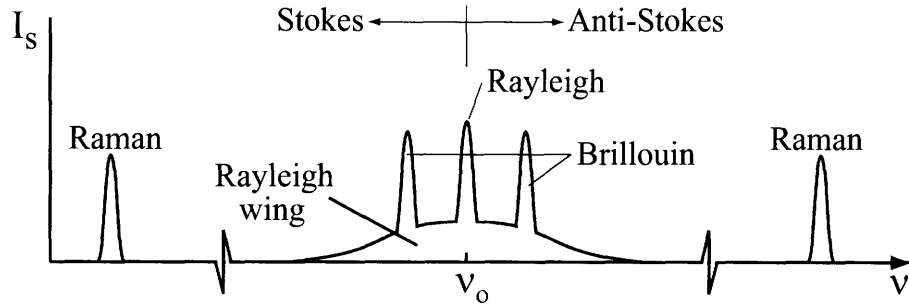
Figure 2-19: Typical spectrum of scattered light in a fiber.

There are three commonly used reflectometric techniques used in fiber-based measurements: optical time domain reflectometry (OTDR), low coherence frequency domain reflectometry (OLCR), and coherent optical frequency domain reflectometry (OFDR). These techniques differ in the basic physics and consequently have trade offs in resolution, speed, sensitivity, and accuracy. OTDR is generally used for long range (km) low-resolution ($\approx$ 1 m) applications, OLCR achieves sub-millimeter resolution over short ranges ($\leq$ 5 m), and OFDR operates in the middle with a range of 10s to 100s of meters and resolution on the mm to cm scale [36].

2.3.1 Rayleigh Scattering

Rayleigh scattering in an optical fiber is generated by fluctuations in the density and radius of the core as a function of length. A baseline measurement of the Rayleigh backscatter along the length of a fiber can be used as a "signature" since it is a permanent feature of the fiber [37]. These random fluctuations are static; therefore, they can be modeled as a continuous FBG in Equation 2.51 [38].

$$\nu_R = \frac{c}{2n\bar{\Lambda}} \tag{2.51}$$

72

Here ν_R is the spectral frequency associated with the grating, n is the index of refraction, c is the speed of light, and $\bar{\Lambda}$ is the average fluctuation period. A change in the local index of refraction or average fluctuation period (due to a stimulus like temperature or strain) will cause shifts in the local spectral frequency of the Rayleigh backscatter. Accumulated changes will be seen as a time shift of the Rayleigh backscatter return loss amplitude. By cross-correlating the backscatter amplitude time domain or frequency domain data, the system will measure the shifts and scale them to a change in temperature or strain [39].

Some systems use swept-wavelength interferometry (SWI) to measure the complex scalar response of the system, including the amplitude and phase [40]. Figure 2-20 shows a simplified diagram of this type of system [37].
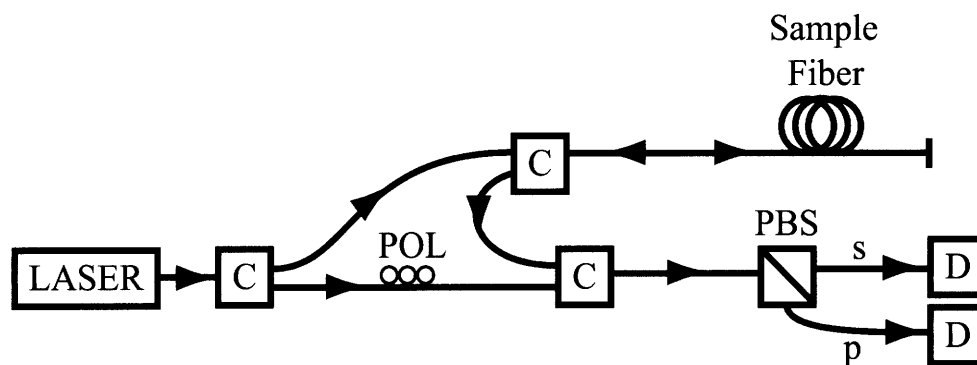
Figure 2-20: Diagram of a typical Rayleigh backscatter system.

Light from a tunable laser source is split by the first coupler with half of the signal going to the fiber under test and the other half going through the reference path and the polarization controller. Another coupler recombines the two signals and a polarization beam splitter splits the signal to detect two polarizations of light independently. The polarization controller is used to align the reference field so that it is split evenly between the polarization states, which ensure that an interference signal will be present on at least one of the detectors regardless of the polarization state coming out of the fiber under test [37].

The frequency response of the fiber under test is a function of amplitude and phase response, as shown in Equation 2.52 [38].

$$H(\omega) = \rho(\omega)e^{i\Phi(\omega)} \tag{2.52}$$

Assuming that the field from the laser is E_{in}, Equation 2.53 is the field at the coupler [38].

$$E_{out} = \frac{1}{\sqrt{2}}E_{in} + \frac{1}{\sqrt{2}}E_{in}\rho(\omega)e^{i(\Phi(\omega)+\omega(t)\Delta\tau)} \tag{2.53}$$

In the above equation, $\Delta\tau$ is the delay difference between the two arms of the interferometer, and $\omega(t)$ is the laser frequency. By squaring the magnitude of the field we can get the detected power shown in Equation 2.54.

$$P(\omega) \approx \frac{1}{2}E_{in}^2(\omega) + \frac{1}{2}\rho^2(\omega)E_{in}^2(\omega) + E_{in}(\omega)\rho(\omega)\cos\left[\Phi(\omega) + \omega(t)\Delta\tau\right] \tag{2.54}$$

This equation is a frequency domain description of the fiber under test. By Fourier transforming this equation into the time domain, we get a representation of the fiber under test as a function of length [37].

LUNA Technologies has developed a commercial temperature and strain measuring system based on Rayleigh scattering. In order to make a measurement, the Rayleigh scattering signature is measured and stored. The scatter profile is then measured after some change in strain or temperature, and the data sets are compared in pre-determined increments [41]. The basic LUNA system cannot simultaneously measure the temperature and strain; but for a constant strain, the change in temperature can be calculated using Equation 2.55 [38].

$$\Delta T = \frac{-\bar{\lambda}}{cK_T}\Delta\nu \tag{2.55}$$

For a constant temperature the strain can be calculated using Equation 2.56.

$$\Delta\varepsilon = \frac{-\bar{\lambda}}{cK_\varepsilon}\Delta\nu \tag{2.56}$$

Shown in Equation 2.57 the maximum sensing length can also be calculated [36].

$$L_{max} = \frac{c\Delta\tau_g}{4n_g} \tag{2.57}$$

Here c is the speed of light in a vacuum, n_g is the group index, and $\Delta\tau_g$ is the delay in the interferometer.

The spatial resolution is directly related to the resolution in the time domain and is determined by the spectral bandwidth of the scan range by Equations 2.58 and 2.59 [36].

$$\Delta z \approx \frac{c}{2n_g\Delta f} \tag{2.58}$$

$$\Delta f \approx \frac{c\Delta\lambda}{\lambda^2} \tag{2.59}$$

The fundamental limits of temperature and strain measurements are not independent of the variables selected for measurement. For distributed sensing, the parameters of the LUNA system are expressed in Table 2.2 [36].

Table 2.2: LUNA's Rayleigh scattering system's specifications.

Spatial Resolution	2.0 cm
Temperature Resolution	$\pm$ 0.1 C
Strain Accuracy	$\pm$ 1 $\mu\varepsilon$
Maximum Fiber Length	70 m
Measurement Timing	3 - 10 sec

Temperature and strain can be simultaneously measured using a polarization maintaining fiber with a spatial resolution of 2 cm with temperature and strain resolution of $\pm$ 3.5 C and $\pm$ 35 $\mu\varepsilon$ [42]. As seen in Table 2.2, although the resolutions and accuracies would be adequate for distributed superconducting magnet thermometry, the measurement time of several seconds would be unacceptable for use as a quench detection system in any conductor with a copper current density greater than 50-100 A/mm^2.

2.3.2 Raman Scattering

Raman scattering occurs in fibers due to the propagating light interacting with the vibrational modes of the silica molecules. This scattering process is also commonly described as the scattering of light off optical phonons [43]. The frequency shift of the scattered light is equal to the vibrational frequency of the molecule it scatters off [44]. A photon excites an electron to a virtual state, which will immediately relax into a certain vibrational energy state. Depending on the initial state of the molecule, the relaxation will generate either Stokes Raman scattering or Anti-Stokes Raman scattering as seen in Figure 2-21.
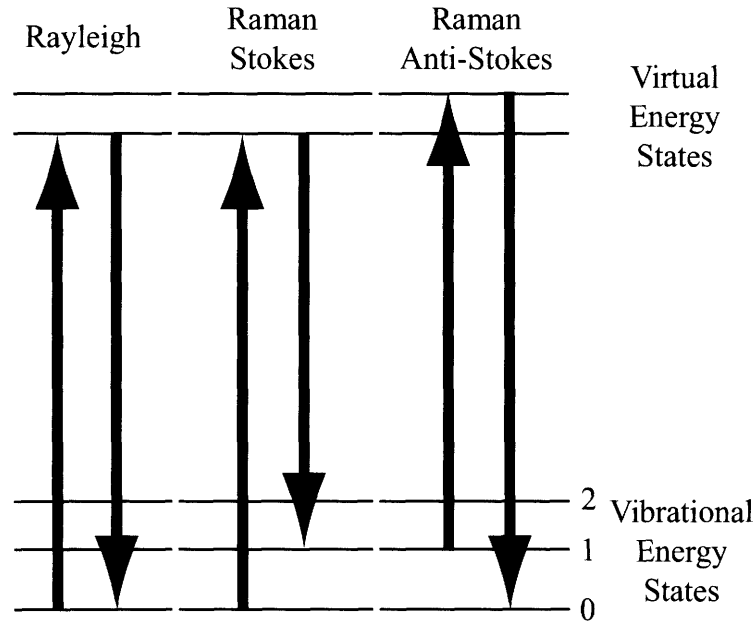
Figure 2-21: Diagram of Raman Stokes and Anti-Stokes scattering compared to Rayleigh scattering.

Most temperature sensors that use Raman scattering compare the Stokes to Anti-Stokes waves. According to Equation 2.60, the higher the temperature, the more Anti-Stokes scattering there will be [45].

$$\frac{P_{AS}}{P_S} = \left(\frac{\lambda_S}{\lambda_{AS}}\right)^4 e^{-\frac{h\Delta\nu}{kT}} \tag{2.60}$$

In Equation 2.60 P_{AS} is the measured Anti-Stokes power, P_S is the measured

Stokes power, λ_S is the wavelength of the Stokes scattered light, and λ_{AS} is the wavelength of the Anti-Stokes scattered light.

The Stokes scattering power of a single molecule can be calculated starting with the power-per-unit solid angle radiated from an oscillating dipole moment, Equation 2.61 [44].

$$\frac{dP_{S,mol}}{d\Omega} = \frac{k_S^3 \omega_S}{32\pi^2 \varepsilon_r \varepsilon_o} |p_S|^2 \sin^2 \theta \qquad (2.61)$$

In Equation 2.61, p_S is the oscillating dipole moment, admitting a Stokes wave with angular frequency ω_S at an angle, θ, from the direction of the dipole moment. Also, $\varepsilon_r = n^2$ and $p_S = \alpha_R E_o e^{j\omega_S t}$. Ignoring the imaginary part of ε_r and using the intensity of the incident light, $I_o = \frac{nc\varepsilon_o |E_o|^2}{2}$, we arrive at Equation 2.62.

$$d^2 P_{S,mol} = \frac{\omega_S^4}{16\pi^2 c^4 \varepsilon_o^2} \alpha_R^2 I_o \sin^3 \theta d\theta d\psi \qquad (2.62)$$

In Equation 2.62, the emitted Stokes light is monochromatic, but realistically it should reflect the statistical properties of the motion of the molecules. Using a function, $g_s(\omega_S)$, to incorporate the motion, we get Equation 2.63, where β is the angle between the incident and scattered waves.

$$d^3 P_{S,mol} = \frac{\omega_S^4}{16\pi^2 c^4 \varepsilon_o^2} \alpha_R^2 I_o \cos^3(\beta) g_s(\omega_S) d\omega_S d\beta d\psi \qquad (2.63)$$

Equation 2.63 gives the Stokes power of a particular frequency, ω_S. By integrating Equation 2.63 over all frequencies we arrive at Equation 2.64.

$$d^2 P_{S,mol} = \frac{d\sigma}{d\Omega} \left(\frac{\pi}{2}, \omega_{So} \right) I_o \cos^3(\beta) d\beta d\psi \qquad (2.64)$$

Equation 2.64 introduces the term $\frac{\partial \sigma}{\partial \Omega} \left(\frac{\pi}{2}, \omega_{So}(T) \right)$, which is the temperature dependant differential Raman cross-section of one molecule. Integrating Equation 2.64 gives us Equation 2.65, which is the total Stokes scattering power of a single molecule.

$$d^2 P_{S,molTOTAL} = \frac{8\pi}{3} \frac{P_o}{\pi r_{eff}^2} e^{-\frac{r}{r_{eff}^2}} \frac{d\sigma_{eff}}{d\Omega} \left(\frac{\pi}{2}, \omega_{So}(T) \right) \qquad (2.65)$$

Using the density and volume of the fiber, the total Stokes scattering power for a fiber can be calculated. The Anti-Stokes power can also be calculated theoretically and plugged into Equation 2.60 to compare with experimental results. While spontaneous Raman scattering can theoretically be used as a temperature sensor, it normally takes on the order of minutes to build up enough signal for a measurement. A common application of a Raman scattering based temperature sensor is embedding the fiber in concrete to monitor the temperature as it dries over the course of days. Other than the time it takes to make a single measurement, the main reason Raman scattering systems cannot be used for low temperature superconducting magnets is that below 77 K, spontaneous Raman scattering is totally ineffective due to the lack of thermal noise at the Raman frequencies [46].

2.3.3   Stimulated Brillouin Scattering

Brillouin scattering is when light is scattered off sound, or propagating density, waves. Similar to Raman scattering coming from light scattering off optical phonons, Brillouin scattering is scattering off acoustic phonons [43]. Brillouin scattering is broken down into spontaneous scattering, which will be discussed in the next chapter, and stimulated scattering. Stimulated Brillouin systems are not as commonly used as the spontaneous systems; however, they have a much better signal to noise ratio which allows a measurement in the time it takes for a single pass of light [47].

Brillouin scattering occurs when light is Bragg reflected 180 degrees due to refractive index modulations produced by acoustic waves [48]. The reflected light is shifted by the Brillouin frequency, ν_B, as described in Equation 2.66.

$$\nu_B = \frac{2nV_a}{\lambda} \tag{2.66}$$

Here n is the index of refraction, V_a is the acoustic velocity, and λ is the wavelength of the incoming light. The frequency shift for Brillouin scattered light is much smaller (GHz) than the frequency shift for Raman scattering (THz) [45].

The Brillouin frequency, calculated in Equation 2.66, varies as a function of strain

and temperature, where ν_{Bo} is the Brillouin frequency at zero degrees Celsius and zero strain, as shown in Equation 2.67.

$$\nu_B = \nu_{Bo} + \frac{\partial \nu}{\partial T} T + \frac{\partial \nu}{\partial \varepsilon} \varepsilon \qquad (2.67)$$

When the difference in frequency of the two counter-propagating waves is equal to the Brillouin frequency, power is transferred from the wave with the lower frequency to the wave with the higher frequency. The Brillouin power can be expressed as the sum of the original pulse power and the additional power due to temperature and strain sensitivity, as written in Equation 2.68, where P_o is the Brillouin power at zero degrees Celsius and zero strain [48].

$$P_B = P_o + \frac{\partial P}{\partial T} T + \frac{\partial P}{\partial \varepsilon} \varepsilon \qquad (2.68)$$

In designing a Brillouin scattering experiment, there are many trade-offs that must be weighed based on the desired measurements. The spatial resolution and the signal power are inversely proportional to the pulse width [49]. However, decreasing the pulse width too much will create other problems. The Brillouin frequency is insensitive to the length of the pulse width if it is above 50 ns, but dependent on the pulse width if it is less than 50 ns, as shown in Figure 2-22 [50].

Stimulated Brillouin scattering requires that the waves have the correct polarizations. As expected, in single mode fibers the state of polarization varies due to polarization mode dispersion, as well as to changes in temperature and strain, which limit the spatial resolution to the order of meters. To solve this problem, polarization maintaining (PM) fiber can be used to provide spatial resolution on the order of centimeters, strain resolution of 10-30 $\mu\varepsilon$, and temperature resolution of 1-2 C [51].

Three measurable quantities can be used to measure the temperature and strain simultaneously: 1) Brillouin power and frequency, 2) Brillouin power and linewidth, 3) Brillouin linewidth and frequency. For 2), there are certain temperature and strain ranges where the power and bandwidth are related, and therefore cannot be used to simultaneously measure both temperature and strain [51].
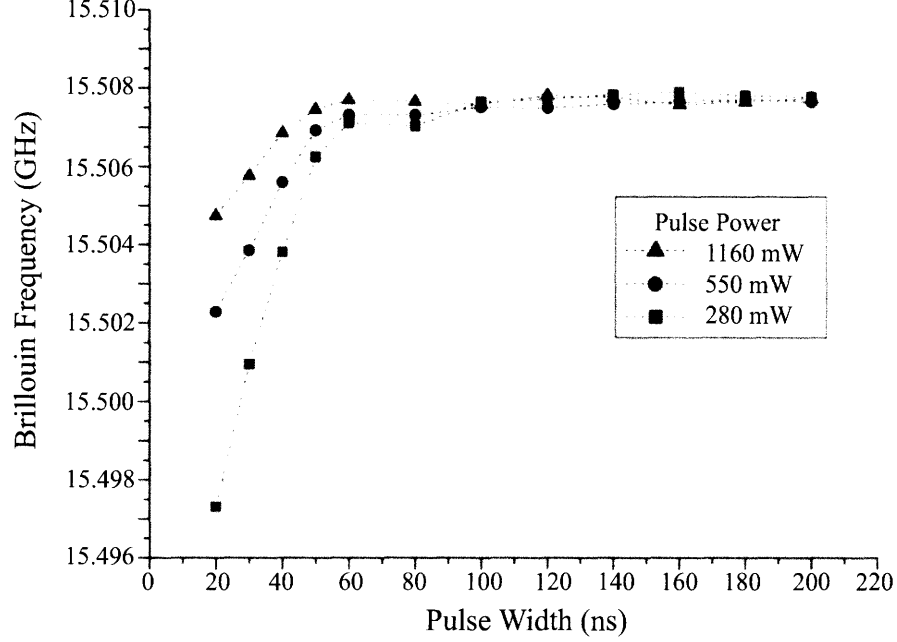
Figure 2-22: Brillouin frequency shift dependence on the pulse length.

Looking at the Brillouin power and frequency shift, the temperature and strain can be calculated using Equations 2.69 and 2.70 respectively [8].

$$\Delta T = \frac{\Delta \nu C_P^\varepsilon - C_\nu^\varepsilon \Delta P}{C_P^\varepsilon C_\nu^T - C_\nu^\varepsilon C_P^T} \tag{2.69}$$

$$\Delta \varepsilon = \frac{\Delta \nu C_P^T - C_\nu^T \Delta P}{C_\nu^\varepsilon C_P^T - C_P^\varepsilon C_\nu^T} \tag{2.70}$$

Equations 2.69 and 2.70 use the shorthand notation explained in Equation 2.71.

$$C_\nu^\varepsilon = \left(\frac{\partial \nu}{\partial \varepsilon}\right)_T, C_\nu^T = \left(\frac{\partial \nu}{\partial T}\right)_\varepsilon, C_P^\varepsilon = \left(\frac{\partial P}{\partial \varepsilon}\right)_T, C_P^T = \left(\frac{\partial P}{\partial T}\right)_\varepsilon \tag{2.71}$$

The values of these "constants" have been experimentally determined, and presented in Table 2.3, in the normal temperature range of 0 C - 50 C for the three most common types of PM fibers: PANDA, Bow Tie, and Tiger.

Existing stimulated Brillouin scattering systems take measurements while the frequency of one of the lasers is changed, so that the difference in frequency between the two lasers sweeps through the range of Brillouin frequencies. At each frequency

Table 2.3: Sensitivities of several types of polarization maintaining fibers to temperature and strain (from Reference [8]).

PM Fiber Type	PANDA	Bow Tie	Tiger
C_v^T (MHz/C)	1.37 $\pm$0.007	2.30 $\pm$0.05	1.66 $\pm$0.07
C_P^T $(\%/C)$	0.26 $\pm$0.03	0.23 $\pm$0.01	0.04 $\pm$0.09
C_B^T (MHz/C)	-0.15 $\pm$0.02	-0.20 $\pm$0.02	
C_v^ε $(MHz/\mu\varepsilon)$	0.077 $\pm$0.002	0.023 $\pm$0.001	0.091 $\pm$0.005
C_P^ε $(\%/\mu\varepsilon)$	-0.028 $\pm$0.003	0.018 $\pm$0.002	0.011 $\pm$0.004
C_B^ε $(MHz/\mu\varepsilon)$	0.058 $\pm$0.004	-0.031 $\pm$0.002	

step a pulse is launched and data at that frequency difference is recorded. The time required for this part is the time of flight for the light, and the data acquisition time: both a small fraction of a second. The part that takes the most time is temperature tuning a laser to obtain the next frequency step. For a temperature tuned laser, this takes on the order of a half of a second, causing scans to take on the order of minutes. While this is too slow to be used for quench detection in a superconducting magnet, a threshold approach could potentially work. The idea behind a threshold approach is to set the frequency difference between the two lasers to a predetermined frequency which corresponds to a threshold temperature. However, strain effects on the frequency shift could cause false signals.

Brillouin scattering has been used in many different systems to measure temperature and strain, including systems that also use Raman scattering. Since Raman scattering does not depend on strain, by measuring the Brillouin scattering's temperature and strain dependent signal, then subtracting out the temperature calculated by the Raman scattering signal, both the temperature and strain can be calculated. As discussed in the previous section, this type of system would not work for superconducting magnets since Raman scattering is not measurable below 77 K. Brillouin scattering also encounters difficulties at cryogenic temperatures, which will be discussed in more detail in the next chapter. Some Brillouin scattering systems also use methods that are similar to the frequency domain analysis used in LUNA's Rayleigh scattering system. While the operating parameters are different from what is needed for a quench detection diagnostic, this type of system would be ideal for other mea-

surements described in Appendix B.

Chapter 3

Spontaneous Brillouin Scattering

Brillouin scattering is due to the interaction between light propagating in a fiber optic cable and acoustic phonons. Acoustic phonons are bulk vibrations in glass that travel at about 6 km/sec. These traveling waves change the local glass densities and indexes of refraction as they move down the fiber, which acts like a moving Bragg grating that backscatters Doppler shifted light. If energy is lost by the photon to the glass, the Brillouin shifted light is lower in frequency than the input light and is called Stokes light. If the photon gains energy from the glass, its frequency is increased and the light is called Anti-Stokes light.

The basis of Brillouin scattering diagnostic systems lies in three parameters of the scattered light: the intensity, the frequency shift, and the linewidth. All three of these parameters are functions of temperature and strain, so theoretically the temperature and strain can be derived by measuring the intensity, frequency shift, and linewidth of Brillouin scattered light. Near room temperature, these parameters vary linearly with temperature and strain, so only two of the three parameters need to be measured to determine both temperature and strain. However, at cryogenic temperatures the frequency shift and linewidth are nonlinear and not everywhere monotonic, so all three parameters need to be measured to determine the temperature and strain.

We have developed a spontaneous Brillouin scattering system that measures all three parameters of the backscattered light. This system's ability to measure the three parameters as a function of position along a fiber transforms the standard fiber optic

cable into a distributed temperature and strain sensor. By incorporating a fiber in a superconducting magnet, our spontaneous Brillouin scattering system can not only act as a quench detection system, but also as a quench locater, quench propagation monitor, and a general magnet diagnostic.

3.1 Derivation of Important Parameters

The three important parameters of the scattered light are the intensity, or power, the frequency shift, and the linewidth, or full width at half maximum (FWHM). These are commonly measured parameters of light, and the next few sections theoretically derive expressions for these parameters.

3.1.1 Intensity

Since Brillouin scattering is the scattering of light by pressure waves, it makes sense to start with the equation of motion for a pressure wave, Equation 3.1 [52].

$$\frac{\partial^2 \Delta \tilde{p}}{\partial t^2} - \Gamma' \nabla^2 \frac{\partial \Delta \tilde{p}}{\partial t} - \nu^2 \nabla^2 \Delta \tilde{p} = 0 \tag{3.1}$$

In Equation 3.1, $\Delta \tilde{p}$ is a pressure wave propagating though a medium as expressed in Equation 3.2. The second term in Equation 3.2 is the complex conjugate of the first term, to ensure that is real, as it must be in order to represent a physical field [43]. Γ' is the damping parameter expressed in Equation 3.3, where η_s is the shear viscosity coefficient, η_b is the bulk viscosity coefficient, and κ is the thermal conductivity. For most optical materials, the last term in Equation 3.3 is much smaller than the first two terms. The speed of sound, v, is expressed thermodynamically in Equation 3.4, where C_s is the compressibility measured at constant entropy [43].

$$\Delta \tilde{p} = \Delta p e^{i(qz-\Omega t)} + c.c. \tag{3.2}$$

$$\Gamma' = \frac{1}{\rho} \left[\frac{4}{3} \eta_s + \eta_b + \frac{\kappa}{C_p} (\gamma - 1) \right] \tag{3.3}$$

84

$$v^2 = \frac{1}{C_s \rho} \tag{3.4}$$

Using the relation described in Equation 3.5, $C_s = \frac{C_T}{\gamma} = \frac{1}{\gamma p}$ can be substituted into Equation 3.4 to give Equation 3.6.

$$\frac{C_T}{C_s} = \frac{c_p}{c_V} = \gamma \tag{3.5}$$

$$v = \left(\frac{\gamma p}{\rho}\right)^{\frac{1}{2}} = \left(\frac{\gamma N k T}{\rho V}\right)^{\frac{1}{2}} = \left(\frac{\gamma k T}{\mu}\right)^{\frac{1}{2}} \tag{3.6}$$

Making these substitutions in Equation 3.1, we find that q and Ω are related by a dispersion equation of the form shown in Equation 3.7.

$$\Omega^2 = q^2 \left(v^2 - i\Omega\Gamma'\right) \tag{3.7}$$

By introducing the phonon decay rate, $\Gamma = \Gamma' q^2$, Equation 3.7 can be simplified to Equation 3.8.

$$q \approx \frac{\Omega}{v} + \frac{i\Gamma}{2v} \tag{3.8}$$

Inserting Equation 3.8 into Equation 3.2, and introducing a sound absorption coefficient, $\alpha_s = \frac{q^2 \Gamma'}{v} = \frac{\Gamma}{v}$, Equation 3.9 shows the spatial variation of the acoustic wave.

$$|\Delta p(z)|^2 = |\Delta p(0)|^2 e^{-\alpha_s z} \tag{3.9}$$

Taking a standard incident optical field, Equation 3.10, we assume that it obeys the driven wave equation, shown in Equation 3.11.

$$\tilde{\mathbf{E}}_o(z, t) = E_o e^{i(\mathbf{k}\cdot\mathbf{r} - \omega t)} + c.c. \tag{3.10}$$

$$\nabla^2 \tilde{\mathbf{E}} - \frac{n^2}{c^2} \frac{\partial^2 \tilde{\mathbf{E}}}{\partial t^2} = \frac{4\pi}{c^2} \frac{\partial^2 \tilde{\mathbf{P}}}{\partial t^2} \tag{3.11}$$

The polarization of the medium is given by Equation 3.12, and a typical component of the thermally excited pressure disturbance is given in Equation 3.13 [43].

$$\tilde{\mathbf{P}}(\mathbf{r}, t) = \frac{1}{4\pi} \gamma_e C_s \Delta \tilde{p}(\mathbf{r}, t) \tilde{E}_o(z, t) \tag{3.12}$$

$$\Delta \tilde{p}(\mathbf{r}, t) = \Delta p e^{i(\mathbf{q} \cdot \mathbf{r} - \Omega t)} + c.c. \tag{3.13}$$

Combining Equations 3.10 through 3.13, we can write the wave equation for the scattered field as Equation 3.14 [43].

$$\nabla^2 \tilde{\mathbf{E}} - \frac{n^2}{c^2} \frac{\partial^2 \tilde{\mathbf{E}}}{\partial t^2} = -\frac{\gamma_e C_s}{c^2} \left[(\omega - \Omega)^2 E_o \Delta p^* e^{i(\mathbf{k} - \mathbf{q}) \cdot \mathbf{r} - i(\omega - \Omega)t} + (\omega + \Omega)^2 E_o \Delta p e^{i(\mathbf{k} + \mathbf{q}) \cdot \mathbf{r} - i(\omega + \Omega)t} + c.c. \right] \tag{3.14}$$

Using the electric field from Equation 3.14, the intensity of the Brillouin scattered light can be calculated using Equation 3.15.

$$I_S = \left(\frac{nc}{4\pi} \right) \left\langle \tilde{\mathbf{E}}_S^2 \right\rangle \tag{3.15}$$

3.1.2 Frequency Shift

The first term in the bracket of Equation 3.14 is the Stokes scattering, and the second term is the Anti-Stokes scattering [43]. As seen in Figure 3-1, the wave vector and frequency for Stokes scattering can be described by Equations 3.16 and 3.17 respectively.

$$\mathbf{k}' = \mathbf{k} - \mathbf{q} \tag{3.16}$$

$$\omega' = \omega - \Omega \tag{3.17}$$

The relationship between the frequency, ω, and wave vector, k, of the initial optical field is given in Equation 3.18. Also, the frequency, Ω, and wave vector, q, of

Stokes Scattering

$\mathbf{k'} = \mathbf{k} - \mathbf{q}$
$\omega' = \omega - \Omega$
sound wave

$\mathbf{k}, \omega$

$\mathbf{q}, \Omega$

Anti-Stokes Scattering

$\mathbf{k'} = \mathbf{k} + \mathbf{q}$
$\omega' = \omega + \Omega$
sound wave

$\mathbf{k}, \omega$

$\mathbf{q}, \Omega$
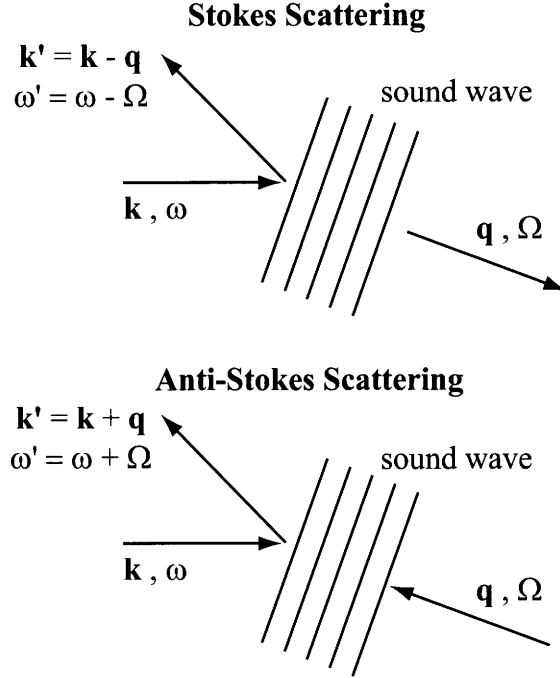
Figure 3-1: Diagram of Stokes and Anti-Stokes Scattering.

the acoustic wave are related according to Equation 3.19.

$$\omega = \frac{|\mathbf{k}|c}{n} \tag{3.18}$$

$$\Omega = |\mathbf{q}|v \tag{3.19}$$

Satisfying Equations 3.16 through 3.19 leads to the acoustic frequency, shown in Equation 3.20.

$$\Omega = 2|\mathbf{k}|v\sin\left(\frac{\theta}{2}\right) = 2n\omega\frac{v}{c}\sin\left(\frac{\theta}{2}\right) \tag{3.20}$$

Equation 3.20 shows that when $\theta = 0$, or forward scattering, the Stokes shift is zero; however, when $\theta = 180$, or backscatter in an optical fiber, the Stokes shift is a maximum, as expressed in Equation 3.21.

$$\Omega_{max} = 2n\omega\frac{v}{c} \tag{3.21}$$

87

A similar procedure can be carried out to calculate the Anti-Stokes frequency shift.

3.1.3 Linewidth

The derivations in the last two sections assumed that the Brillouin scattered light was monochromatic, which is not the case. The scattered light has a spread in angular frequency whose full width at half maximum (FWHM) is given in Equation 3.22 [43].

$$\delta\omega = \frac{1}{\tau_p} \tag{3.22}$$

The phonon lifetime, τ_p, is given by Equation 3.23, so Equation 3.22 can be rewritten as Equation 3.24.

$$\tau_p = \frac{1}{\Gamma} = \frac{1}{q^2\Gamma'} \tag{3.23}$$

$$\delta\omega = q^2\Gamma' \tag{3.24}$$

Referring to Figure 3-1, $|q| = 2|k|sin\left(\frac{\theta}{2}\right)$, where θ is the angle between k' and q, which leads to Equation 3.25, the linewidth of Brillouin scattered light.

$$\delta\omega = 4n^2\Gamma'\frac{\omega^2}{c^2}\sin^2\left(\frac{\theta}{2}\right) \tag{3.25}$$

3.2 Temperature Effects

The Brillouin frequency shift, derived in Equation 3.2, varies with strain and temperature based on the fact that the acoustic velocity depends on both the strain and temperature of the medium [53]. This can be represented by Equation 3.26, where ν_{Bo} is the frequency shift at zero Celsius and zero strain.

$$\nu_B = \nu_{Bo} + \frac{\partial\nu(v_a)}{\partial T}T + \frac{\partial\nu(v_a)}{\partial\varepsilon}\varepsilon \tag{3.26}$$

The power of the Brillouin scattered light is also a function of both strain and temperature, and is represented in Equation 3.27 [54].

$$P_B = P_{Bo} + \frac{\partial P}{\partial T}T + \frac{\partial P}{\partial \varepsilon}\varepsilon \tag{3.27}$$

Similarly, the linewidth of the Brillouin scattered light is also a function of strain and temperature, as expressed in Equation 3.28 [48].

$$\delta\omega_B = \delta\omega_{Bo} + \frac{\partial(\delta\omega)}{\partial T}T + \frac{\partial(\delta\omega)}{\partial \varepsilon}\varepsilon \tag{3.28}$$

3.2.1 Brillouin Scattering at Room Temperature

Equations 3.26 through 3.28 can be used as a set of three equations and two unknowns, the temperature and strain. In order to determine the temperature and strain, a sensor may only need to measure two out of the three parameters. For example, if we experimentally measure the Brillouin scattered frequency and the power of the scattered light, we can calculate the temperature and strain using Equations 3.29 and 3.30 from the previous chapter [51].

$$\Delta T = \frac{\Delta\nu C_P^\varepsilon - C_\nu^\varepsilon \Delta P}{C_P^\varepsilon C_\nu^T - C_\nu^\varepsilon C_P^T} \tag{3.29}$$

$$\Delta\varepsilon = \frac{\Delta\nu C_P^T - C_\nu^T \Delta P}{C_\nu^\varepsilon C_P^T - C_P^\varepsilon C_\nu^T} \tag{3.30}$$

Equations 3.29 and 3.30 use the short hand expressions described in Equation 3.31.

$$C_\nu^\varepsilon = \left(\frac{\partial\nu}{\partial\varepsilon}\right)_T, C_\nu^T = \left(\frac{\partial\nu}{\partial T}\right)_\varepsilon, C_P^\varepsilon = \left(\frac{\partial P}{\partial\varepsilon}\right)_T, C_P^T = \left(\frac{\partial P}{\partial T}\right)_\varepsilon \tag{3.31}$$

In order for Equations 3.29 and 3.30 to produce a unique solution, the coefficients in Equation 3.31 have to be monotonic throughout the range of measurement. This is a good approximation for measurements around room temperature, and even at higher temperatures; however, at cryogenic temperatures, these coefficients are no

longer monotonic.

3.2.2 Brillouin Scattering at Cryogenic Temperature

Many functions that are linear and well-understood around room temperature become non-linear and unexplained as temperature decreases from 300 K to 4 K. The coefficients in Equation 3.31, which are all constant around room temperature, change drastically at cryogenic temperatures. The main effect of this on Brillouin scattering systems is that the frequency shift, intensity, and linewidth are no longer single-valued functions: a single value can represent more than one temperature.

These changes can be attributed to similar nonlinearities in the acoustic velocity and attenuation at cryogenic temperatures. The Brillouin frequency shift in Equation 3.21 is a direct function of the acoustic velocity, so any temperature dependence of the acoustic velocity will change the frequency shift. At room temperature, the temperature dependence of the acoustic velocity is linear, but at cryogenic temperatures it is non-linear as seen in Figure 3-2 [55].

The behavior of the acoustic velocity in the range of 1 - 6 K is consistent with the prediction of a model based on a tunneling process in a distribution of two-level systems [56]. Also, the acoustic velocity in the range of 7 - 70 K is explained as an effect due to thermally activated relaxation processes. However, the increase of the acoustic velocity from 70 K up to room temperature is still unexplained [5].

It is clear from Figure 3-2 that measuring the acoustic velocity below 5.89 km/s will correspond to two different temperatures. Due to the direct correlation between acoustic velocity and frequency shift, there will be frequency shift measurements that correspond to more than one temperature as well, as shown in Figure 3-3.

The linewidth of Brillouin scattered light is a function of the acoustic phonon damping parameter, as shown in Equation 3.25. Figure 3-2 shows the attenuation of fused silica, which is directly related to the acoustic phonon damping. It is apparent that although the slope is linear around room temperature, it becomes non-linear as the temperature decreases. There are two mechanisms that could account for these changes: the anharmonic or three-phonon interaction, which is the usual case for this
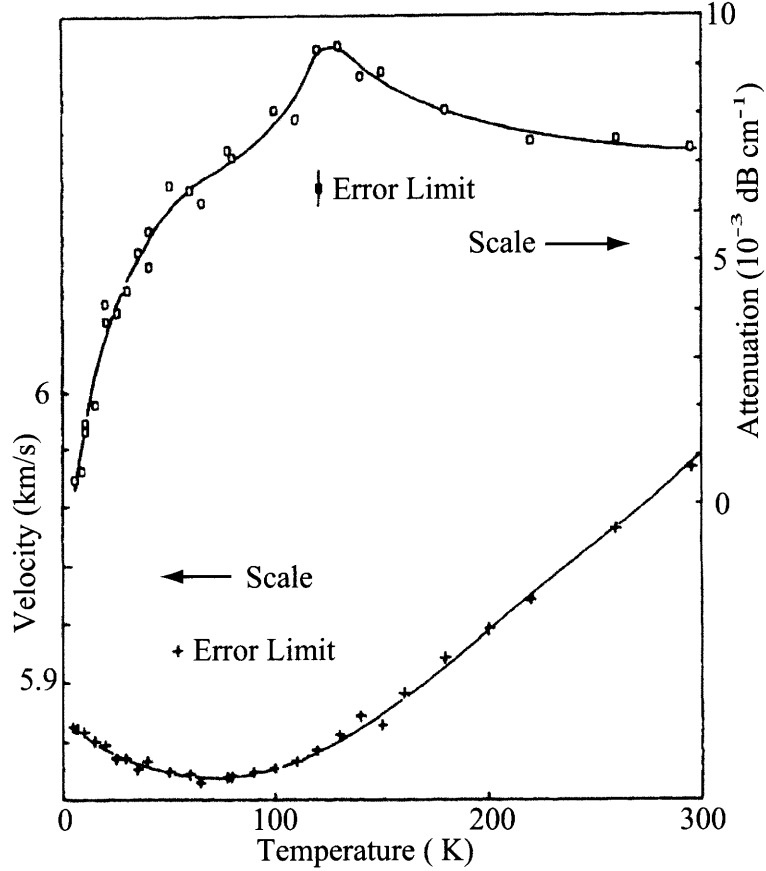
Figure 3-2: The acoustic velocity (+) and the attenuation (o) in fused quartz are not linear in the 0 - 300 K range.

type of damping, or a structural relaxation process [57].

The first mechanism, the anharmonic model, was first derived by Bommel and Dransfeld as an explanation of acoustic absorption measurements in quartz [58]. They derived the damping rate in Equation 3.32 based on Akhieser's model of sound-induced changes in thermal-phonon distributions. The assumptions going into the derivation of Equation 3.32 can be found in reference [57], but the important point is that they are valid for the fused quartz used in fiber optics.

$$\Gamma = \frac{\gamma^2 \omega T c_v}{8\rho v_i^2} \frac{\omega\tau}{1 + (\omega\tau)^2} \tag{3.32}$$

In Equation 3.32, ρ is the crystal density, T is the temperature, ω is the frequency of the sound wave, and v_i is the sound wave's velocity. τ is the thermal phonon damping time, and c_v is the heat capacity. γ^2 is an average Gruneisen constant, of

91
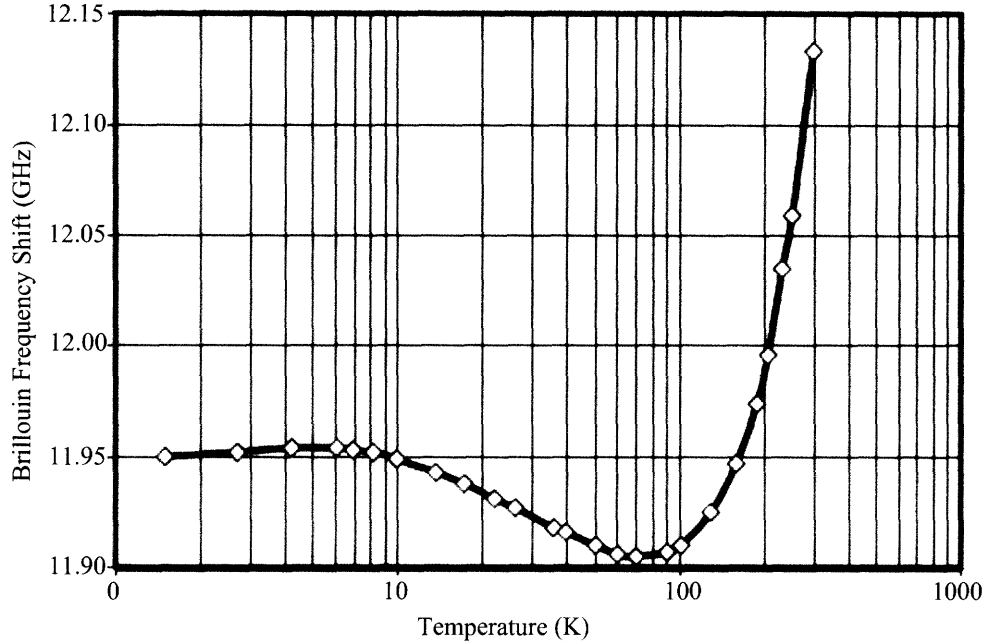
Figure 3-3: Brillouin frequency shift as a function of temperature down to 4 K (from Reference [5]).

order unity, which measures anharmonicity. As mentioned previously, the Brillouin scattering linewidth is related to the phonon damping rate, expressed in Equation 3.33.

$$\delta\omega = \frac{\Gamma}{\pi} \tag{3.33}$$

Due to the relation expressed in Equation 3.33, the linewidth as a function of temperature should look somewhat similar to the phonon attenuation curve in Figure 3-2. Experimental results, seen in Figure 3-4 from Reference [5], show that the linewidth of Brillouin scattered light has a similar shape to that of the acoustic phonon attenuation as a function of temperature.

Similar to the problems encountered by the non-linearity of the Brillouin frequency shift as a function of cryogenic temperatures, the non-linearity of the linewidth also has a range where the linewidth could represent two different temperatures. By measuring both the linewidth and frequency shift, one could determine the temperature only if the strain effects were also known. If the strain that the sensor fiber is expe-

92
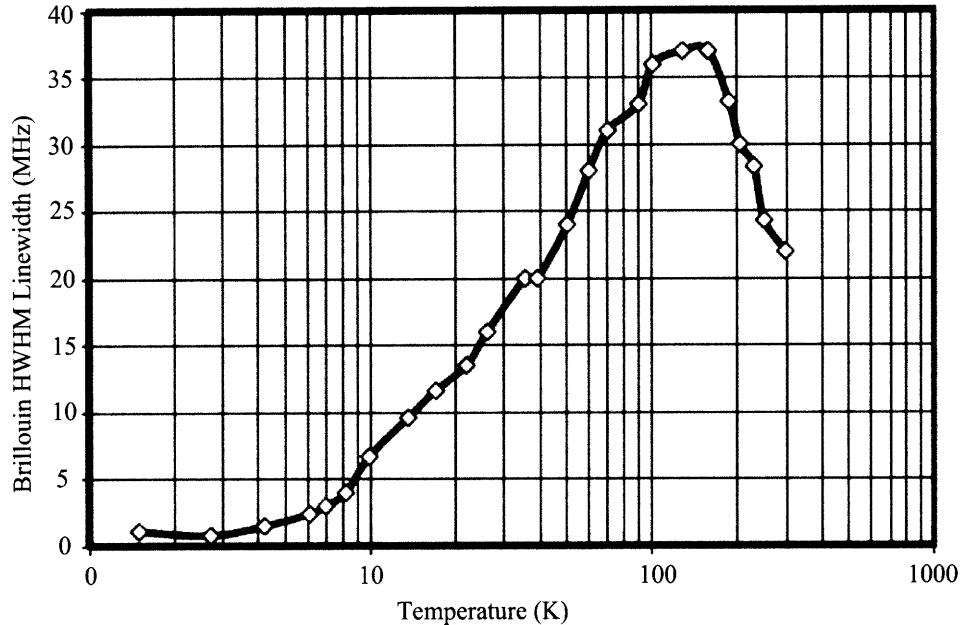
Figure 3-4: Brillouin scattered light's linewidth as a function of temperature down to 4 K (from Reference [5]).

riencing is not known, the third parameter, intensity of the Brillouin scattered light, also needs to be measured to determine the temperature and strain in the fiber.

3.3 Comparison to Other Magnet Diagnostics

The purpose of developing a fiber optic diagnostic for superconducting magnets is not to simply replace existing sensors, but to improve and broaden the information that can be derived from measurements as well. As mentioned in the previous chapter, a fiber optic interferometer would work as well as a co-wound voltage tap for quench detection; however, it does not provide any additional information. On the other hand, a spontaneous Brillouin scattering sensor could make measurements in a superconducting magnet that have not been possible in the past.

3.3.1 Quench Detection

A reliable quench detection system is the most important diagnostic in actively protected superconducting magnets. As discussed in the previous chapter, many different

93

methods have been used to detect quenches in magnets of all shapes and sizes. Large superconducting magnets being developed for nuclear fusion experimental reactors are state-of-the-art, and therefore, their diagnostic systems should be as well. While the co-wound voltage taps will work for ITER-sized magnets, they will work only as a quench detector.

Implementing a fiber optic sensor based on spontaneous Brillouin scattering would not only work as a quench detector, but also as a quench locater. Voltage taps can get some degree of spatial resolution by implementing a system with voltage taps of different lengths, monitoring different parts of the magnet, but this does not come close to the resolution capabilities of a Brillouin scattering system. For example take the ITER central solenoid with its six sub-sections, each a little over six kilometers long. In order to get "spatial resolution" on the order of one kilometer, 36 voltage taps would be needed. On the other hand, a single fiber could give spatial resolution on the order of five meters, 200 times better resolution.

Using Optical Time Domain Reflectometry, sending pulses of light down the sensing fiber allows distributed measurements based on the time of flight of light and the time that signals are detected. The spatial resolution of the system is determined by the pulse length of the light. The shorter the pulse length, the shorter the physical length of the light pulse excited in the fiber at any given time. Although decreasing the pulse length improves the spatial resolution, the signal to noise ratio decreases with decreasing pulse length. This continues down to a fundamental limit of about a 50 ns pulse, which corresponds to about 5 meter spatial resolution, when the frequency shift becomes a function of pulse length as well as temperature and strain [50]. Chapter 5 will discuss the these tradeoffs in more detail.

3.3.2 Quench Propagation

Quench propagation throughout superconducting magnets is an interesting area of study since there is very little experimental data to confirm the theoretical calculations. As discussed in Section 1.2.3, several numerical codes have been developed to predict how a quench will propagate through a magnet. Quench experiments have

explored a moderate sample of possible quench behavior and the existing codes have had some success in simulating quench behavior, after the fact. However, the possibility of distributed thermometry would greatly improve the ability to understand magnet behavior during routine operation and quench. Thousands of thermocouples could be positioned in a three dimensional array in an operating magnet to measure a distributed temperature. However, aside from the wiring nightmare, the lead wires from the thermocouples through the insulation would alter the thermal transport of the magnet, not to mention the electrical integrity of the magnet.

Winding an optical fiber in the cable and using our spontaneous Brillouin scattering system would provide a real-time distributed temperature measurement throughout the magnet, without interfering with any electromagnetic or structural properties of the magnet. Because of the ability to spatially resolve the temperature measurements in real-time, the propagation of a quench could be tracked as the magnet quenches. Experimental data tracking the propagation of a quench through a magnet would be a superior method of calibrating the theoretical simulations that are currently used in the design of superconducting magnets.

3.3.3 Heat Treatment

Depending on the type of superconductor used in a magnet, a heat treatment may be necessary to react the metals. Of the two most common superconductors, NbTi does not need to be heat treated, but Nb_3Sn requires a lengthy heat treatment. During the drawing of a Nb_3Sn wire, the niobium and tin are separate. A several hundred hour heat treatment at temperatures around 600 C - 700 C allows the niobium and tin to diffuse together and form the Nb_3Sn superconducting alloy. For large superconducting magnets, the heat treatment process occurs in a huge oven which is heated very slowly to allow the magnet to warm uniformly. Obviously there is no way to measure the temperature in the inner windings of the magnet, so the approximate temperature throughout the magnet has to be theoretically calculated based on thermal diffusion times. While these calculations are conceptually straightforward, it is desirable to have real-time temperature measurements throughout the magnet during

this process.

Brillouin scattering in fused silica has been studied through the glass transition temperature of 1200 C, up almost to the melting point of the glass, 1700 C [59]. Obviously, the normal plastic coating on a fiber would not survive these temperatures. The plastic coating vaporizes at around 200 C, but some metal coated fibers can survive the temperatures of the heat treatment. However, once the fiber is in place as a sensor, the evaporation of its plastic coating may not matter. Depending on how the metal coating is applied to the fiber, there could be stresses in the fiber due to the coating, but a thermal cycle can relieve these stresses [60]. Fiber survival is one of the engineering issues of our spontaneous Brillouin scattering system that will be discussed more in Chapter 6.

While studying the high temperature characteristics of Brillouin scattering in fused silica, a noticeable hysteresis was observed. A discrepancy of about 50 MHz between the heating and cooling was measured during a thermal cycle between 20 C and 850 C, as seen in Figure 3-5 [61].
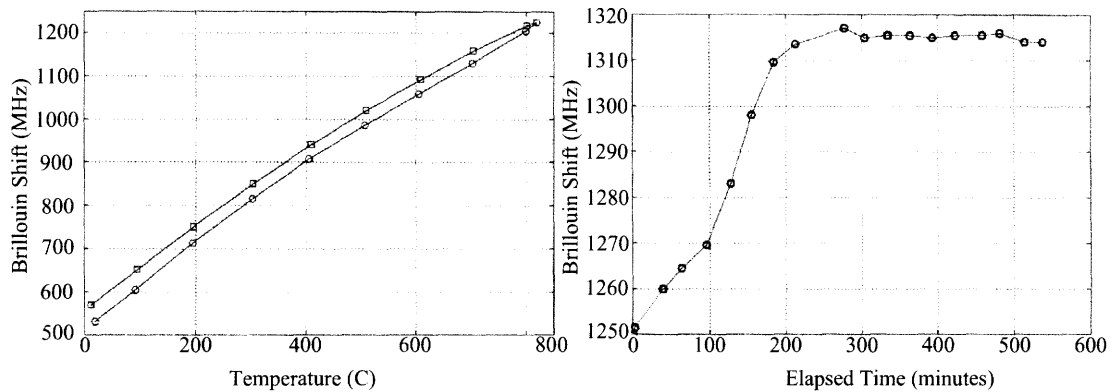
Figure 3-5: Hysteresis in the Brillouin frequency shift during a thermal cycle (left). An annealing process at 850 C that eliminates the hysteresis (right).

Although a 50 MHz discrepancy is a large deviation, Figure 3-5 also shows that several hours into an annealing process at 850 C, the Brillouin frequency shift levels out. This process eliminates the hysteresis, as shown in a post-annealing thermal cycle in Figure 3-6 [61].

These experiments imply that our spontaneous Brillouin scattering system should
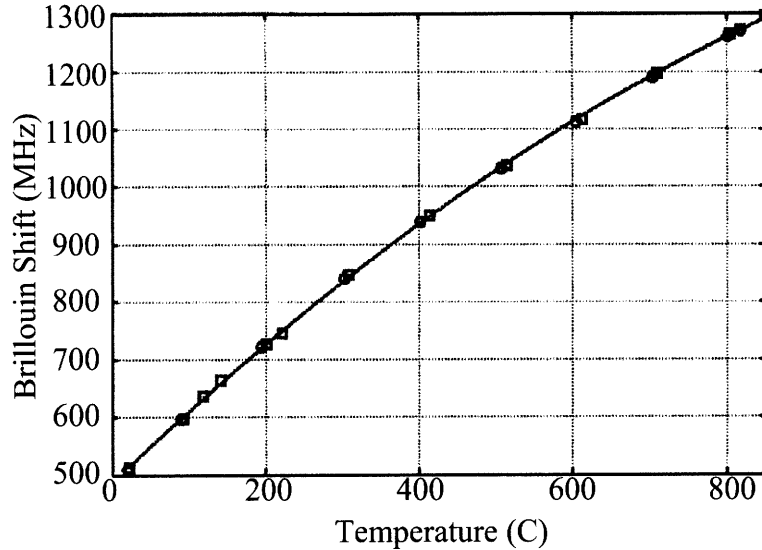
Figure 3-6: Brillouin frequency shift during a thermal cycle after the fiber has been annealed.

work well at the temperatures encountered during a heat treatment. By annealing, and calibrating our fiber before winding it in the magnet, we could eliminate the hysteresis and be able to use it as a distributed temperature sensor during the heat treatment. By obtaining spatially resolved temperature measurements, our system would be able to confirm that the magnet is heating at a uniform temperature, which is a measurement that has not been possible in the past.

3.3.4 Strain Measurement

Another measurement that has been impossible to date is an internal distributed strain measurement. Strain gages can be placed on the surface of the magnet; however, there is no strain diagnostic that can measure the internal strains in a magnet. By winding a fiber in the magnet's wires, our spontaneous Brillouin scattering system can measure distributed strain. Theoretically, the distributed strain could be measured throughout the cabling process, the heat treatment, and even during magnet operation. Quenches and other electromagnetic variations exert forces on the magnet that can be simulated, but having experimental data to confirm these calculations would be very helpful. Not only could a distributed strain sensor confirm the pre-

dicted strains, but it could also potentially find unexpected strains that would lead to a better understanding of a magnet during normal operation and quenches.

Chapter 4

Experimental Data

The experiments of this thesis were designed as a proof of concept that a spontaneous Brillouin scattering system can work as a superconducting magnet diagnostic. Other Brillouin scattering systems have worked as distributed temperature and strain sensors. However, their measurements take on the order of minutes, and these measurements are all approximately room temperature. In order to be used as a quench detection system, a measurement needs to be taken at cryogenic temperatures, within seconds, not minutes. The previous section presented figures of the frequency shift and linewidth at cryogenic temperatures, but the data for them was generated using Thévenaz's stimulated Brillouin scattering system. Although stimulated and spontaneous Brillouin scattering are based on the same physics for the most part, it is still necessary to verify the cryogenic temperature dependence of the frequency shift, linewidth, and intensity for a spontaneous scattering system.

Previous experiments have addressed the effect of strain on the key parameters; however, these experiments were in the linear, room temperature range. Chapter 3 discussed how the introduction of non-linear effects makes a set of two equations and two unknowns inadequate to solve for the two unknowns. We needed to verify that a spontaneous Brillouin scattering system did not need a fourth parameter and equation to solve for the temperature and strain.

To complete the proof of concept we also needed to plot the Brillouin frequency shift, intensity and linewidth as functions of temperature and strain. Once these

plots were generated, they could be used as a multi-dimensional lookup table. After measuring the frequency shift, intensity, and linewidth, a unique temperature and strain can be determined.

4.1   Our Spontaneous Brillouin Scattering System

The problem with previous stimulated Brillouin scattering systems was that they required several minutes to make a measurement. Stimulated Brillouin scattering systems need to temperature tune a laser many times for each measurement, requiring approximately 30 seconds for each tuning. One solution to this problem is to tune the laser with something other than temperature so that the tuning time is greatly reduced. NP Photonics has developed a fiber laser that can be piezo-electrically re-tuned thousands of times per second.

Previous spontaneous Brillouin scattering systems also required several minutes of data acquisition in order to achieve a good signal to noise ratio. NP Photonics has developed a spontaneous Brillouin backscatter system that is capable of acquiring a good signal to noise ratio in less than a second. The system uses Optical Time Domain Reflectometry (ODTR) to spatially resolve measurements, as discussed in Chapter 2. A fiber laser sends light at 1550 nm through a coupler that splits the light into two different paths, as shown in Figure 4-1.
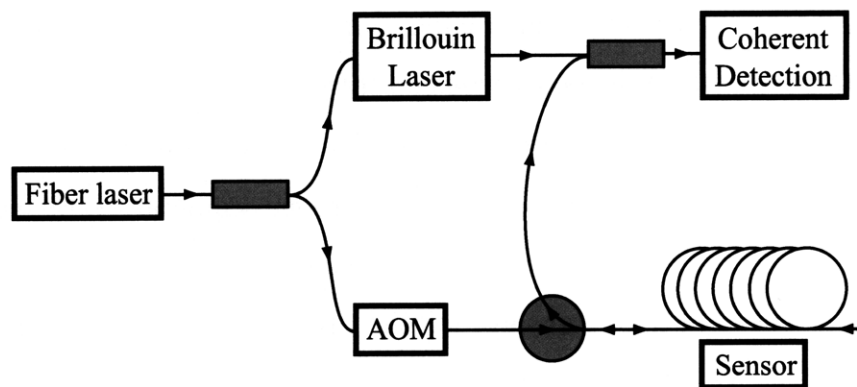
Figure 4-1: Diagram of spontaneous Brillouin scattering system.

The light from the fiber laser going to the upper path is used to pump NP Photon-

ics' Brillouin laser, which is an ultra-narrow linewidth (100 Hz)laser [62]. The light leaving the Brillouin laser is combined with the Brillouin backscattered light from the lower path in Figure 4-1. The Brillouin laser is used as a frequency-shifted local oscillator for the heterodyne detection of the spontaneous Brillouin scattered signal. Since the Brillouin frequency shift is in the 11 GHz range, measuring the frequency of the light within a few MHz is very difficult and expensive. By using a Brillouin laser as a local oscillator, with a frequency nearly 11 GHz lower than that of the fiber laser, the beat signal is heterodyned from the microwave range to the radio frequency range [63]. It is now possible to use a standard detector to measure the frequency shift of the spontaneous Brillouin scattered light.

In order to measure the linewidth of the spontaneous Brillouin scattered light, a MATLAB program was used to take the Fast Fourier Transform (FFT) of the signal. These experiments were done under a Department of Energy Small Business Innovative Research (SBIR) Phase I grant whose main purpose was to show feasibility of this measurement approach. In Phase I, there was insufficient funding and time to develop high speed hardware in addition to the existing system. Instead, the signal was split and run through a General Purpose Interface Bus (GPIB) cable to a second computer, where the signal was recorded. The signal data was run through the MATLAB FFT program to convert the signal data in time-space to frequency-space. Limited by the maximum data transfer speed of the GPIB cable, we were not able to get as many averages of data for the linewidth measurements as we would have liked.

4.2 Temperature Experiment (Zero Strain)

The main goal of the temperature experiment was to characterize the effect of temperature on the spontaneous Brillouin scattering in optical fibers at cryogenic temperatures. We measured the frequency shift, linewidth, and power at many different temperatures from 4 K to room temperature. We also determined that the best spatial resolution of our system at 4 K was around 8 meters. A secondary goal was to measure the effect of pulse length on the parameters at specific temperatures.

We were able to measure the frequency shift, intensity and linewidth over a temperature range from 4 K to room temperature. The frequency shift and linewidth data agree qualitatively with data from other experiments. Two different DAQ systems were used to measure the frequency shift and intensity, and both gave very similar results. We were able to achieve a spatial resolution of 8 m along 40 meters of gold coated fiber at 4 K, with a measurement time of less than a second.

4.2.1 Experimental Probe

One of the most important factors in the design of this experiment was that the fiber needed to be at a uniform temperature during data acquisition. The probe had to be cooled down to 4 K, and then the temperature needed to be stepped back up to room temperature as measurements were being recorded. The experiments needed to be done at NP Photonics in Tucson Arizona, because all of the optical components were set up there spanning several optical tables. Consequently the probe was designed to fit in a six-inch Dewar that was easy to ship. The Dewar, shown in Figure 4-2, has a central helium reservoir that is thermally protected from room temperature air by two vacuum layers and a liquid nitrogen reservoir.
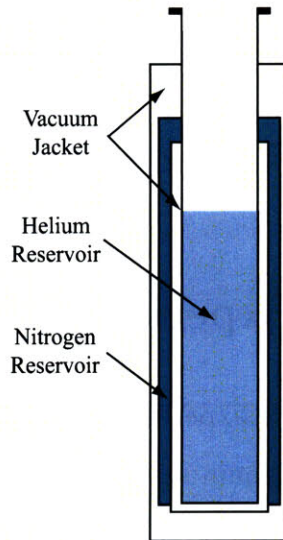
Figure 4-2: Diagram of a cryogenic Dewar.

To provide a uniform temperature we loosely wound the fiber in a channel cut

into an aluminum disk as seen in Figure 4-3. The aluminum holder was 4 inches in diameter, 0.75 inches thick (with the top on), and the quarter inch by quarter inch channel had an average diameter of 3 inches.
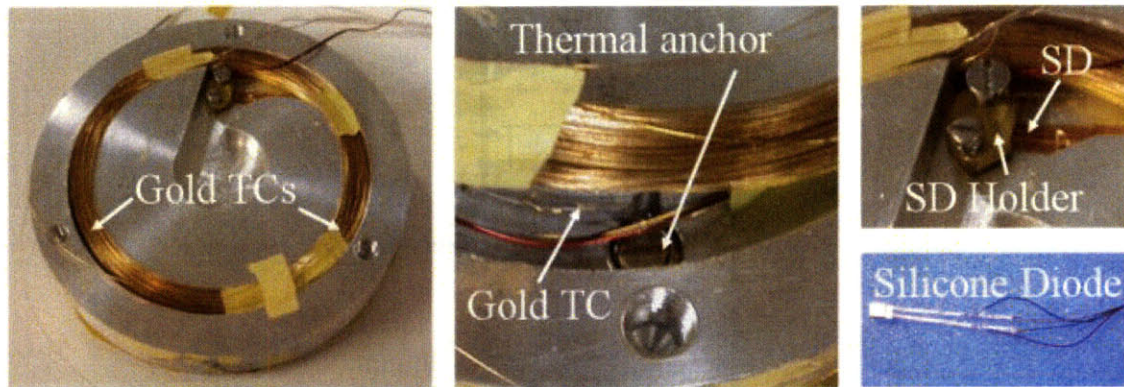
Figure 4-3: Location of the thermocouples and silicon diode relative to the coiled fiber.

An initial experiment was run at MIT to check the temperature uniformity using 7 thermocouples, and it showed that the temperature was uniform in the channel to within the accuracy of the thermocouples. In the experiment at NP Photonics, two gold-chromega thermocouples and a silicon diode were equally spaced in the channel to confirm that the fibers were heating uniformly, as seen in Figure 4-3. The silicon diode and thermocouples were thermally anchored to the probe by winding them one lap around the fiber channel.

In order to achieve the most accurate measurement at low temperatures, the thermocouples were set up to measure a differential temperature, not the absolute temperature. The temperature in the probe was measured compared to 4 K, so the low temperature measurements were measuring a much smaller temperature difference than when the probe was near room temperature. Since we were interested mostly in the cryogenic temperatures where a magnet would be superconducting, it made sense to have more accurate temperature measurements at low temperatures as opposed to closer to room temperature. The differential thermocouples were set up as seen in Figure 4-4.

Once the probe and fibers were cooled down in liquid helium to 4 K, the probe was
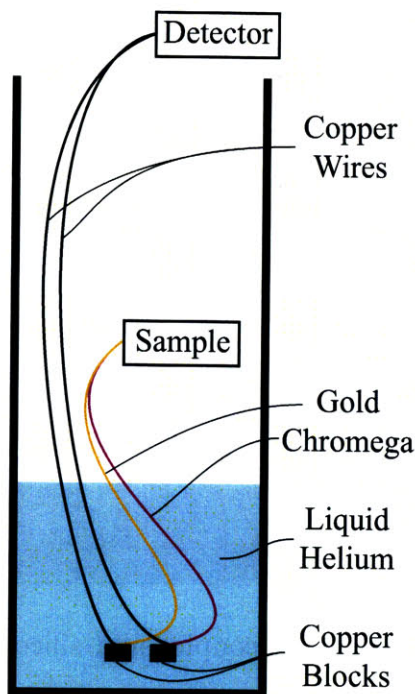
Figure 4-4: Diagram of a differential thermocouple setup.

lifted up to a position directly above the liquid helium. The silicon diode interacted with a Lake Shore temperature controller that read the temperature measured by the silicon diode and the output current to a heater. For our probe, the heater was 2.3 meters (25 ohms) of a constantan wire that was non-inductively wound and held against the top and bottom of the aluminum fiber holder, as seen in Figure 4-5. The thermal contact was improved by applying Apiezon grease between the aluminum holder, heater wire, and the fiberglass plate that held the heater wire in place.

Styrofoam was fitted around the probe to limit the effect of convection from the boiling helium on the temperature stability of the probe. A full view of the probe, including the thermocouple anchor, liquid helium level sensor, and insulation can be found in Appendix C.

4.2.2 Results

The sample fiber in the probe was made up of 40 meters of gold coated fiber and 40 meters of copper alloy coated fiber. Light from the laser system came through a

104
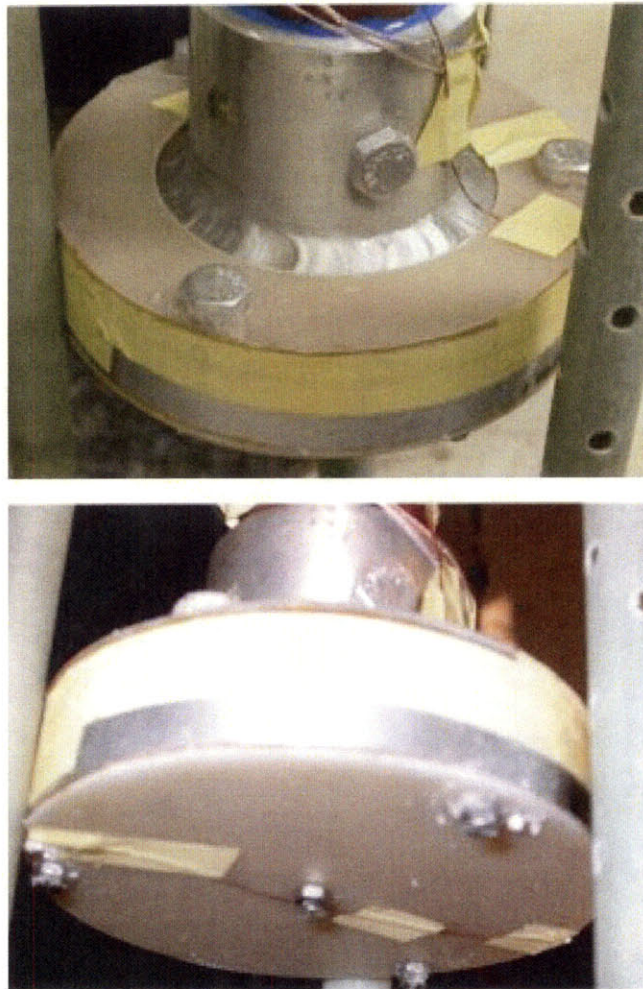
Figure 4-5: View of the top and bottom inductively wound constantan wire heaters.

standard single mode fiber that was fusion spliced to one end of the gold coated fiber outside the cryostat at room temperature. The other end of the gold coated fiber was fusion spliced to the one end of the copper alloy coated fiber inside the probe. The other end of the copper coated alloy fiber in the probe was cleaved at 7 degrees to minimize Fresnel reflection from the end of the fiber. The plan was to use ODTR to analyze the data from the gold and copper coated fibers separately, but at 4 K the attenuation in the gold coated fiber was so high that the signal through the copper coated fiber could not be analyzed.

Cryogenic Results

In the temperature measurement experiment we used a silicon diode and two gold-chromega thermocouples, equally spaced in the channel to monitor the temperature in different locations. As seen in Figure 4-6, the temperature was uniform at the three measuring points.
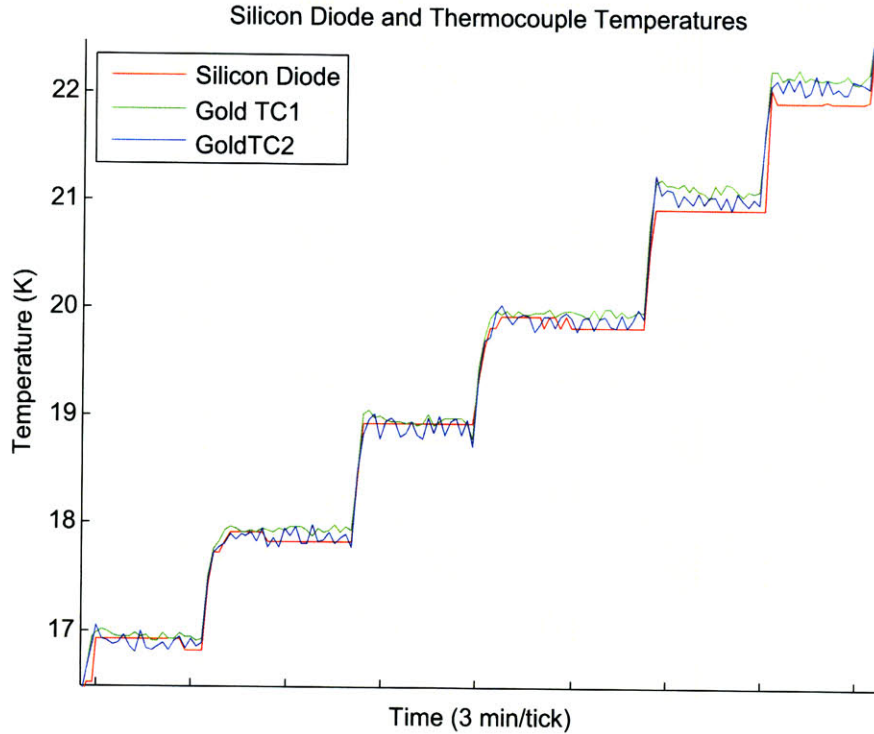
Figure 4-6: Low temperatures measured by the thermocouples and silicon diode are almost exactly the same.

The first day of the experiment, when temperatures from 4 K to 85 K were studied, liquid helium was used in the central reservoir of the cryostat. The differential thermocouple reference was in the liquid helium at the bottom. On the second day, when temperatures from 77 K to room temperature were studied, liquid nitrogen was used as the cooling fluid in the cryostat, and the differential thermocouple reference was in the liquid nitrogen at the bottom of the cryostat. Like the low temperatures measured on the first day, the three measurement points were similar for the second day, as seen in Figure 4-7.

Gold-chromega thermocouples are very accurate at cryogenic temperatures. A
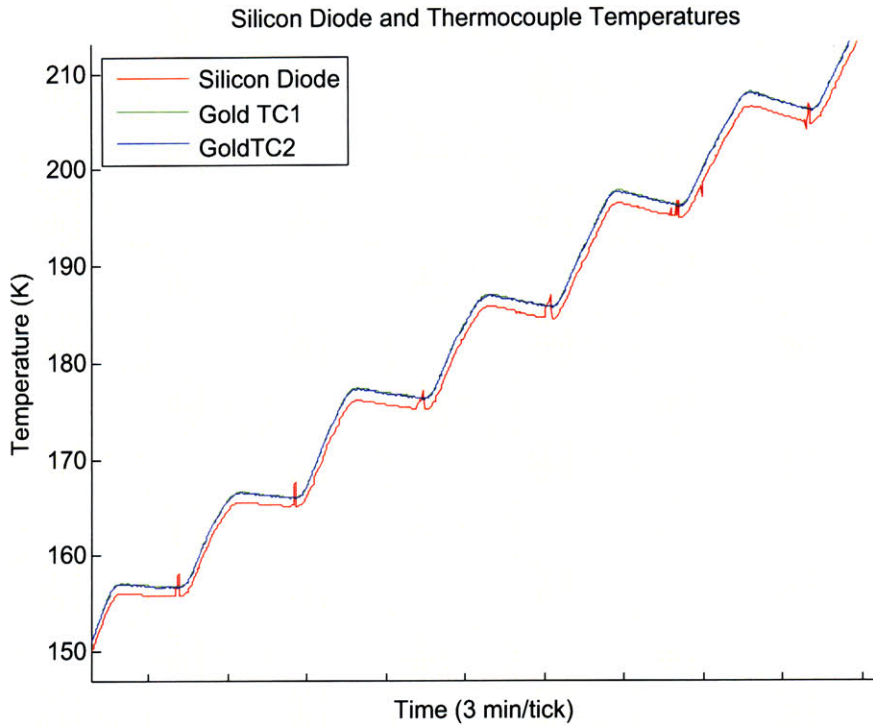
Figure 4-7: Higher temperatures measured by the thermocouples and the silicon diode are the same within measurement error (the two thermocouple lines are on top of each other).

one degree difference near 4 K corresponds to about a 12 μV difference in the signal. The DAQ system was accurate to 1 μV, corresponding to an error of about 0.1 K. The copper lead wires from the cryogenic soldering blocks to the DAQ system were made from adjacent pieces of a single spool of copper wire, so the lead wires should not significantly contribute to the error. The silicon diode has an error of $\pm$ 0.5 K for 2 - 100 K and 1 % of the temperature from 100-305 K. Its signal was on the order of mV, and the DAQ system was accurate to μV, so the overall error from the silicon diode was about $\pm$ 0.5-3 K depending on the temperature. All three signals were extremely close and within their respective error ranges, implying that the temperature measurements were very accurate, and the sample fiber was uniformly heated.

Brillouin Frequency Shift Results

One of our main goals for this experiment was to measure the spontaneous Brillouin frequency shift as a function of temperature. The probe was placed in liquid helium to obtain the 4 K data; then the probe was raised slightly above the liquid helium and the heater was used to warm up the fiber 1 degree at a time up to 25 K. From 25 K, the temperature was stepped up by 2 or 3 K until 85 K. At that point we removed the probe and let it warm up to room temperature overnight as the remaining liquid helium evaporated. The following day the probe was cooled to 77 K by liquid nitrogen, and the temperature rose from 77 K to 300 K in 5 degree steps. Figure 4-8 shows the data we recorded compared to a similar plot from the literature [5]. Thévenaz's data is the absolute Brillouin frequency shift as a function of temperature, while our data is the frequency shift relative to the local oscillator (NP Photonic's Brillouin fiber laser). In order to make this plot, we subtracted a little over 11 GHz (the difference between the pulse and the Brillouin laser frequency) from Thévenaz's data to compare it to our data.

As expected, Figure 4-8 shows that the frequency shift does not depend significantly on the pulse width. Overall our curve is very similar to the one produced by Thévenaz. An exact match between spontaneous and stimulated Brillouin scattering would not be expected. Furthermore, Thévenaz used standard single mode fiber and our data is from a gold coated fiber. Before we did our first cryogenic experiments, Jihong Geng (at NP Photonics) did several experiments with several types of fibers with different coatings in an oven, recording the frequency shifts at different temperatures. His results, shown in Figure 4-9, show that different types of fibers and coatings have different responses to temperature changes. This is not a problem for Brillouin scattering sensors, but it means that the sensing fiber, or a fiber of similar type and coating, needs to be calibrated.

The spontaneous Brillouin scattering frequency shift range that we are most interested in for superconducting magnets is shown in Figure 4-10.

There are several interesting results shown in Figure 4-10. Until the second day
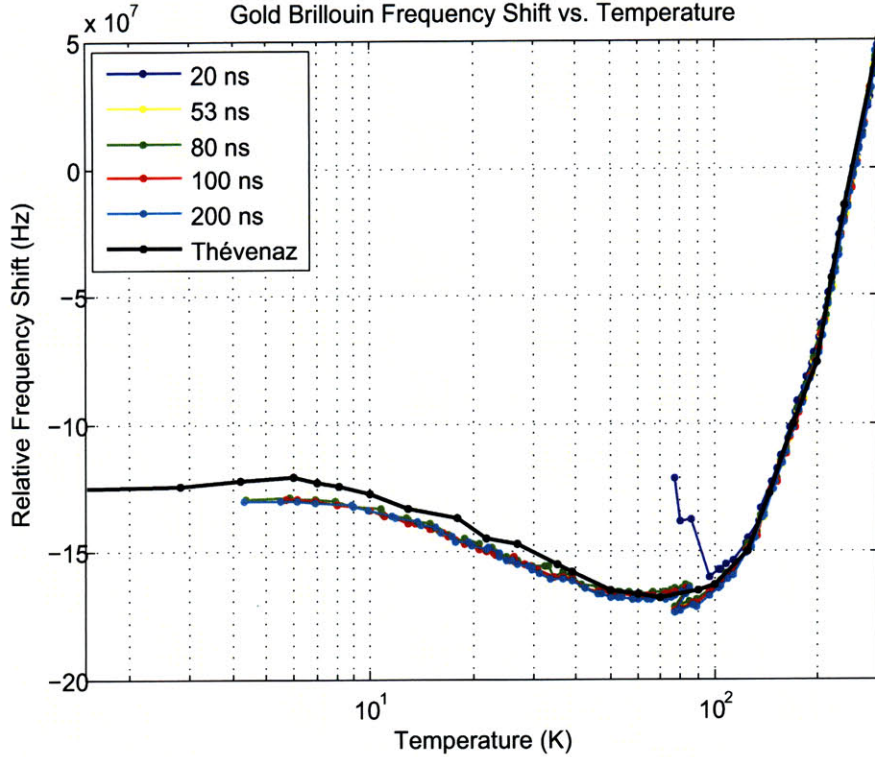
Figure 4-8: Our relative spontaneous Brillouin frequency shift agrees well with Thévenaz's stimulated Brillouin frequency shift.

we did not take data for 20 and 53 ns pulses because the signal to noise ratio was not good enough to get reliable data. Figure 4-8 shows that there was still too much noise for the 20 ns pulses up to about 100 K, so that the 20 ns data points below 95 K are dominated by noise. Above 100 K, the signal intensity was high enough that even the 20 ns pulse was reliable. The signal to noise ratio can be improved in several ways that will be discussed further in Chapter 5, including improved hardware and fibers with better attenuation properties.

Another interesting aspect of Figure 4-10 is the jump in frequency shifts around 77 K. One path follows from 4 K to 85 K (the data from the first day), and the second path is continuous from 77 K to 300 K (the second day). This is due to the effect of thermal cycling of the fiber. The slopes of the curves in Figure 4-11 show that the attenuation in the gold coated fiber actually got better after a thermal cycle by a factor of about 2.5. There is not enough data to quantify these changes accurately; however, one can clearly see that there was a significant change in the attenuation of

109
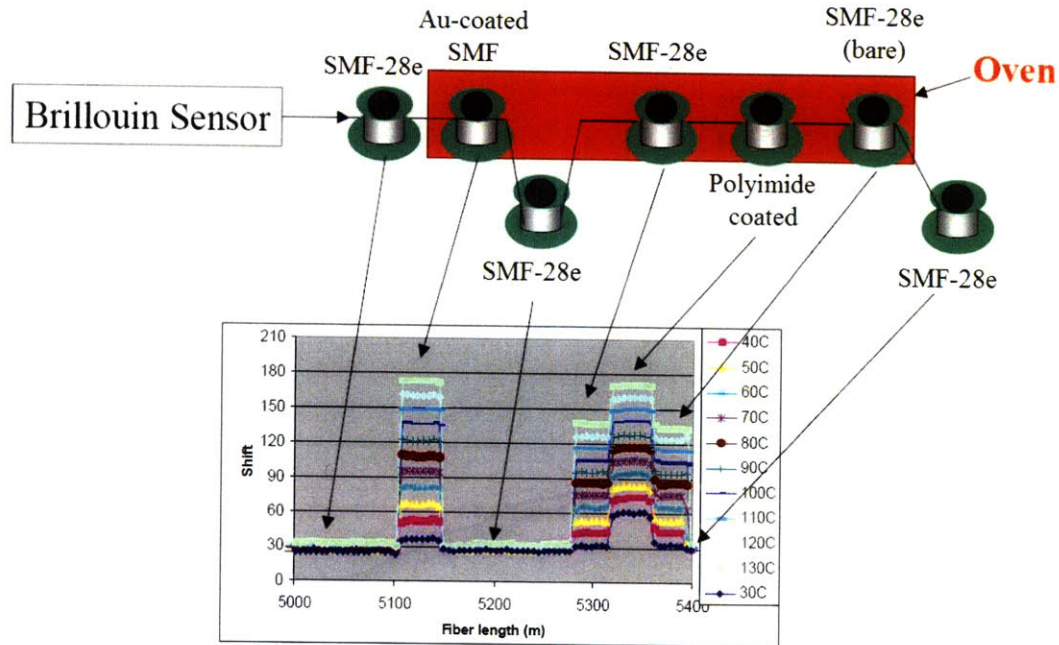
Figure 4-9: Different coatings and fibers will result in different frequency shifts (MHz) at the same temperature.

the gold coated fiber between day one and two. The data for the copper coated fiber is not as accurate, since it has the fewest data points and it has inaccuracies from being adjacent to the end cleave. When the fiber was cooled down to 4 K, some of the stresses in the fiber from the fabrication process were relieved, making the fiber behave more like a standard single mode fiber (with better attenuation).

Even though both the gold coated fiber and copper coated fibers were affected by the thermal cycle, it seems that the copper coated fiber was affected less. This is evident in Figure 4-11 because the attenuation (slope) did not change as much as it did for the gold coated fiber. Figure 4-12 also shows that the copper coated fiber was less affected than the gold coated fiber, because the frequency jump between the two days is not as large: about 10 MHz difference for the gold coated fiber and only about 5 MHz difference for the copper coated fiber.

Determining the errors for the frequency shift measurements is relatively straight-forward. The frequency shift is measured between the backscattered light and the light coming from the local oscillator (the Brillouin laser). These two signals are op-tically combined, and their frequency differences create a beat signal, which is mea-
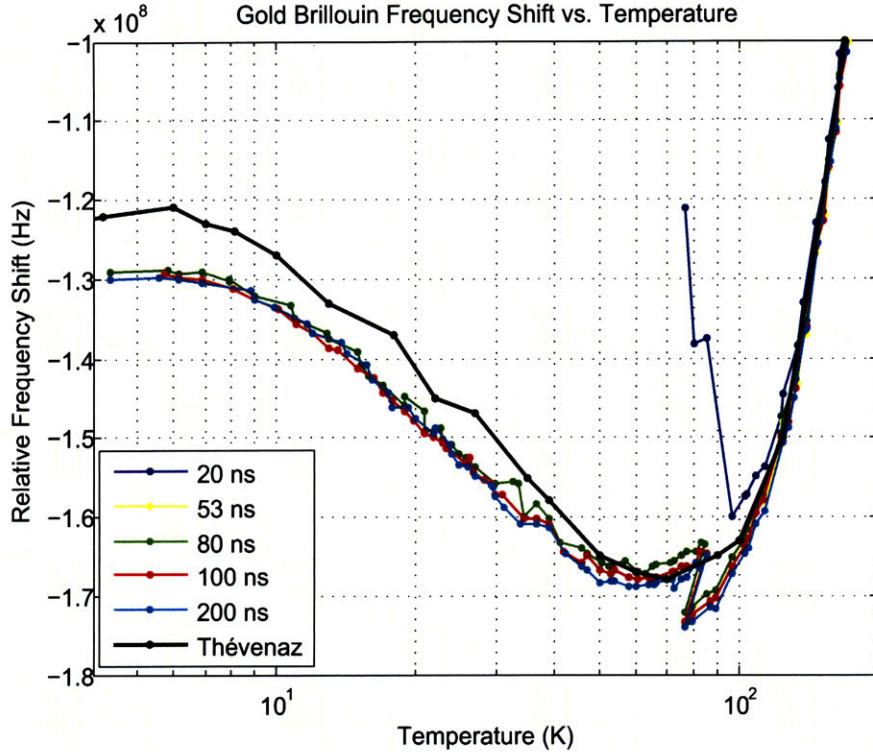
Figure 4-10: Area of interest for low temperature superconducting magnets.

sured using an embedded Field Program Gated Array (FPGA) which is run through a MATLAB program. This is the only significant source of error for the frequency measurement, and is mainly dependant on the number of averages. For our experiments we took 65,000 averages which corresponds to an accuracy of better than 500 kHz.

There are a couple other factors that can come into play, such as the stability of the lasers, but these errors should be insignificant, which is a major advantage of this system. In order for the laser's frequency stability to matter, the Brillouin laser (which is an actively stabilized laser) would have to shift after the pulse is sent down the fiber but before the backscattered light returns. Consequently for a 1 km sensing path, the lasers would have less than 3 μs to shift to be detected. Even if the laser shifts an order of magnitude more than its linewidth, 200 Hz, the error still would only be in the kHz range. Also a control fiber at a known temperature and strain is used as a reference to ensure that the lasers are not shifting, and to calculate the shift if they do. Therefore, the major source of error for the frequency shift calculations is
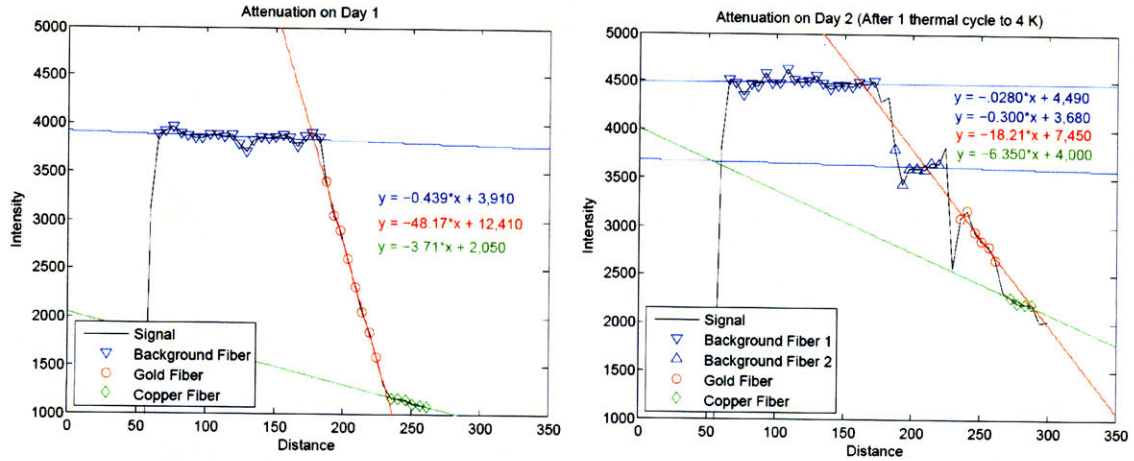
Figure 4-11: Room temperature intensity plots from day 1, before any cryogenic temperature cycle, and from day 2 after going to 4 K and back to room temperature on day 1.
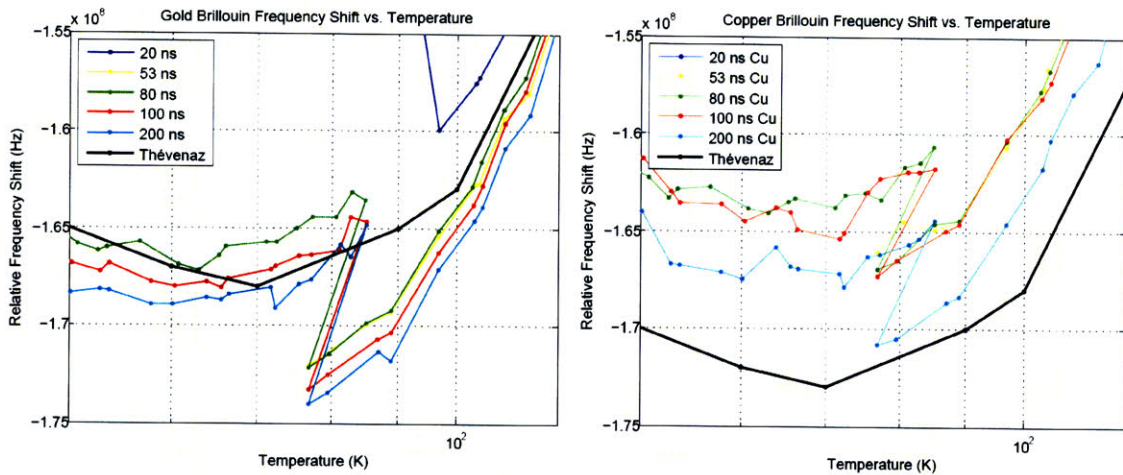
Figure 4-12: Gold and copper coated fiber frequency shifts after a thermal cycle.

the error of the frequency counter, which is accurate to better than 500 kHz.

Brillouin Intensity Results

The intensity of the Brillouin backscattered light is also an interesting variable that can help determine the temperature and strain in a fiber. Theoretically, one would think that as the temperature goes down, the intensity of the backscattered light will also go down since the scattering is off acoustic phonons, and movement slows down as the temperature approaches absolute zero. This is the general trend we found in our experiment. However, there is some interesting behavior when the temperature

gets down to around 15 K, as shown in Figure 4-13.
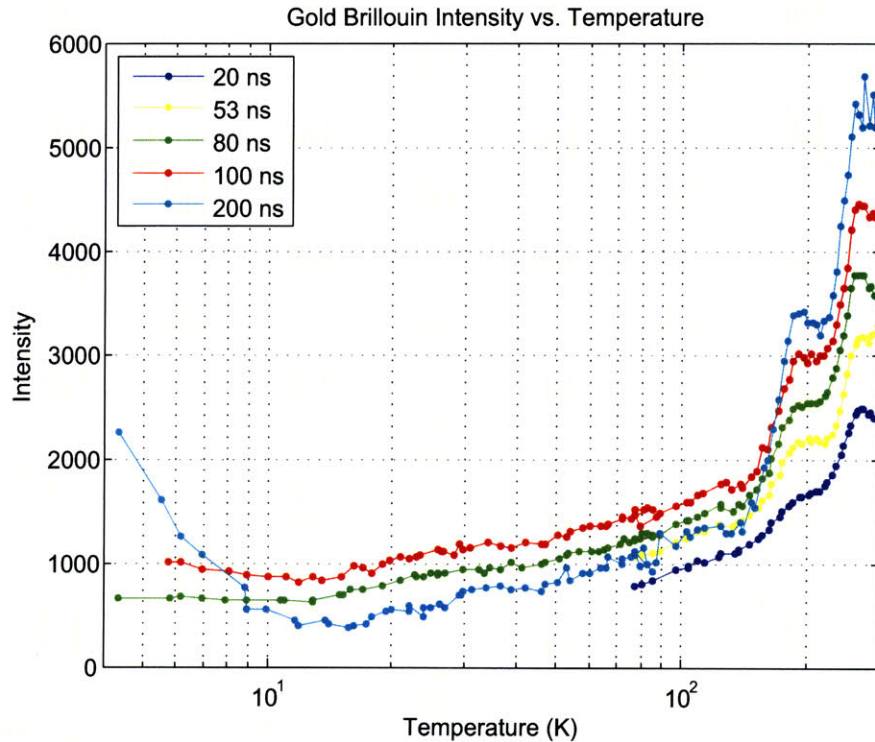
Figure 4-13: Intensity generally increases as a function of temperature, except for the range below about 15 K.

As we expected, there was a general decreasing trend of the intensity of the signal as we lowered the temperature. Below about 15 K, the intensity begins to rise as the temperature decreases. While this is counterintuitive, it follows the qualitative shape of the acoustic velocity curve in Figure 3-2. Similar to the non-monotonic Brillouin scattered light's frequency shift as a function of temperature, the intensity of Brillouin scattered light is also non-monotonic.

The error of the intensity measurements should be very small since the voltage is directly related to the power at the detector, written in Equation 4.1, where the responsivity, $\Re(\lambda)$, is a function of wavelength, but is constant around 1550 nm, where we are operating.

$$V_{out} = P\Re(\lambda)R_{load} \qquad (4.1)$$

The digitizer we used has 10 bit resolution, so the estimated instrumental error for

113

the intensity measurements is only about 0.1 % of the measured quantity. Adding in the errors of the resistive load and the responsivity, the overall error of the intensity measurements is on the order of a few percent. In a long-length distributed sensor system, attenuation will become a factor in the intensity measurements as a function of distance. While this was not a factor in this experiment which only measured a single section of fiber, a distributed sensor that is a few kilometers long will have to account for the attenuation of the scattered light as a function of distance. This will be discussed further in Chapter 5.

FFT Results

As part of the SBIR Phase I, we developed a second DAQ system to measure the linewidth of the scattered light. This system was connected to the original DAQ system with a GPIB cable, so the speed was limited. Instead of taking 65,536 averages in a half of a second, we took 230 averages in about 30 seconds. However, if this system were connected directly to the detector as the original DAQ system was, it would have an equivalent sampling rate and measurement time.

In the temperature experiment, we took data with the original NP Photonics system to get the frequency shift and intensity, and then we acquired data with the new system to measure the linewidth. The new system takes a Fast Fourier Transform (FFT) of the signal to get the frequency spectrum for a particular region. Due to the speed of data acquisition, we decided to do 230 averages on a single 30 meter section of the fiber. On the first day (for temperatures 4 K - 85 K), we recorded only 30 m of the gold section of the fiber, due to the lack of signal in the copper coated fiber. On the second day (for temperatures 77 K - 300 K), we recorded a sample for the gold coated fiber and a sample for the copper coated fiber. Each of these measurements was done using an 80 ns pulse, a 100 ns pulse, and a 200 ns pulse to determine whether the pulse width affects the linewidth.
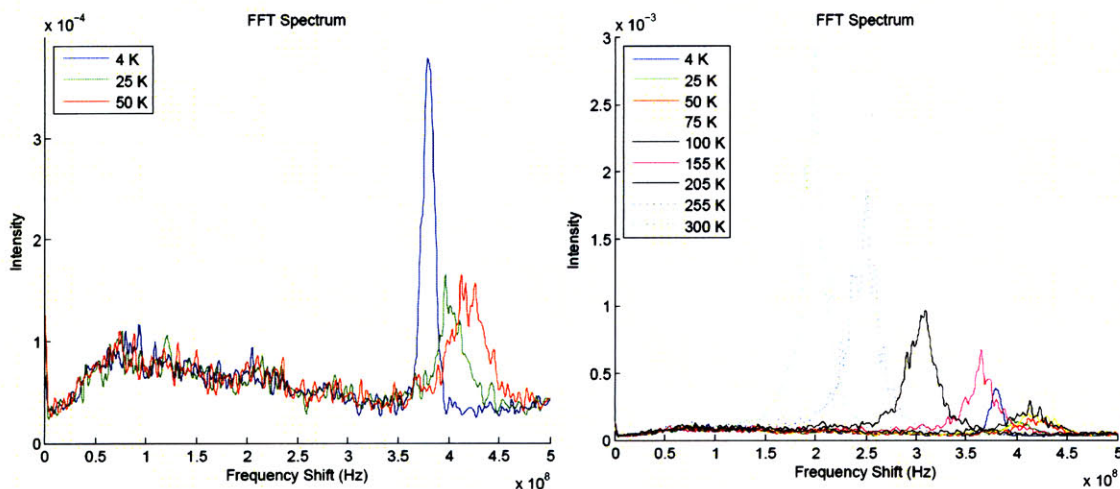
Figure 4-14: FFT of 100 ns pulses at different temperatures gives linewidth, frequency shift, and intensity. The left plot shows temperatures from 4 K to 50 K, and the right plot includes temperatures up to room temperature.

115

Figure 4-14 shows the raw FFT data for 230 averages of a 30 meter section of the gold coated fiber at different temperatures. From this data, we can get the linewidth, frequency shift, and intensity of the section of the fiber we are measuring. Just from a quick glance, one can tell that the frequency shifts and intensities follow the same trends as were recorded using the original NP Photonics system.

Although this data is qualitatively what we were expecting, the signal to noise ratio for many of the data points is not good. In the range of 30 K to 50 K, the raw data is similar to that shown in Figure 4-15. The intensity of the background noise is close to the intensity of the signal spectrum, and subtracting out the background noise changes the linewidth significantly. Due to the small number of averages, the data is very rough, so a smoothing function was used to analyze the data. When the DAQ system is upgraded, the number of averages per measurement will be increased significantly, so that smoothing the data should be unnecessary, and subtracting the background noise will not have such a large effect on the linewidth.
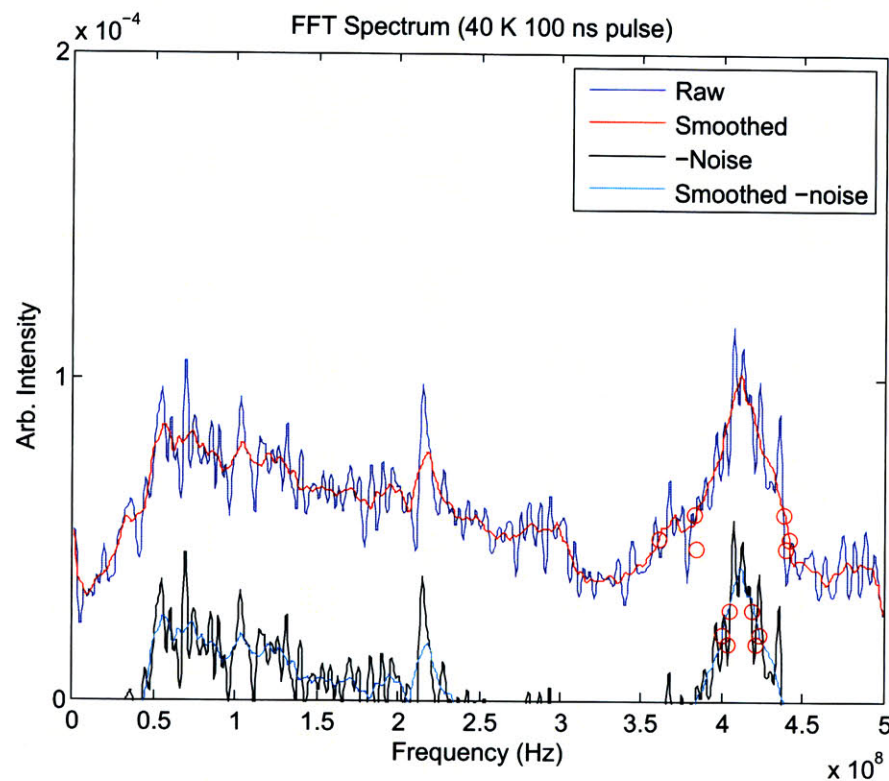
Figure 4-15: Raw FFT data does not have a good signal to noise ratio in the 30 K - 50 K region, and smoothing functions only help a little.

116

For the FFT linewidth data analysis, we used the smoothed data to calculate the FWHM from 4 K to 300 K, and compared it to the linewidth of stimulated Brillouin scattering that Thévenaz measured, as shown in Figure 4-16.
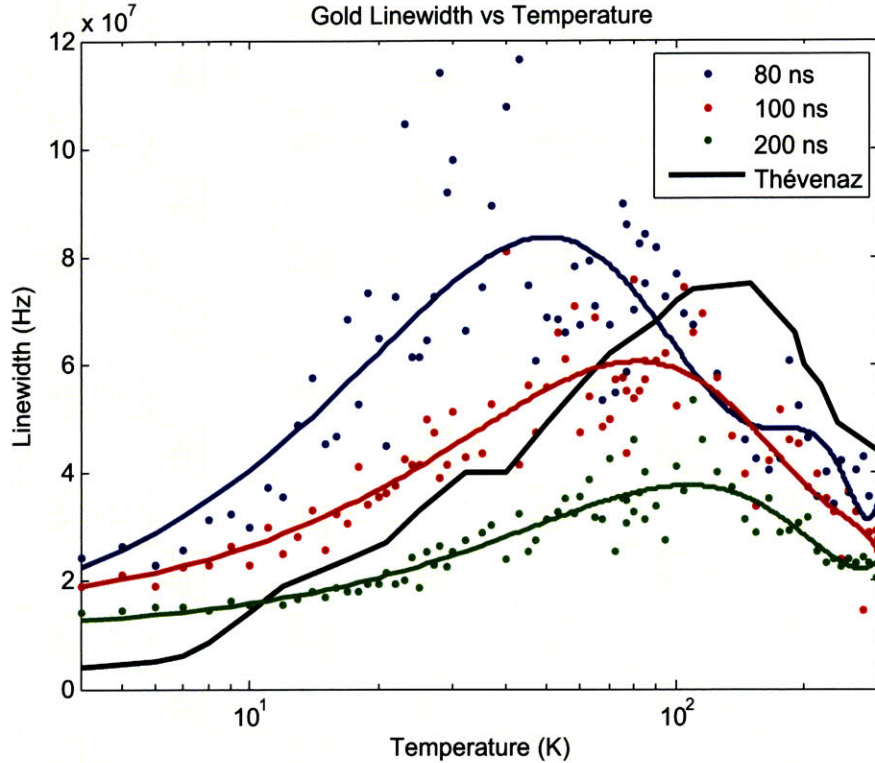
Figure 4-16: Linewidth as a function of temperature is qualitatively the same as Thévenaz's.

Again, our data does not exactly match Thévenaz's data. But this would not be expected since our experiments used a different type of fiber and measured spontaneous, rather than stimulated scattering. One very interesting aspect of Figure 4-16 is the dependence on the pulse length. This could also be an effect of the low signal to noise ratio and the smoothing technique. When we have a system that will average thousands of pulses, we should be able to tell if there is a difference in linewidth based on the pulse length, or whether this is an artifact of the low signal to noise ratio. Theoretically the dependence on pulse length does not matter, as long as we calibrate each pulse length we use.

I mentioned earlier that all three of the interesting parameters (frequency shift, linewidth, and intensity) can be taken from this one data-set in frequency space. In

order to compare the two systems, we need to take the negative value of the frequency shift from the FFT data and add 250 MHz to compensate for optical components that differ for the two systems. Figure 4-17 shows that the frequency shifts from the two systems are almost exactly the same, and that they both agree with Thévenaz's data.
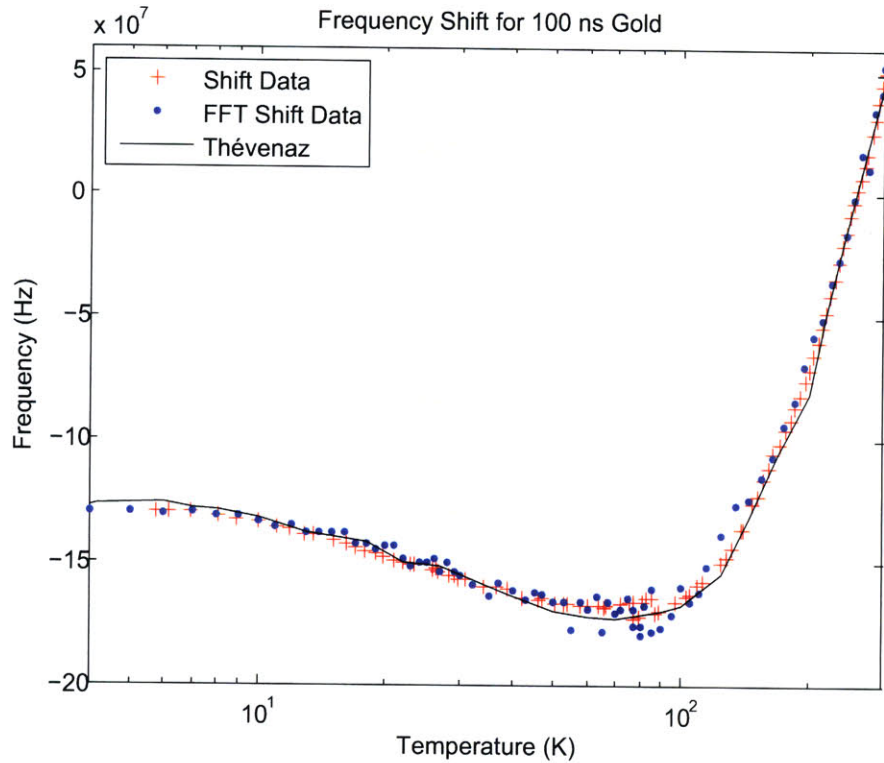
Figure 4-17: The frequency shift from the FFT and original system are the same and in good agreement with the literature.

The frequency shift is almost exactly the same for both systems, but the intensities are slightly different. The intensity measurements are on an arbitrary scale in each DAQ system, so in order to get them to be the same order of magnitude, the FFT intensity data of the lower one was multiplied by 5×10^6. The data from the two DAQ systems can then be compared, as shown in Figure 4-18. They follow the same general trend of higher intensity at high temperatures. But the minimum intensity from the FFT data is around 40 K, whereas the minimum is around 10 K for the original NP DAQ system. Again, these differences may come from the low signal to noise ratio data of the FFT system, which will be corrected with DAQ upgrades to the system.
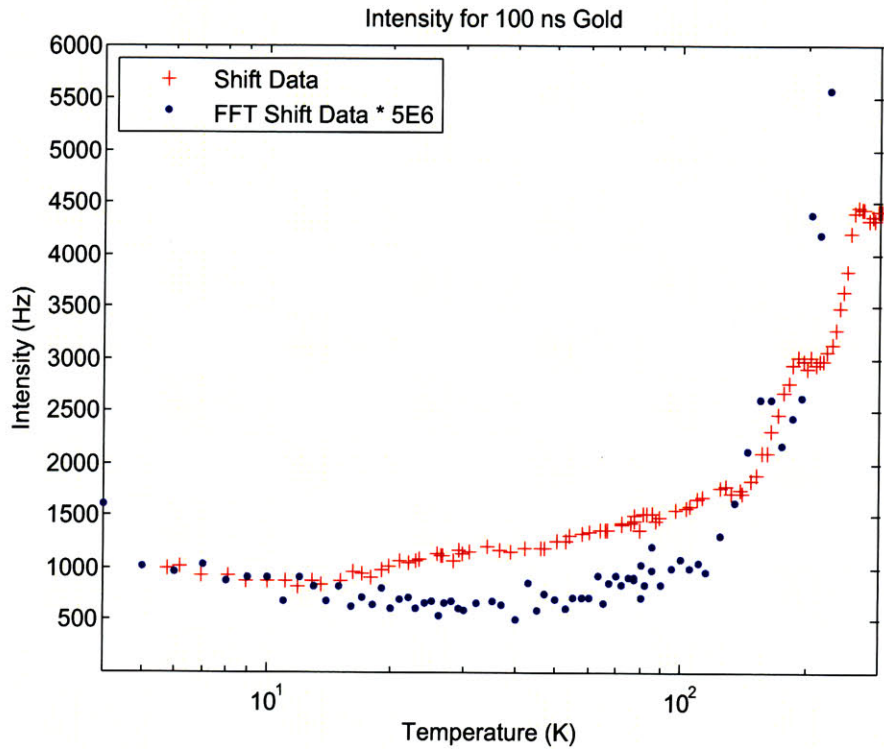
Figure 4-18: The intensity measurements from the two systems are not exactly the same.

Comprehensive error calculations were not performed for the linewidth data. As seen in Figure 4-15, the raw signal has a very bad signal to noise ratio and depending on the data manipulation and processing, the data has large errors. After system upgrades, when more averages and better data have been obtained, meaningful error calculations can be carried out. For this experiment, the error ranges are very large, but we are just looking for qualitative agreement with the expected data, which is apparent in Figure 4-17 and 4-18.

4.3 Strain Experiment

The main goal of the strain experiment was to characterize the effect of strain on the spontaneous Brillouin scattering parameters (intensity, linewidth, and frequency shift) in our fibers at cryogenic temperatures. Prior to this experiment, there was no data available on the effects of strain on Brillouin scattering at cryogenic temperatures. Measuring the effect of strain on these parameters is difficult due to the low spatial resolution of ODTR Brillouin scattering systems. Since the best theoretical spatial resolution is on the order of meters, the experiment needs to uniformly strain a few times that length of a fiber. Uniformly straining tens of meters of fiber is not too difficult at room temperature, but when it has to be done in liquid helium most of the commonly used straining systems are no longer feasible.

Since we wanted to map the effect of strain on the Brillouin scattering parameters as a function of temperature as well, the probe also had to be able to control the temperature of the sample fiber. The following section will describe the probe design, and how it uniformly strained about 50 meters of fiber at a controlled temperature. In the experiment, the temperature controller was used to heat the fibers to a desired temperature and then the fibers were strained to around 3000 $\mu\varepsilon$, taking data throughout the strain run. This was done at many different temperatures from 4 K to room temperature to get a good sample of temperature-strain space data points. The temperature was not exactly constant through a strain run, but the temperature was recorded every time the frequency shift, intensity, and linewidth were measured. By making these measurements throughout a range of temperatures and strains, this experiment allowed the mapping of the frequency shift, intensity, and linewidth as a function of temperature and strain.

4.3.1 Experimental Probe Design

The most difficult part of the strain experiment was designing a probe that would uniformly strain 50 meters of fiber. Since the expected strain range for ITER magnets is around 2000 $\mu\varepsilon$, and fibers can survive about 10,000 $\mu\varepsilon$ at room temperature,

we decided to strain our fibers to around 4000 $\mu\varepsilon$. While this is a relatively small strain, it is higher than the yield strain in most metals, especially in liquid helium. Several probe designs were discussed and rejected due to a number of complications, as discussed in Appendix D.

The probe design that we decided to use is similar to the probe on the cover of Ekin's book on cryogenic experimental technique [64]. When two cone-shaped disks are pressed together, their overall diameters will increase slightly, as seen in Figure 4-19.
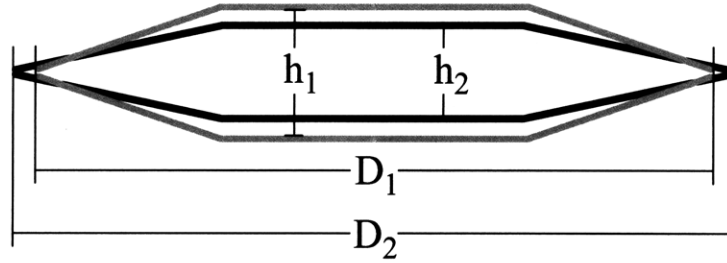
Figure 4-19: Cross section of two disks being pressed together. As the disks are pushed together, their diameter increases.

Although the concept is conceptually simple, the constraint of working in a cryogenic environment made the design more difficult. For example, below 10 K, most steels become brittle. Fortunately, some metals, like titanium, become stronger and more ductile at cryogenic temperatures. We used a titanium-aluminum-vanadium alloy, Ti-6Al-4V, which had the best cryogenic properties for our experiment [65]. Not only did we need to find a material that is ductile at 4 K, but we also had to design the probe so that it would not buckle under the forces, as discussed in Appendix E.

Since we needed to strain 50 meters of fiber, we could not have the two disks simply pushing on each other, because we needed a large area to wrap the fibers. In order for the experiment to be carried out in a six-inch dewar (for shipping and cryogen costs), the sample wrapping diameter of the probe could be at most four inches. Wrapping 50 meters of fiber around a cylinder with a diameter of four inches means that the fiber will be wrapped about 150 laps. Since the fibers are about 160 μm in diameter, 150 laps of fiber will cover about one inch of the cylinder vertically.

Including space for temperature and strain sensors on the probe, we made the fiber wrapping area 3.5 inches, as shown in Figure 4-20.
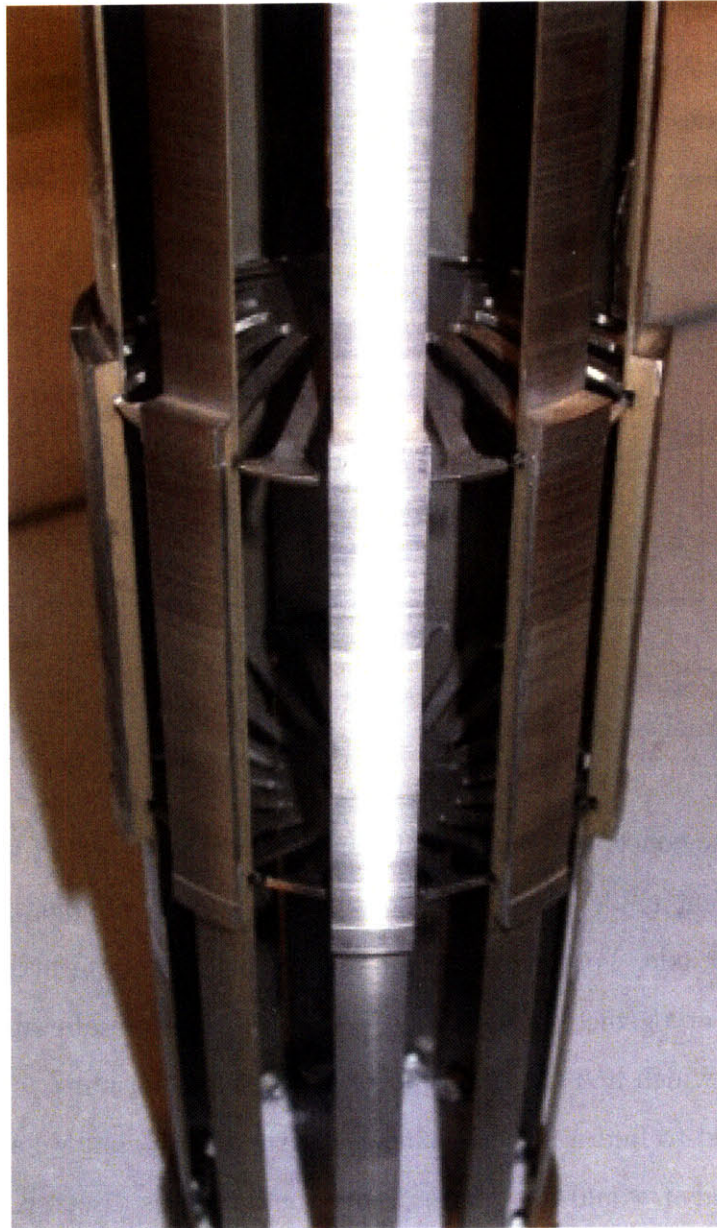
Figure 4-20: Strain probe with a few sections removed to see the disks.

The probe uses a threaded push-pull rod combination to force the two disks together in order to radially expand the cylindrical fiber holder. Using a threaded rod with 40 threads per inch, the two disks can be forced together in a very controlled fashion. However, knowing the actual strain applied is much more complicated. Due to the thermal expansions of the different types of materials used, as well as the chang-

ing level of liquid helium throughout the experiment, an exact correlation between the number of turns and strain applied is not possible. Many strain experiments use an extensometer to very precisely measure displacement, but there was not enough room in and around our probe for an extensometer. A fiber strain gage was utilized in order to measure the exact strains felt by the sample fiber. FBGs are commonly used as strain gages, but they are not calibrated at cryogenic temperatures. In order to use FBGs as strain gages at the cryogenic temperatures in our experiments, we needed to first calibrate the FBGs at these temperatures, as described in Appendix A.

Figure 4-21 shows the final view of the sample fibers epoxied to the probe before the experiment. For more photos, see Appendix F.

Figure 4-21: Final view of the strain probe.

4.3.2 Results

The sample fiber wrapped around the probe was made up of three fiber sections, because the gold coated fiber broke while removing it from the temperature experiment probe. The gold coated fiber samples were about 10 and 15 meters long, and the copper coated fiber was about 30 meters. Each of these sample fibers had leads that went in and out of the probe from room temperature. The fiber path from the laser started with 100 meters of standard single mode fiber (SMF) at room temperature as a reference fiber. This fiber was fusion spliced to the copper coated fiber, which descended and wrapped around the probe and came back out to room temperature. The end emerging from the probe was fusion spliced to 20 meters of SMF at room temperature, followed by the 15 meter gold coated fiber sample, another 20 meters of SMF at room temperature, and finally the other 10 meter gold coated sample fiber with a 7 degree cleave to minimize Fresnel reflection.

Cryogenic Results

One of the most difficult parts of the design of this experiment was uniformly straining 50 meters of fiber at a constant temperature. Since the frequency shift, intensity and linewidth are all functions of temperature and strain, in order to measure the effect of strain, the fiber has to be at a uniform temperature. In any system there are temperature gradients, but the probe design must ensure that these gradients are negligible. On the inside of the probe, a silicon diode was epoxied using Stycast 2850 epoxy which has high thermal conductivity throughout the temperature range of our experiment. Also, on the outside of the probe, two gold-chromega thermocouples were soldered to the surface. As seen in Figure 4-22, the thermocouples are above and below the copper coated and gold coated fibers, and the silicon diode is positioned at the mid-plane on the inside.

As seen in Figure 4-23, the temperatures recorded by the silicon diode are within a degree or two of the two thermocouples. The top thermocouple (green line), and the bottom thermocouple (blue line) are also extremely close together, which proves
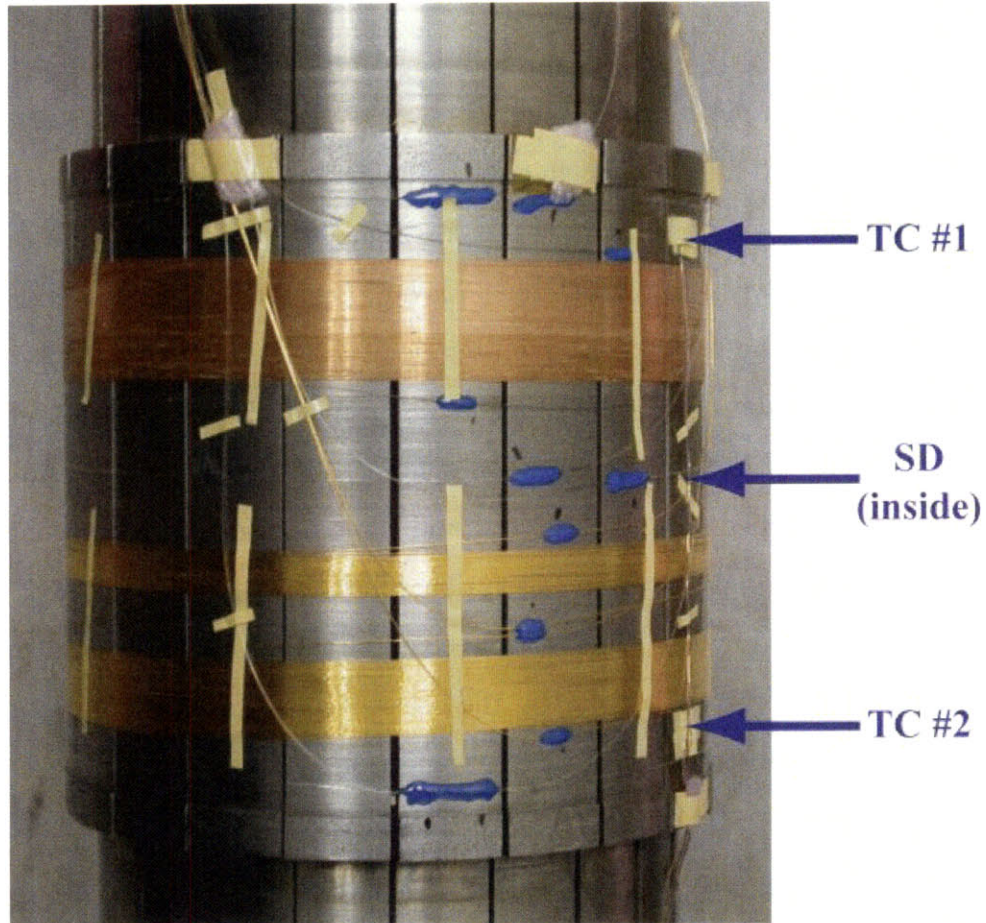
Figure 4-22: Locations of the silicon diode (on the inner surface) and thermocouples (on the outer surface).

that the temperatures at the top and the bottom of the fiber samples were very close.

The gold-chromega thermocouples and the silicon diode are the same as those used in the temperature experiment. The DAQ system is also the same, meaning the errors are less than 1 K for the thermocouples and $\pm$ 0.5-3 K for the silicon diode at all temperatures.
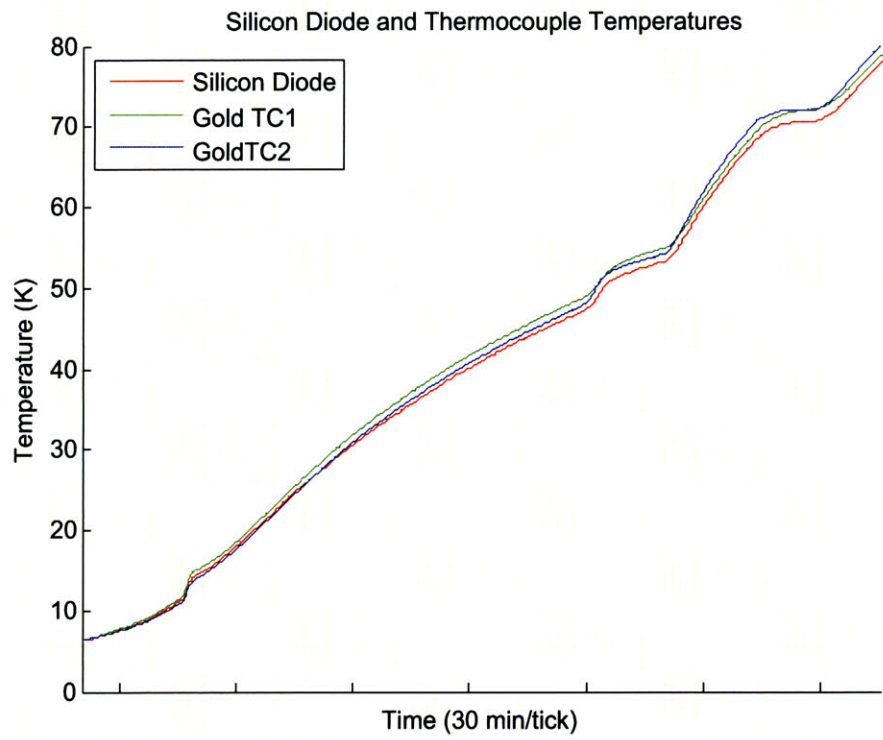
Figure 4-23: The temperatures of the silicon diode and thermocouples are within a few degrees or less.

FBG Strain Gage Results

In order to determine the actual strain applied in the sample fiber, we decided to use Fiber Bragg Gratings as the strain gage. The strain comes from the disk fingers pushing out the steel fiber holder, which increases the gaps between them. It is assumed that the fibers slide on the steel surface to distribute the strain as uniformly as possible. Regular strain gages cannot be used across the gaps, and the apparatus is too small to use an extensometer. Furthermore, standard laser-to-point measurement systems do not work while submersed in liquids.

Since the FBGs can be wrapped on the same surface as the sample fiber and measure the exact strain a fiber feels, they are ideal for use as a strain gage. However, the FBGs had not been calibrated for use at cryogenic temperatures. Therefore, a preliminary experiment was conducted to calibrate the FBGs at cryogenic temperatures, see Appendix A, and the data from that experiment was used to determine the actual strain in the sample fiber.

Three FBGs were used in this experiment: one at the top, one at the bottom, and one in the middle as seen in Figure 4-24. By comparing the strain experienced by these fibers, we could verify that the cylinder expanded uniformly. An optical switch was used to switch between the three FBGs during the experiment, and the separated data is shown in Figure 4-25. The optical spectrum analyzer had an accuracy of $\pm$ 0.005 nm, which converts to $\pm$ 3 to 8 $\mu\varepsilon$ depending on the temperature.

As previously mentioned, the strain measured in the three FBGs was used to verify that the cylinder is expanding the same amount at the top and bottom, proving that the top of the fiber sample is being strained the same amount as the bottom of the sample fiber. Figure 4-26 also shows the associated Brillouin frequency shift vs. strain plot, which has three lines depending on which FBG is used. For the rest of the fiber data analysis, an average of the top (red) and middle (green) FBG is used since the copper alloy coated fiber is between them.
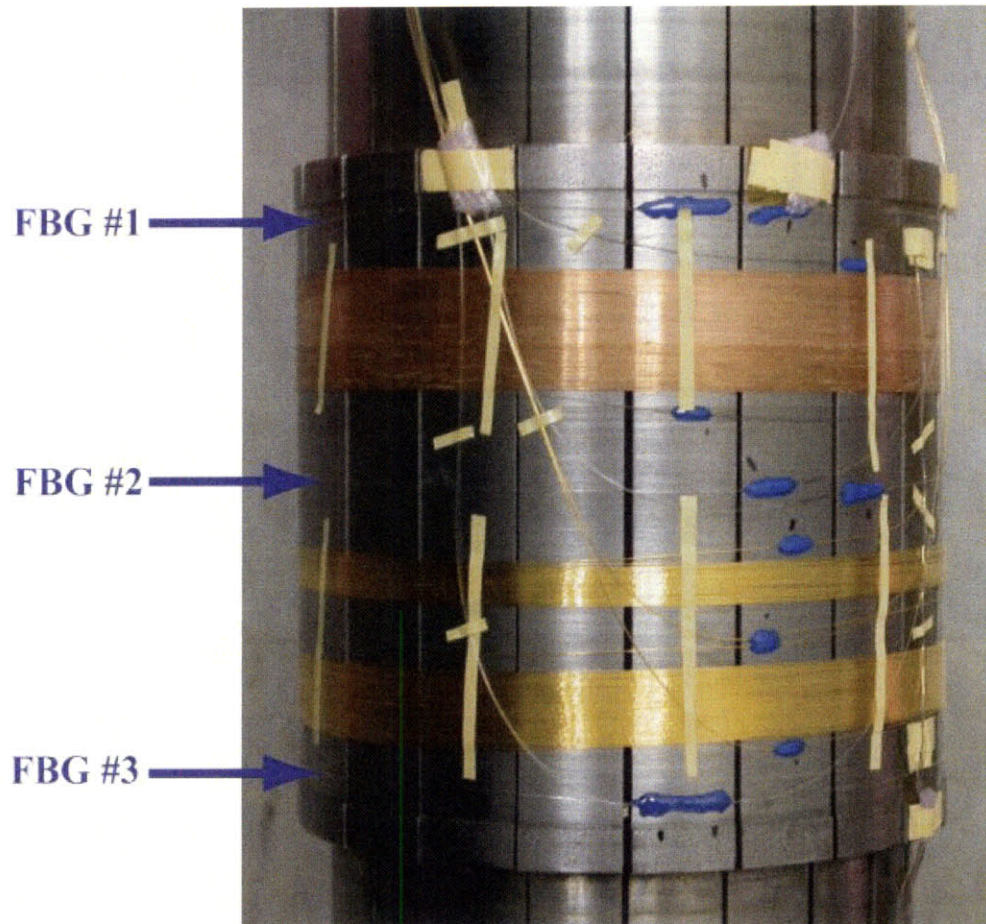
Figure 4-24: Location of the Fiber Bragg Grating strain gages.
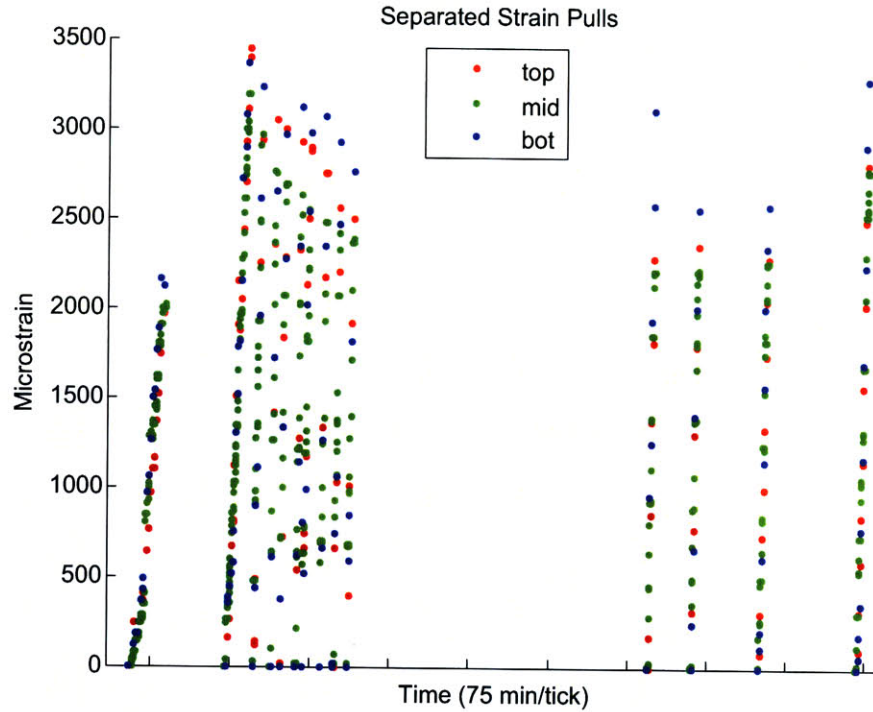
Figure 4-25: Strain measured by the three FBGs.
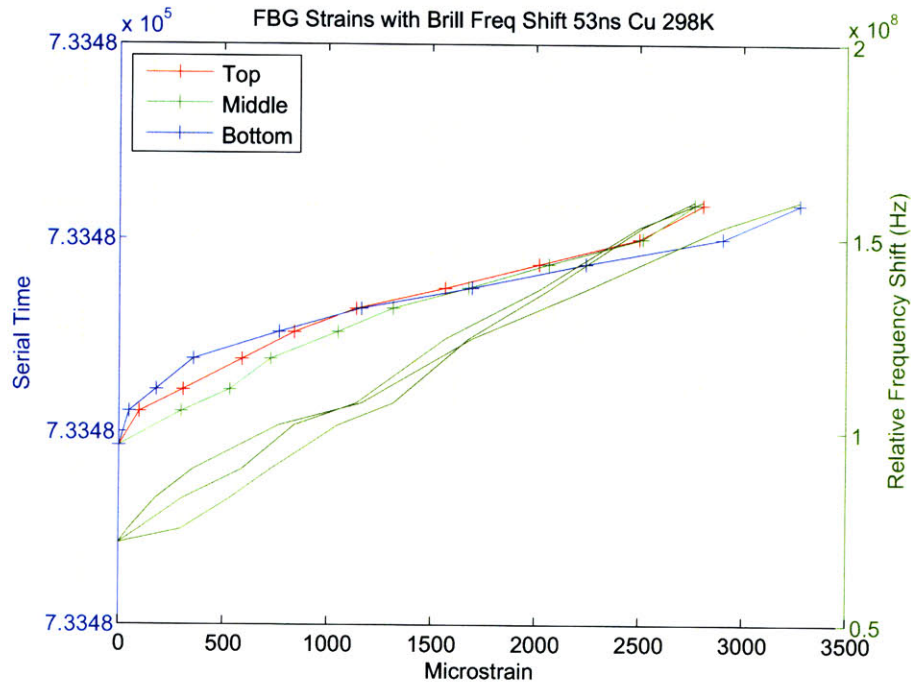
Figure 4-26: The strains measured by the three FBGs are very similar, especially the top and middle FBGs which surround the copper coated fiber. Depending on which FBG is used, the Brillouin frequency shift as a function of strain is also plotted.

130

Brillouin Frequency Shift Results

The frequency shift as a function of temperature at zero strain was measured from 4 K to room temperature in our first experiment and by Thévenaz. Before each strain run, data was recorded as a baseline zero-strain reference point. Plotting these points as a function of temperature gives us a figure that is qualitatively the same as the measured results from the temperature experiment. It is not quantitatively the same, since the first experiment's data was generated by the gold coated fiber, and the data reported here is from the copper alloy coated fiber. This second experiment confirms the results from the temperature experiment and adds strain as a third dimension.

Since the data was generated from the copper alloy coated sample fiber, located between the top two FBGs, we used the average strain recorded by FBGs 1 and 2. Figure 4-27 shows the frequency shift, relative to the Brillouin laser local oscillator, at 15 different temperatures as a function of strain. These measurements were made using both 53 ns and 80 ns pulses, corresponding to approximately 5 m and 8 m spatial resolution, respectively.
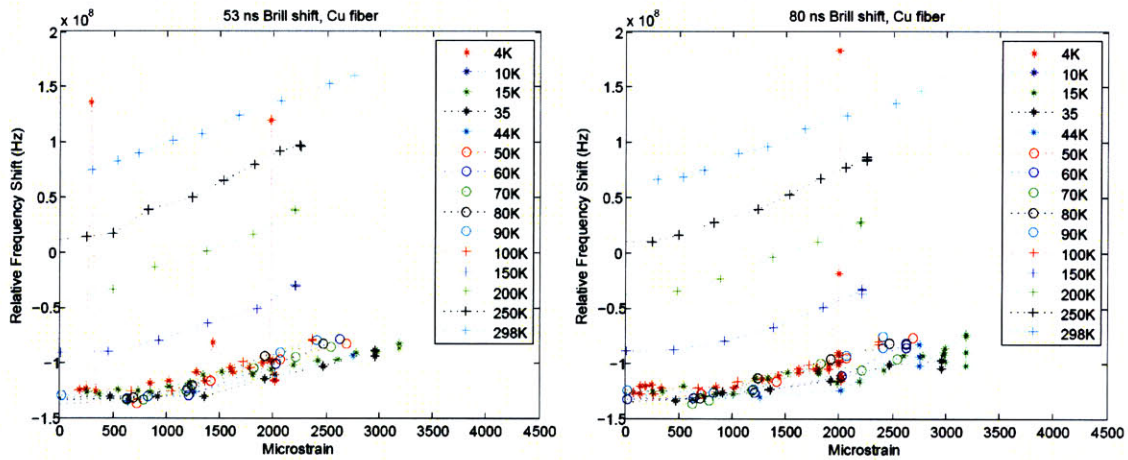
Figure 4-27: Relative frequency shift at different temperatures as a function of strain.

There were several points in the 4 K data set that were extreme outliers, mostly at the final position of the strain run. Since the 4 K strain run was the first run, we originally attributed the outlying data points at the beginning to an initial non-uniformity in the probe that was eventually fixed. For example if one of the fingers

was initially not in the groove of a cylinder piece, causing that piece to push out more than the rest, this could account for the increased strain, until the piece popped back into place. However, since we know that the temperature was 4.2 K because the probe was submersed in liquid helium, the frequency-strain curve can be extrapolated, indicating a strain of over 2 % for the measured frequency shifts. This is beyond the limit where the fiber would break, so the anomalous frequency shifts must be incorrect. Three possible explanations are a potential power surge, other electrical abnormality in the detector, or more likely a cooling effect on the optical equipment caused by the cryogens. The experiment was run in a laboratory, in which the cryogenic containers were very close to the optical table and optical equipment. After filling the cryostats, there were random bursts from the liquid nitrogen dewar as the pressure built up and relieved itself. If these vibrations disturbed the temperature-controlled frequency stabilizer of the lasers, it could easily cause a frequency shift in the laser for a second or two. Since the measurements only take half of a second, this is the most likely cause of the outlying data points. After the 4 K data was taken, the cryogenic dewars were moved out of the room, and there were no more gross data abnormalities for the rest of the experiment.

In order to compare the baseline zero-strain points of the strain experiment to the literature and to our previous results from the temperature experiment, the zero-strain points were plotted as a function of relative frequency shift and temperature, as seen in Figure 4-28.

Figure 4-28 shows the raw data from the 53 ns and 80 ns pulse length measurements, along with their averaged data. A 6th degree polynomial was fitted to the data because it had the best fit. For later smoothing purposes, the zero-strain point was changed to the fitted value, which is a change of at most a few MHz. It is apparent that the curve in Figure 4-28 has the same qualitative shape as Figure 4-8. We do not expect quantitative agreement, since the data in Figure 4-8 comes from the gold coated fiber, while the data in Figure 4-28 is from the copper alloy coated fiber.

Each strain run from Figure 4-27 was fitted to a 2nd degree polynomial, since that gave the best fit to the data. The first data point in the data set, the zero-strain
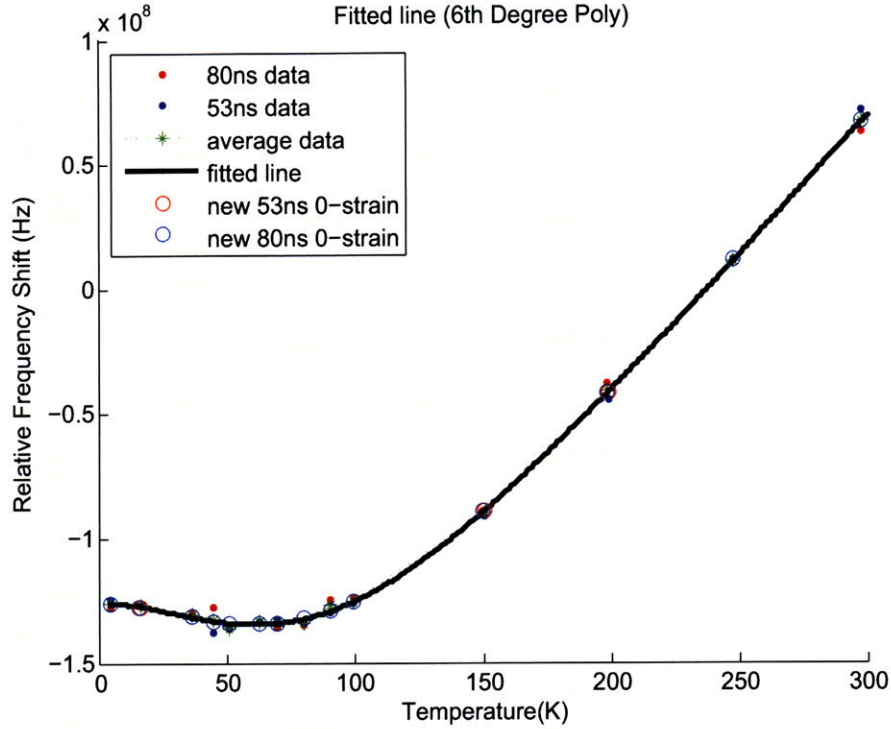
Figure 4-28: Zero-strain data as a function of relative frequency shift and temperature show the expected shape.

data point, was weighted heavier than the rest of the data to anchor that data point. Several times during the experimental run, data acquisition was repeated several times at the same temperature and strain. These data points were averaged and counted as a single data point. Two examples of the data fitting are shown in Figure 4-29.

Not all of the strain runs went to the same maximum strain. At the beginning of the experiment, during the very low temperature measurements, we were hesitant to strain the fibers much past 2000 $\mu\varepsilon$, for fear of breakage. Later, at higher temperatures, the fibers were routinely strained past 3000 $\mu\varepsilon$. In order to eventually create a full three-dimensional plot, we used the fitted curve to extrapolate all of the strain runs to 3500 $\mu\varepsilon$, as seen in Figure 4-29.

As previously mentioned, the temperature was slowly increasing throughout the strain runs. This is not a fundamental problem, since the temperature was also recorded for these data points, but it should be understood that the temperature was not constant for the data points in Figure 4-29. The temperature increase over a strain run was recorded, and it was easy to correlate the correct temperature to
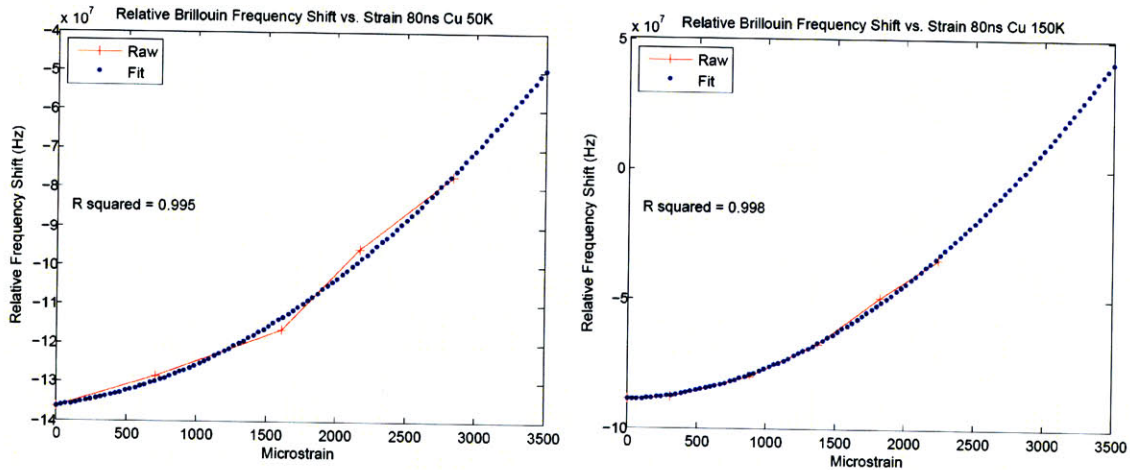
Figure 4-29: Second degree polynomial fit to the data in frequency-strain space.

the data. MATLAB has a function named GRIDDATA, which takes an array of non-uniformly spaced data and plots the matrix in three-dimensions. GRIDDATA will interpolate between data points, but always goes through all of the data points. Using the fitted data from Figure 4-29, as well as the appropriate temperatures for the data, the relative frequency shift was plotted as a function of temperature and strain as shown in Figure 4-30.

Raw data is included as circles in Figure 4-30 to show how good the fit is. On the top left, the 4 K outlying point can be seen; however, as discussed earlier, this point should be neglected. The data has been fitted in the increasing strain direction, and then it was also fitted in the increasing temperature direction along a few strains. For this system to eventually be used as a magnet diagnostic, Figure 4-30 will have to be measured with many more data points to get a very accurate surface. However, a detailed calibration curve was not the goal of these experiments. These experiments were designed to obtain the general shape of the surface, which is apparent in Figure 4-30.

The errors for the frequency shift and temperature in Figure 4-30 are very similar to those discussed for the data in Figure 4-8: the frequency shift errors are on the order of 500 kHz, and the temperature errors are on the order of $\pm$ 0.5 - 3 K depending on the temperature. This experiment is different from the temperature experiment in that the fibers are wound around the probe and have a vertical span
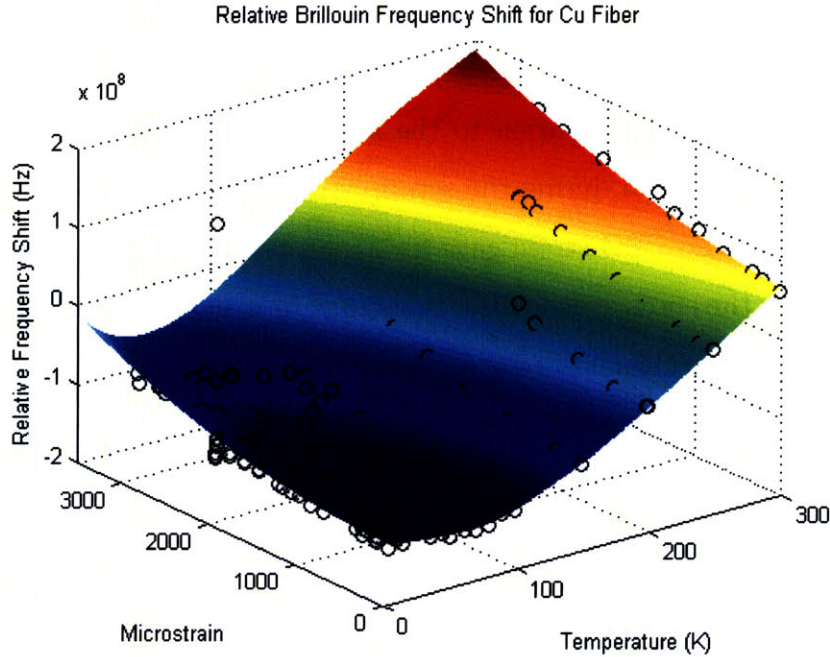
Figure 4-30: Relative spontaneous Brillouin frequency shift as a function of temperature and strain (using 80 ns pulse length data).

of about 2 cm, which is more than the channel in the temperature experiment. The vertical temperature gradients could lead to more temperature error, but the three temperature measurements, spanning over 8 cm vertically, never differed by more than a few degrees, which is within their error bars.

The error of the strain measurement is largely dependent on the FBG calibration experiment. This experiment did not produce as exact of results as we would have liked; however, the results were good enough to use in the strain experiment. The general trend of decreasing sensitivity to strain as the temperature decreased form 200 K to 4 K, along with the general value of $\frac{d\lambda}{d\varepsilon}$ is all that was needed to make Figure 4-30. Since this ratio is really only a scaling factor, the qualitative shape of the plot would not change even with calibration errors in the ratio of $\pm$ 0.3 or even 0.4, which is well within the error bars of the ratio calculations. For example, at 200 K, $\frac{d\lambda}{d\varepsilon} = 1.4 \times 10^{-3} \ nm/\mu\varepsilon$, which lead to the highest strain point being around 2000 $\mu\varepsilon$ in Figure 4-30. If the correct value was $1.0 \times 10^{-3} \ nm/\mu\varepsilon$ or $1.8 \times 10^{-3} \ nm/\mu\varepsilon$, the highest strain point would be located at 1500 $\mu\varepsilon$, or 2500 $\mu\varepsilon$ respectively. While

this would change the surface quantitatively, qualitatively the surface would look the same.

Another potential contribution to the strain errors is the initial tension in the fibers from winding them during the setup. We made a conscious effort to wind all the sample fibers and FBG strain gage fibers the same way, and tape them with the same tension as the epoxy dried. Still, there may be a slightly different initial tension in the fibers. If the FBGs and sample fiber had different initial tensions, the FBGs' wavelengths would begin to shift at a different point in time than the frequency would begin to shift, which was not observed.

In summary, the frequency shift and temperature errors are relatively small compared to the errors of the applied strain. However, none of these errors would significantly change the qualitative shape of Figure 4-30, or any of the figures in the following sections.

Brillouin Intensity Results

The intensity as a function of temperature (at zero-strain) was also measured from 4 K to room temperature in the first experiment. Before each strain run in this experiment, the intensity data was recorded as a baseline zero-strain reference point. Similar to the zero-strain frequency shift data, plotting the zero-strain intensities as a function of temperature gives us a figure that is qualitatively the same as the measured results from the temperature experiment, as seen in Figure 4-31.
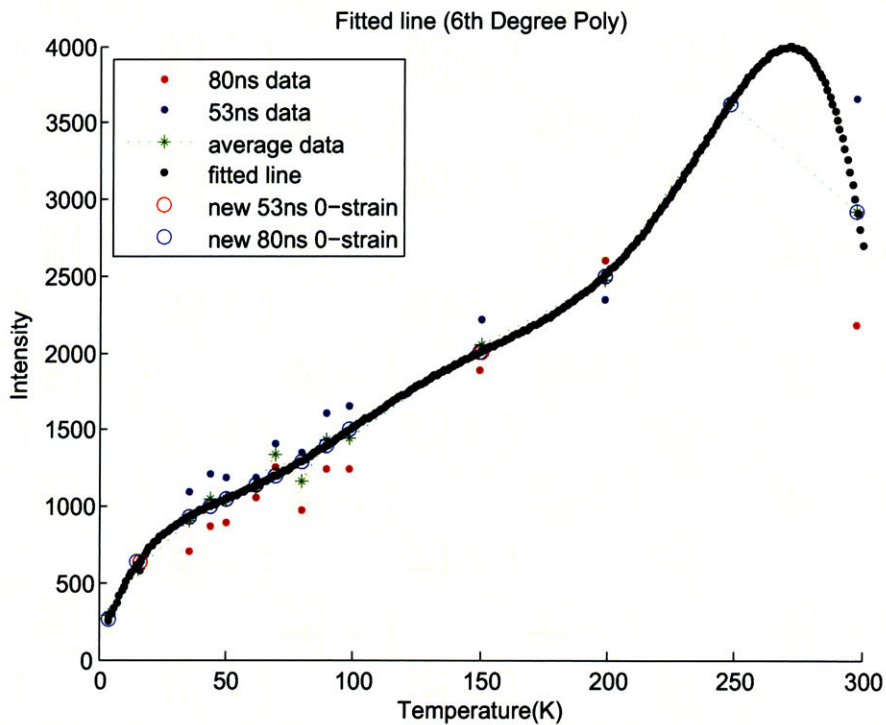
Figure 4-31: Zero-strain data as a function of intensity and temperature match the results from the temperature experiment.

Figure 4-31 shows the raw data from the 53 ns and 80 ns pulse length measurements, as well as their averaged data. The zero-strain point of each strain run was changed to the fitted value to improve smoothing. Figure 4-31 shows that the zero-strain intensity data points as a function of temperature are similar to those plotted in Figure 4-13, especially the green line, which is the 80 ns data. The intensity decreases above 250 K, as it did in the temperature experiment. However, this is not seen in either the FFT intensity measurements of the temperature experiment or in

this experiment. Again, we do not expect the same quantitative curve as in the temperature experiment since the data in Figure 4-13 is from the gold coated fiber, and the data in Figure 4-31 is from the copper alloy coated fiber.

Each strain run was linearly fitted and extrapolated to 3500 $\mu\varepsilon$. The first data point in the data set, the zero-strain data point, was weighted more heavily than the rest of the data to anchor that data point. As mentioned above, data was collected several times at the same temperature and strain, and these data points were averaged and counted as a single data point. Two examples of the data fitting are shown in Figure 4-32.
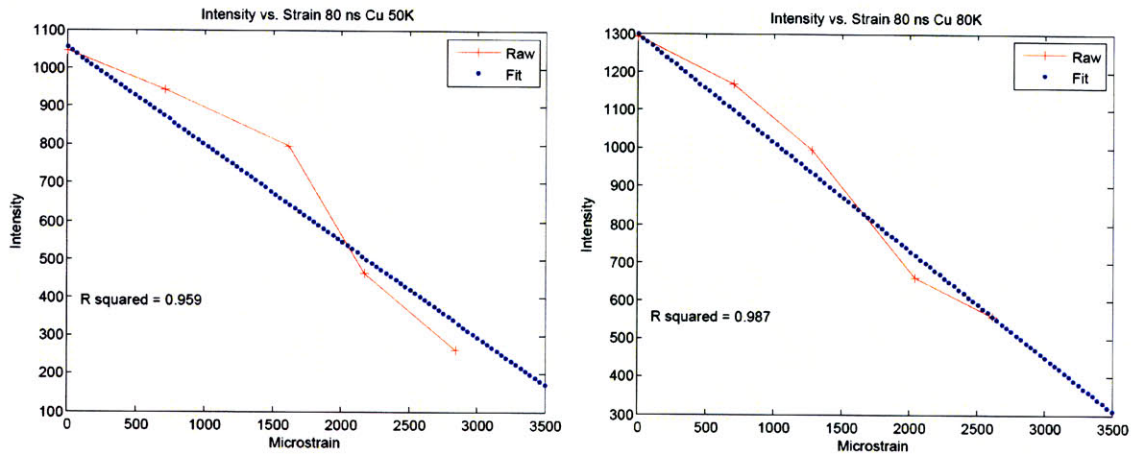
Figure 4-32: Linear fit to the data in intensity-strain space.

A plot of intensity vs. strain and temperature was generated using MATLAB's GRIDDATA function, as had been done for the frequency shift, as shown in Figure 4-33. The fitted data from Figure 4-32, as well as the appropriate temperatures for those data points were used as the input data.

The raw data was also plotted in Figure 4-33 and fit the curved surface very well at low temperatures. As in Figure 4-13, there was a lot of variation at the higher temperatures; however, this experiment was not designed to get exact values for a calibration. The generally monotonically decreasing intensity as a function of strain throughout the temperature range was the main result that we were seeking to prove, as is shown in Figure 4-33.

The errors for strain and temperature are the same as described in the previous
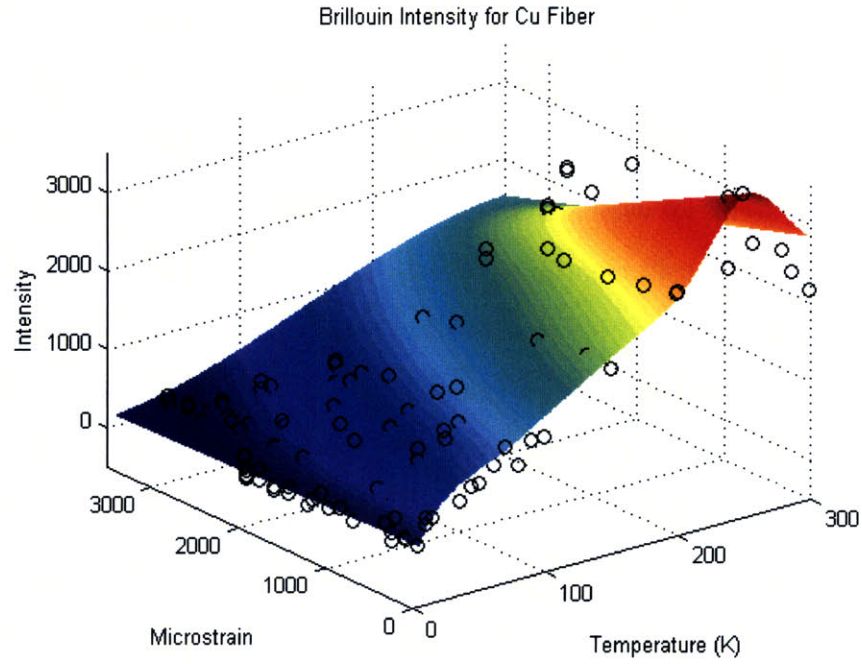
Figure 4-33: Spontaneous Brillouin intensity as a function of temperature and strain (using 80 ns pulse length data).

section. Similar to the intensity error calculations in Section 4.2.2, we would expect the errors on the intensity measurements to be on the order of a few percent of the measured quantity.

FFT Frequency Shift Results

As part of the SBIR grant, we added a new DAQ system to the prototype spontaneous Brillouin scattering system. By splitting and routing the signal through a GPIB to the new DAQ system, we were able to use a MATLAB program to take the FFT of the signal data. As previously mentioned, since the data was run through a GPIB cable, the acquisition rate was very slow. Instead of being able to take 65,000 samples in less than a second, we were only able to take 230 samples in approximately 30 seconds. This gave our FFT data a very low signal to noise ratio, leading to very large errors. In the future, this DAQ system will be upgraded, increasing the sampling rate until it is comparable to that of the original system with about a 17,000 times higher sampling rate. Although the data was not ideal, we were able to map out the frequency shift, intensity, and linewidth in temperature-strain space from 4 K to room temperature.

By examining the raw time-domain data, the locations of the different fibers can easily be deduced. Figure 4-34 shows the raw time-domain data for a single measurement, as well as a magnified view to see the divisions more easily, composed of the sum of the absolute values of the data from 230 measurements.
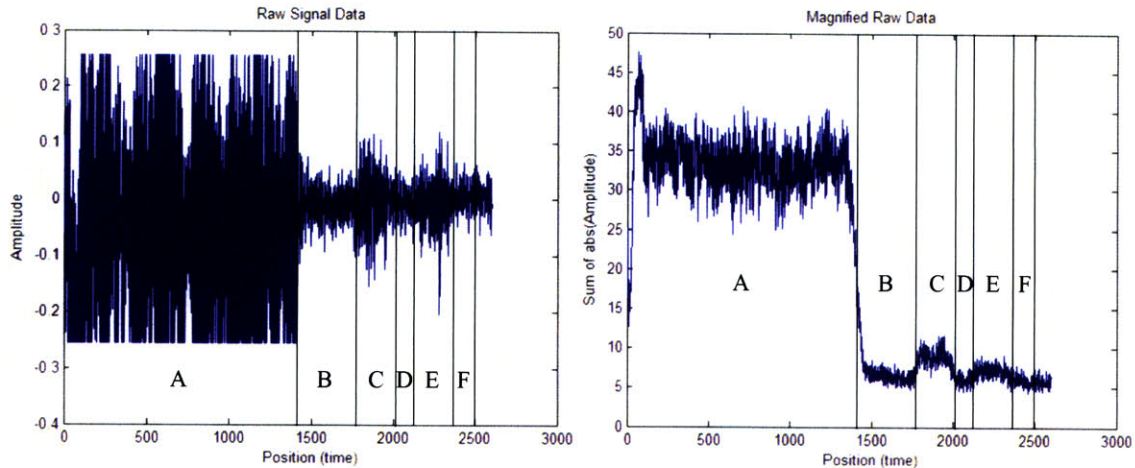
Figure 4-34: Raw signal and a magnified version of the signal showing where the different fibers are located (on the x-axis 10 points equals about 1 meter of fiber).

In Figure 4-34 section A is about 140 meters of standard single mode (SMF) spooled on the optical table at room temperature, which was used as a reference fiber. Section B is the 30 meter copper alloy coated fiber, section C is 20 meters of

SMF at room temperature, section D is the shorter gold coated sample fiber, section E is another 20 meters of SMF at room temperature, and section F is the longer sample of gold coated fiber. According to the locations of these sections, the copper coated fiber data, used for the rest of this section, is the data from section B. Since the copper coated fiber spanned from about 1450 to 1750, data from 1500 to 1700 was used to exclude any data from the few meters going in and out of the probe.

Since this was part of a separate DAQ system, the absolute time at which the files were saved was used to correlate them to the temperatures and strains, measured at the same time with the other DAQ system. The FFT of the data in the 1500-1700 range was taken for each of the 230 measurements, and then the data was averaged in the frequency domain to get the final frequency domain data, as plotted in Figure 4-35.
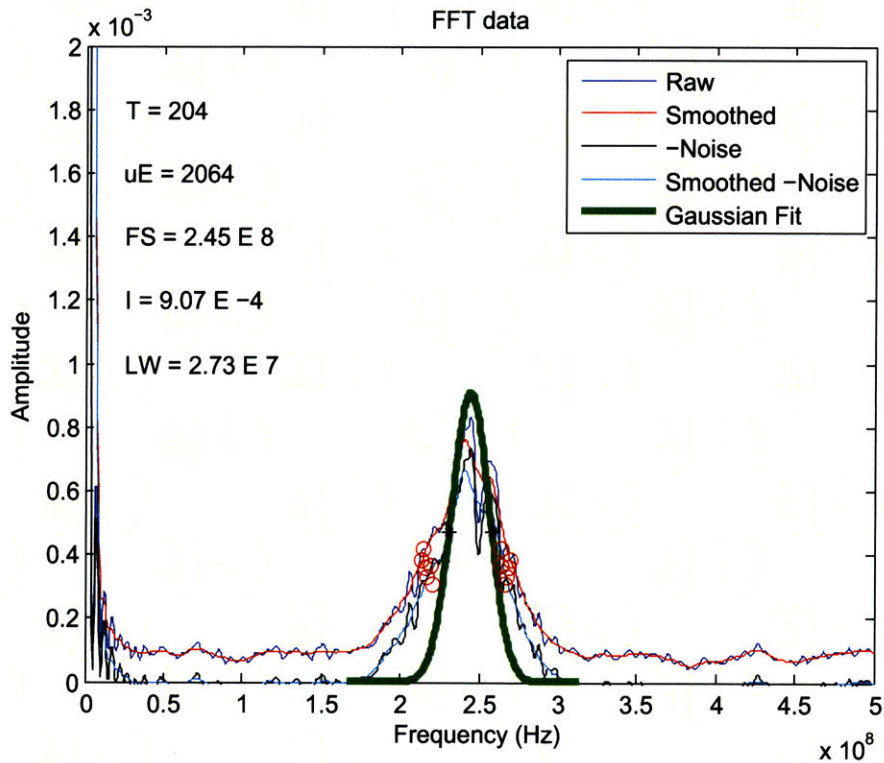
Figure 4-35: FFT of the signal showing several smoothing techniques.

Using the smoothing methods shown in Figure 4-35, the rough FWHM and frequency shift was calculated. A sub-dataset, centered on the frequency shift and extending 1.5 times the FWHM in each direction, was then fit to a Gaussian distri-

bution and used to calculate the FWHM, frequency shift, and intensity. Ideally the data would look like the green Gaussian fit, and hopefully with the planned DAQ upgrades, the unfit FFT will look similar in the future. However, using the available data, this method seemed like the most consistent way to calculate the parameters of interest.

The spontaneous Brillouin frequency shift from the FFT measurements was fitted with the same method used on the prototype system data, as described in Section 4.3.2. Using the frequency shift calculated from the Gaussian fit shown in Figure 4-35, the zero-strain points were plotted in Figure 4-36. These red points were then fitted and changed to the values associated with the new fitted line to help with later smoothing. Considering the noisiness of data shown in Figure 4-35, the frequency shift data in Figure 4-36 follows the expected shape extremely well.
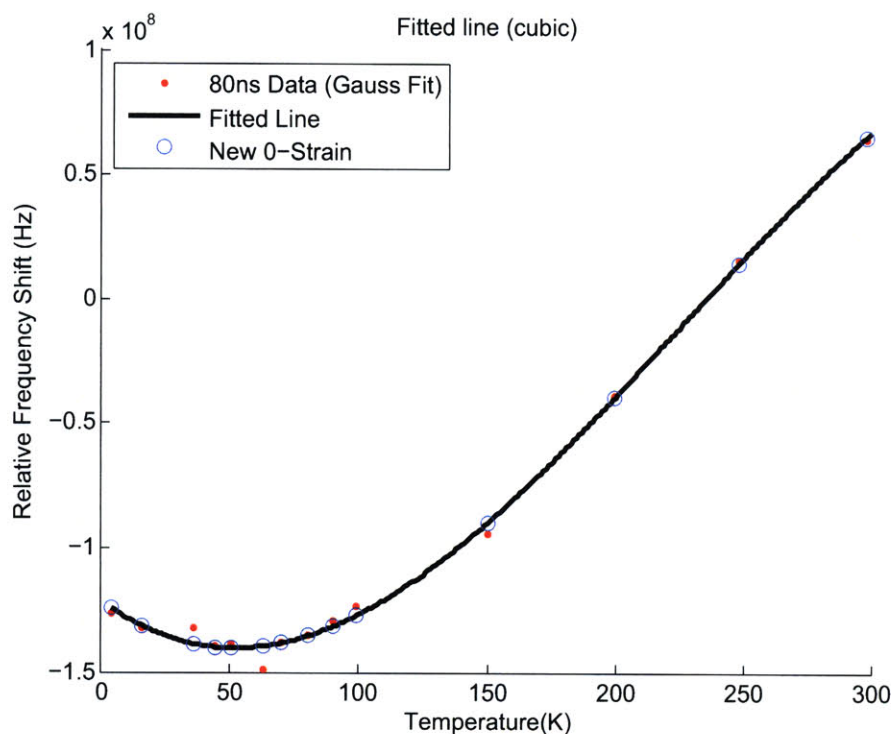
Figure 4-36: Zero-strain frequency shift data from the FFT calculations have the expected shape.

Similar to the way the frequency shift was fitted in Figure 4-29, the FFT frequency shift data was fit to second degree polynomials, as shown in Figure 4-37.

How good the fit is to the data is described by the R-squared value of the fit,

142
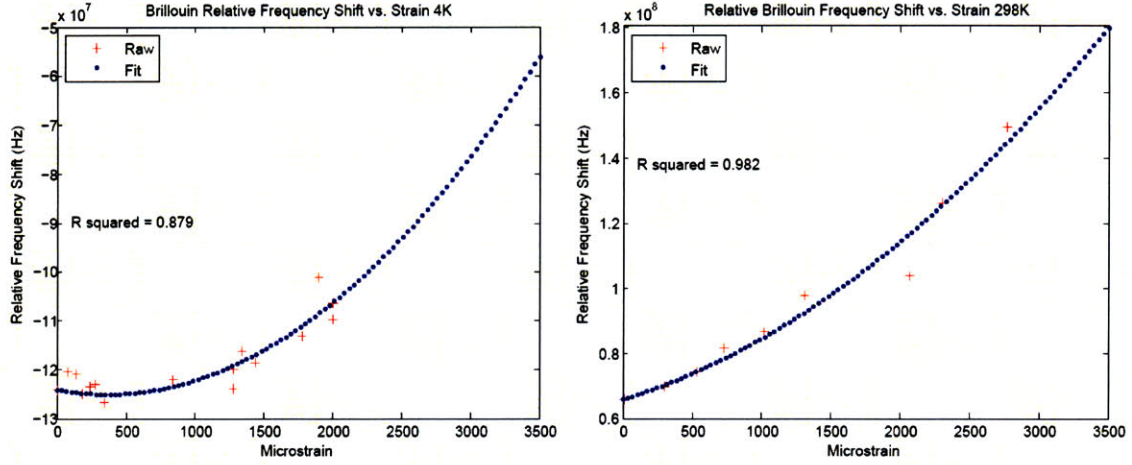
Figure 4-37: Second degree polynomial fit of frequency shift from the FFT data.

which is also called the coefficient of determination [66]. Assuming that $\hat{y}$ is the value of y predicted by the fit at the initial data points, as shown in Equation 4.2.

$$\hat{y}_i = c_1 x_i + c_2 \tag{4.2}$$

We can calculate the residual, r_i, of each fitted data point by subtracting the fitted data point from the initial data point, as shown in Equation 4.3.

$$r_i = y_i - \hat{y}_i \tag{4.3}$$

The coefficient of determination is then defined in Equation 4.4.

$$R^2 = \frac{\sum (\hat{y}_i - \bar{y})^2}{\sum (y_i - \bar{y})^2} \tag{4.4}$$

Equation 4.4, $\bar{y}$ is the average value of the data, given by Equation 4.5.

$$\bar{y} = \frac{1}{m} \sum_{i=1}^{m} y_i \tag{4.5}$$

Performing some algebra transforms the coefficient of determination, or R-squared value, to the form shown in Equation 4.6.

$$R^2 = 1 - \frac{\sum (y_i - \hat{y})^2}{\sum (y_i - \bar{y})^2} \tag{4.6}$$

143

The fits shown in Figure 4-37 are not as good as the fits in Figure 4-29, but their R-squared values are mostly in the 90s with a few exceptions in the high 80s. However, looking at the raw data in Figure 4-35, it is amazing that the R-squared values are not much lower.

Using the same GRIDDATA function in MATLAB, a three-dimensional plot of the spontaneous Brillouin frequency shift from the FFT data as a function of temperature and strain was created, as seen in Figure 4-38.
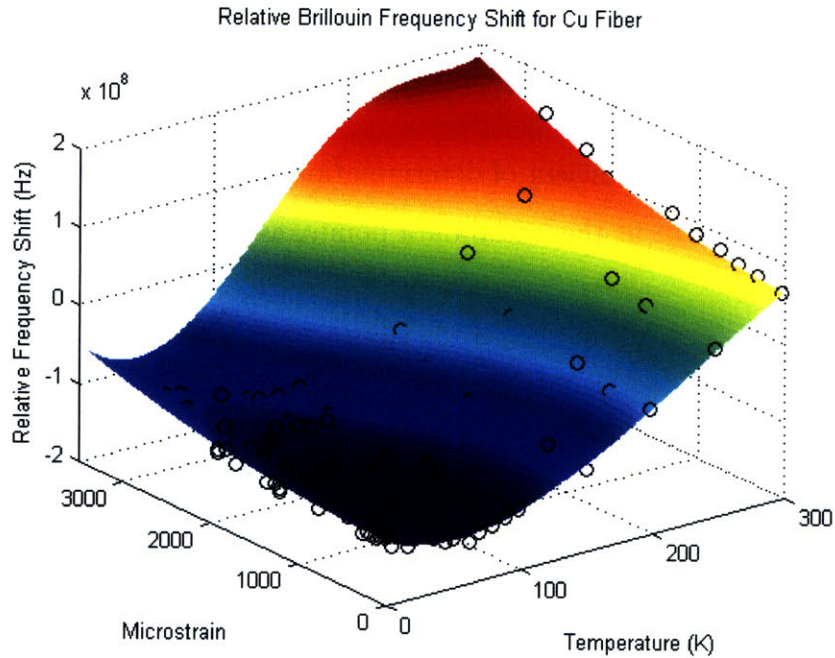
Figure 4-38: Spontaneous Brillouin scattering frequency shift from the FFT data as a function of temperature and strain.

The unfitted data is included in Figure 4-38 to show that even though the quality of the data is less than ideal, a reasonably good fit is still possible.

FFT Intensity Results

The Brillouin intensity from the FFT measurements was analyzed in the same way as described in the previous sections. Figure 4-39 shows the zero-strain fit of the intensity measurements of the Gaussian fit.
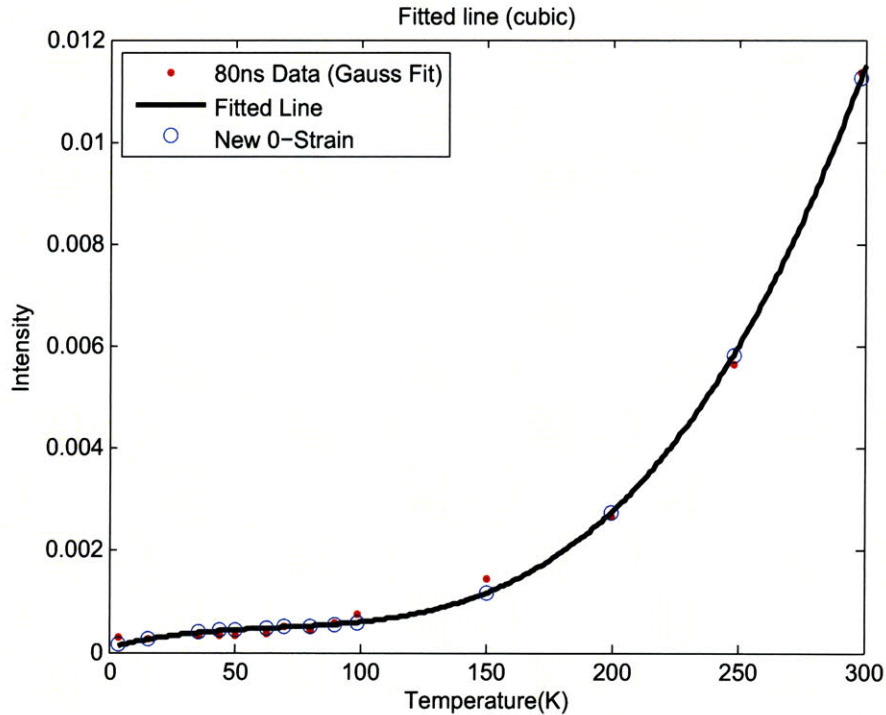
Figure 4-39: Zero-strain intensity from the FFT data.

As expected, Figure 4-39 has the general trend of increasing intensity with increasing temperature. Again there is a discrepancy with the intensity at temperatures above 250 K. The prototype system for both the temperature experiment and the strain experiment showed the intensity decreasing from 250 K to 300 K. However, the FFT intensity data from the temperature experiment and the strain experiment both show increasing intensities form 250 K to 300 K. The reason for this discrepancy is not known; however, the new DAQ system will provide more reliable data that should clear this up.

The data from each strain run was then linearly fitted as described in Section 4.3.2 and shown in Figure 4-40.

Again, there was a range of R-squared values, but they were mostly in the 90s.
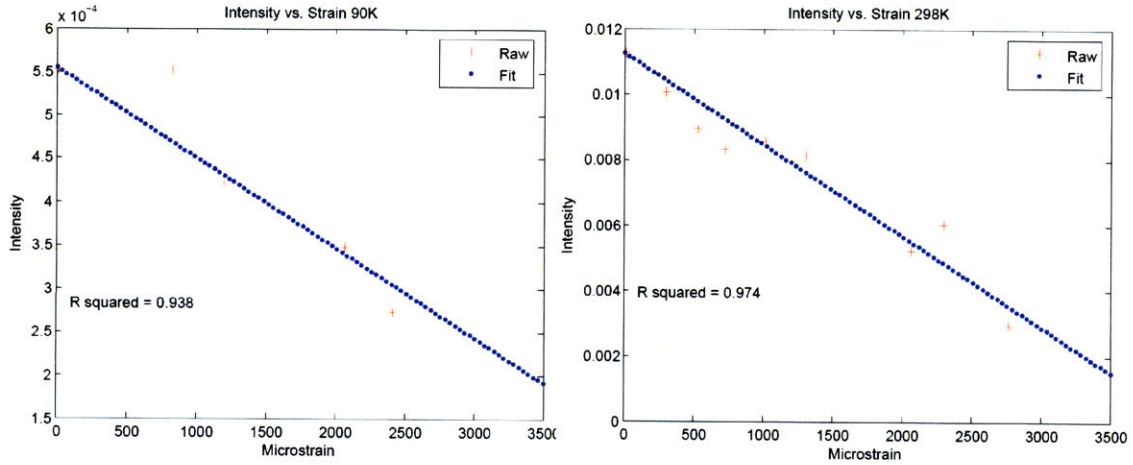
Figure 4-40: Linear fit of the intensity from the FFT data.

These linear fits for the strain runs were used with **GRIDDATA** to produce a plot of the spontaneous Brillouin scattering intensity as a function of temperature and strain, as shown in Figure 4-41.

It is hard to determine visually whether the surface is a good fit to the data in Figure 4-41, since the scale is small at low temperatures. However, the surface is a good fit to the unfitted data, when the noisiness of the unfitted FFT signal data is considered.

146
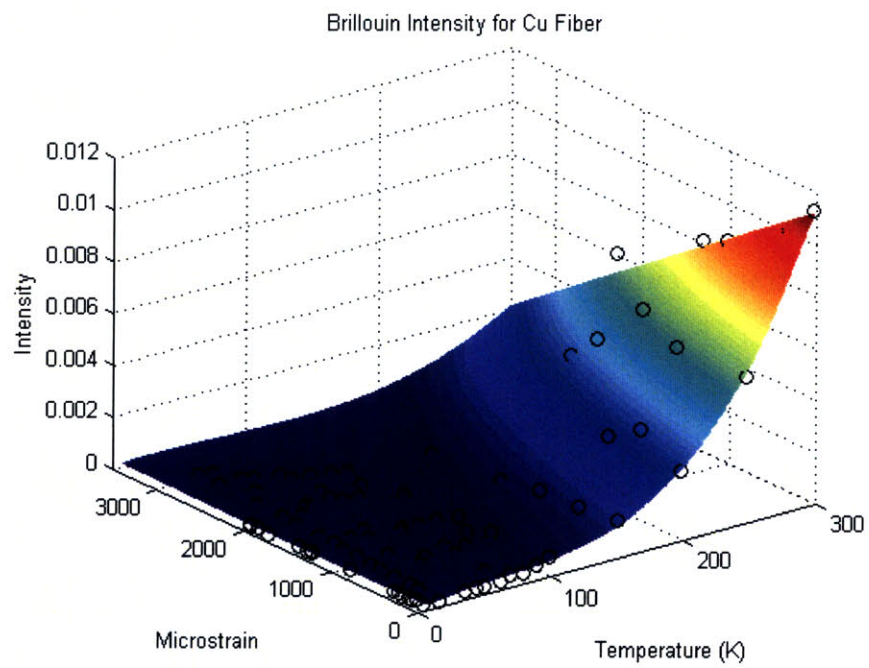
Figure 4-41: Brillouin intensity from the FFT data as a function of temperature and strain.

FFT Linewidth Results

The goal of developing the FFT data analysis system was to be able to measure the linewidth of the Brillouin scattered light. Unfortunately, calculating the FWHM with the non-ideal data shown in Figure 4-35 was not easy. Depending on the smoothing technique used, the frequency shift and linewidth do not change much, but the linewidth changes significantly. As long as the same method of smoothing and calculating the FWHM was used for all of the data analysis, the result should provide a qualitative description of the effect of temperature and strain on the linewidth of Brillouin scattered light.

For the linewidth calculations, the data was smoothed and analyzed in the same way as it was for the frequency shift and intensity calculations. The FWHM from the fitted Gaussian as seen in Figure 4-35 was used for the data analysis. Figure 4-42 shows the zero-strain linewidth as a function of temperature for a variety of different smoothing methods.
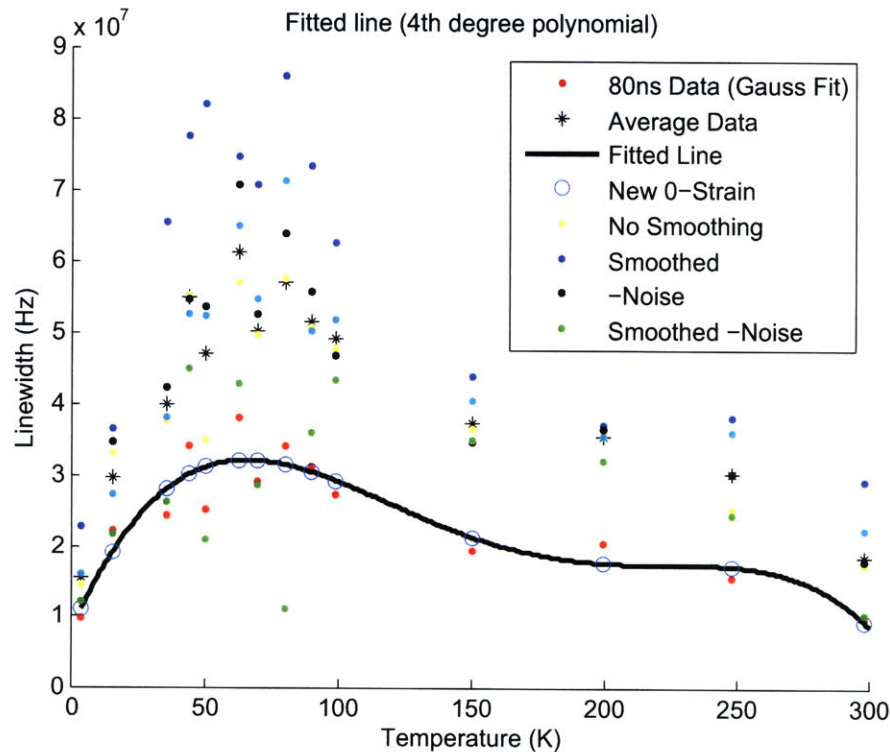
Figure 4-42: Linewidth calculations showing the effects of different smoothing methods.

The fitted line in Figure 4-42 used the red Gaussian fitted data; however, the general shape is the same as it would be for any of the other smoothing methods. This indicates that although the smoothing methods do have an effect on the linewidth result, the general shape is the same. This curve also matches well with the curve from the temperature experiment, shown in Figure 4-16. The exact quantitative results shown in the two figures are unimportant because any fiber used in a real diagnostic would probably not be the same type of fiber used in these experiments and would have to be independently calibrated.

Although the zero-strain data as a function of temperature had the expected values, the strain analysis was more difficult than expected. Due to the non-ideal data, fitting the linewidth as a function of strain was not as easy as it was for the frequency shift and the intensity. Figure 4-43 shows the linewidth data being fitted linearly for the 4 K and 298 K strain runs.
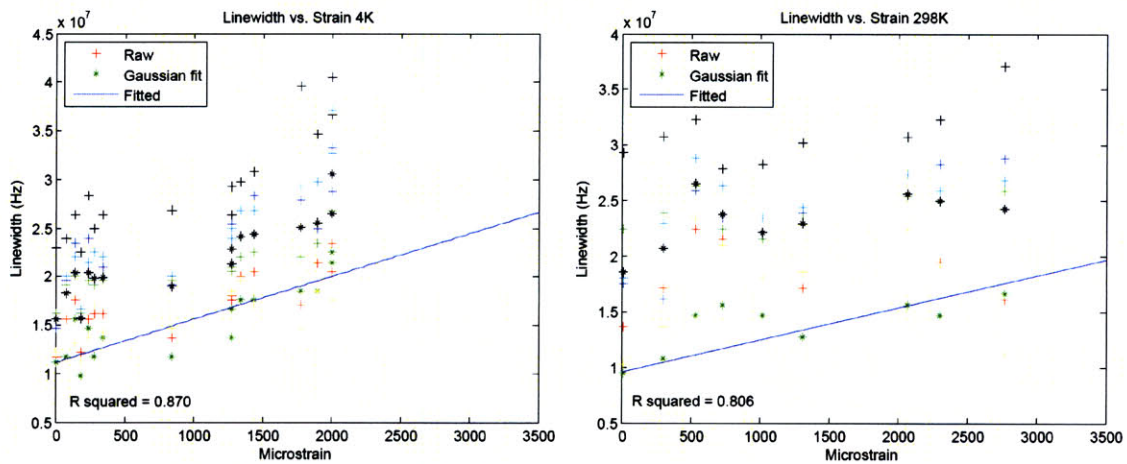
Figure 4-43: Linear fits of the linewidth as a function of strain at 4 K and 298 K.

As seen in Figure 4-43, a linear fit looks like the appropriate fit to try; however, the R-squared values are not nearly as good as those in the previous sections. Also plotted in Figure 4-43 are the data points from the other smoothing methods. The Gaussian fitted data was used for the actual fit since this is what was used for the frequency shift and intensity analysis. But the other data sets also look like a linear fit would be the most appropriate choice.

The strain runs at different temperatures were all fitted linearly, and used with

GRIDDATA to produce Figure 4-44.
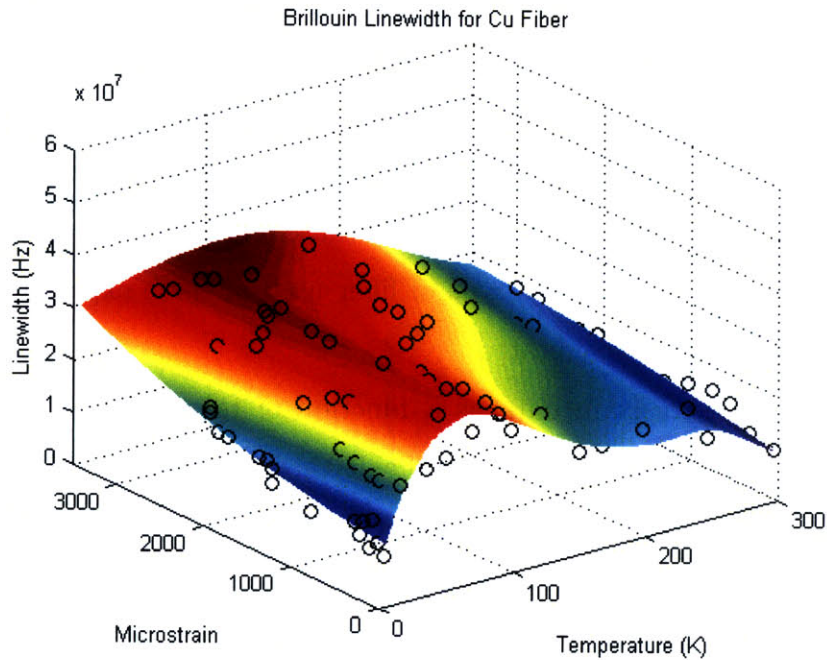
Figure 4-44: Spontaneous Brillouin scattering linewidth as a function of temperature and strain.

The surface in Figure 4-44 appears to fit the data reasonably well; however, there are a few strain runs that do not fit the surface. For all but two of the strain runs, the linear fit of the linewidth as a function of strain had a positive slope: an increase in strain increased the linewidth. However, for the 60 K and the 90 K strain runs, the slope was slightly negative. It is important to note that the R-squared values of these lines were below 20. An R-squared value this low means that there was not an acceptable linear fit; but since the rest of the data had been fit linearly, these strain runs were as well. Once again, the new DAQ upgrades should provide us with much more reliable data with points much closer to the surface, but Figure 4-44 shows the general shape of the surface.

4.4   Temperature and Strain Calculations

The goal of this system is to be able to determine the spatially resolved temperature and strain throughout the length of the fiber sensor. Using OTDR we can separate measurements and provide spatial resolution. The data from the previous sections allows us to calculate unique values of temperature and strains, according to the spatially resolved data. For most of the strain-temperature range we are interested in for use with superconducting magnets, only the frequency shift and intensity are needed. However, there are certain times when the linewidth is also needed to uniquely determine both the temperature and strain.

4.4.1   Using Frequency Shift and Intensity

Determining the temperature and strain from the measured frequency shift and intensity data is possible at room temperature since both of their functions with respect to temperature and strain are monotonic. Since these functions become non-monotonic at cryogenic temperatures, there will be some sets of temperature and strain that can not be distinguished. However, there is a large range over which the temperature and strain can be determined.

Now that we have both the Brillouin frequency shift and intensity as a function of temperature and strain, we can take any shift and intensity and look up the temperature and strain it corresponds to. As an example, assume that we have measured the relative Brillouin frequency shift of -100 MHz. We can look at the -100 MHz plane in the 3-D data set for frequency shift and narrow down the possible temperatures and strains, as shown in Figure 4-45. If we know that the fiber (or superconducting magnet) was not strained at the time of measurement, we would know that the point of interest is at zero microstrain, so the temperature would be 135 K, as seen in Figure 4-45.

In an operating magnet we will not know that there is no strain, so we will need another measurement to determine the temperature and strain. (Also a slightly lower measured frequency may pass through the zero-strain plane twice). Continuing the
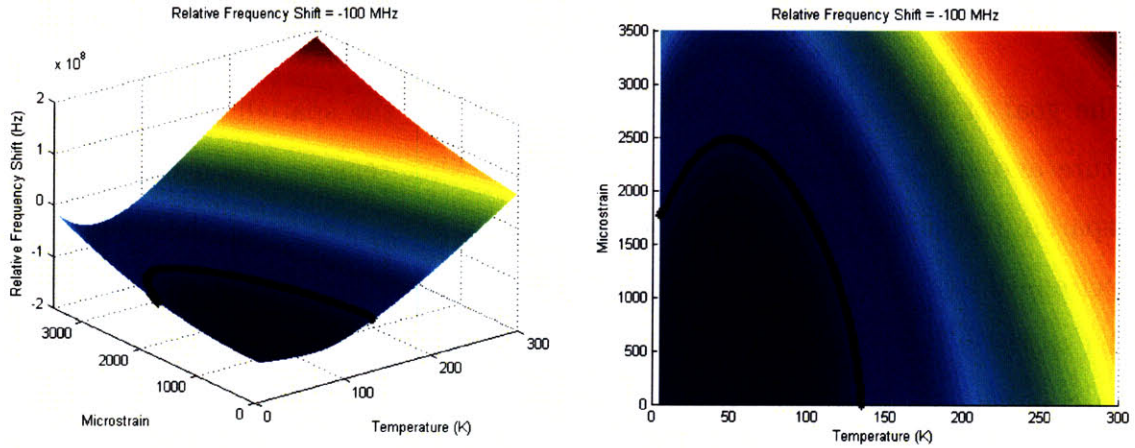
Figure 4-45: Possible temperatures and strains causing a relative frequency shift of -100 MHz.

example, if we also measure an intensity of 1000, we get another set of possible temperatures and strains, as displayed in Figure 4-46.
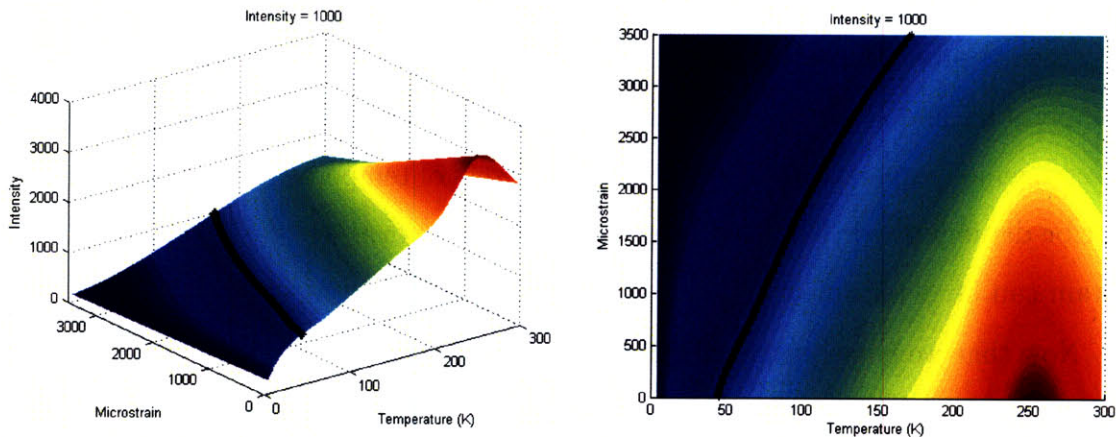
Figure 4-46: Possible temperatures and strains causing an intensity of 1000.

Now that we have two sets of possible temperatures and strains, we can figure out what the actual temperature and strain are, corresponding to the measured values of -100 MHz and an intensity of 1000. By plotting the possible temperatures and strains from both the frequency and intensity measurements, we can easily see the intersection point and determine the unique temperature and strain of 95 K and 1800 $\mu\varepsilon$, as seen in Figure 4-47.

Since the frequency shift and intensity are both non-monotonic with respect to temperature and strain, theoretically we would need another measurement to deter-
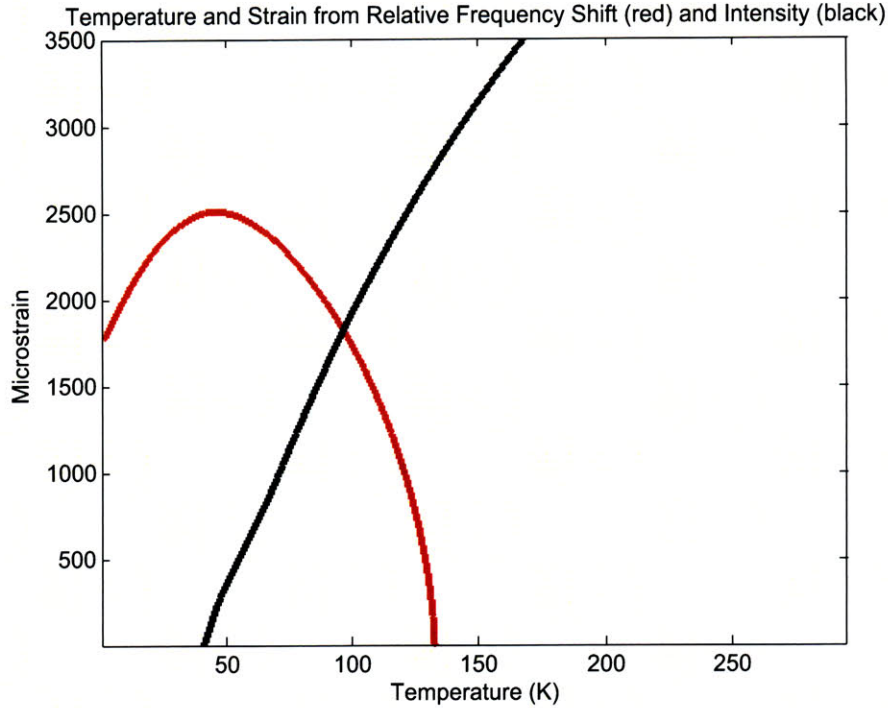
Figure 4-47: Comparing the possible temperatures and strains from the frequency shift and intensity, we can find the unique temperature and strain.

mine the exact temperature and strain if the two data sets shown in Figure 4-47 crossed more than once. Fortunately, the non-monotonicity of the frequency shift and the non-linearity of the intensity occur in different regions of strain-temperature space, as seen in Figure 4-48.

In Figure 4-48 it is clear that although both functions are non-monotonic, they are non-monotonic in different regions, allowing the unique determination of the temperature and strain over most of the plotted range. This is not the case in the region of less than 1000 $\mu\varepsilon$ and temperatures less than 75 K, where the relative frequency shift and intensity contours can cross each other in more than one place. Another potential problem is when the contours are parallel, leading to a set of temperatures and strains. For example, between 250 K and 300 K and at strains below 2000 $\mu\varepsilon$ the contours are close to parallel. In regions like this, and when the contours cross in more than one place, the linewidth is needed to uniquely determine the temperature and strain.

153
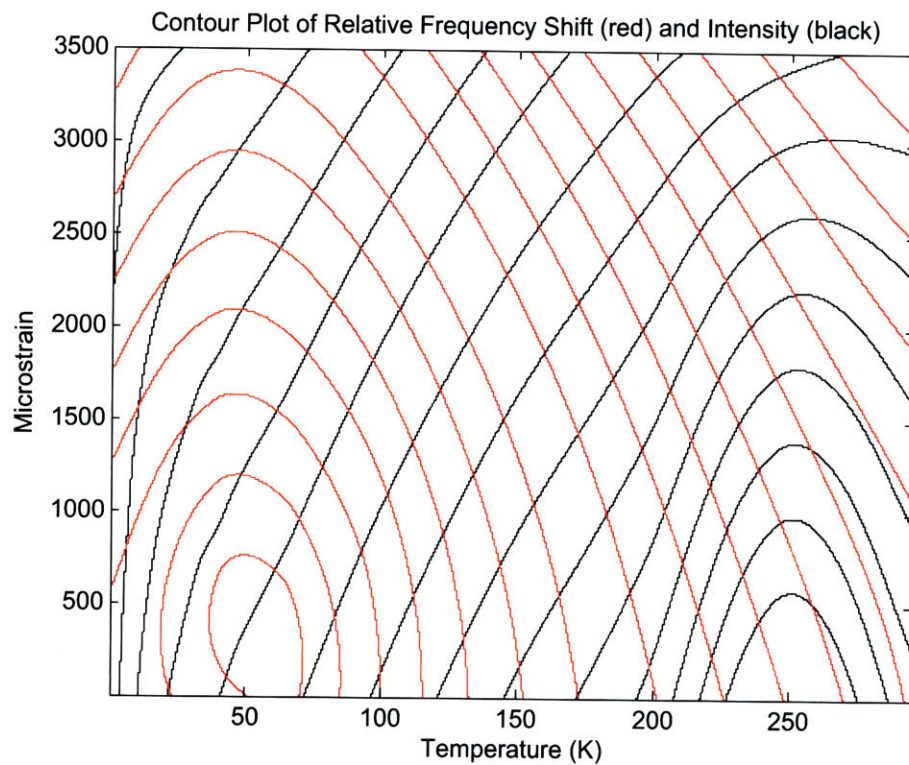
Figure 4-48: A contour plot of the frequency shift and intensity shows where the linewidth may be needed to uniquely determine the temperature and strain.

4.4.2 Using Frequency Shift, Intensity and Linewidth

As mentioned in the previous section, there are certain regions of temperature-strain space where the frequency shift and intensity alone cannot uniquely determine the temperature and strain. This is where the linewidth is needed. Now that we have the Brillouin frequency shift, intensity, and linewidth as a function of temperature and strain, we can take the measured parameters and look up the corresponding values of temperature and strain. Although the linewidth data is less than ideal, the fitted curves are still adequate to specify a single value of temperature and strain, as shown in Figure 4-49. For example, if we measure a frequency shift of -100 MHz, and an intensity of 0.0022, the lines are parallel where they cross. By measuring the linewidth as well, for example 31 MHz, we can determine that correct temperature and strain is 28 K and 2750 $\mu\varepsilon$, respectively.

The contour lines in Figure 4-49 are clearly different than those in Figure 4-47 and Figure 4-48. This is because the data used for Figure 4-49 is from the FFT calculations, which is much less accurate due to the poor sampling rate. Although the actual lines are different, the qualitative idea is the same. Using the updated DAQ system in the future, the surfaces should come out the same for the FFT and original methods. Examining the contours of the three parameters from the FFT calculations, it is clear that in no region are all three contours parallel, which proves that a unique temperature and strain can be calculated throughout the range of temperature and strain, as shown in Figure 4-50.

An RGB plot can illustrate how measuring the frequency shift, intensity, and linewidth will give a unique temperature and strain. Each variable is assigned a color and is normalized independently. Frequency shift, intensity, and linewidth values were normalized to a range of 0 to 1 for red, green, and blue respectively. At every point in temperature-strain space there is a single value for red, green, and blue, which combine to make a unique color, as shown in Figure 4-51. The human eye cannot quantify the distinction between the unique colors at each point in Figure 4-51. However, a simple MATLAB program shows that these colors are unique using

a grid size of less than one degree and around 1 $\mu\varepsilon$.
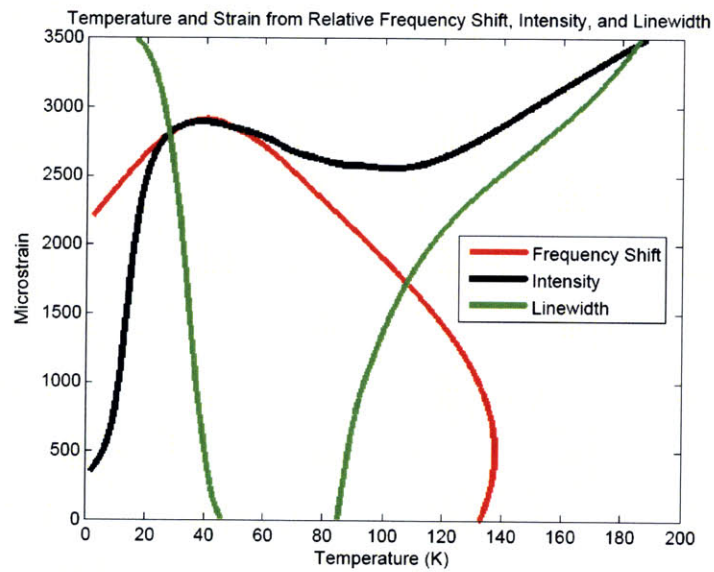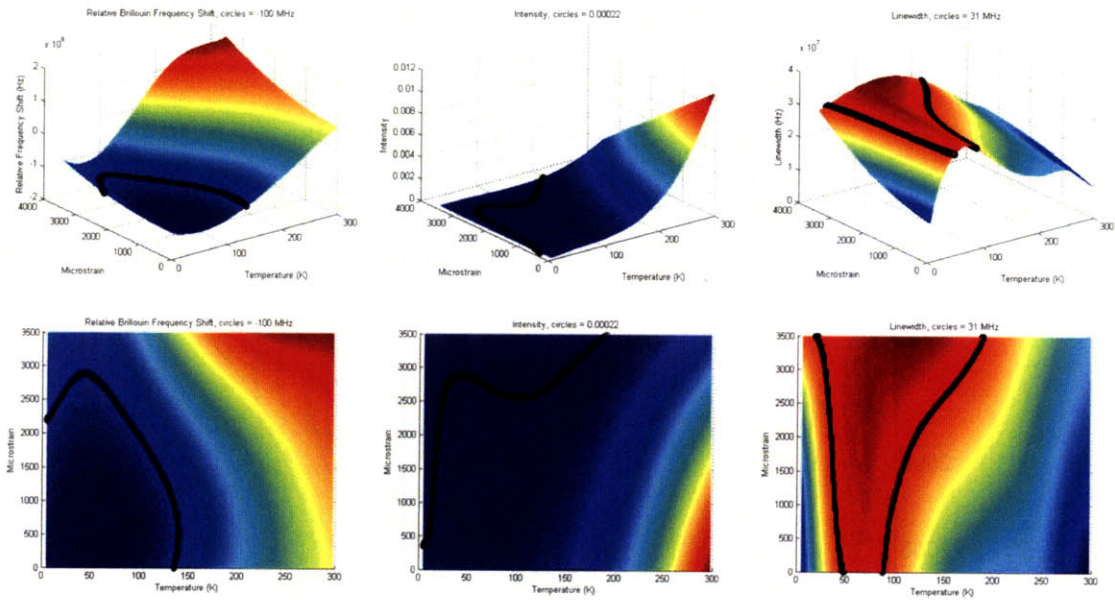
Figure 4-49: Using the spontaneous relative Brillouin frequency shift, intensity, and linewidth from the FFT of the signal data, the temperature and strain can be uniquely determined.

Contours of Relative Frequency Shift (R), Intensity (B), and Linewidth (G)
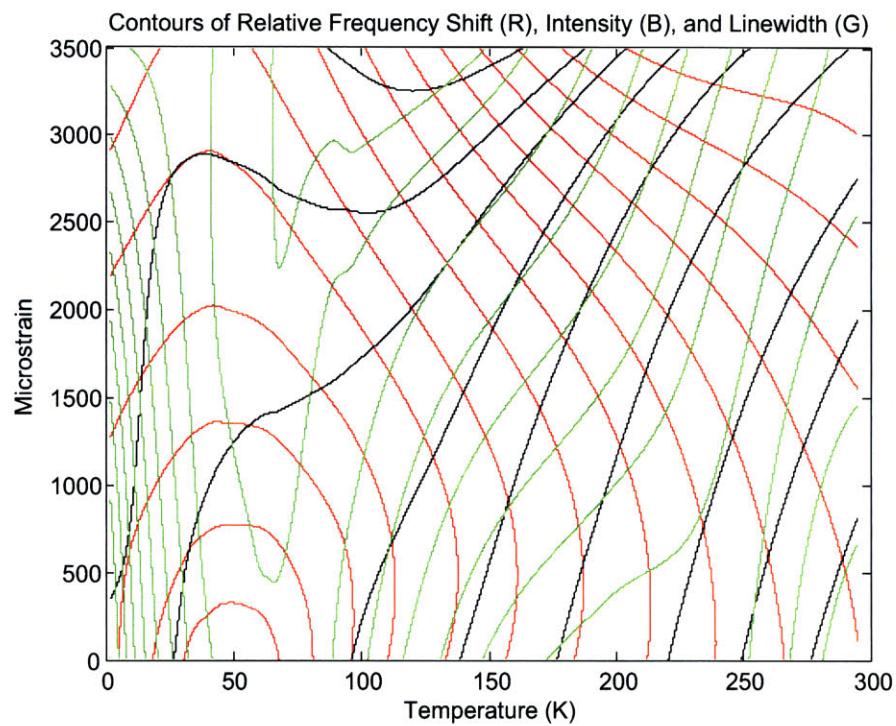
Figure 4-50: Contours of the FFT data showing that using all three parameters, unique determination of temperature and strain is possible throughout the range plotted.
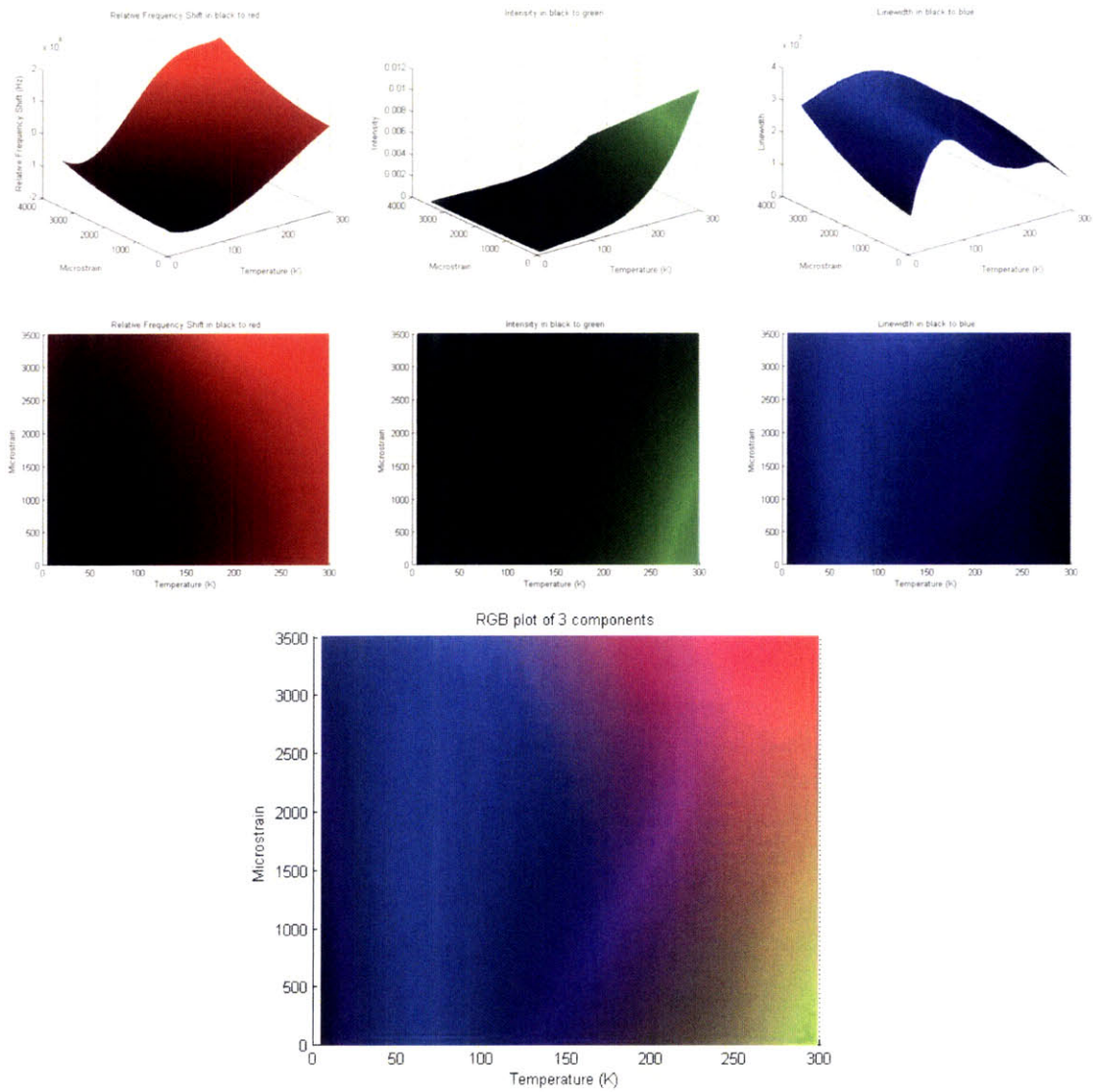
Figure 4-51: RGB plot showing uniqueness of temperature and strain measurements using the frequency shift, intensity, and linewidth.

Chapter 5

Accuracy Analysis

Like any system, spontaneous Brillouin scattering sensors have many interdependent variables that determine the system limitations. There are several parameters that can be changed regarding the timing of the optical system, including the pulse length, repetition rate, number of averages, and sensing fiber length which will affect other variables, such as the sampling rate and measurement time. The accuracies of the measurements are not only a function of the DAQ hardware, but also of the temperature and strain, as will be discussed later in this chapter.

5.1   Overview of Variables

The Brillouin scattering system has several key variables that affect the measurement time, spatial resolution and signal to noise ratio. The number of averages taken is an input parameter. Increasing the number of averages increases the signal to noise ratio; however it also increases the measurement time. For our frequency shift and intensity measurements we used 65,536 averages, and for the FFT measurements we used 230 averages, since 230 averages took 30 seconds. The repetition rate and pulse length are also parameters that are input before recording data. The repetition rate is the rate at which the acousto-optic modulator (AOM) sends pulses of light down the fiber. For our experiments we sent a pulse of light every 10 μs. The pulse length is the time the EOM allows the light to go through in order to form pulses, which directly

determines the spatial resolution of the system. For the temperature experiments, pulse lengths from 20 - 200 ns were used, and for the strain experiments, pulse lengths of 53 and 80 ns were used since they gave the best spatial resolution with acceptable signal to noise ratio.

5.1.1 Spatial Resolution

The pulse length is directly related to the spatial resolution in that the physical length of the pulse of light in the fiber is two times the spatial resolution. This can be calculated according to Equation 5.1.

$$SpatialResolution = PulseLength[ns]\frac{c}{2n} \qquad (5.1)$$

In Equation 5.1 the index of refraction, n, is on the order of 1.5, and the factor of 2 is needed since the special resolution is one half of the pulse length in the fiber [50]. This equation reveals that the spatial resolution is approximately 1 meter per 10 ns. According to this relation, decreasing the pulse length will give better spatial resolution; however, there are limits and consequences of decreasing the pulse length.

First of all, as the pulse length is decreased, the signal is weakened. However, if the laser power is not already at the limit at which it will induce thermal effects in the fiber, the signal to noise ratio can be strengthened by increasing the laser power. Figure 5-1 shows that when the pulse length is shortened from 53 ns to 20 ns, the signal to noise ratio degrades significantly, as shown by the variation in the 20 ns data. Another interesting aspect of Figure 5-1 is that the frequency shift is not a function of the pulse length, except when the signal to noise ratio is unacceptable, as for the 20 ns data. The independence of the pulse length and the frequency shift is not the case for intensity and linewidth where the measurement are dependent on pulse lengths.

There is also a fundamental limit on the minimum pulse length because of the damping time of the acoustic phonon, expressed in Equation 5.2 [43].

162
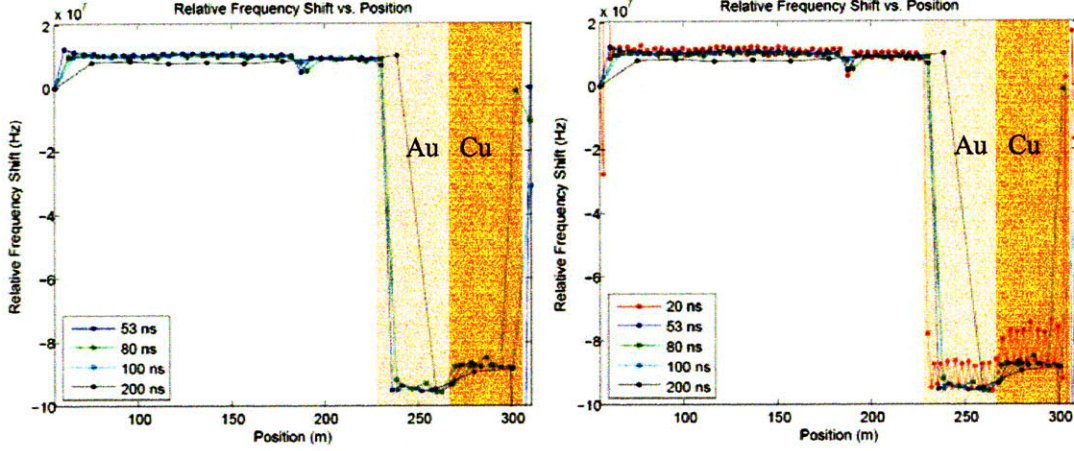
Figure 5-1: Frequency shift vs. position using pulse widths of 20, 53, 80, 100, and 200 ns (corresponding to spatial resolutions of 2, 5.3, 8, 10, and 20 meters respectively) at 175 K.

$$\tau_p = \frac{1}{\alpha_A v_A} = \frac{1}{\nu_B^2 v_A} \tag{5.2}$$

By assuming that the acoustic attenuation coefficient, α_A, is proportional to the acoustic frequency squared, ν_B^2, the phonon lifetime of a 1550 nm light source is approximately 20 ns [67]. When the pulse length gets close to this damping time, nonlinear effects distort the measured parameters. Reference [50] discusses this in more detail, but the end result is that pulse lengths less than 50 ns begin to show these nonlinear effects. Pulse lengths shorter than 50 ns can be used, but the calibration is much more complicated. Below 20 ns, the nonlinear effects overtake the actual signal, meaning that the physical limit of a pulse-based system is 20 ns, corresponding to roughly 2 meter spatial resolution. It should be noted that the spatial resolution can be improved by modulating the pulses and overlapping the measurements. However, this will significantly increase the measurement time.

5.1.2 Measurement Time

Calculating the measurement time of the system is relatively straight forward, as described in Equation 5.3.

163

$$MeasurementTime = (\# of Averages) \cdot (RepetitionRate) \qquad (5.3)$$

Decreasing the repetition rate will decrease the measurement time, but for long sensing lengths the repetition rate is limited by the speed of light. The rate has to be longer than two times the length of the fiber divided by the speed of light in the fiber. Decreasing the number of averages will obviously decrease the measurement time, but the accuracies of the measurements are correlated to the number of averages. The repetition rate was not limited by the length of the sensing fiber in our experiments, so using a 10 μs repetition rate, and taking 65,536 averages of the data, our measurements took about 0.655 seconds.

5.1.3 Measurement Length

The maximum length of a sensing fiber depends on the fiber attenuation properties. Spontaneous Brillouin scattering sensors have been demonstrated in lengths of fibers up to 100 km [68]. These tests were run around room temperature, where the fiber attenuation is better than the cryogenic fiber attenuation. Depending on the fiber type and coating, the sensing length at cryogenic temperatures should be on the order of kilometers. The attenuation limited sensing length of the sensing fiber for superconducting magnets for fusion reactors like ITER would not be a problem, since the magnets are wound in hexapancakes on the order of 700 meters long. Each of these hexapancakes requires a liquid helium extraction, and therefore a fiber extraction would also be feasible every 700 meters.

The other factor that limits the length of the sensing fiber is time of flight of light through the fiber. As discussed in the previous section, the time of flight of light can limit the repetition rate. For short sections of fiber, on the order of 700 meters, the time of flight is not an important factor, since the time it takes for light scattered at the far end to reach the detector is only 7 μs compared to a pulse rate of 10 μs, allowing 50,000 averages in 0.5 seconds. If the length of the sensing fiber was increased to 70 km, then the time of flight would be about 700 μs, which would force

164

the pulse repetition rate to be slightly larger than 700 μs, and consequently require 35 seconds for 50,000 averages.

Long lengths will also have other inconveniences, such as the need to account for attenuation in the intensity measurements as a function of position in the fiber. Fortunately, the superconducting magnets need to have cryogenic outlets every few hundred meters, which allows the sensing lengths to be on the same order of magnitude.

5.2   Accuracy

The accuracy of a diagnostic measurement is obviously important to understand. In our system, different variables and conditions lead to different accuracies for the same measurement. Since our system can be implemented to measure the temperature only (with zero strain), and also to measure the temperature and strain, the accuracies of both strain and temperature measurements will be discussed separately in the following sections.

5.2.1   Temperature Sensor (Zero Strain)

As discussed in the following chapter, the fiber can be implemented into a magnet in a way that it does not feel any strain. By spiraling the fiber inside a capillary tube, and also spiraling the capillary tube in the central cooling channel, about 5% excess fiber can be implemented compared to the length of the CICC. Since the magnet is only strained a fraction of that amount during operation, the fiber will not be strained. This way only the temperature is being measured, so only two of the three Brillouin scattering parameters need to be measured. However, the accuracies of all three measurements will be discussed.

Relative Frequency Shift

The relative frequency shift is measured using an embedded Field Program Gated Array (FPGA) which is run through a MATLAB program. Since the laser frequency

165

stability is much better than the frequency resolution, the resolution is limited only by the number of data averages. As discussed previously in this chapter, the more data averages used, the longer the measurement time. As a frame of reference, using 10,000 averages (in ≈ 0.1 sec) gives 1 MHz resolution, and by increasing to 100,000 data averages (in ≈ 1 sec) a resolution of 100 kHz can be achieved. In our system we used 65,000 averages, which corresponded to a resolution of slightly better than 500 kHz. For the rest of the frequency shift accuracy analysis, we will assume that the resolution of our measurements is 500 kHz.

Since the main source of error is due to the finite number of data averages, the error bars are constant and can be plotted for our measurements. Figure 5-2 shows our data with red error bars corresponding to the 500 kHz accuracy of our measurements, as well as 100 kHz error bars which are obtainable with longer measurement times or a better DAQ system.
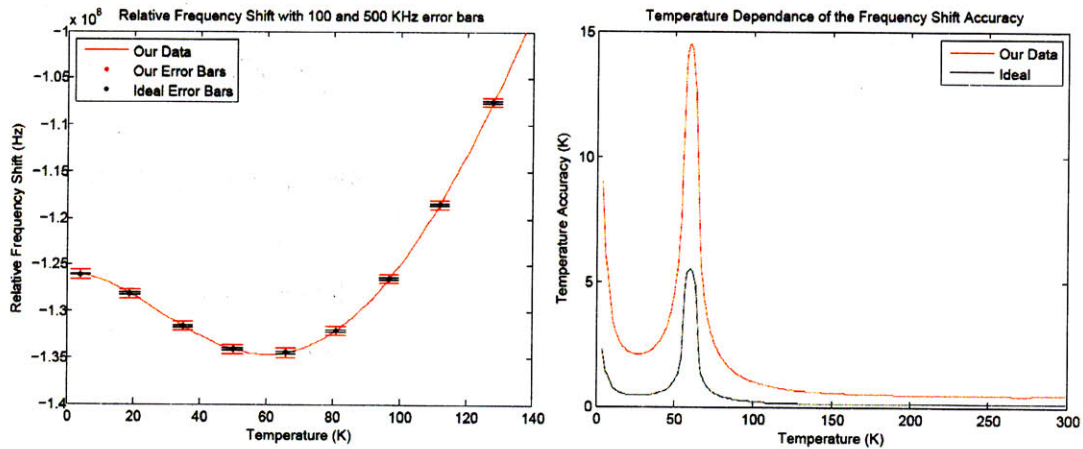
Figure 5-2: Error bars of 500 and 100 kHz leading to the accuracy of zero-strain temperature measurements.

The error bars of the frequency shift measurements are not functions of temperature; however, the accuracies of the temperature measurements are functions of temperature. Since the slope of the relative frequency shift changes as a function of temperature, the measurement error will lead to worse accuracy where the slope of the curve is small, and better accuracy where the slope is steep. By dividing the resolution of the measurement by the slope of the curve, the accuracy of the temperature

166

measurement can be expressed as a function of temperature, as seen in Figure 5-2. Where the slope of the frequency shift is flat as a function of temperature around 60 K, our system would provide ± 14 K, and an upgraded system would have an accuracy of ± 5 K. This does not seem good, but this is the worst accuracy. Most of the temperature range would have an accuracy of ± 1 K or less.

Intensity Accuracy

The error bars for the intensity measurements are determined by the number of data averages, the value of the intensity counts, the laser intensity variation, and the acoustic wave variation in the modulator. Obviously, the resolution improves with the number of data averages, as was the case for the frequency shift measurements. The detector we used had a resolution of 4 % of the measured value; however, better detectors are available that would give a resolution of 1 % of the measured value. The lasers are very stable in the short-term (sub-microsecond) timescale, but in the long term (minute) timescale, the power can fluctuate up to 0.5 % [69]. Also the acoustic wave variation in the modulator can cause variations in both the width and intensity of the pulse on the scale of a fraction of a percent. For the rest of the intensity accuracy analysis, we will assume that the resolution of our measurements was 5 %, with the potential to improve that to 2 % with a better detector and modulator.

The error bars for our intensity measurements can be plotted with our zero strain intensity vs. temperature data, as seen in Figure 5-3. Error bars of 5 % corresponding to our data are plotted in green, and the potential 2 % error bars are plotted in black.

Since the error is a percent of the overall measurement, the error bars are functions of temperature. Similar to the frequency shift accuracy, the slope of the intensity vs. temperature will also play a role in determining the temperature's accuracy. Figure 5-3 also shows the intensity accuracy as a function of temperature for our data and the potential accuracy of an upgraded system. Due to the curve's flat part around 275 K, the accuracy of the intensity measurement in that region is not good, but over the rest of the cryogenic range, the intensity measurement of an upgraded system can provide an accuracy of plus or minus a few degrees.

167
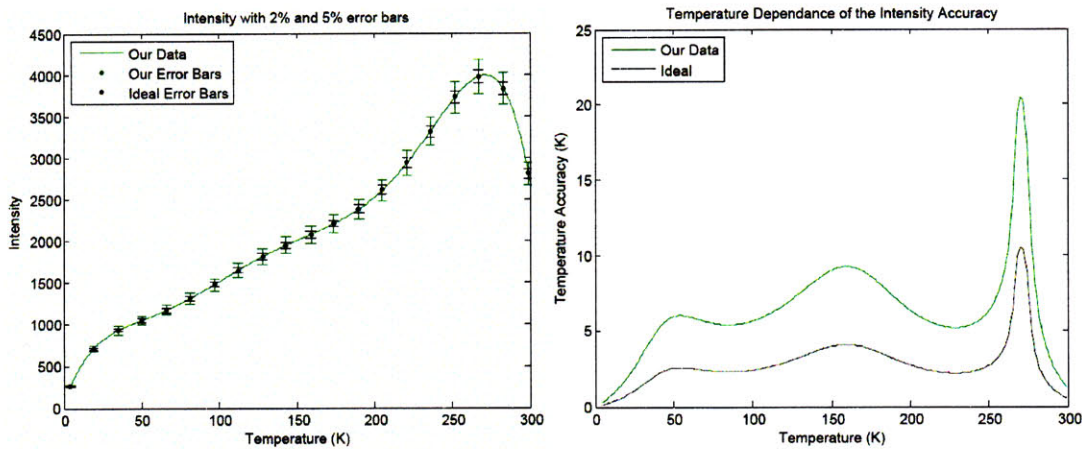
Figure 5-3: Error bars of 2 and 5 % leading to the accuracy of zero-strain intensity measurements.

Linewidth Accuracy

Similar to the frequency shift measurement, the accuracy of the linewidth measurements are proportional to the number of data averages. For our experiments, we only used 230 averages, which corresponds to worse than 10 MHz resolution. Improvements to the system will permit the same order of magnitude of data averages as the frequency shift measurements, which will improve the 10 MHz resolution to the hundreds of kHz range. Due to the data processing, including the FFT and calculating the linewidth from the data in frequency space, the accuracy of the linewidth data will be worse than the accuracy of the frequency shift data by roughly a factor of 5.

Plotting the error bars from our experimental data of the linewidth vs. temperature shows that the error bars basically cover the whole range of linewidth, as seen in Figure 5-4. Also plotted are the expected error bars of the upgraded system, which are only 500 kHz, as compared to the original 10 MHz.

While the accuracy of the experimental linewidth data is very poor, the upgraded system's linewidth accuracy should be good. Other than flat spots around 60 K and 225 K, the linewidth should give temperature accuracies of a few degrees throughout the rest of the cryogenic temperature range.

168
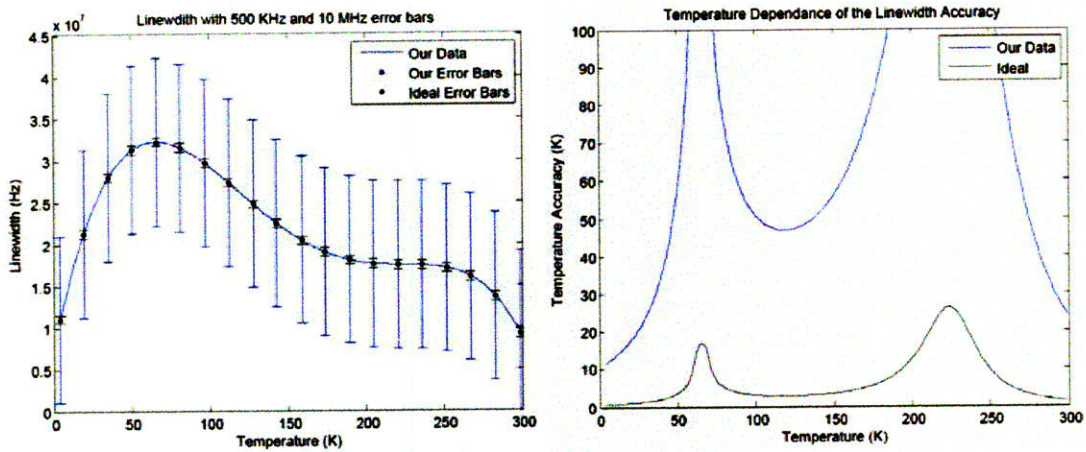
Figure 5-4: Error bars of 10 MHz and 500 kHz leading to the accuracy of zero-strain linewidth measurements.

Zero Strain Temperature Measurement Accuracy

If the system is implemented as a temperature sensor only, it will be able to achieve extremely good accuracy. In fact, at every temperature, the achievable accuracy will be the best accuracy of the three measurements. Depending on the temperature, the parameter that gives the best accuracy will vary. Referring back to a contour plot of the frequency shift, intensity, and linewidth from Chapter 4, all three contours will cross in temperature-strain space at the location of the appropriate temperature and strain. In this case, the strain is zero, so all three lines will meet at the correct temperature on the zero strain line. One way to illustrate the accuracy of the different parameters is to give their actual contour line the width of their temperature accuracy. By plotting these "weighted" contour lines at a specific temperature, it is apparent that the accuracy of the temperature measurement will be determined by the parameter with the best accuracy, as seen in Figure 5-5.

By plotting the accuracy of all three parameters over the temperature range of interest, we can determine the zero strain temperature accuracy, as seen in Figure 5-6.

Two important conclusions can be drawn from Figure 5-6: 1) The accuracy of the temperature measurement is less than ± 1 degree over all but 20 degrees, where it is still less than ± 3 degrees and 2) Only the frequency shift and intensity are

169
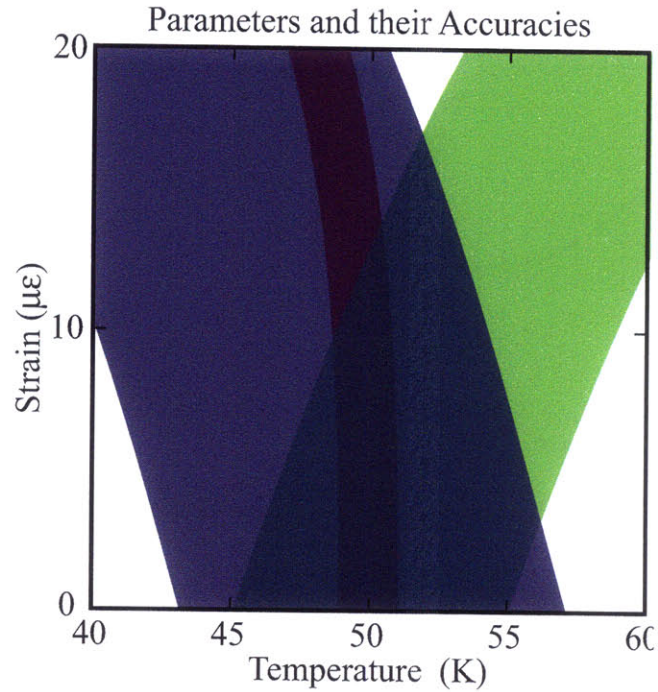
Figure 5-5: For the zero-strain case, the parameter with the best accuracy determines the accuracy of the temperature measurement.

used to get these accuracies. This means that for the zero-strain case, the linewidth parameter is not only not needed, but also not useful in determining the temperature. However, if the accuracy of the linewidth system is improved to a resolution of 100 kHz as opposed to the 500 kHz used for Figure 5-6, the linewidth measurement will provide the best accuracy for the 4 - 25 K range.
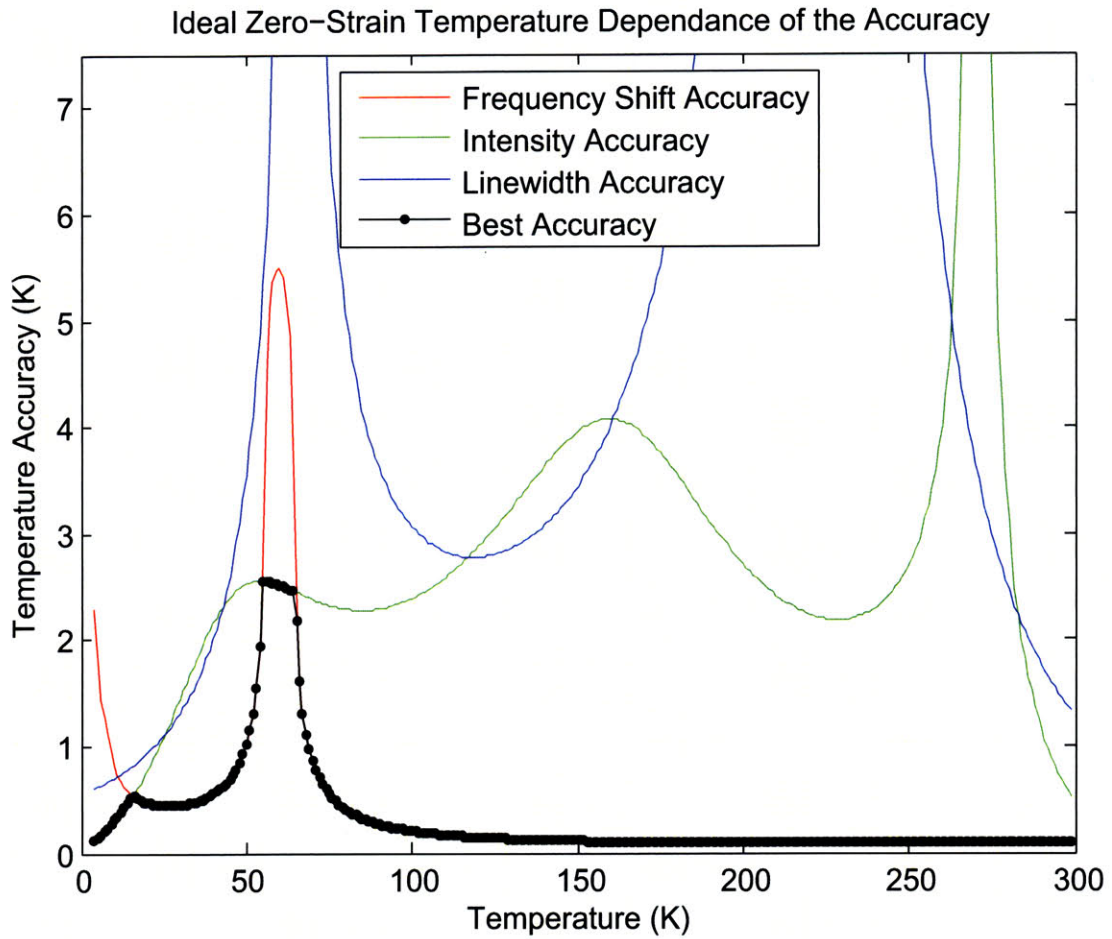
Figure 5-6: Zero-strain accuracy of a temperature measurement as a function of temperature.

5.2.2 Temperature and Strain Sensor

One of the most exciting benefits of this spontaneous Brillouin scattering system is that it can simultaneously measure both the temperature and strain. If a sensing fiber is implemented in a way in which it will sense both the temperature and the strain, we will need to know the accuracies of both measurements. The following calculations are done assuming that the frequency shift, intensity, and linewidth calibration surfaces in temperature and strain space are exactly correct. Obviously, these surfaces will have some error as well, but this error will be determined by the calibration experiments. Since the calibration experiments do not need to be real-time, orders of magnitude more averages can be taken, which will make the calibration error contribution to the total error insignificant compared to the measurement errors discussed in the following sections. The following sections also use the ideal measurement experimental errors, the black lines in Figure 5-2, Figure 5-3, and Figure 5-4, which are the projected experimental errors for the future system.

Relative Frequency Shift Accuracy

As seen in Figure 5-2, the relative frequency shift has a flat spot around 60 K, which causes the worst temperature accuracy to be in that region. Including strain in the measurement, and looking in temperature-strain space, the flat spot shifts to around 50 K for higher strains. The accuracy of the temperature measurement can be calculated and plotted in the same way it was done for Figure 5-2, using the gradient of the surface in the temperature direction and the 100 kHz resolution, as seen in Figure 5-7.

Similarly, the accuracy of the strain measurement can be calculated based on the gradient of the surface in the strain direction and the 100 kHz resolution, as also seen in Figure 5-7. It is apparent from these figures that the accuracy of the temperature measurement due to the frequency shift is less than ± 1 degree over almost all of the temperature-strain space. There is a region in the temperature range between 50 K and 60 K for which the frequency shift measurement can have accuracies no better

172
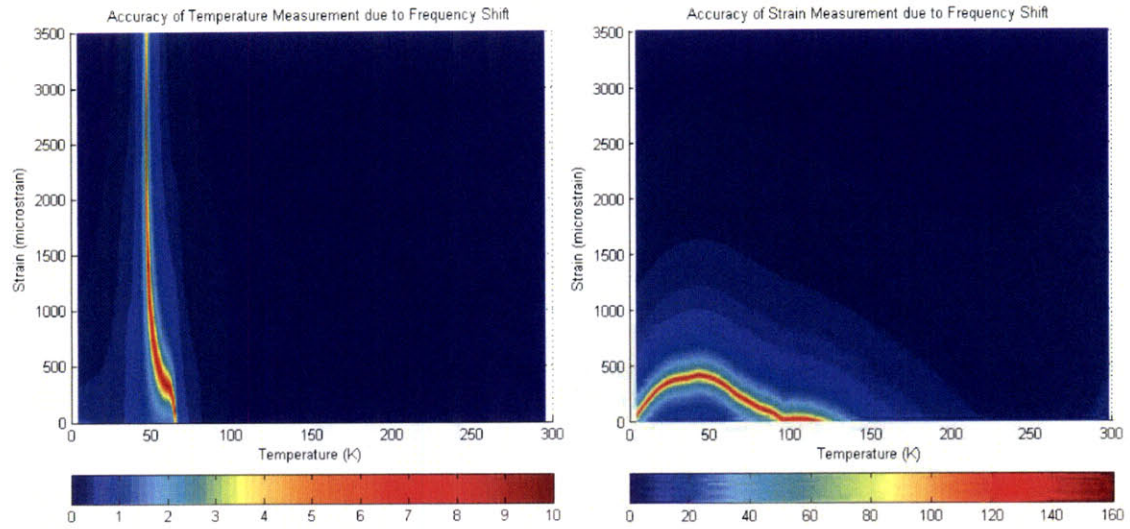
Figure 5-7: Accuracies of temperature and strain measurements due to the frequency shift.

than ± 10 K, but as we will see later, the other parameters have decent accuracies there. Similarly, there is a small area where the accuracy of the strain measurement due to the frequency shift reaches 150 $\mu\varepsilon$, but over most of the temperature-strain space the strain accuracy is less than 20 $\mu\varepsilon$.

Intensity Accuracy

The accuracies of the temperature and strain due to the intensity measurement can also be calculated in a similar way. Taking the gradient of the intensity surface in temperature-strain space and using the intensity error of 2 % of the measured value, the accuracies due to the intensity measurement are plotted in Figure 5-8.
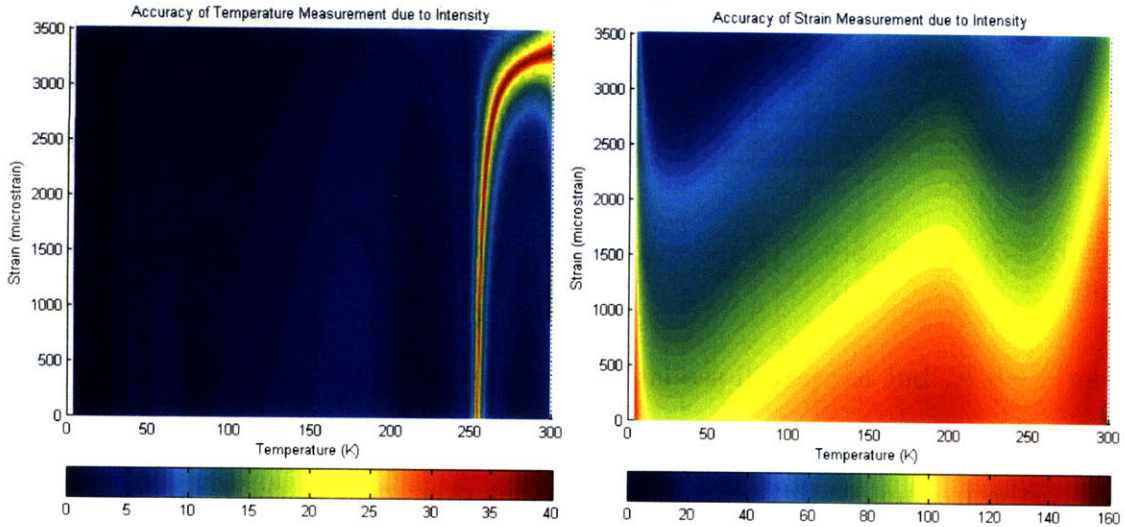
Figure 5-8: Accuracies of temperature and strain measurements due to the intensity.

Figure 5-8 shows that the accuracy of the temperature due to the intensity measurement is less than ± 5 degrees (looking in more detail it is mostly around ± 2.5 degrees) over most of the temperature-strain space, with worse accuracy around 250 K. Fortunately this is a temperature region that is of no great interest for superconducting magnet applications. The intensity is not a very strong function of strain, which leads to worse strain accuracy. Also, since the intensity is inversely proportional to strain, the worst accuracies are at the lowest strains. Fortunately, both the frequency shift and linewidth functions increase with increasing strains, which provides better strain accuracies at low strains.

Linewidth Accuracy

Assuming a linewidth accuracy of 500 kHz, as was done for Figure 5-4, the temperature and strain accuracies due to the linewidth measurement can be determined, as shown in Figure 5-9.
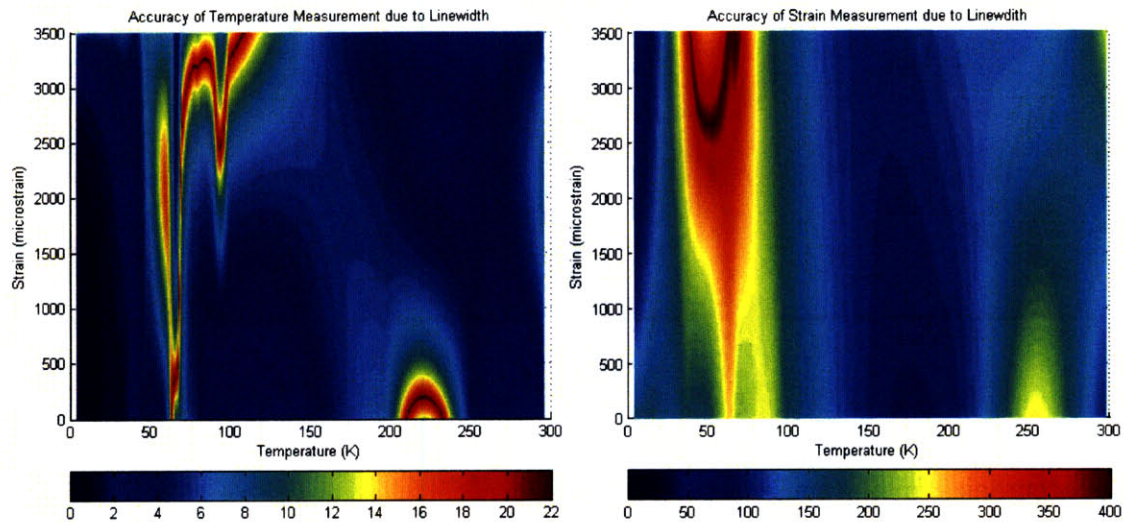
Figure 5-9: Accuracies of temperature and strain measurements due to the linewidth.

Figure 5-9 shows that the accuracy of the temperature due to the linewidth measurement is less than $\pm$ 6 degrees (looking in more detail it is mostly around $\pm$ 3 degrees) over most of the region of interest. At high strains and temperatures from 50 - 100 K, as well as at low strains and temperatures around 225 K, the accuracy of the temperature measurement is as bad as $\pm$ 20 degrees. Again, we are fortunate that the other parameters have good accuracies in those regions. Since the linewidth is not a strong function of strain, the accuracy of the strain derived from the linewidth measurement is not good. Using the upgraded system, a better calibration surface can be created, and it may be a stronger function of strain, but using the data from these first experiments, the strain accuracies are mainly on the order of $\pm$ 100 $\mu\varepsilon$ or more.

Total Temperature and Strain Measurement Accuracy

As discussed in Chapter 4, most of the time the temperature and strain can be determined by measuring two of the three parameters. There are two cases when the third parameter is needed: 1) When parameters cross more than once, and 2) When parameters are parallel at some point. Depending on which scenario causes the need for the third parameter, the overall accuracy is different, as shown in Figure 5-10.
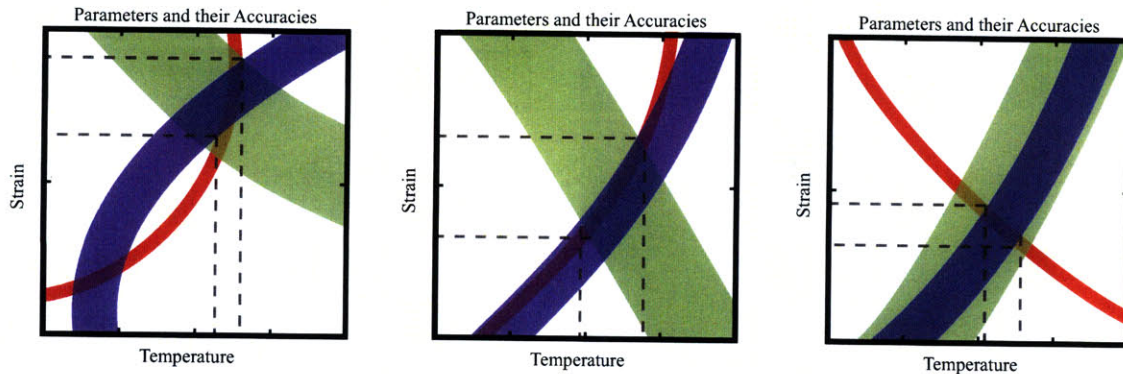
Figure 5-10: Three possible scenarios when all three Brillouin scattering parameters are needed to uniquely determine the temperature and strain. The dashed lines are the accuracies for the temperature and strain.

In the case of two intersections, the worst case overall accuracy can be approximated by the parameter with the second worst accuracy. On the other hand, when the contours are parallel, the overall accuracy can be determined by the parameter with the worst, or the second worst accuracy, depending on which contours are parallel, as seen in Figure 5-10. Figure 5-11 shows the contours of the frequency shift and intensity from the initial Brillouin scattering system, and the newer measurements of linewidth contours.

Figure 5-11 is split into zones where all three parameters are needed to uniquely determine the temperature and strain. In zone "A", the frequency shift and linewidth contours cross in more than one place, so the intensity is needed to determine which position is correct. In this region, the accuracy is determined by the second worst accuracy of the three parameters. In zone "B", the intensity and linewidth contours are parallel in certain regions, which means that the frequency shift is needed to determine the accuracy. The total accuracy is determined by first determining the

176
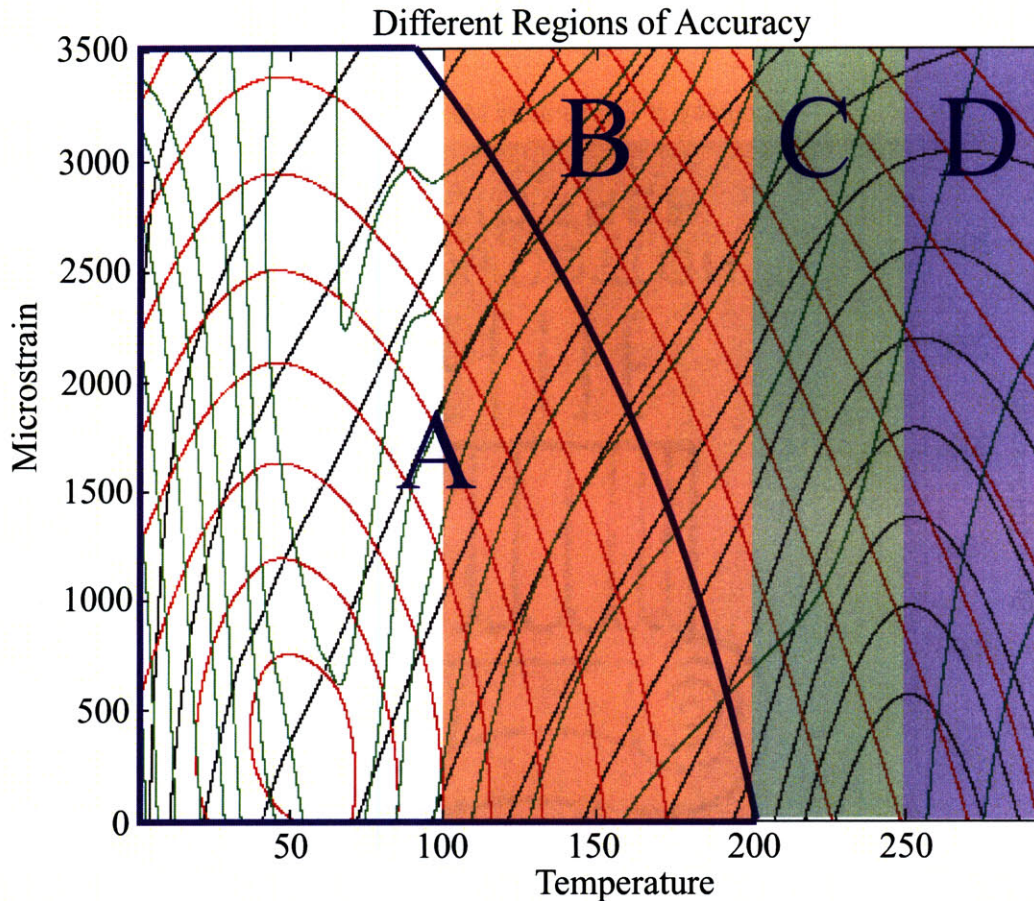
Figure 5-11: Contour plot separated into regions of double crossing frequency shift and linewidth contours (A), parallel intensity and linewidth contours (B), double crossing intensity and linewidth contours (C), and parallel frequency shift and intensity contours (D).

best accuracy between the intensity and linewidth at each point. Comparing this accuracy with the accuracy of the frequency shift and taking the worse of the two gives the final accuracy of the measurements at that point. In zone "C", the intensity and linewidth contours cross in more than one place. Similar to zone "A", the accuracy is determined by the second worse accuracy of the three parameters. In zone "D", the frequency shift and intensity contours are parallel, so the linewidth must be used as well. Taking the best accuracy between the frequency shift and intensity at each point, comparing it to the linewidth accuracy, and taking the worse of those accuracies gives the final accuracy at each point. This has been done at all points in temperature-strain space, and the final temperature accuracies, taking all three

177

measurements into account, are shown in Figure 5-12.
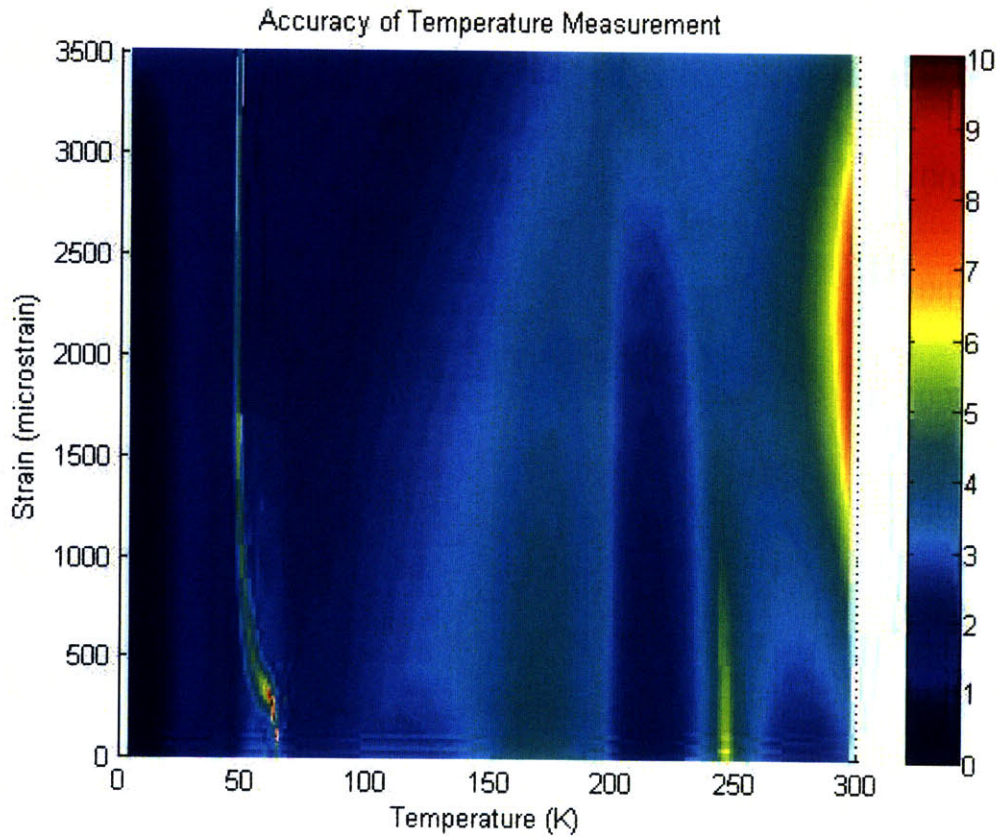
Figure 5-12: The ideal accuracy of temperature measurements.

Except for a small sliver in temperature-strain space, the cryogenic temperature accuracy is ± 2 or 3 degrees. By editing the color-map and zooming in, it is evident that over the measured strain range, from 4 to 25 K the temperature accuracy is actually ± 1 degree or less.

Using the same guidelines for the zones used to make Figure 5-12, the accuracy of the strain measurements can also be plotted, as shown in Figure 5-13.

Over most of the cryogenic region of interest, the strain accuracy is ± 100 $\mu\varepsilon$ or less. There is a small sliver in the low strain range where the accuracy gets up to ± 150 $\mu\varepsilon$, but the rest of the cryogenic range is much better. Above 250 K, the accuracy is much worse, and is dominated by the accuracy due to the linewidth. This region is the worst case scenario, where the two parameters with good accuracy have parallel contours and the parameter with the worst accuracy decides the accuracy as seen in
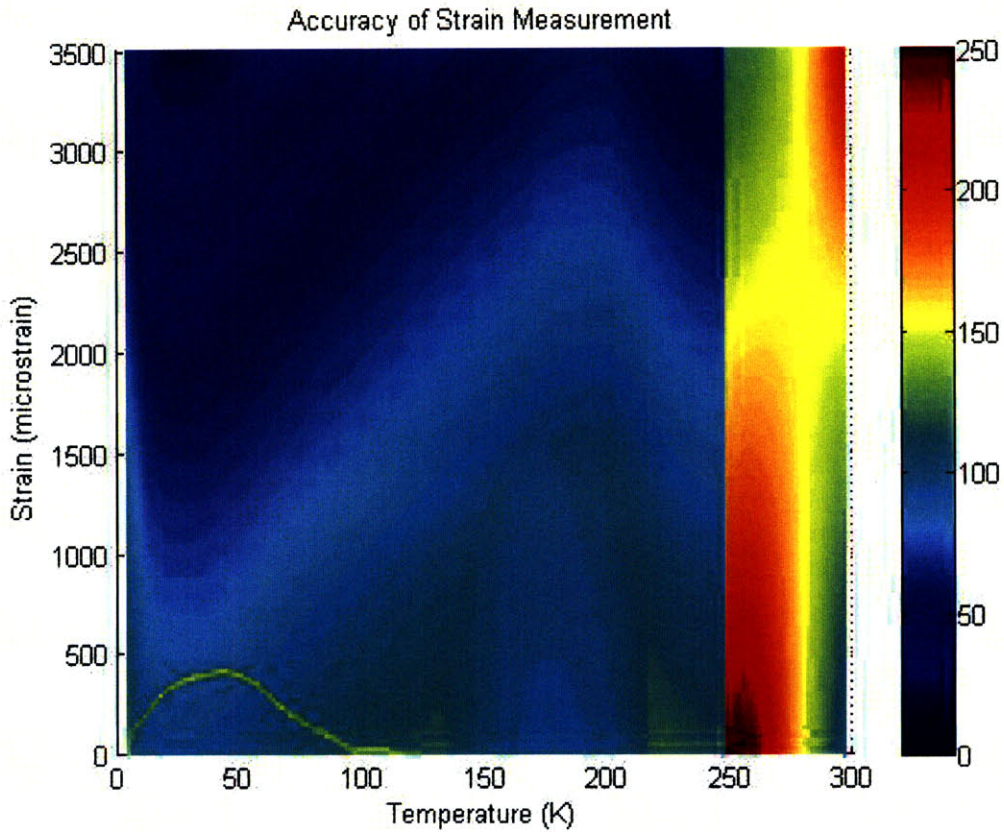
Figure 5-13: The ideal accuracy of strain measurements.

Figure 5-10. The sharp line occurs because the intensity changes slope at around 250 K, and the contours suddenly become parallel to the frequency shift contours. The accuracy of $\pm$ 100 $\mu\varepsilon$ can potentially be improved by better DAQ hardware and more averages, but it is ultimately limited by the weak effect of low strain on the three Brillouin scattering parameters. On the other hand a distributed strain measurement of $\pm$ 100 $\mu\varepsilon$ is a huge improvement over no strain measurement at all.

Chapter 6

Engineering Issues

All state of the art technologies have engineering issues that have to be solved before the system can be implemented. Our spontaneous Brillouin scattering system is no exception. The previous chapters have proved, both theoretically and experimentally, that our system will work as expected; however, a lot of engineering issues still need to be ironed out. Most of the remaining issues deal with fiber positioning and survival throughout the manufacturing and operation of the magnet. All of the theoretical and experimental results from the previous chapters assume that the fiber is in place and operational in the magnet, but even getting to that point requires engineering solutions to several problems.

The location of the fiber in the cable was briefly discussed in Chapter 2, but has not yet been resolved. Fiber survival through the manufacturing of the magnet is also a big issue that will be discussed later in this chapter. During magnet operation, the fiber has to survive both thermal and strain cycles without modification to the spontaneous Brillouin scattering parameters. Many of the fiber survival issues can be solved by placing the sensing fiber in a steel capillary tube; however, this introduces new issues associated with thermal transport times from the conductor to the sensing fiber. The last, and potentially most difficult engineering issue, is the extraction of the fiber from the pressurized supercritical helium inside the conduit to the room temperature optical components and lasers.

6.1 Fiber Location

As mentioned in Chapter 2, the placement of a fiber sensor in a CICC depends on the mechanical integrity of the fiber as well as the thermal diffusion time from the superconducting strands to the fiber. There are several potential locations where the fiber could be positioned, as seen in Figure 6-1.
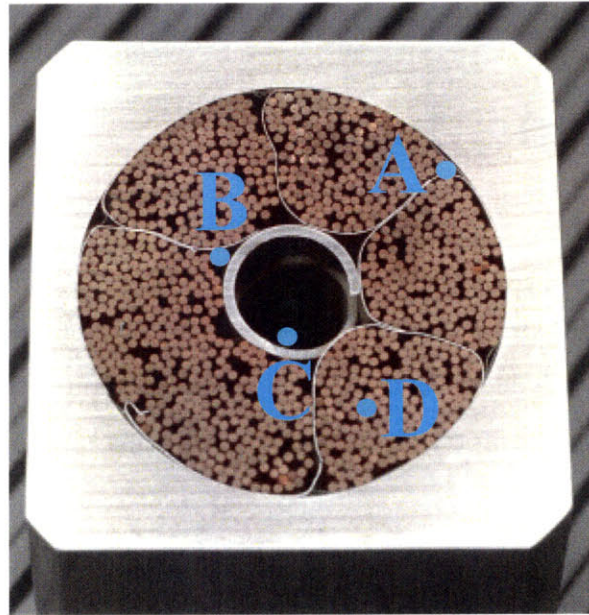
Figure 6-1: The fiber can be placed in the valleys due to the winding, in the central cooling channel, or co-wound with the superconducting wires.

Wherever the fiber is placed, the most important consideration is that it should not be crushed during the magnet fabrication or due to Lorentz loads during a magnet pulse. Location "A" is in the outer channel formed by the final cable winding. This location will experience minimal forces from Lorentz loads since the six stages of cabling are individually wrapped, which holds the conductors in place and forms the channel. However, since the location is on the wall between the conductors and conduit, the time it takes for the temperature to diffuse from the inside, or far side, to the sensor is the longest diffusion time of all sensor positions.

Position "B" is similar to position "A" mechanically, since it is also located in a channel formed by the final stage of conductor winding. The major difference between positions "A" and "B" is that position "B" is closer to the center of the conduit, so

the thermal diffusion time for a quench to reach the sensing fiber is less than for position "A". One disadvantage of position "B" is that the central cooling channel's spiral has sharper edges than the inner conduit wall, so there is a better chance that the fiber breaks if it is pushed against the central cooling channel.

Position "C" is located in the central helium cooling channel. This is the safest spot for the fiber mechanically, since there will be no forces on the fiber during manufacture and no Lorentz forces during magnet pulses. It is also the most centrally located position, so the average thermal diffusion time should be less than the other positions. One disadvantage is that the fiber will be up against the sharp spiral edges since it is impossible to center the fiber in the channel. The use of a protective capillary tube should eliminate this concern. Since the central cooling channel is usually formed by a spiraled wire to increase thermal exchange by inducing turbulent flow, the heated liquid helium due to a quench will appear in the central cooling channel in a relatively short time. That being said, placing a fiber in turbulent flow will cause the fiber to vibrate, and also lead to the need for stronger fibers. Theoretically, vibrations should not affect any of the important parameters we measure of spontaneous Brillouin scattering; however, this would need to be verified experimentally.

The last location, position "D", requires including the fiber in one of the initial triplets in the winding pattern. Since the fiber is about 165 microns, and the standard superconducting wire is on the order of 800 microns, the fiber would have to be put into a capillary tube about the size of the wires in order for the triplet to wind properly. This is also a location of intense Lorentz loads, so the capillary tube would need to provide structural support for the fiber. The benefit of including the fiber in an initial conductor triplet is that it would be in the middle of the conductors, and therefore show a more realistic measurement of temperature and strain.

Taking all of these factors into consideration, we would elect to put the fiber in position "C", as the favored design option. This location would still require the use of a capillary tube around the fiber for fiber protection, and to contain the vaporized acrylate coating if the standard single mode fiber is used.

6.2 Fiber Survival

Since our system is based on the signal from a fiber, the most important component of the system is the actual fiber. Problems with other optical components can be addressed and fixed outside of the magnet, but once the fiber is put into the magnet, it cannot be easily changed. Several fibers can be included in the conductor, but depending on the type of fiber and coating, redundant fibers can be prohibitively expensive. The three main threats to the survival of a fiber are the manufacturing processes, the temperature ranges and thermal cycles, and the maximum strain on the fiber.

6.2.1 Manufacture

The manufacture of a CICC is extremely involved. Complex machines are used to twist the conductors into the specific winding patterns, and also to compact the conductors to achieve the desired dimensions and void fractions. A loose fiber lead will complicate these processes, but the end benefits of an internal distributed temperature and strain sensor may be worth the added complication during the fabrication.

Assuming that the fiber will be in located in position "C", the fiber will either have to be pulled into the central cooling channel spiral, or the channel will have to be formed around the fiber, as seen in Figure 6-2. Each central solenoid hex and quad winding is less than 1 km, and it has been shown that 1 km of cable can be pulled through 1 km of conduit. This means that most likely 1 km of fiber can be pulled into the central cooling channel as well. The rest of the cabling process will remain unchanged, except for the need to be careful with the fiber optic leads at both ends of the channel.

6.2.2 Temperature

As mentioned in Chapter 2, the coating for the fiber also has to be chosen carefully, since the fiber will have to survive several thermal cycles from room temperature down to cryogenic temperatures. Also, depending on the superconducting alloy used,
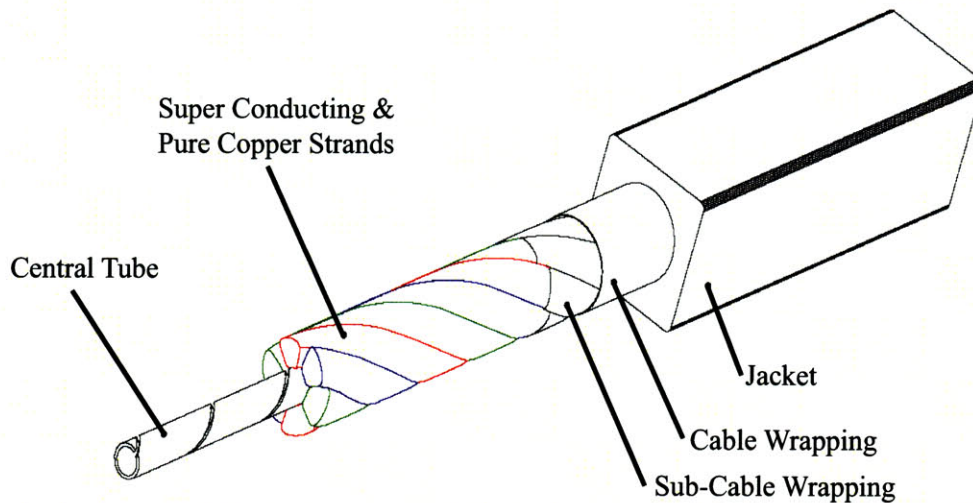
Figure 6-2: CICC layout showing the central tube where the fiber would be.

the fiber may have to survive a heat treatment of from tens to hundreds of hours at temperatures up to 700 C. While there are many different coatings that can be applied to a fiber, this discussion can be broken down into two categories: standard acrylate coated fibers, and specially coated fibers.

Normal fibers will potentially encounter problems both at high temperatures and cryogenic temperatures. At 200 C, the acrylate coating will be vaporized, leaving a bare fiber. Depending on how the fiber is protected, this may or may not be a problem. The principal purpose of the coating is to protect the glass from water and oxidation. The heat treatment must be performed in a vacuum or inert gas environment, so exposed glass may be able to survive, if it is never exposed again to atmospheric conditions. A bare fiber is much more fragile than a coated fiber, but this may not be a problem if the fiber is in its final position when the coating is vaporized, which is basically the case for the magnet when it is heat treated. If the fiber is wrapped in a fiberglass braid or is positioned in a capillary tube, or both, the bare fiber should be relatively safe (the vaporized acrylate coating will have to be contained in something so that it is not distributed throughout the magnet). Using a bare fiber is much riskier than a coated fiber; and if the fiber breaks, the sensor is rendered useless. In the case of alloys that do not have to be heat treated, the acrylate coating would still be intact when the magnet is cooled. This could lead to

micro-bending losses in the fiber, and potentially cause a break in the fiber, due to the coating freezing unevenly and cracking. Whether the fiber would actually break or not is uncertain, but micro-bending will lead to an increased attenuation of the signal in the fiber.

Although micro-bending will lead to losses in the fiber, specialty coatings on fibers tend to increase the losses in the fibers as well. Specialty coatings can be applied to fibers either during the fiber drawing, or after the fiber is made. Usually, once the fiber is formed, only small lengths are coated, but if the coating is applied during the fiber formation, kilometers of continuous coated fiber can be produced. There are a number of different types of coatings for different applications, as discussed in Chapter 2. For our application we want a coating that will add further protection for the fiber, and for this there are a number of choices, such as copper, gold, aluminum, graphite, polyimide, as seen in Figure 6-3.

Depending on the superconducting alloy, which governs the needed heat treatment, certain coatings are ruled out due to their survivable temperature ranges, as seen in Table 6.1.

Table 6.1: Temperature limits for coated fibers, and their associated prices.

	Temperature Limit (C)	Cost ($/meter)
Standard SMF	200	$0.45
Polyimide Coated SMF	300	$5.50
Aluminum Coated SMF	400	$22.00
Copper Alloy Coated SMF	700	$22.00
Gold Coated SMF	700	$35.00

Table 6.1 also shows the approximate prices for the coated fibers. Obviously, it would be desirable to demonstrate the integrity of standard fiber, since it is far and away the least expensive. For example, the ITER central solenoid is made of a little over 36 kilometers of conduit length. Standard single mode fiber for the central solenoid would cost about $16,000 whereas the gold and copper coated fibers would cost $1,260,000 and $792,000 respectively. Fiber survival experiments need to be designed and run to determine if the standard acrylate coated fiber can be used without a high probability of fiber failure.

186
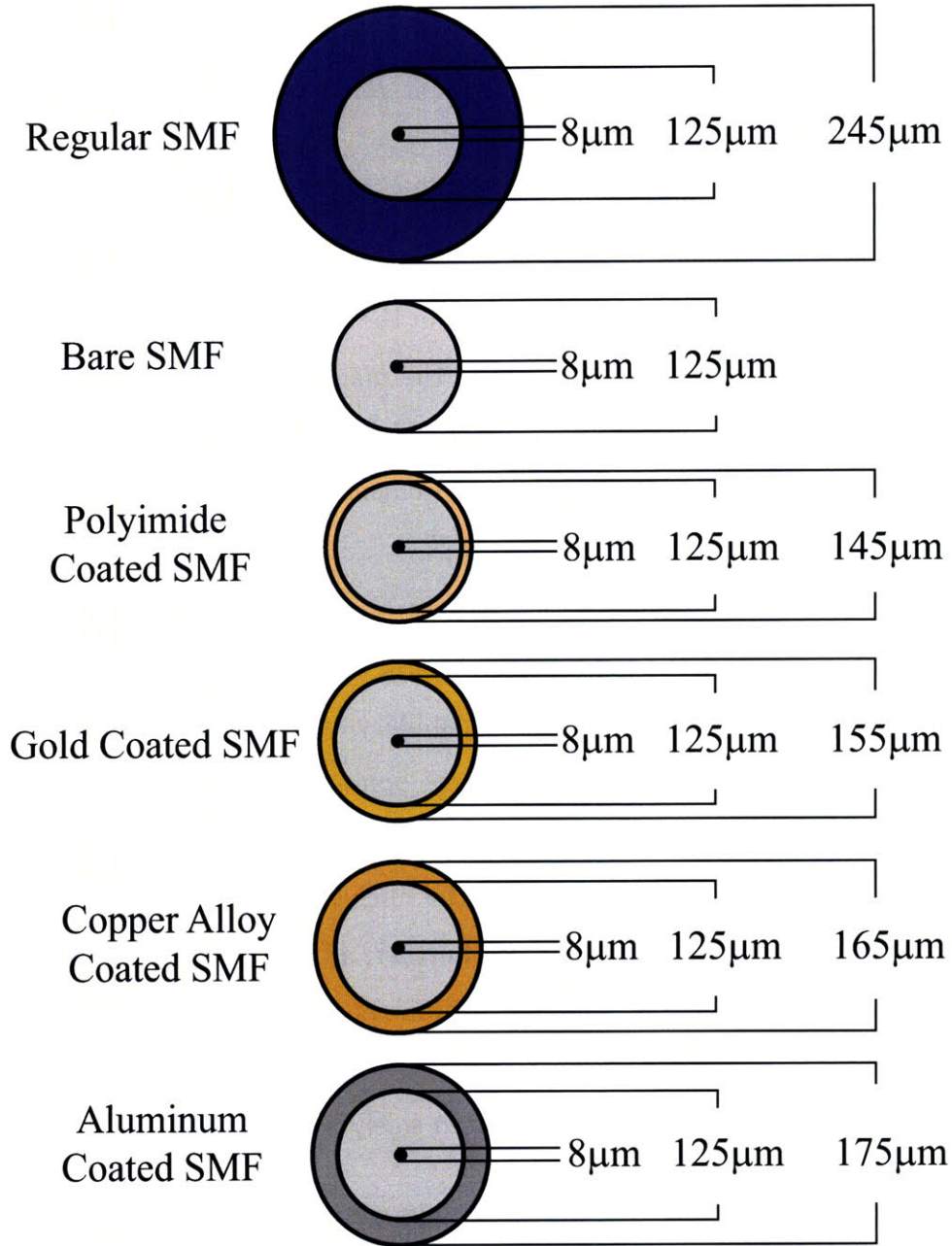
Figure 6-3: Different single mode fiber (SMF) coatings and their dimensions.

6.2.3 Strain

When the magnet is operating, it will experience normal operating strains of around 0.15 % [70]. It must also go through a complex history, including the possibility of tensioning, winding, thermal contraction, and transverse loads, so care must be taken to limit fiber strains at all times. A fiber at room temperature can take up to 2 % strain without breaking; however, this is decreased at cryogenic temperatures to about 1 % strain. If everything is calculated correctly, and there are no pre-strains in the fiber before the magnet is turned on, the pulsing strain of 0.15 % should not be a problem. However, if the fiber is loose in the CICC, then it will not be capable of giving accurate strain measurements of the magnet, as would be the case if the fiber is put in the central cooling channel. There is an obvious trade off between fiber safety and accuracy of the strain measurements that has to be considered in the system design.

If the fiber is to be used for thermometry alone, several modifications can be made. First of all, the capillary tube can be spiraled in the central cooling channel so that when the CICC is strained, the spiraled capillary tube straightens before the fiber experiences any strain. The fiber can also be spiraled in the capillary tube, adding up to 2 % to the length of the fiber compared to the length of the capillary tube. Using both of these spiraling techniques, the fiber can actually be 5 % longer than the length of the central cooling channel. Further, a fiberglass braid can be wrapped around the fiber to further decouple the strain experienced by the capillary tube and the strain felt by the fiber, as seen in Figure 6-4. Using these techniques, the fiber should be nearly strain-free, and can be used solely as a temperature sensor.
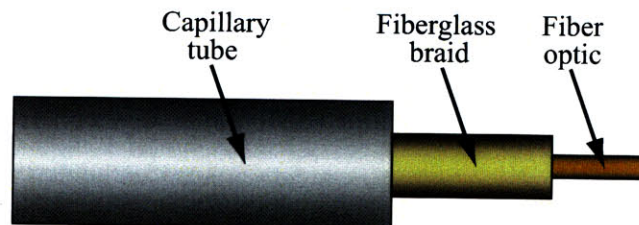
Figure 6-4: Capillary tube with fiber wrapped in fiberglass braid inside.

Although the protection of the fiber is a major issue, there are solutions that can provide a reliable sensor system. The most important decision is determining what exactly the goals of the system are. There will be trade-offs in price, system capabilities, and failure probability that need to be considered in the final system design, but a distributed temperature and strain system is definitely possible.

6.3 Extraction

One of the major benefits of spontaneous Brillouin scattering over stimulated Brillouin scattering is that for spontaneous systems, access to only one end of the fiber is needed for the laser signal and data acquisition. While this is the case for our system, having access to both ends of the sensing fiber would allow the sensing fiber to still be able to sense the entire magnet, even if it breaks somewhere along the path. During the lifetime of a superconducting magnet, it will experience many thermal cycles from room temperature to cryogenic temperatures. Every part of a magnet has to be leak tight to hold the helium throughout these thermal cycles, as well as during magnet operation and quenching. If the magnet leaks anywhere, the liquid helium coolant will leak out, which would cause the magnet to quench, as well as lead to a significant amount of down-time until the leak is located and repaired.

6.3.1 Potential Problems

One obvious cause for a leak would be a plug in the conduit that is made of a different material than the conduit and that has different thermal expansion properties. At a fiber extraction point, the fiber is basically a plug in a hole through the conduit. Since the thermal expansion coefficient for the glass fiber is significantly smaller than that of the conduit material, the fiber can either be crushed if the conduit contracts more than the fiber during the cool-down, or a leak can form if the conduit hole increases much more than the fiber during the heat treatment. Obviously, both of these cases are unacceptable. It turns out that the coefficient of expansion for the fused silica goes through zero at around 200 K, meaning that the fiber shrinks with decreasing

temperature down to 200 K and then begins increasing with decreasing temperature below 200 K. This can be seen in a normalized plot of change in length relative to the initial length, as shown in Figure 6-5 [71].
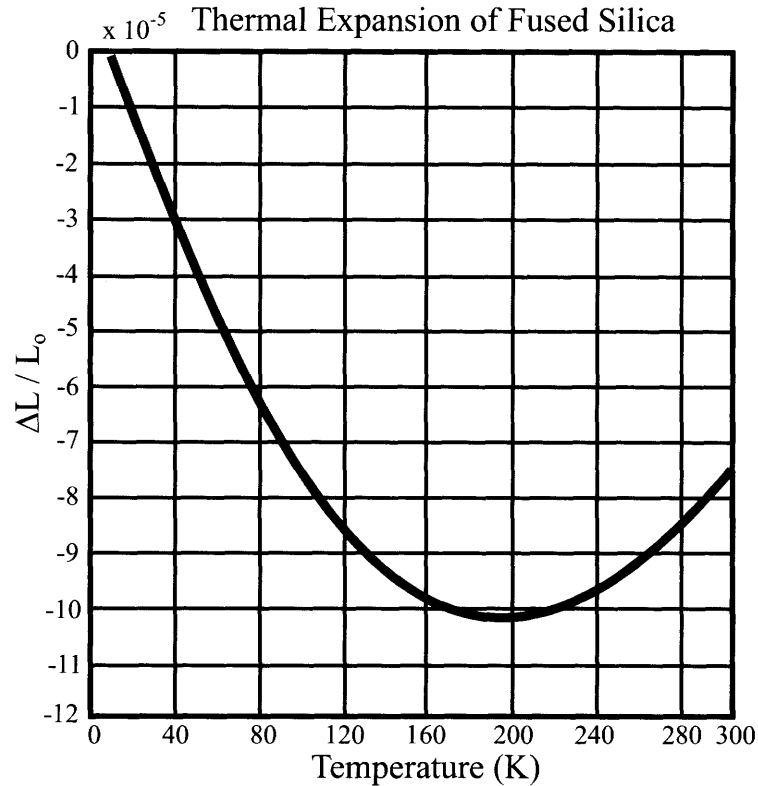
Figure 6-5: Thermal expansion of fused silica (fiber optics) at cryogenic temperatures. The slope of the curve is the coefficient of thermal expansion.

Another engineering issue with the fiber extraction is the pressure swings that it will have to survive. As a magnet quenches, the temperature increase causes a significant increase in pressure in the CICC. Pressure sensors that were tested on the QUELL experiments recorded pressure increases of 0.6 bars up to 14.5 bars during a quench [24]. High differential pressure across an extraction plug can easily lead to leaks. A stycast plug has been shown by Pourrahimi to be leak free at 70 atm, but no plug has been qualified for cyclic pressure loads [20].

The location of the extraction point can be very important in its ability to survive. When strong magnets are energized, their outer surface geometry changes slightly due to the magnetic forces. If the fiber extraction point is in a region where the conduit

is expanding or contracting, it will be stressed, which could again lead to the fiber breaking or a leak forming.

6.3.2 Potential Solutions

One of the easiest ways to seal a hole or crack is by using epoxy. Epoxies are made with a full range of thermal expansion coefficients that are designed to match different types of materials. Many epoxies do not survive cryogenic temperatures, but STYCAST epoxies have very good cryogenic properties. STYCAST epoxies are thermally conductive with low thermal expansion, and they are designed to have low stress on embedded components [72]. Table 6.2 shows some of the potential candidate materials for fiber extraction [64].

Table 6.2: Thermal expansion of materials that could be used in an extraction.

Material	Use	Thermal Expansion at 293 K x $10^{-6}K^{-1}$
Fused Silica	Fiber Optic	0.4
Copper	Fiber Coating	16.7
Gold	Fiber Coating	14.1
Standard Epoxy	Extraction Seal	660
STYCAST 2850 FT	Extraction Seal	28
STYCAST 2850 FT-FR	Extraction Seal	21
50-50 Pb-Sn Solder	Extraction Seal	23.4
Inconel	Conduit Jacket	13.0
316 Steel	Conduit Jacket	15.2

If epoxies are not strong enough, or too brittle when strained at cryogenic temperatures, another potential solution is solder. The fibers we used in our experiments can be soldered into place due to their metal coatings [73]. Similar to epoxies, there are many different types of solders to choose from depending on the desired specifications. For our application, we would want a solder that is ductile in liquid helium so it would flex and not break. The solder would ideally have a coefficient of expansion that is close to both that of the conduit and the fiber optic cable. As long as the solder forms a good seal with the conduit and the metal coated fiber, without having

to heat it to a temperature high enough to damage the fiber or its coating, filling a fiber extraction hole in a conduit may work.

If the above ideal solder does not exist, another solution is to solder, weld or braze the steel capillary tube into the hole in the conduit. Since the capillary tube is thicker than the coating on the fiber, and it is not directly attached to the fiber, a higher temperature can be used to solder or weld the capillary tube into place. The most difficult part would be solved if the seal between the capillary tube and conduit can be made leak tight and remain intact through thermal cycling. The capillary tube and fiber can go through the conduit, and the fiber-capillary tube interface can be addressed at room temperature. Most likely the inside of the capillary tube will be under vacuum, or maybe filled with some type of heat conducting gel. Either way, closing the end of the capillary tube and extracting the fiber is an easy process at room temperature, with many potential solutions.

Although many extraction methods may be leak tight for a small number of pressurizations, they may not last through thousands of thermal cycles. A fiber optic interferometer for quench detection was included in the design for the Korean Superconducting Tokamak Advanced Reactor (KSTAR), but was not included in the final design and construction. They ran an extensive program to solve the extraction issue, and were able to create a seal that survived 10,000 thermal cycles, but the seal around the fiber extraction would not last past 20,000 cycles [74]. Similar to this KSTAR example, no superconducting magnet design team will approve the use of a fiber optic sensor unless the extraction can be experimentally proven not to leak.

Chapter 7

Conclusions and Future Work

7.1   Summary

The main goal of my thesis research was to show a "proof of concept" that a spontaneous Brillouin scattering system can work as theoretically described over lengths of superconductor with good spatial resolution and short integration times. For the first time, the spontaneous Brillouin frequency shift, intensity, and linewidth as a function of strain and temperature have been measured down to 4 K. Using a copper alloy coated fiber, we obtained a spatial resolution of 5 meters at 4 K, and were able to map out the important Brillouin scattering parameters in temperature and strain space as shown in Figures 7-1, 7-2, and 7-3.

193
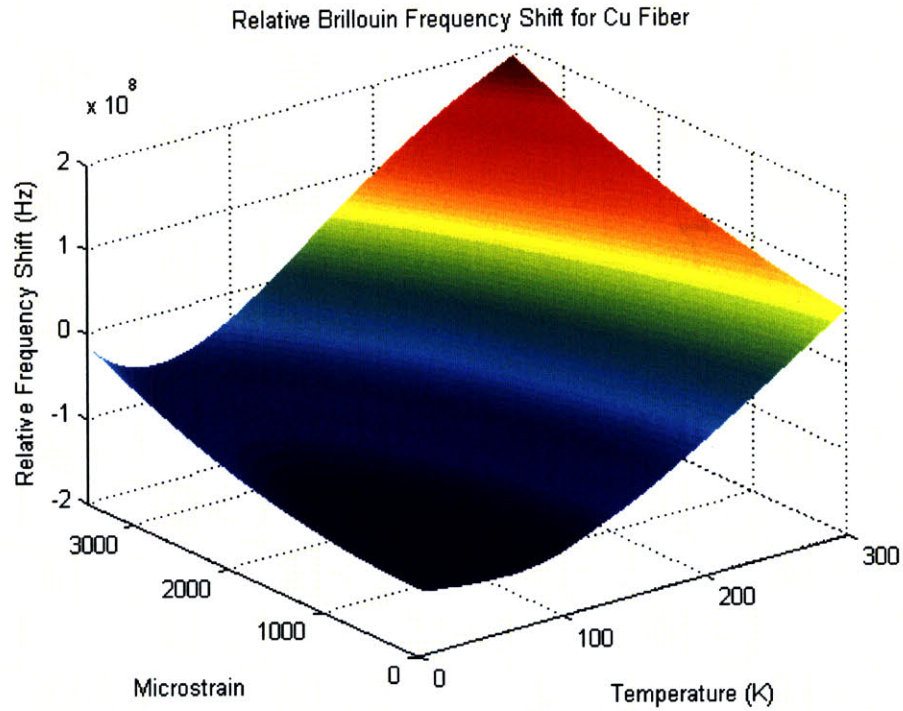
Figure 7-1: Relative frequency shift of spontaneous Brillouin scattered light as a function of temperature and strain.
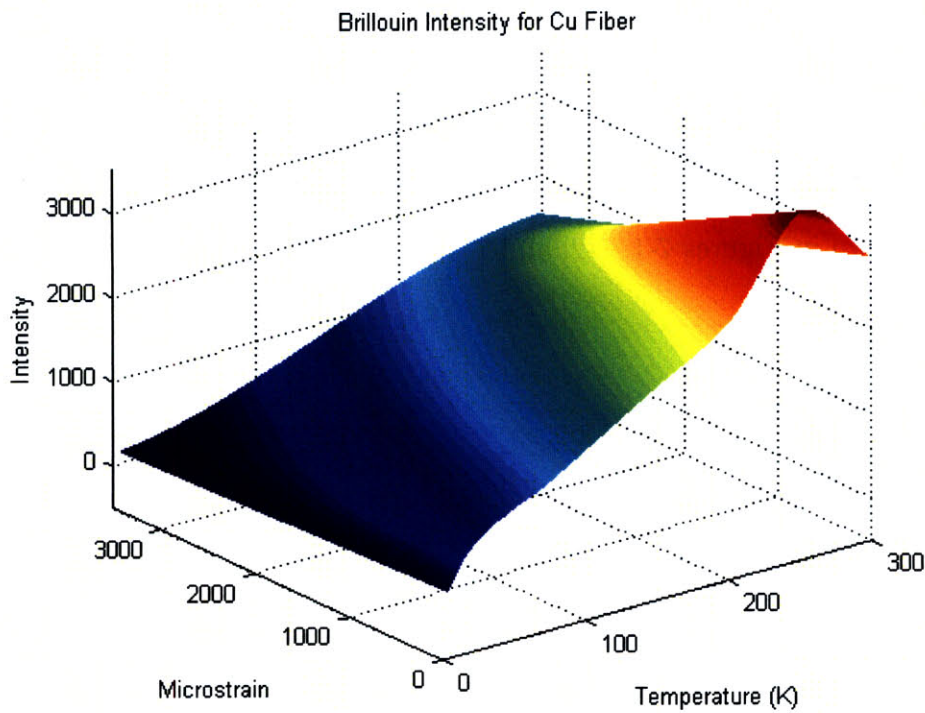
Figure 7-2: Intensity of spontaneous Brillouin scattered light as a function of temperature and strain.

194
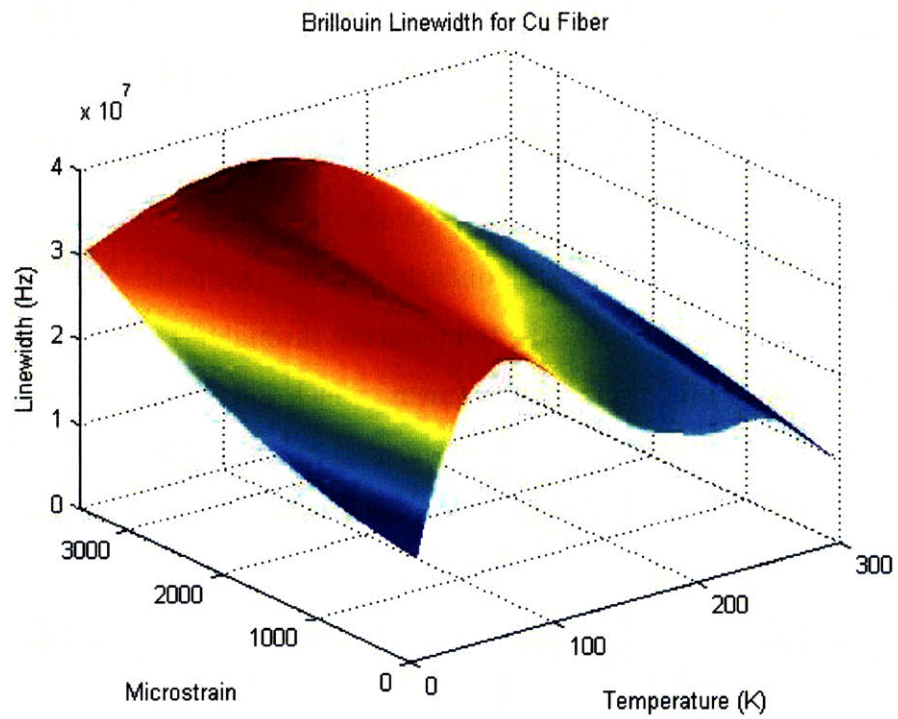
Figure 7-3: Linewidth of spontaneous Brillouin scattered light as a function of temperature and strain.

These surfaces proved that a unique temperature and strain can be calculated simply using the frequency shift and intensity for most of the region of interest for superconducting magnets (4-200 K, and 0 - 3500 $\mu\varepsilon$). The linewidth measurement can be used as a check, and is sometimes needed in regions where the frequency shift and intensity measurements provide more than one possible solution. Using all three parameters will uniquely determine the temperature and strain throughout the entire range of interest, as shown in Figure 7-4.

The accuracies of the temperature and strain measurements, as a function of temperature and strain, are shown in Figures 7-5 and 7-6.

The measurement time is on the order of 0.5 seconds, which allows this system to be used as a quench detection system for large superconducting magnets. The spatial resolution allows the systems not only to locate the origin of the quench, but also to track the temperature changes as the quench spreads. During the heat treatment of a magnet, this system can monitor the temperature throughout the magnet to measure the spatial uniformity of the heat treatment, which has previously been done only from the outer surface. Depending on the positioning of the fiber in the winding, this system will also be able to provide the first ever spatially resolved strain measurement in an operating magnet.
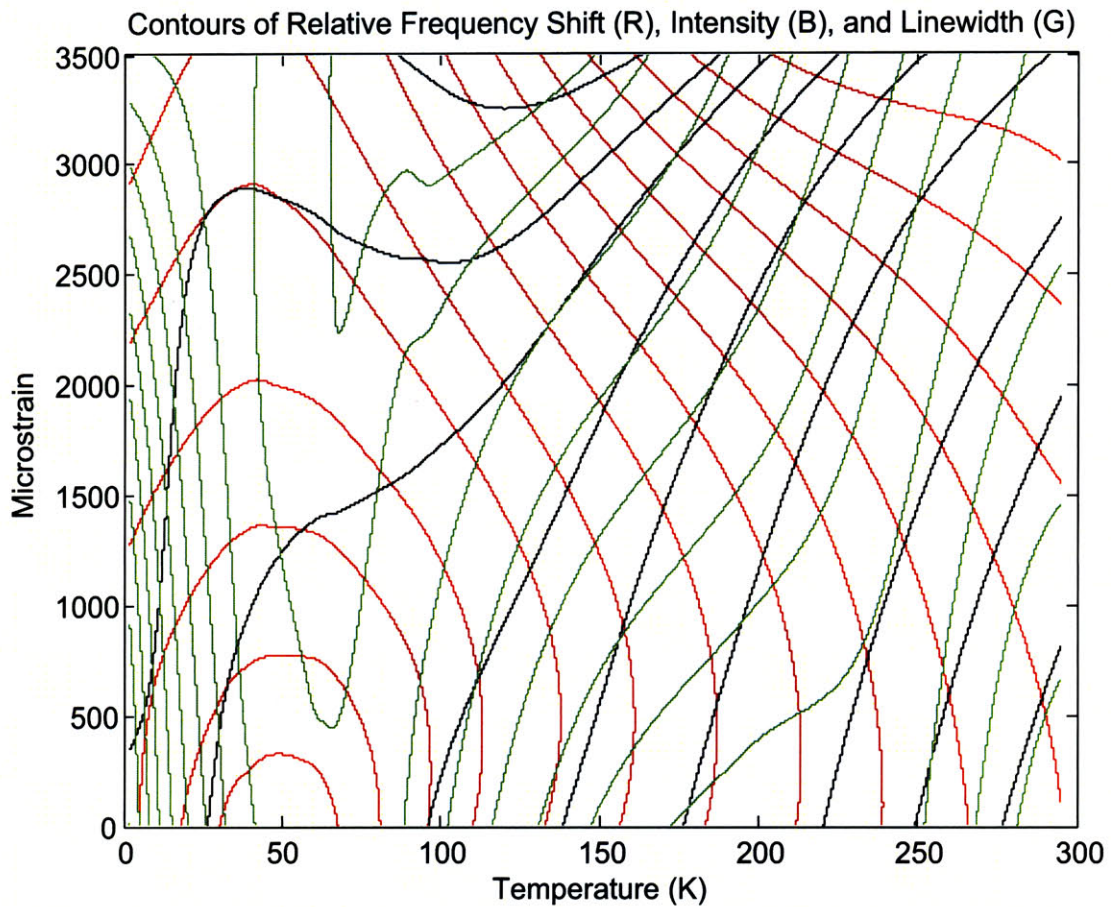
Figure 7-4: Contour plots of the three spontaneous Brillouin scattering parameters in the range of interest. Since there are no areas where all three contours are parallel, these three parameters can be used to uniquely determine the temperature and strain.
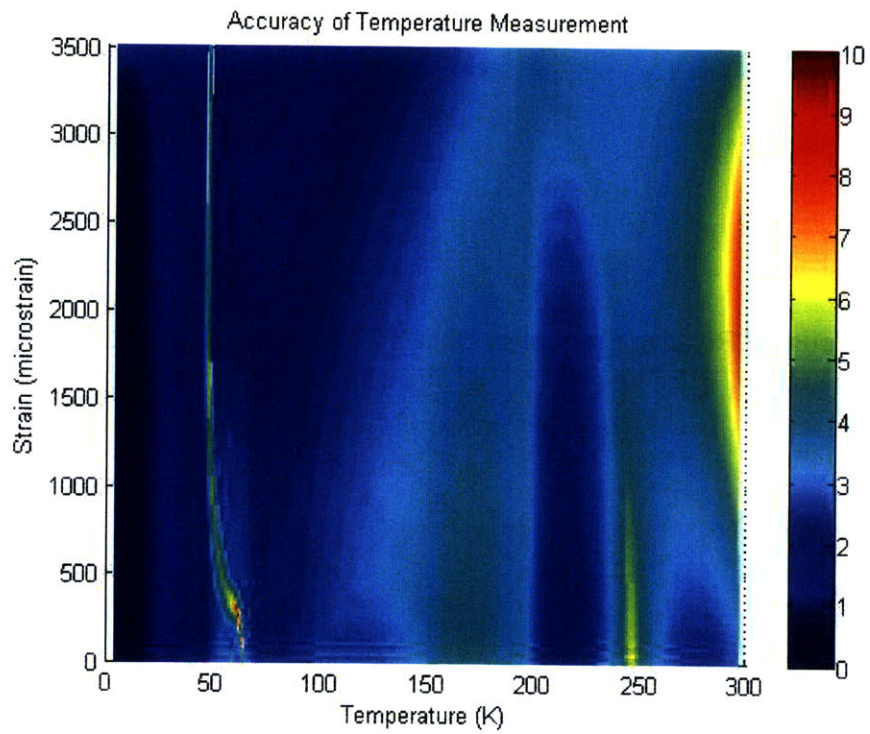
Figure 7-5: The ideal accuracy of temperature measurements.
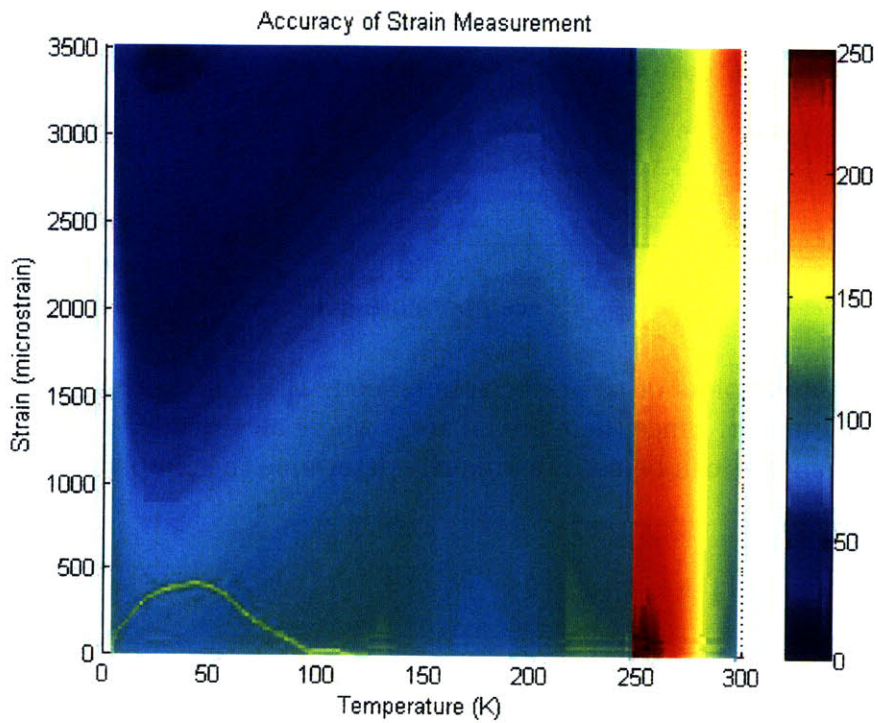
Figure 7-6: The ideal accuracy of strain measurements.

7.2 Future Work

In order for this system to be used reliably in an actual magnet, a more precise calibration experiment needs to be run with an upgraded data acquisition system for the FFT data. There are also several engineering issues that need to be solved, including leak-tight extraction of the fiber from pressurized, supercritical helium to a room temperature fiber going to the lasers and DAQ systems.

7.2.1 Theory and Analytical Tool Development

Since this is a new system, additional analytical tool development needs to be done. Existing simulation codes, such as SOLXPT3D, simulate the development of temperature, pressure losses, and thermal diffusion in cable-in-conduit superconductors. These codes can also model the quench signal and voltage noise on voltage tap and co-wound internal voltage sensors. These codes must be upgraded to predict the output signals, including intensity, frequency shift, and linewidth, from a Brillouin scattering sensor. Used as a SOLXPT3D subroutine, this would be the main tool for predicting fiber optic measurements, and analyzing fundamental limitations in resolution and strain rejection.

Figures of merit that evaluate the spatial resolution, analysis time, and accuracy of the measurements also need to be developed. There are many variables in the system that will affect these figures of merit, and their effects on each other need to be theoretically analyzed in detail. Also, comparison parameters need to be developed to compare our Brillouin system to other options currently used for quench detection and magnet diagnostics, in particular advanced voltage sensors.

7.2.2 Engineering Experiments

As discussed in Chapter 6, there are several engineering problems that need to be solved before our system is implemented in a magnet. The location of the fiber in the CICC needs to be analyzed theoretically based on thermal diffusion times and projected stresses and strains. If the fiber goes in the central cooling channel,

vibration tests with the fiber in some sort of turbulent flow need to be designed and run. Fiber survival experiments also have to be run to determine whether standard plastic coated fibers can survive the heat treatment and cryogenic thermal cycles, as well as the strain cycles. Based on these results, the ideal fiber coating has to be selected. The size and material of the protective capillary tube must be determined, as well as whether or not to use a fiberglass sleeve between the fiber and capillary tube for added protection and strain decoupling.

The most difficult engineering problem facing our system is the reliable extraction of the fiber from a cable-in-conduit, filled with pressurized cryogenic helium, to vacuum, and ultimately to room temperature air. The fiber extraction must remain leak-tight and vacuum-tight over hundreds of thermal cycles and thousands of pressure cycles. A variety of sealant concepts need to be implemented and cycled in order to determine the best extraction design. This problem must be solved before implementation of internal fiber optics in an actual CICC magnet.

7.2.3   Model Superconducting Magnet Experiments

Another important goal is to show that our system works in a more realistic experiment. For this, a superconducting coil needs to be designed and built with the fiber optic sensing cable installed as determined by the results of the other engineering experiments previously described. This magnet also needs to be outfitted with standard voltage taps, thermocouples, and strain gages to be able to compare our measurements with conventional measurements. The coil should have heaters in different areas of the coil in order to be able to quench the magnet at different locations to demonstrate the spatial resolution and quench propagation capabilities of our system.

Appendix A

Fiber Bragg Grating Strain Gage Calibration

Fiber Bragg Gratings are used routinely to measure either temperature or strain in experiments operating at room temperature. Special FBGs known as Long Period Gratings, or LPGs, can be used together with regular FBGs to simultaneously determine temperature and strain since LPGs can be designed to be insensitive to temperature [75]. However, these also are commonly used at room temperature. In our experiments, it is necessary to know the strain in the sample fiber at all temperatures from 4 K to room temperature, but standard FBGs are not calibrated very far below 0 C.

The change in the reflected wavelength of an FBG is dependent on both the change in temperature and the change in strain, as seen in Equations A.1 - A.3.

$$\Delta\lambda_{FBG} = \Delta\lambda_\varepsilon + \Delta\lambda_T \tag{A.1}$$

$$\Delta\lambda_T = \lambda_{FBG}(\alpha + \xi)\Delta T \tag{A.2}$$

$$\Delta\lambda_\varepsilon = \lambda_{FBG}(1 - P_e)\Delta\varepsilon \tag{A.3}$$

The temperature dependence of α, the thermal expansion coefficient, and ξ, the thermo-optic coefficient have been measured down to cryogenic temperature, and are non-linear. Since we plan to use the FBGs as strain gages at constant temperatures, we are not interested in the temperature dependence of the thermo-optic coefficient. On the other hand P_e, the photo-elastic "constant", has not been studied extensively at cryogenic temperatures.

In order to effectively use FBGs as strain gages, we needed first to develop a calibration experiment to determine the cryogenic temperature dependence of the photo-elastic "constant". A few years ago, an experiment was run to look at the response of FBGs to temperature and strain down to 2.2 K, using a cantilever to strain the fibers [76]. The FBG response to temperature was as expected, with relatively no wavelength shift below 100 K. In fact, the response to strain up to 350 $\mu\varepsilon$ showed that $\frac{d\lambda_\varepsilon}{d\varepsilon}$ was independent of temperature [76]. However, another experiment, which strained the fibers past 5000 $\mu\varepsilon$, showed that $\frac{d\lambda_\varepsilon}{d\varepsilon}$ is dependent on the temperature [77]. Although the two experiments contradict each other, they both agree that the temperature dependence is very small for small strains. The second experiment only tested down to 123 K, so we needed to perform another experiment to verify this result down to 4 K.
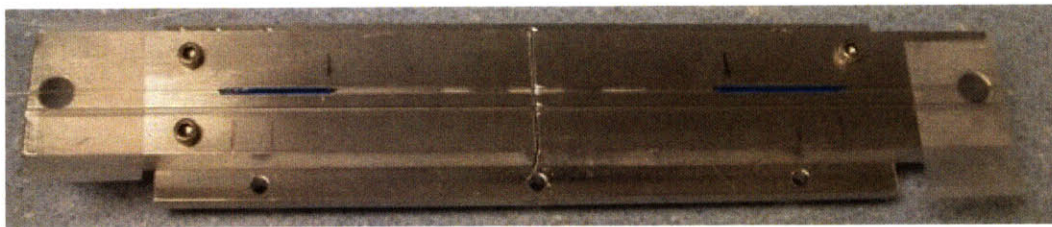
Figure A-1: Fiber holder that slides apart to strain the fibers. The section of the fiber between the blue Stycast epoxy will be strained.

Our FBG calibration experiment compared the wavelength shifts of two FBGs: one that was strained and one that was unstrained at the same temperature. To do this we made an aluminum guide with two channels that was pulled apart to strain the fibers. One fiber was epoxied to both sliding pieces so it was strained when they were pulled apart as seen in Figure A-1. One end of the aluminum holder was bolted

to a pull rod, and the other end was bolted to a base that did not move relative to the other end.

The other fiber was in a wider channel, and not epoxied, so it experienced the same temperature as the strained fiber, but was not strained. It was held in place using gummy vacuum tape in two locations on the same sliding piece so the movement of the second slider did not affect this fiber. Figure A-2 also shows that this fiber had some slack, so that even if the moving piece pulled on this fiber, it would not be strained.
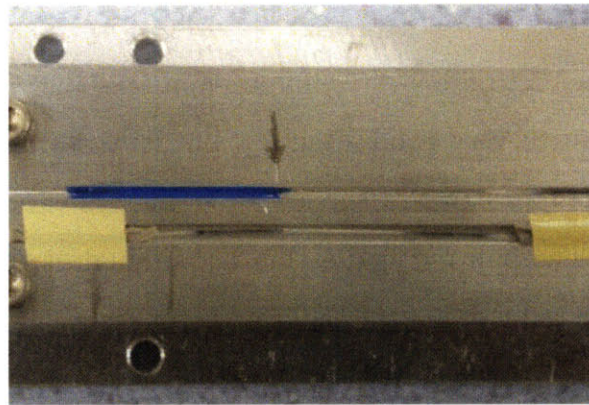
Figure A-2: View of the Stycast epoxy holding the FBG to be strained in the top channel and unstrained fiber in the lower channel with some slack.

Since we wanted to calibrate the FBG's response to strain at several different temperatures, the aluminum sliding guides were made to fit onto another piece that enclosed the FBGs, as seen in Figure A-3. This other piece had a silicon diode (Lake Shore DT 470-DS-12A) that worked with a thermostat and heater to control the temperature of the FBGs. The cryogenic wires coming from the silicon diode are loosely wrapped in the channel in order to thermally anchor the silicon diode.

In Figure A-4, the grooved plates with the FBGs are mounted to the base and the pull rod. On the right, the box has been closed with the FBGs and silicon diode inside, and constantin heater wire has been wrapped around the box. The Lake Shore temperature controller is made to use a 25 Ω heater, so 2.4 meters of 0.01 inch diameter constantin wire, totaling 25 Ω was used. The wires and aluminum box were covered with Apiezon grease to improve the thermal conductance, and then wrapped
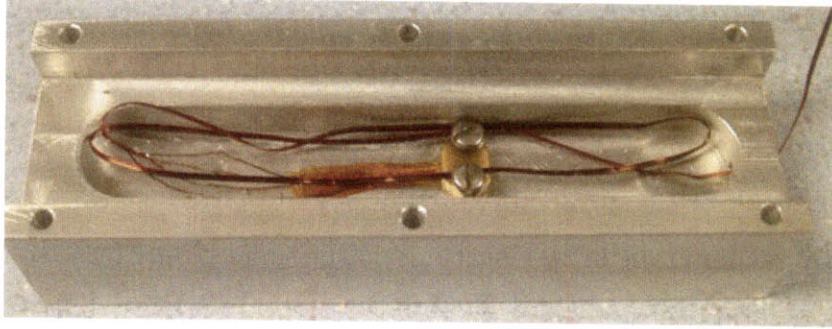
Figure A-3: Aluminum enclosure for the FBGs with a mounted silicon diode to measure the temperature.

in aluminum foil.

It had been intended to use a cryogenic Instron tensometer to move the pull rod the desired amount with very good accuracy, but it was broken at the time of the test. Instead of using an Instron, a threaded rod with 40 threads per inch was used to strain the fiber. The pull rod had a thin bar through it that also went through the brown G-10 push rod, so that the pull rod would not spin, as seen in Figure A-5. Above the thin bar was a stationary steel bar with a through hole for the pull rod. Two threaded steel bars were above the stationary bar, so by turning the middle bar with respect to the stationary bar, the pull rod was raised up. The top threaded steel bar was designed to be used as a lock nut; however, the static friction was enough to hold the pull rod in place. As seen in Figure A-5, there were washers between the bars so that they could be turned more easily.

Since there was thermal contraction when the probe was cooled down, as well as a temperature gradient from 4 K to room temperature during the experiment, we needed to be able to measure the actual relative movement of the two fiber holders. To do this we used a Linear Variable Differential Transformer (LVDT). A brace held the LVDT stationary with respect to the support cylinder, as shown in Figure A-5. A thin bar went from the middle of the LVDT down to the aluminum fiber holder where it was attached to the top moving guide.

At the beginning of the experiment, the limits of the tensile strain measurements were approached cautiously. At first, the FBG was only strained at 4 K up to about 2000 $\mu\varepsilon$. The first strain pull was also performed slowly, but the level of the liquid
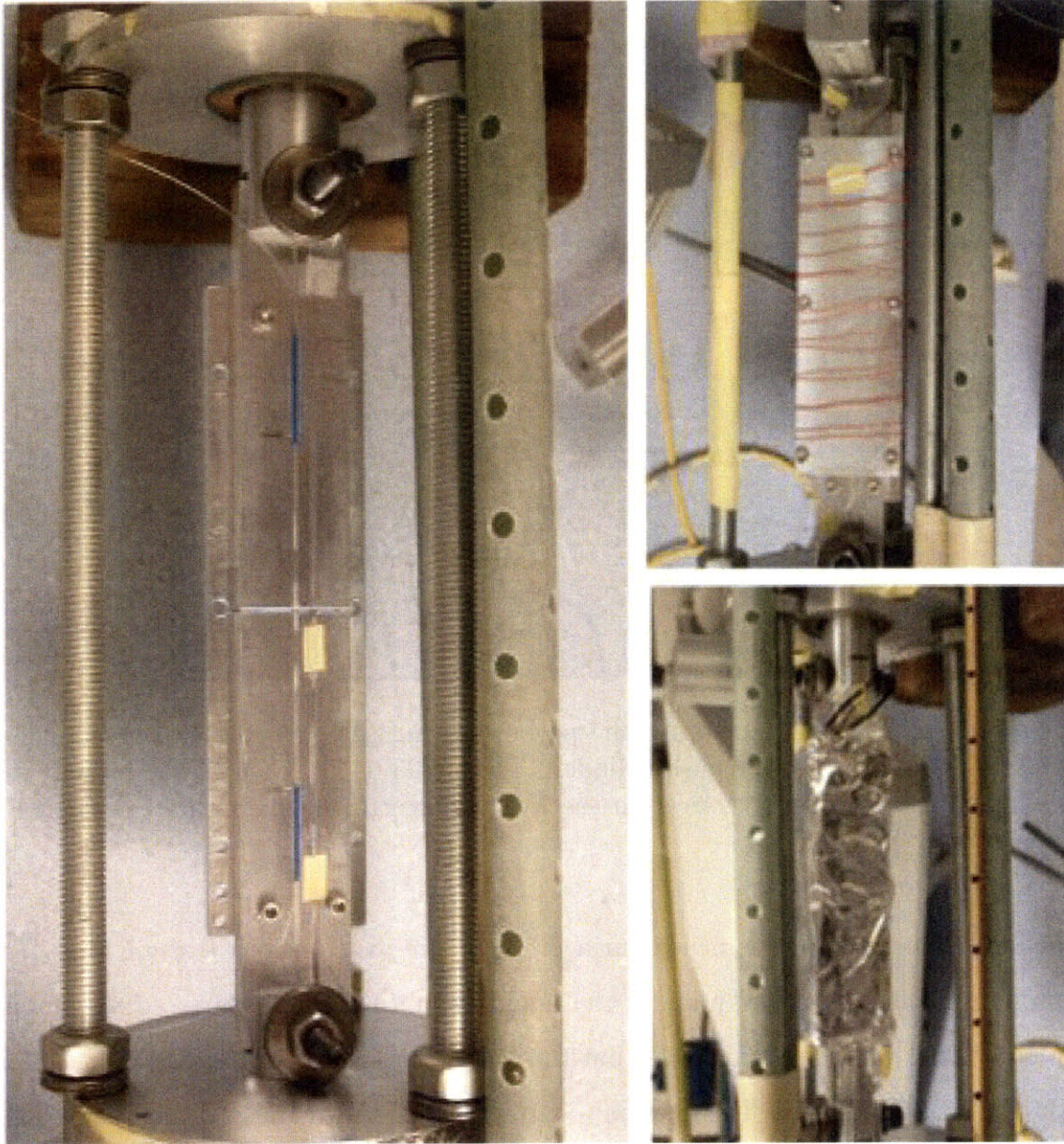
Figure A-4: Sliding aluminum FBG holders are mounted to the base and the pull rod (left), enclosed by the silicon diode holder, wrapped with 25 ohms of constantin heater wire (right top), and then wrapped in aluminum foil (right bottom).
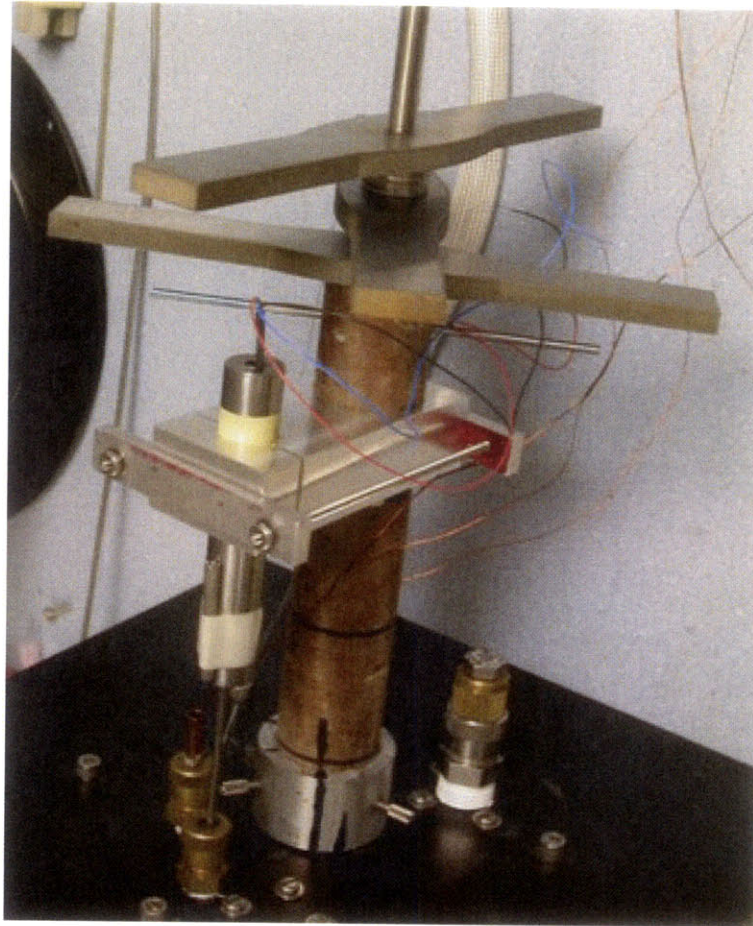
Figure A-5: View of the top of the probe showing the $\frac{3}{8} - 40$ steel threaded pull rod, and the brown G-10 push cylinder. The LVDT is attached to the brown G-10 cylinder, and a thin rod goes from the LVDT down to the sliding part of the FBG holder.

helium changed about 2 inches during the time it took to do the strain run. The probe remained completely under the liquid helium the whole time, so the sample temperature was constant at 4 K, but the change in level may have had other effects on the measurements. The thermal contractions of the metal rod attached to the LVDT, and the G-10 push rod are different, so a change in the temperature over a few inches of these materials would look like relative motion due to the relative thermal contractions. To avoid this in future strain runs, we waited for the temperature to equilibrate so that the liquid helium level would be as steady as possible. The strain pulls themselves from then on were performed in as little time as possible.

The results were not as linear as desired, but they were the best that could be

achieved with the available equipment (and also good enough for the calibration needed for the strain experiment). Nine strain pulls were performed at 4 K, followed by two or three strain pulls at each temperature, as the probe was incrementally heated.

For the strain pulls at 250 K, the raw data is plotted in Figure A-6. As in other literature, there is a slight difference between loading and unloading, but the slopes are nearly identical.
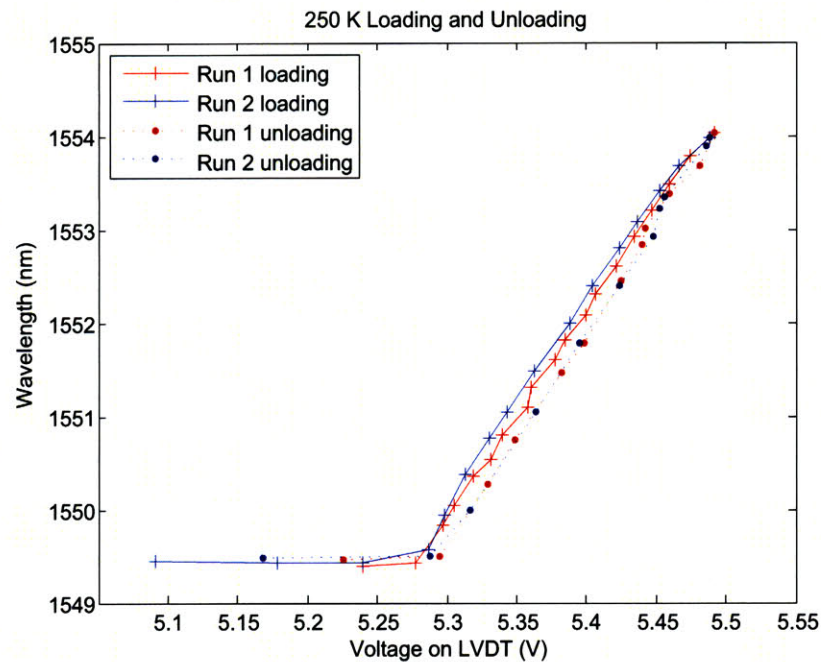
Figure A-6: Raw data showing 2 strain runs at 250 K. The loading (solid lines) and unloading (dotted lines) are slightly different; however, they both have the same overall slope.

In order to calculate $\frac{d\lambda_\varepsilon}{d\varepsilon}$, we first had to determine the voltage where the straining began, and disregard the data points before that. Knowing that our calibrated LVDT (SE-750-500) produces 20.092 ± 0.0005 volts/inch, and that the length of the sample fiber under strain was 2.318 ± 0.0005 inches long, the voltage was converted to strain and plotted in Figure A-7.

After obtaining data points for $\frac{d\lambda_\varepsilon}{d\varepsilon}$ at different temperatures, $\frac{d\lambda_\varepsilon}{d\varepsilon}$ was plotted as a function of temperature in Figure A-8. Each of the "Raw data" points is the linear fit to the data from a strain run at a specific temperature. A weighted average of
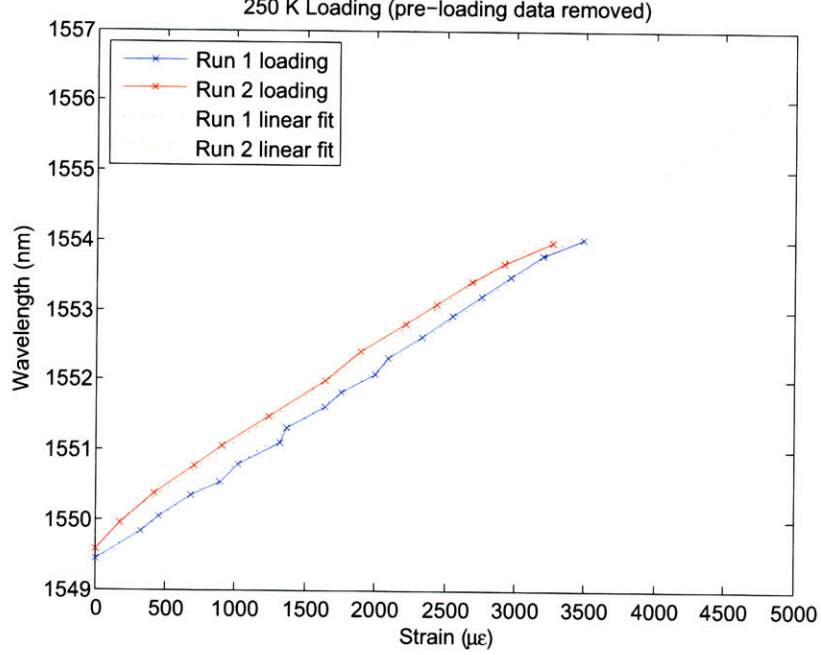
Figure A-7: The loading data for the 2 strain runs at 250 K (solid lines) and the linear fit (dotted lines) of the data provide the slope $\frac{d\lambda_\varepsilon}{d\varepsilon}$.

these data points was taken, based on the R-squared values of each fit. The better the linear fit for a strain run, the more weight that point received in the averaging.

From this data, we can clearly see that as the temperature decreases from 300 K to around 200 K, the strain-sensitivity of the FBGs increases. For decreasing temperatures below 200 K, the strain-sensitivity of the FBGs decreases.

From our data we can calculate the photo-elastic "constant", P_e, as a function of temperature, according to Equation A.4.

$$P_e = 1 - \frac{1}{\lambda_{FBG}} \frac{d\lambda_\varepsilon}{d\varepsilon} \tag{A.4}$$

Using Equation A.4 and our measured values of $\frac{d\lambda_\varepsilon}{d\varepsilon}$, we can plot the photo-elastic "constant", P_e, as a function of temperature, as shown in Figure A-9. Our photo-elastic data agrees well with the room temperature value of 0.22 [47].

The photo-elastic coefficient can be used to calculate the strain coefficient using Equation A.5.
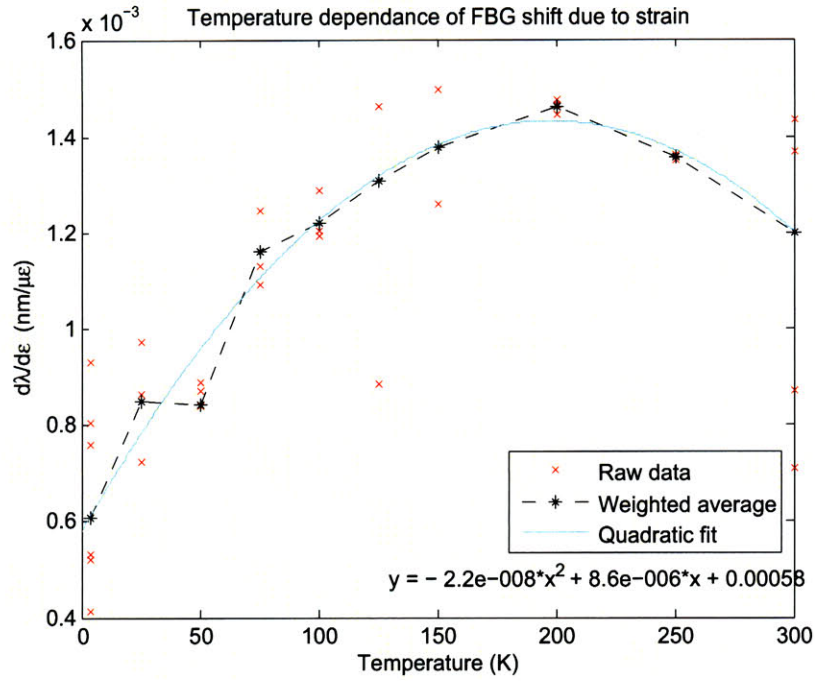
Figure A-8: $\frac{d\lambda_\varepsilon}{d\varepsilon}$ increases as the temperature drops from 300 K to 200 K, but as the temperature drops below 200 K, $\frac{d\lambda_\varepsilon}{d\varepsilon}$ decreases.

$$K_\varepsilon = \frac{1}{\lambda_{FBG}} \frac{d\lambda_{FBG}}{d\varepsilon} = 1 - P_e \tag{A.5}$$

A plot of the strain coefficient as a function of temperature is plotted in Figure A-10. Our strain coefficient also agrees well with the theoretical value of 0.78 at room temperature.
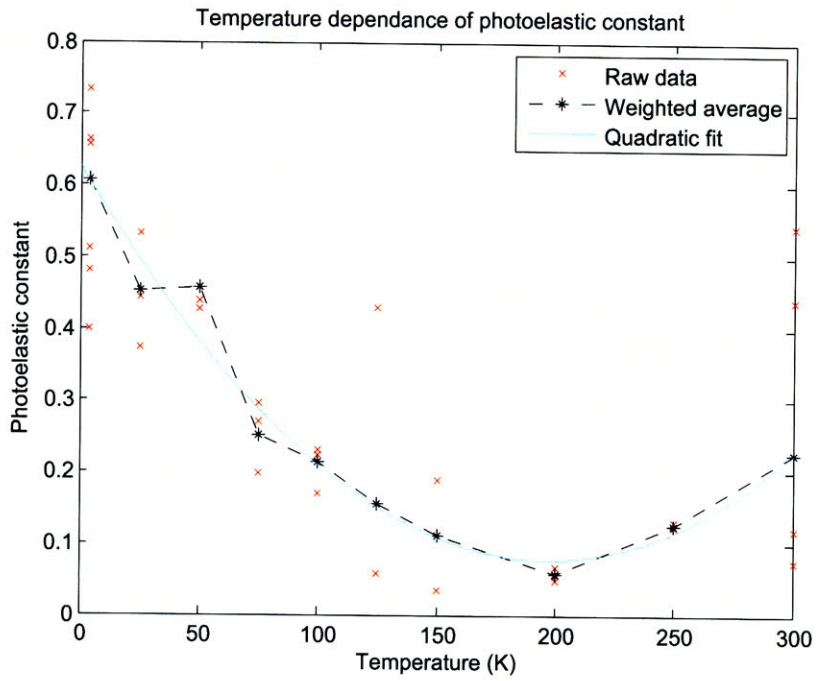
Figure A-9: The photo-elastic "constant" is not constant as a function of temperature.
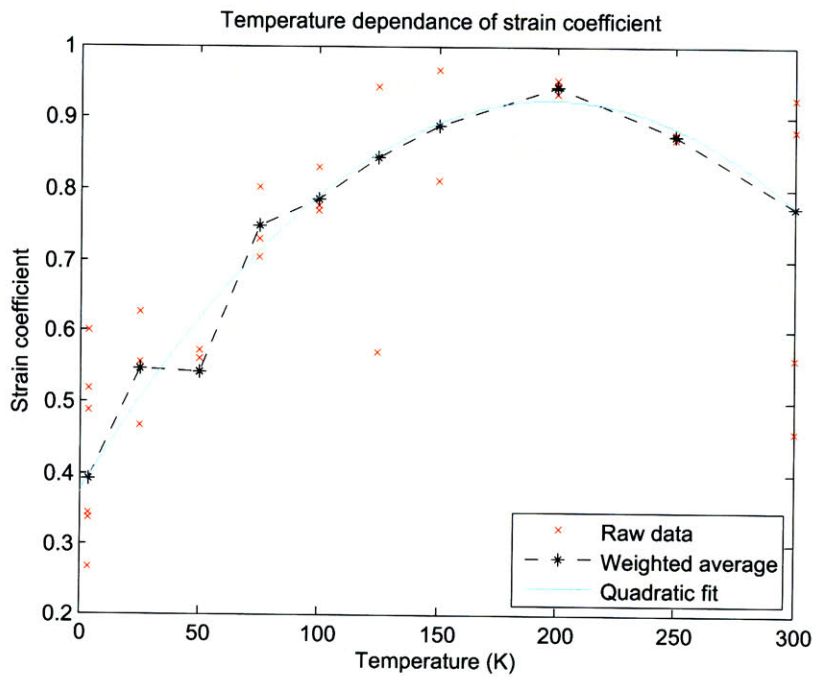
Figure A-10: The strain coefficient is not constant as a function of temperature.

Appendix B

Twisting Cable Diagnostic

As described in the Introduction, the cabling pattern in a CICC is very intricate. Figure B-1 shows the $3 \times 3 \times 4 \times 5 \times 6$ cabling pattern used to make this superconducting cable
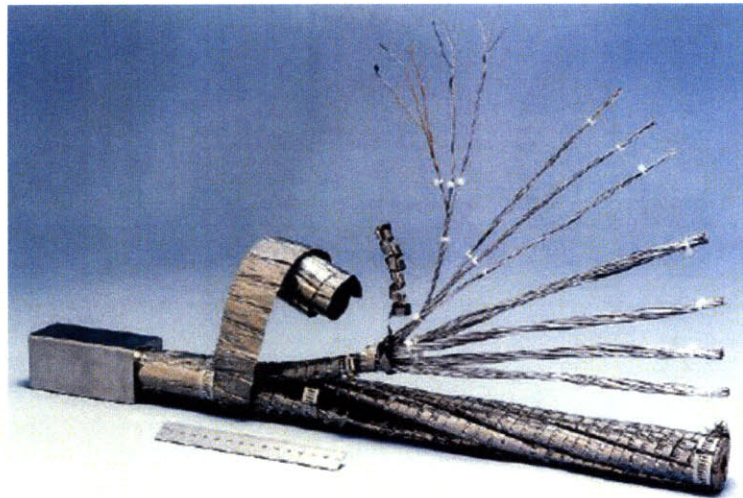
Figure B-1: Partially untwisted CICC showing the cabling pattern.

During operation, the transverse Lorentz loads on the superconducting cable creates bending strain in the strands and pinching strains, where the conductors cross over each other due to the cabling pattern. This causes reversible strains that degrade performance of the strain-sensitive superconductor, as well as irreversible degradation, due to breakage of individual filaments by local tensile strain. By sensing the strain in the wires, a better understanding of these loads can be achieved. Due to the

intricate winding pattern, theoretical calculations of the loads are complex. Actual measurements of the loads on the wires are impossible, due to the geometry. However, using an optical fiber sensor to measure the strains could give detailed information, adequate to calibrate numerical models of the strain distribution in the CICC. There are several different sensing methods and several different configurations that can be used to get this information.

B.1   Fiber Optic Sizing

Since a normal fiber optic cable has a diameter of 0.125 mm, and an ITER strand is approximately 0.8 mm in diameter, we need to increase the size of the fiber optic to be closer to that of the other wires. Several options are discussed below.
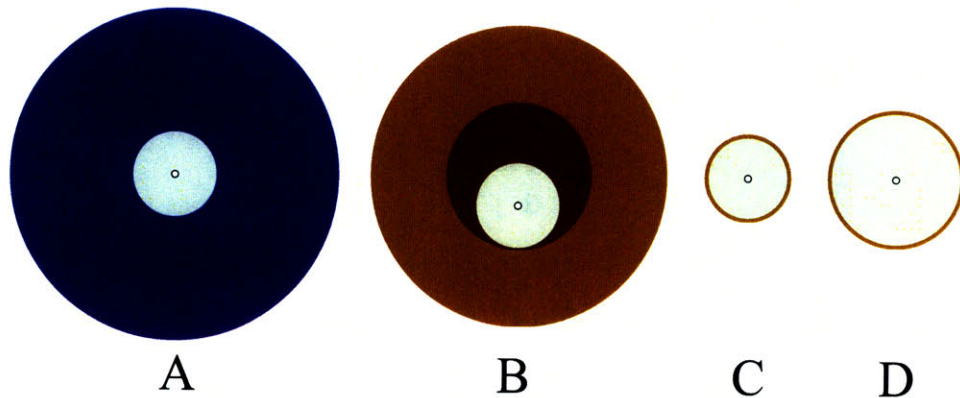
Figure B-2: Several choices of cladding, coating, and protection.

- If the strain tests are using only a bundle of fibers and no superconductor, a regular fiber with a 0.9 mm plastic coating is a standard product. This would be the cheapest and easiest way to put a couple of fibers distributed in the bundle, but it would not protect against lateral stresses, which may break the fiber. Figure B-2A.

- If the strain tests are using only a bundle of fibers and no superconductor, the fibers need to be either bare fibers or metal coated. These fibers need to be protected inside a capillary tube. The fiber can be pulled into a copper tube with an OD of 0.8 mm and filled with an epoxy to hold it in place (Or a steel capillary tube to avoid

any lateral stresses. The Young's modulus of the steel tube can be matched to that of a solid copper strand.). Figure B-2B.

- Coating a fiber with copper will increase the diameter to 0.165 mm. It is physically possible to coat the fiber with enough copper to increase the diameter to 0.8 mm, but since the different coefficient of expansion between the copper and silica glass is very different, a large temperature change may crack the coating Figure B-2C.

- The cladding of the fiber can be increased to 0.2 mm without any harmful side effects. Coating this fiber with the appropriate amount of copper would increase the diameter to 0.26 mm. This would be expensive, since it would require a custom fiber to be designed and drawn. Figure B-2D.

B.2 Fiber Optic Positioning

There are also several different positioning schemes that can be used based on the desired measurement, as shown in Figure B-3.
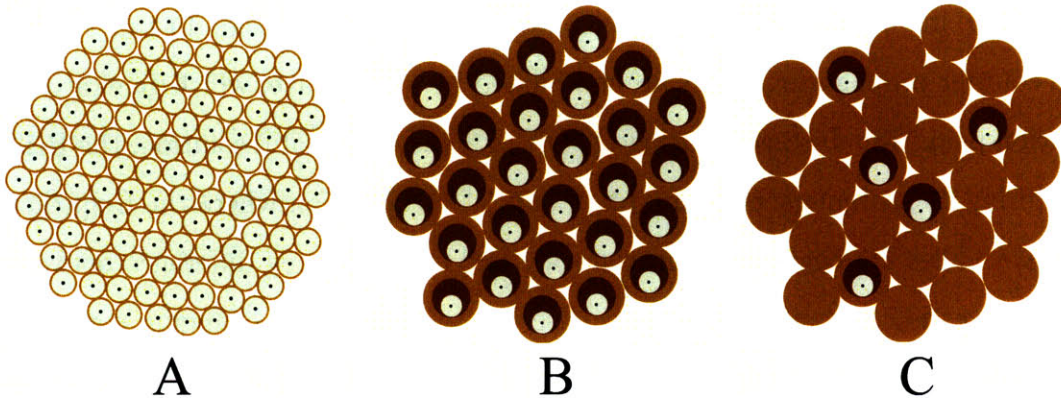
Figure B-3: Several choices of fiber positioning.

- If this is strictly a geometry based strain measurement, a bundle with only metal coated fibers can be used. This would allow standard metal coated fibers to be used and the strain in every fiber can be measured; however, it will be using fibers with much smaller diameters than ITER strands. Figure B-3A.

- If this is a geometry strain measurement that cannot be scaled down, a bundle of copper capillary tubes with the correct OD (or an OD scaled to match the Young's

modulus of an ITER strand) can be used. The fiber optic can be epoxied in the capillary tube and strain can be measured for each strand. Figure B-3B.

- If we want to change as little as possible in the strand bundle, we could use the actual ITER strands and replace a couple with a sensing fiber (either 0.9 mm plastic coated fiber, or a fiber in a copper capillary tube). This would give the most realistic data, but only in a few positions. Figure B-3C.

B.3   Strain Measurement Method

The actual strain measurement can also be done in several ways. The LUNA Rayleigh scattering system described in Chapter 2 could be used to measure the strain induced in the sensor. A measurement time on the order of 10 seconds is not a problem, since this would be a steady-state measurement. Using this system, 2 cm spatial resolution and 1 $\mu\varepsilon$ strain resolution is possible.

A Brillouin scattering measurement that uses a correlation-based continuous-wave technique, instead of a time-based technique, could also be used. In this system the two counter-propagating waves are modulated by a sine wave, which generates a correlation peak [78]. Instead of using OTDR to achieve spatial resolution, the Brillouin scattering measurement is taking place only at the position where the frequencies of the two waves are changing synchronously and the frequency difference between the two sources is constant. Everywhere else the two waves are changing continuously, which results in suppression of the gain and therefore no signal. This size of the correlated region (spatial resolution) can be changed by changing the modulation of the two lasers. This system has been shown to work with as low as 1 cm spatial resolution at a 57 Hz sampling rate [79].

A system using Fiber Bragg Gratings may be the easiest system to implement. "Distributed measurements" that the LUNA and Brillouin scattering systems measure are only as good as their spatial resolution. For this experiment, systems being able to measure several closely spaced points are more "distributed" than the LUNA and Brillouin scattering systems. Since the FBGs are a few mm long, this means we can

get a spatial resolution of a few mm using FBGs. This system would use wave division multiplexing (WDM) of FBGs where each grating reflects a different wavelength of a broadband light source.

Table B.1: Three potential measurement systems, including their best spatial resolution and a short list of pros and cons.

	Res	Pros	Cons
LUNA (Rayleigh)	2 cm	· Commercial product	· Spatial resolution not as good · Expensive
Brillouin Scattering	1 cm	· Good resolution · Inexpensive fibers	· Expensive components · Development needed
Fiber Bragg Grating	Few mm	· Very good resolution · Inexpensive laser	· Expensive custom fibers · Need protective Cu tube

As in discussed in Table B.1, there are many different ways to use fiber optics in sensor systems. Depending on the desired parameters to be measured, the actual fiber properties and the layout of the fiber sensors, including the optical system, need to be optimized.

Appendix C

Temperature Experiment Pictures

Figure C-1 is a picture of the probe used in the temperature experiment. The square black G-10 plate sat on top of the cryostat, while the rest of the probe hung in the central reservoir. The top 24 inches of the probe in the cryostat have Styrofoam wrapped in the yellow tape to provide a thermal barrier between the cryogenic and room temperatures.

The brown G-10 cylinder is attached to the fiber holder at the bottom, and can be raised and lowered by pulling the cylinder through the top plate and locking it into place with three set screws, which can be seen better in Figure C-2.

The copper wires seen in Figure C-2 are the lead wires for the thermocouples and heaters. The liquid helium transfer line penetrated the brass and steel connectors located to the right of the central cylinder in Figure C-2. During the experiment, the fiber optic cable traveled through the small copper tube and then through the brown G-10 tube to the sample holder, which also was insulated with Styrofoam as seen in Figure C-3.

At the bottom of the probe, there is a base holding the copper blocks used for the differential thermocouple connections, as shown in Figure C-4. This part of the probe was submersed in the reference cryogen, either liquid helium or liquid nitrogen. Nine copper block pairs were made to allow the use of nine thermocouples. Seven were used in the initial tests at MIT, but only two were used in the actual temperature experiment.

Figure C-1: Photo of the experimental probe used in the temperature experiment.
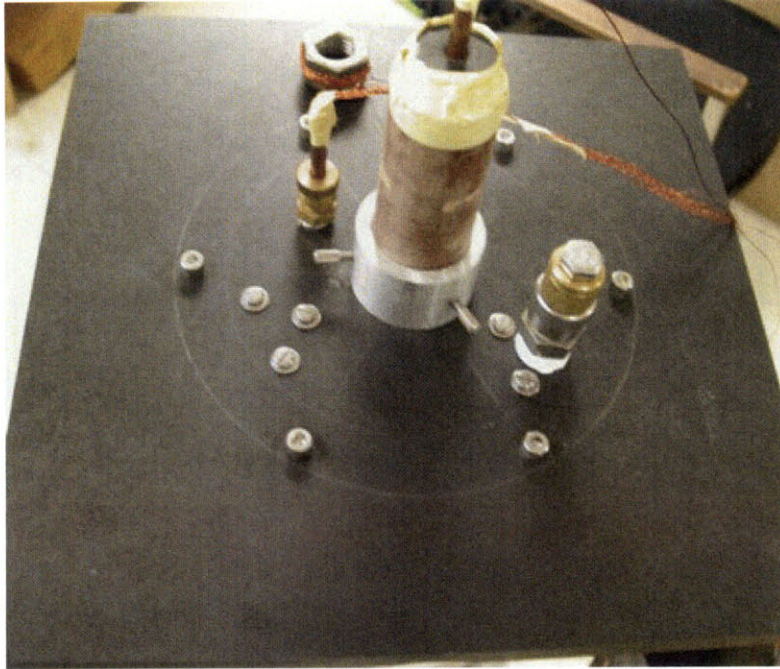
Figure C-2: View of the top of the probe.

Also seen in Figure C-4 is the bottom of the liquid helium level sensor inside the tube on the left with the holes. The gold-colored sensor also has holes to permit filling with liquid helium. Inside the level sensor is a superconducting wire that is partially cooled by the liquid helium. Based on the level of the liquid helium, only the fraction of the superconducting wire submersed in the liquid helium will be superconducting. The measured resistive voltage is used to determine the fraction of the superconducting wire that is in the superconducting state, which is then correlated to the level of the liquid helium in the cryostat.

Figure C-3: Sample fiber holder with its Styrofoam insulation.
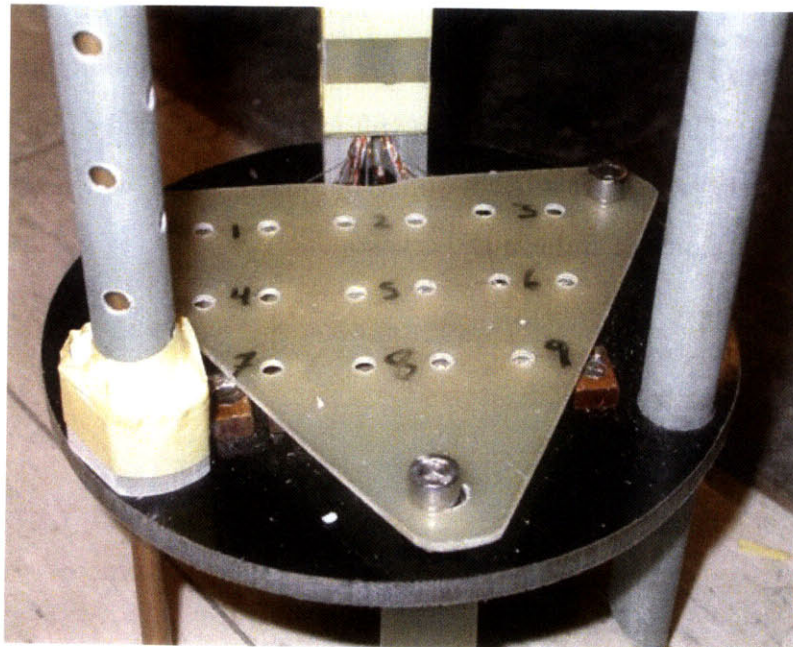
Figure C-4: Base of probe with the differential thermocouple blocks and a view of the liquid helium level sensor.

Appendix D

Other Strain Probe Ideas

Many ideas were considered and four strain probe designs were considered seriously for the uniform strain apparatus, and the "disks in a cylinder" concept was chosen as the best system. Other designs included pulleys, a tapered pull-rod to expand a split disk, and using radial expansion of compression springs. These designs, and why they were not chosen, will be discussed further in this appendix.

One of the first methods considered to strain the sample fiber was using a pulley system, as shown in Figure D-1. At room temperature, all Brillouin scattering strain experiments have been done using pulleys. However, in these experiments, the tens of meters of fibers were part of a multi-pulley system the size of a table. Although this works well at room temperature, cooling an area that large would be prohibitively expensive. Also, trying to uniformly change the temperature would be almost impossible for a system that large.

In order to cryogenically cool, and provide a uniform temperature throughout the range from 4 K to room temperature, the whole probe needs to be small. Vertical temperature gradients are a common problem in trying to obtain a uniform temperature in a cryogenic environment, which means that the pulley system either needs to be horizontal, or short if it is in the vertical direction. The shorter the pulley system, the higher the effect of pulley friction on the results. In the room temperature test, where there were several meters of fiber between pulleys, followed by a few centimeters rounding the pulley, the non-uniformity caused by the friction between the fiber and

Figure D-1: Probe design using a pulley to strain the fiber.

the pulley was very small relative to the total length of the sample fiber. However, when this ratio is closer to unity, the non-uniformity from the friction significantly impacts the measurement. A compromise could not be found between the need for a large ratio of straight section to pulley diameter and that of a small overall vertical height. Using a horizontal pulley system also will not work, since the overall length cannot be very large without increasing the size of the cryostat, which would lead to prohibitively high helium costs.

Since a vertical fiber loop had been ruled out by the vertical temperature gradients, the next obvious thought was to wrap the fibers horizontally. By wrapping the fibers

around a split disk, and then radially expanding the pieces of the disk using a tapered pull-rod, the fiber would be strained much more uniformly than by using a pulley system, as seen in Figure D-2.
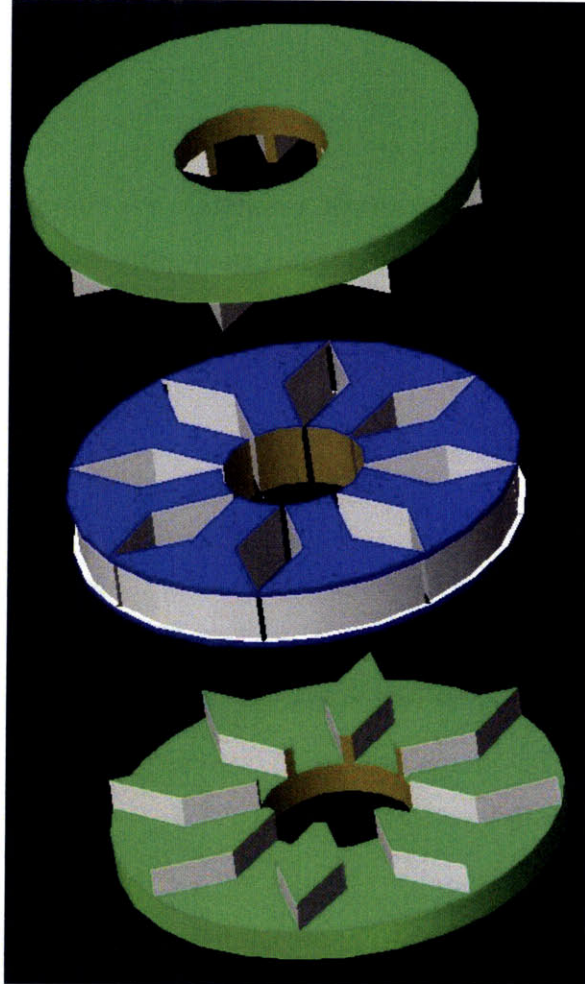
Figure D-2: Split disk which would use a tapered pull-rod.

There would still be friction between the outer edge of the disk and the fibers, but it would be more uniform than the pulley system. The friction will cause a strain distribution along each piece of the disk. However, increasing the number of pieces that the disk is cut into decreases the non-uniformity. Although this design eliminated the vertical temperature gradient, the calculations showed that the machining tolerances were too tight, making this design prohibitively expensive.

Retaining the idea of horizontally wrapping the sample fiber around a split cylinder and radially expanding it somehow, we realized that the radial expansion of a

compression spring is nearly equal to the amount of expansion needed for the experiment. When a spring's ends are fixed and not allowed to rotate during compression from its free length to its solid length, the change in diameter is given by Equation D.1 [80].

$$\frac{\Delta D}{D} = 0.05 \cdot \frac{p^2 - d^2}{D^2} \tag{D.1}$$

In Equation D.1, D is the mean coil diameter, d is the diameter of the wire, and p is the pitch, which is the distance between the middle of a wire to the middle of the adjacent wire. The pitch can also be calculated using Equation D.2, where N is the number of active coils [81].

$$p = \frac{Full Length - 2d}{N} \tag{D.2}$$

We want to maximize $\frac{\Delta D}{D}$, so we have several options. Increasing the pitch would work, but if the system is about 5 to 10 inches tall, the pitch can not be much more than 1 inch. The wire diameter can be decreased, but it still has to be strong enough to expand a cylinder. The diameter can be decreased, but it still needs to be at least 3 inches to avoid bending losses in the fiber.

Wrapping 50 meters around a cylinder with a 4 inch diameter is about 1 inch in height of wrapped fiber. A readily available spring from McMaster has an outer diameter of $3\frac{5}{32}$ inches and a wire diameter of 0.375 inches, leading to a mean diameter of 2.781 inches. It is 5 inches tall, and the pitch is 0.835 inches. Compressing this spring from its free to solid lengths should give an expansion calculated in Equation D.3.

$$\frac{\Delta D}{D} = 0.05\frac{0.835^2 - 0.375^2}{2.78125^2} = 0.003598 \approx 0.36\% \tag{D.3}$$

An experiment was run with this spring in which the spring was compressed 1.4 inches and then 1.6 inches (not all the way to its solid length which would be 2.5 inches), and increases in circumference of 0.062 inches ($\Delta D = 0.0197$ inches) and 0.071 inches ($\Delta D = 0.0226$ inches) respectively were measured. These numbers give

the strains calculated in Equations D.4 and D.5.

$$\frac{\Delta C}{C} = \frac{0.062}{2.781\pi} = 0.00710 \approx 0.71\% \approx 7100\mu\varepsilon \tag{D.4}$$

$$\frac{0.071}{2.781\pi} = 0.00813 \approx 0.81\% \approx 8100\mu\varepsilon \tag{D.5}$$

These values are high enough to measure the strain from 0-4000 $\mu\varepsilon$ easily at room temperature; however, there would be problems if a probe was cooled down to cryogenic temperatures. One problem is that when the probe is cooled from room temperature to 4 K, everything will shrink significantly more than the fibers. The spring is made out of Spring Tempered Steel (ASTM A229), which will noticeably shrink 0.25 % when cooled from room temperature to 4 K. This will shrink the initial circumference of the spring, as calculated in Equation D.6.

$$C|_{4K} = C_o - C_o \cdot \alpha = 3.15625\pi - 3.15625\pi \cdot 0.0025 = 9.94041" \tag{D.6}$$

The circumference will have to increase 0.0248 inches to get back to the initial room temperature circumference where the strain in the fiber is zero. The ΔC will also decrease due to the temperature change as expressed in Equation D.7.

$$\Delta C|_{4K} = \Delta C_o - \Delta C_o \cdot \alpha = 0.071 - 0.071 \cdot 0.0025 = 0.0708" \tag{D.7}$$

Assuming that the spring is compressed 1.6 inches at 4 K, 0.0248 of the 0.0708 inches will go towards getting the circumference back to the initial size, and the remaining 0.0460 inches will strain the fiber, according to Equation D.8.

$$\frac{\Delta C|_{Remaining}}{C|_{fiber@0-strain} = C_o} = \frac{0.0460}{3.15625\pi} = 0.00464 \approx 0.46\% \approx 4600\mu\varepsilon \tag{D.8}$$

This would barely be enough to do our experiment. Another cryogenic problem is that below 10 K, steel is brittle, and the spring would break. Using a titanium or Inconel spring would solve this problem, but these springs would have to be custom made. Assuming that a custom spring is made with the appropriate dimensions, it

could be used in a probe, as shown in Figure D-3, to strain the sample fiber.
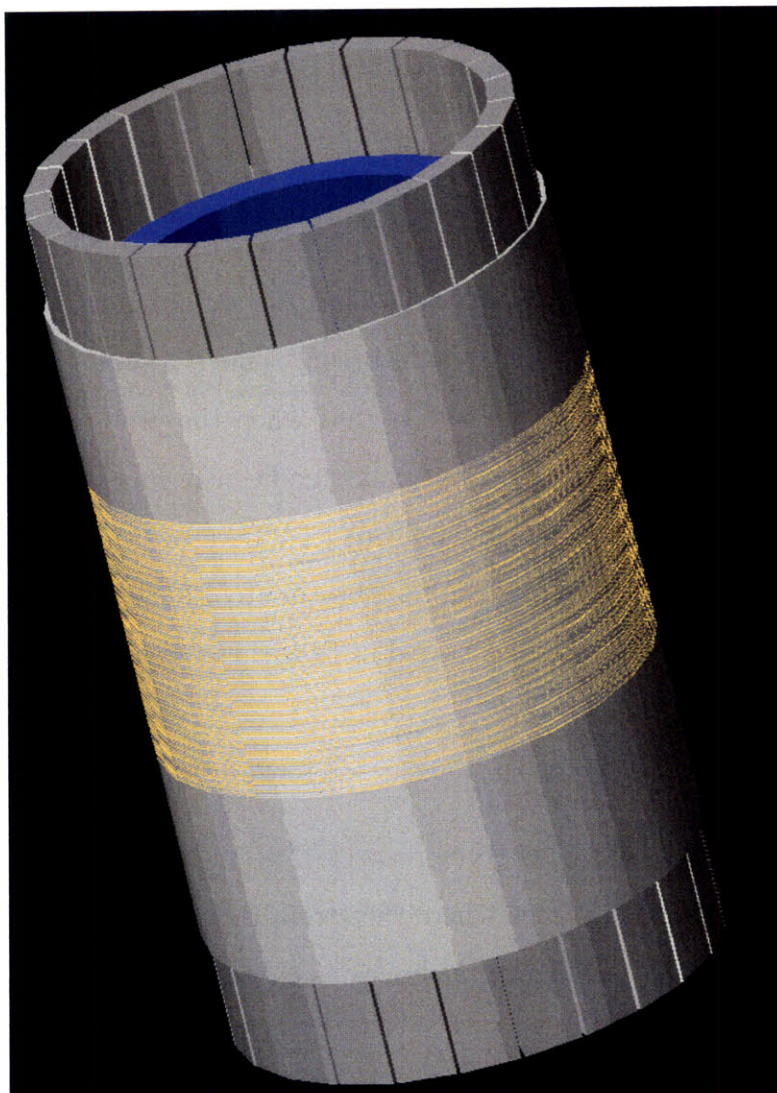
Figure D-3: Basic design for a spring based fiber straining probe.

In Figure D-3 the blue represents the spring. A steel cylinder would be machined and sliced to fit right on the spring's surface, so that the fibers are not affected by the individual coils of the spring. The flat gray part simply represents the sample area; it would not be an actual material. While this design looked very promising, and may have worked as well, we decided to go with the "disks in the cylinder" probe.

Appendix E

Strain Probe Calculations

Many calculations supported the design of the strain probe in order to guarantee that it could strain the fibers uniformly to the design limits and that the probe would retain structural integrity at the design stresses and cryogenic temperatures. It was necessary to demonstrate that none of the fingers would be over stressed, and that the probe would not buckle under the applied load. A summary of the calculations, which will be described in further detail, is given in Figure E-1. (All of the equations from this appendix come from Roark and Young [82], with a special thanks to discussions with Peter Titus as to which equations applied.)

The top three sections of Figure E-1 are the main design variables and constants. Once the equations were set up, several of the parameters were varied until the desired safety ratios were achieved. These parameters were the disk thickness and average finger width, as well as the thickness and length of the cylinder's bending portion. All calculations are done for one finger, or one piece of the sliced cylinder. The middle two green sections are the geometrical calculations for the disk and cylinder. The gray sections are the stress calculations for a single finger, and the orange section is the buckling calculations for a single finger. The bottom two sections are the summaries of the stress and buckling calculations, with the ratios of the expected stresses compared to the allowed stresses. We wanted the ratio, or "safety factor", for the stresses on the fingers to be over two vs. ultimate strength, and over five for the buckling.

Disk Variables			
X initial (L,diag)	1.20	thickness	0.063
sections	20	E (disk)	1.80E+07
kerf	0.025		
max strain	0.01		
mid disk dia	1.5		

Fiber Variables (1/2)	
E (fiber)	1.06E+07
E (fiber)	1.06E+07
D (fiber)	6.50E-03
A (fiber)	3.31E-05
# fiber laps	130

Cylinder Variables	
thickness	0.05
length	5
tube ID	3.5
EDM kerf	0.01
E (cyl)	3.00E+07

Disk Calcs						
Initial		**After Bend**		**Strained 1.00%**		
C cut	12.25	X (bent)	1.12	X (strain)	1.14	
D cut	3.90	Y (bent)	0.43	Y (strain)	0.37	
fiber wrap OD	3.99	angle (bent)	20.98	Delta Y (ea)	0.06	
delta C bend	0.50	D (bent)	3.74	D (strain)	3.78	
width (in)	0.21					
width (out)	0.59					
width (avg)	0.24					

Cylinder Calcs	
width (b)	5.40E-01
delta	2.00E-02

Buckling Calcs

$$\sigma = \frac{F}{A} = \frac{\pi^2 E t^2}{12(KL)^2} \qquad I = \frac{b_{avg} t^3}{12} \qquad F = \frac{\pi^2 EI}{(KL)^2}$$

K	0.7
Inertia	5.00E-06
F	1.26E+03
stress (buc)	8.33E+04

Stress Calcs

$$\sigma_{fingers} = \frac{6PL}{b_{min} t^2}$$

$$\delta = \frac{PL^3}{3EI} \Rightarrow P = \frac{3\delta EI}{L^3}$$

$$I = \frac{b_{avg} t^3}{12}$$

Inertia	5.00E-06
P (load)	8.78E+00
stress (fingers)	7.56E+04

$$\sigma_{fiber} = \frac{P_{fiber}}{b_{min} t}$$

$$P_{fiber} = \frac{F_{fiber}}{Rb} \frac{2\pi b}{(\# cuts)}$$

$$F_{fiber} = E A_o \frac{\Delta L}{L_o}$$

F (fiber)	4.57E+02
load	7.36E+01
stress (fiber)	5.55E+03

$$\sigma_{cyl} = \frac{6P_{cyl} L_{cyl}}{b_{cyl} t_{cyl}^2}$$

$$\delta_{cyl} = \frac{P_{cyl} L_{cyl}^3}{12 E_{cyl} I_{cyl}} \Rightarrow P_{cyl} = \frac{12\delta_{cyl} E_{cyl} I_{cyl}}{L_{cyl}^3}$$

$$I_{cyl} = \frac{b_{cyl} t^3}{12}$$

Inertia	5.62E-06
P (load)	3.23E-01
stress (cyl)	7.18E+03

Stress Check

$$\sigma_{fingers} < \sigma_{TUS}$$

σ (fingers)	σ (TUS)	Ratio
7.56E+04	2.20E+05	2.91

Buckling Check

$$\sigma_{fiber} + \sigma_{cyl} < 5\sigma_{buc}$$

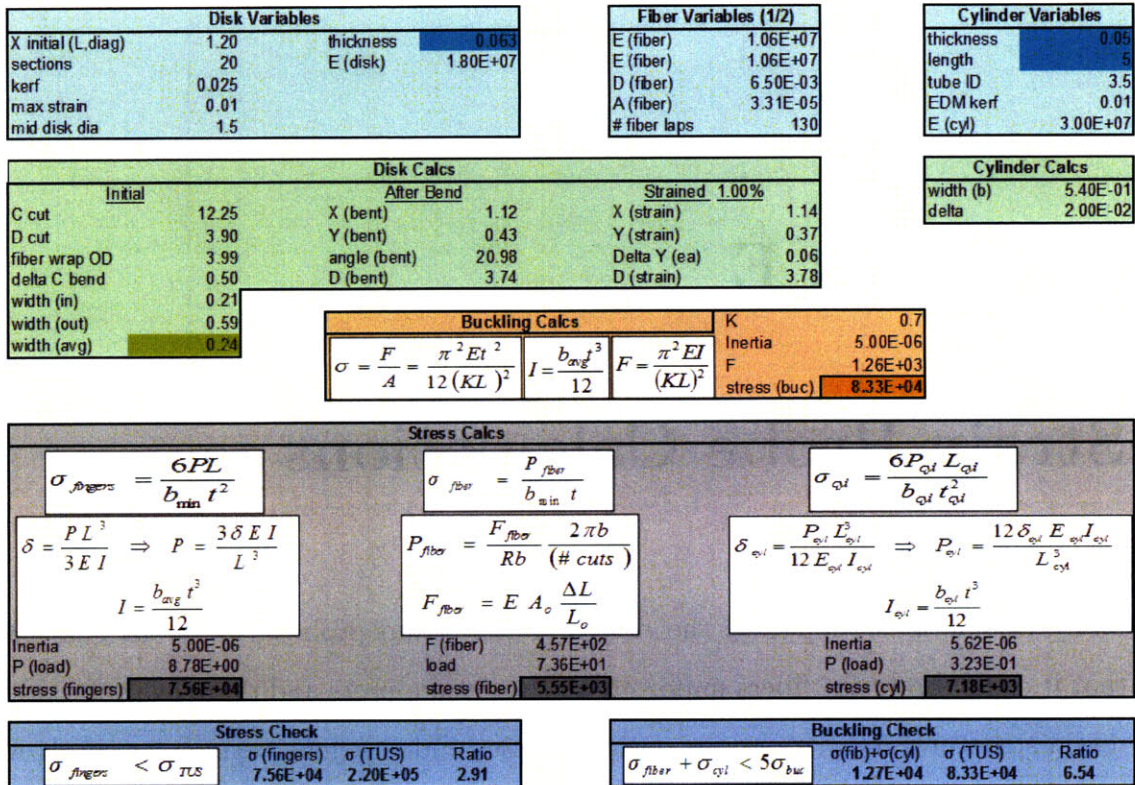| σ(fib)+σ(cyl)	σ (TUS)	Ratio
1.27E+04	8.33E+04	6.54

Figure E-1: Summary of calculations for the strain probe.

The stress on a finger of the disk comes from transverse load and axial compression. Stress from actually bending the finger by the cylinder pushing on the end is the transverse load, while the axial compression comes from the opposing load of the fibers and cylinder, as seen in Figure E-2.

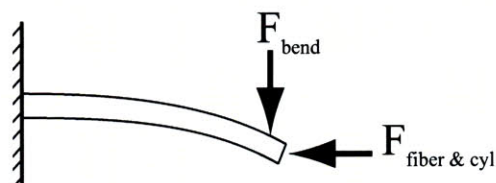Figure E-2: Forces on a finger due to the vertical movement causing bending and the axial compression from the fibers and cylinder.

First we will look at the stress from the finger deflecting a small amount as the two disks are pulled together. This can be simplified to a simple cantilever beam problem, where the load applied to bend a finger of the appropriate dimensions can be expressed by Equation E.1.

$$P = \frac{3\delta EI}{L^3} \tag{E.1}$$

The deflection needed to strain the sample fiber 1 % is given in the "Disk Calcs" section of Figure E-1, the length of the finger as well as the modulus of the titanium alloy are also given in Figure E-1. The moment of inertia of the finger is given by Equation E.2, where the average width of the finger is used.

$$I = \frac{b_{avg}t^3}{12} \tag{E.2}$$

To calculate the stress, we substitute these values into Equation E.3, where t is the thickness of the finger and the minimum width is used because that is where the stress will be the maximum.

$$\sigma_{fingers} = \frac{6PL}{b_{min}t^2} \tag{E.3}$$

Another force on the fingers is the resistive force of the fibers against being strained. The force needed to strain the fibers is calculated according to Equation E.4.

$$F_{fiber} = EA_o\frac{\Delta L}{L_o} \tag{E.4}$$

The area in Equation E.4 is the area of the cross section of a fiber times the number of laps around the probe. Using this force, the load on a single finger is calculated using Equation E.5.

$$P_{fiber} = \frac{F_{fiber}}{Rb}\frac{2\pi b}{\#cuts} \tag{E.5}$$

Next, the stress on the part of the finger with the minimum width is calculated according to Equation E.6.

$$\sigma_{fiber} = \frac{P_{fiber}}{b_{min}t} \tag{E.6}$$

229

Since the cylinder is held together at the top and bottom, a force is needed to expand the fiber sample diameter. The bending will be different from that in Figure E-2, since the cylinder is held both at the top and the bottom, as shown in Figure E-3.
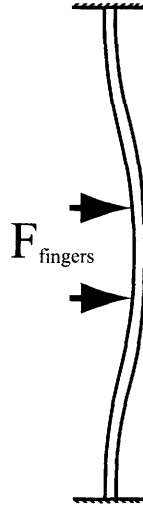

Figure E-3: The bending of a cylinder section that is held fixed at both ends.

This force is calculated by pretending the cylinder slice is another simple beam, as shown in Equation E.7. Obviously, there is a slight curvature to the "beam" since it is cut from a cylinder, but this effect is minimal.

$$P_{cyl} = \frac{12\delta_{cyl}E_{cyl}I_{cyl}}{L_{cyl}^3} \quad (E.7)$$

The deflection of the cylinder used in Equation E.7 is easily calculated, based on the assumption that we are expanding the diameter by 1 %. The moment of inertia in Equation E.7 can be calculated using Equation E.8.

$$I_{cyl} = \frac{b_{cyl}t^3}{12} \quad (E.8)$$

Using Equations E.7 and E.8, we can calculate the stress due to the cylinder according to Equation E.9.

$$\sigma_{cyl} = \frac{6P_{cyl}L_{cyl}}{b_{cyl}t_{cyl}^2} \quad (E.9)$$

Adding the stresses calculated in Equations E.3, E.6, and E.9 gives the total stress expected in the fingers. According to the parameters used in the probe design, the total stress expected in the smallest width section of a finger is on the order of 75 ksi. The titanium alloy has an allowable stress of 220 ksi, giving us a safety factor of almost 3.

Another potential problem is that probe can buckle because of compressive force on a finger. Although the fingers on the disk are pre-bent and have a lateral force that will bend them during the experiment, calculating the Euler buckling still gives an accurate estimate of the buckling strength. A force diagram illustrating the Euler buckling forces on a finger is shown in Figure E-4.
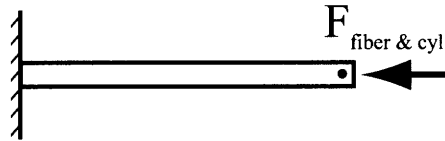

Figure E-4: Diagram of Euler buckling with one end fixed and one end pinned.

The Euler equation for buckling is given in Equation E.10.

$$F = \frac{\pi^2 EI}{(KL)^2} \tag{E.10}$$

K is a constant that depends on the support conditions at the ends of the fingers. For our probe, one end is fixed and the other end that fits into the cylinder's groove can be thought of as being pinned, giving Equation E.11.

$$K = \frac{1}{\sqrt{2}} \approx 0.7 \tag{E.11}$$

The moment of inertia in Equation E.10 is the same moment of inertia for the finger, expressed in Equation E.2. In order to calculate the stress that would cause the finger to buckle, we divide the force by the area as shown in Equation E.12.

$$\sigma_{Euler} = \frac{F}{A} = \frac{\pi^2 E t^2}{12(KL)^2} \tag{E.12}$$

If the finger experiences a stress more than calculated in Equation E.12, the fin-

ger will buckle. A design safety factor of five is standard. Since the stresses that contribute to the potential buckling come from compressive forces on the finger, both the fiber and cylinder section contributions need to be summed as in Equation E.13.

$$\sigma_{fiber} + \sigma_{cyl} \leq 5\sigma_{Euler} \qquad (E.13)$$

Assuming that the fingers will not break due to the bending stress, and that they will not buckle due to the compressive forces, the next potential problem is the cylinder pieces bowing, instead of expanding radially. Since the cylinder sections are held in place at the top and bottom, a radial increase at the center will cause the cylinder to bow, which would lead to a non-uniform straining of the sample fiber. In order to make sure that the sample fiber holder area on the cylinder sections does not bow, the part of the cylinder section between the fiber area and the top was machined down to 0.05 inches thick, whereas the fiber area was 0.235 inches thick. Since the stiffness is proportional to the moment of inertia, which is a function of t^3, the middle section is over 100 times stiffer than the upper and lower sections and will bend 100 times less. Since the radial expansion is only 0.02 inches, the curvature of the fiber holder section is negligible.

A final potential problem is that the fibers may be strong enough to bend the sample holder. As shown below in Figure E-7, the fibers are wrapped somewhere in the white area, which is radially expanded by the two disks pushing out where the red grooves are. This is simplified by looking at a single section of the cylinder and assuming that it is rectangular, ignoring the slight curvature, as shown in Figure E-5.

Calculating the maximum deflection of the beam shown in Figure E-5 can be done using Equation E.14.

$$\delta y = \frac{1}{384}\frac{PL^4}{EI} = 7.5 \cdot 10^{-4} inches \qquad (E.14)$$

The load, P, is the load due to the fibers, as expressed in Equation E.5. The length, L, is defined as the distance between the two support points, and the moment of inertia is defined in Equation E.8. As seen in Equation E.14, the maximum deflection
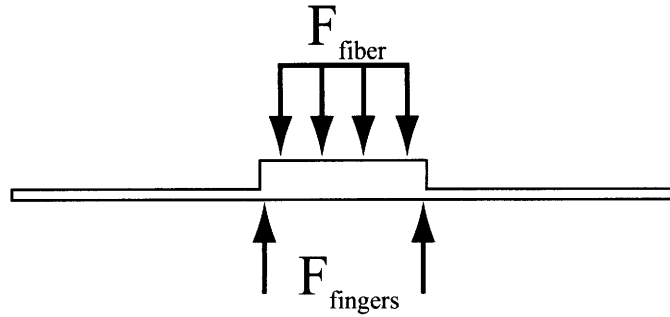
Figure E-5: The distributed load from the wrapped fibers opposing the two point forces from the fingers.

is on the order of 0.75 mils, which is negligible. Thus, we can safely assume that the sample holder remains flat during the straining experiment.

Based on the calculations just described, and summarized in Figure E-1, a 0.63 inch thick Ti-6Al-4V sheet was ordered. This piece was used to machine two disks according to the dimensions in Figure E-6.
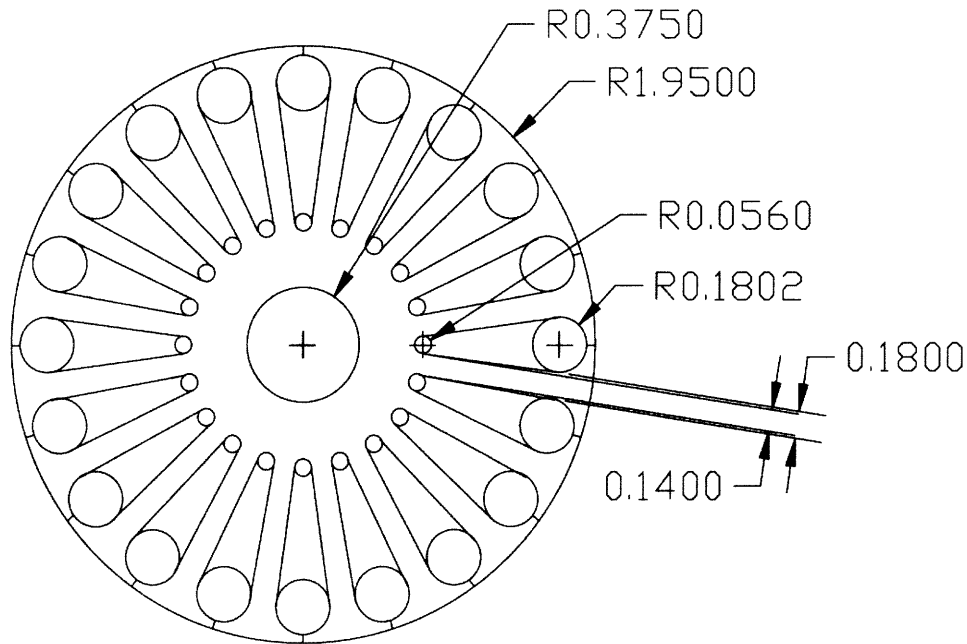

Figure E-6: Dimensions of the titanium disks.

The cylinder was machined according to calculations described in Figure E-1. After it was machined to the appropriate dimensions, it was Electric Discharge Machined (EDM) into twenty equal slices, as shown in Figure E-7.
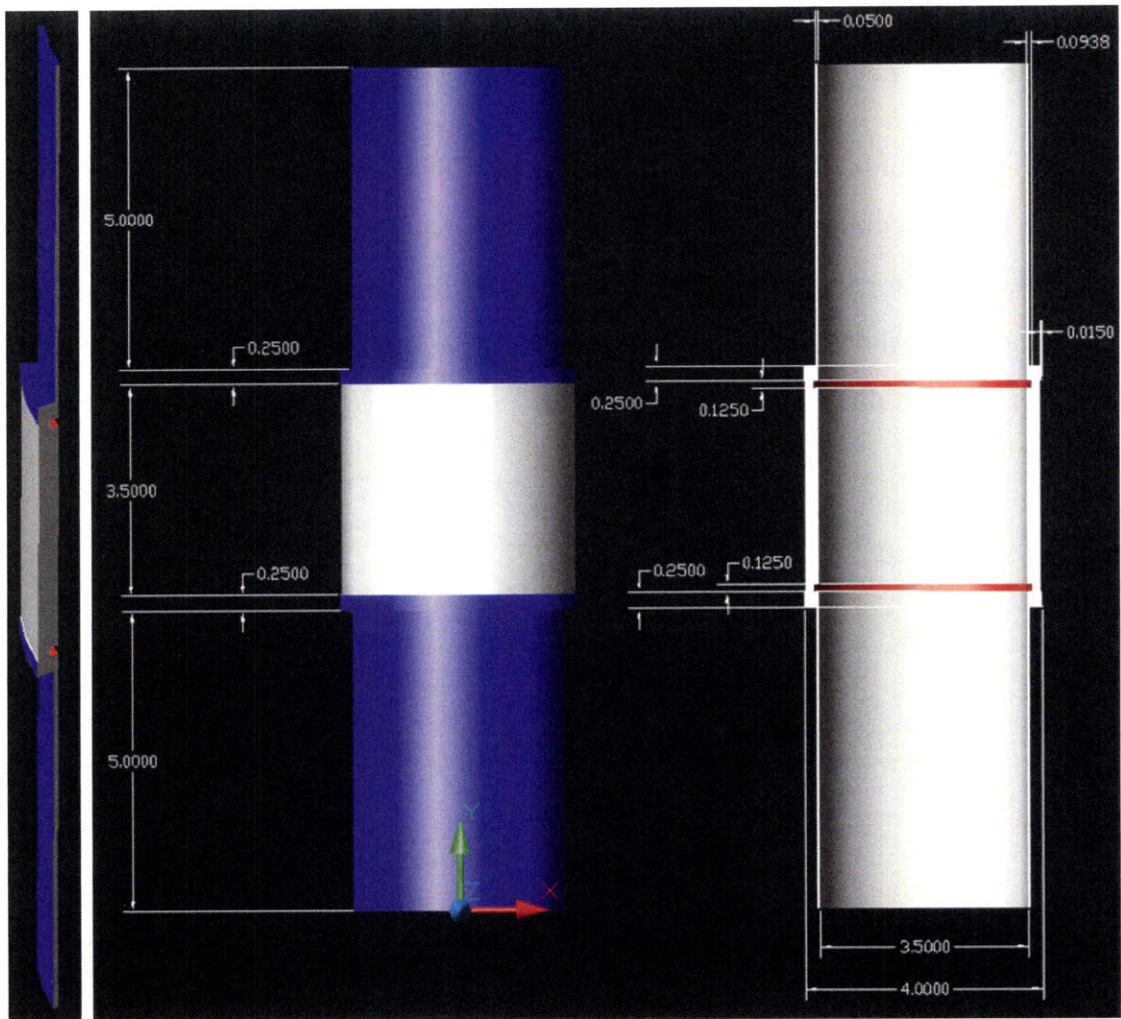
Figure E-7: Dimensions of the cylinder, as along with a view of a single cylinder piece.

Appendix F

Strain Experiment Pictures

The disks used in the strain gage experiment were machined out of Ti-6Al-4V with the specifications calculated in Appendix E, and are shown in Figure F-1. The fingers were then bent to 21 degrees by pushing them through a hole with a smaller diameter to evenly bend the fingers.
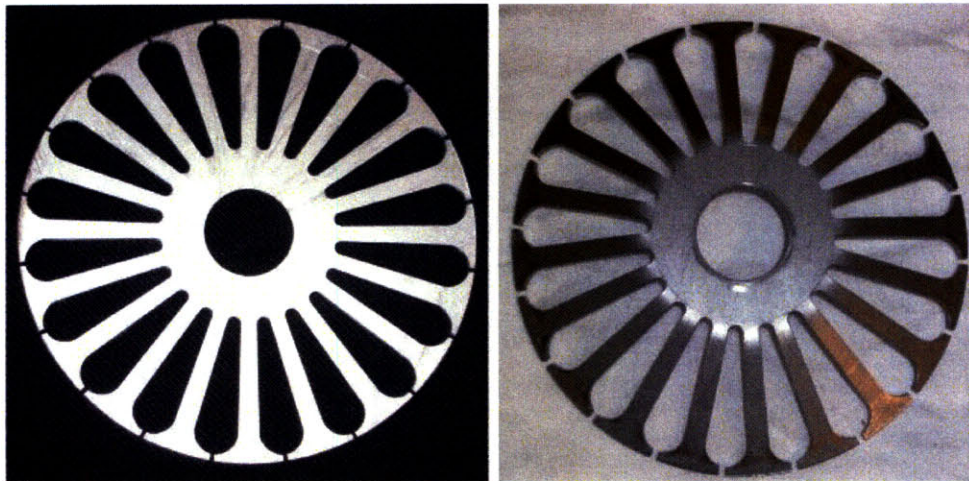
Figure F-1: Machined disk (left), and bent into shape (right).

The cylinder was machined from steel to the specified dimensions. Next, the cylinder was cut into twenty separate pieces using Electrical Discharge Machining (EDM), as shown in Figure F-2.

Figure F-3 shows the push rod (top) and the threaded pull rod (bottom) with the disks attached. The top picture also shows the top disk and some connectors to
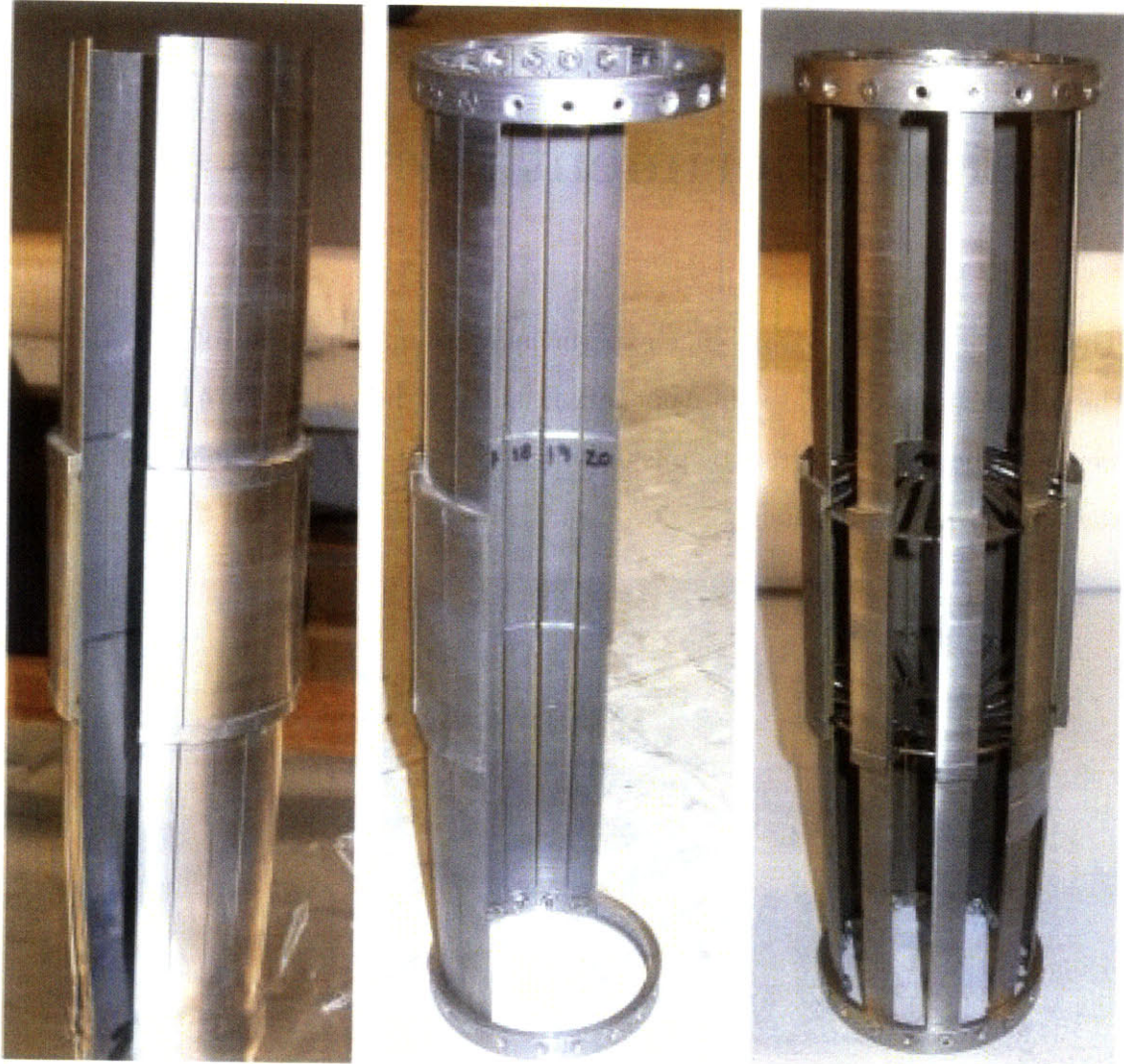
Figure F-2: Machined and EDMed cylinder (left), re-forming the sample holder (middle), sample holder with a few missing pieces to see disks inside (right).

a steel cylinder that eventually surrounded the entire probe to provide a thermally stable environment.

Figure F-3: Push and pull rods with the disks attached.

The temperature of the fiber sample probe was controlled by constantin heater wire and a thermostat. The wire was run along the back of the sample holder, on the inside of the cylinder. Apiezon grease was added to improve the thermal conduction from the heater wire to the sample holder. Finally, the wires were taped into place,

as seen in Figure F-4.

Figure F-4: Constantin heater wire and Apiezon grease on the inside of the cylinder before (left) and after (right) being taped into place.

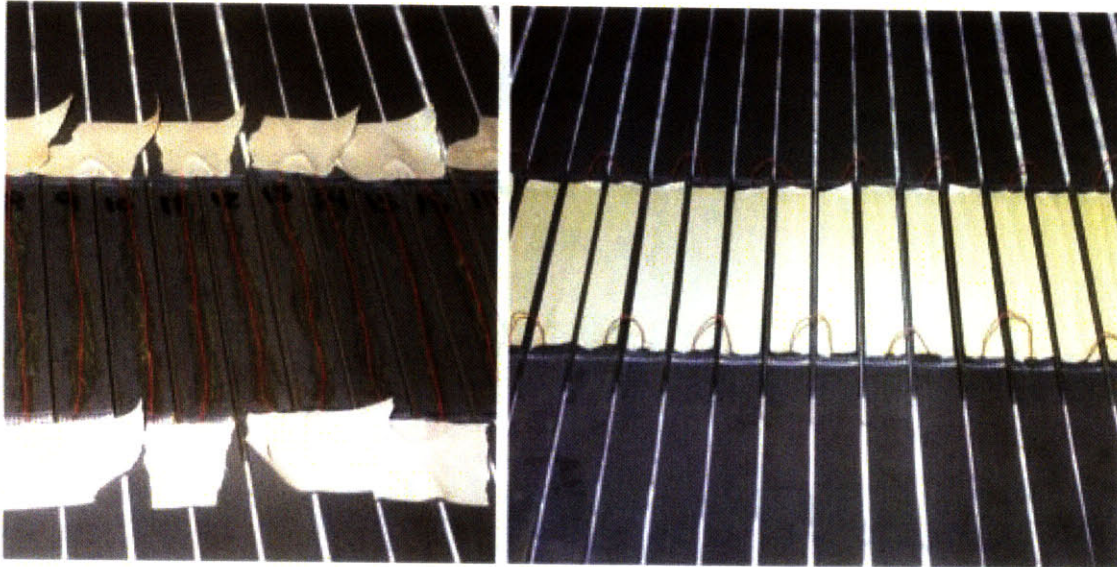Figure F-5 shows the probe as it is being closed up. The push-pull rods and disks from Figure F-3 can be seen, as well as several steel foil circles taped into place. These foils were used to prevent thermal fluctuations due to convection. The bottom photo in Figure F-5 shows the probe with all but the last piece in place.

Stycast epoxy was used to hold the fibers in place because of its excellent bonding properties and its good thermal contraction match with glass and steel throughout the temperature range in the experiment. In order to hold the actual glass fiber, and not just the metal coating, the metal coatings were removed from the sample fibers. In order to remove the copper alloy coating from the fiber sample, a 3:1 mixture of hydrochloric to nitric acid was used. After soaking the fiber in the acid mixture for 15 minutes, the metal had dissolved and the glass fiber was cleaned with alcohol. The acid mixture could also be used to remove the gold coating; however, heat from a blow torch was adequate to remove the gold coating. A blow torch was also used to remove the plastic coating from the FBG fibers in order to be able to epoxy the glass directly. The fibers were held in place with tape overnight as the Stycast dried, bonding the glass fibers to the probe, as seen in Figure F-6.
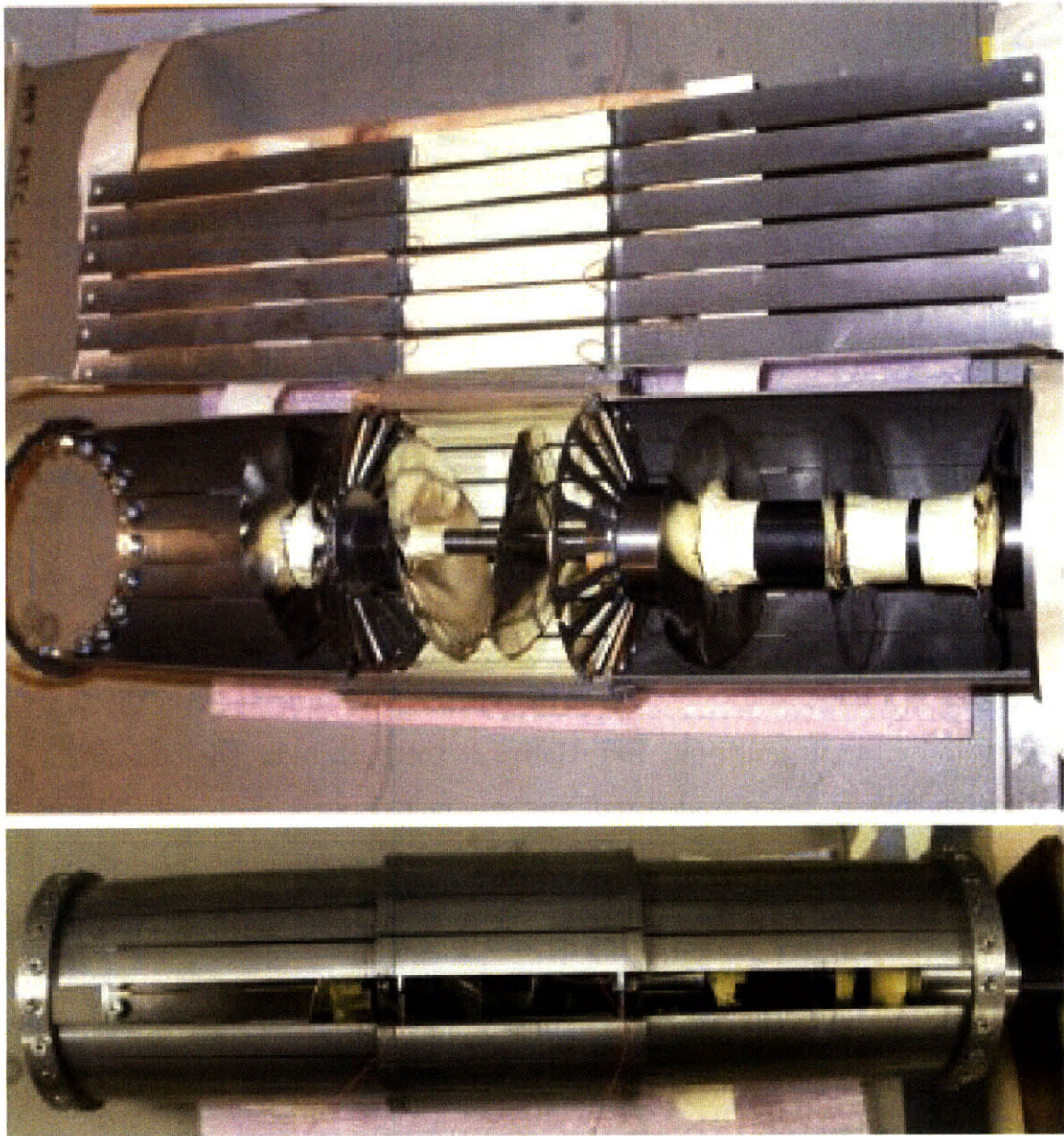
Figure F-5: View of the inside of the probe with the steel foil thermal shields (top), and closing up the probe (bottom).
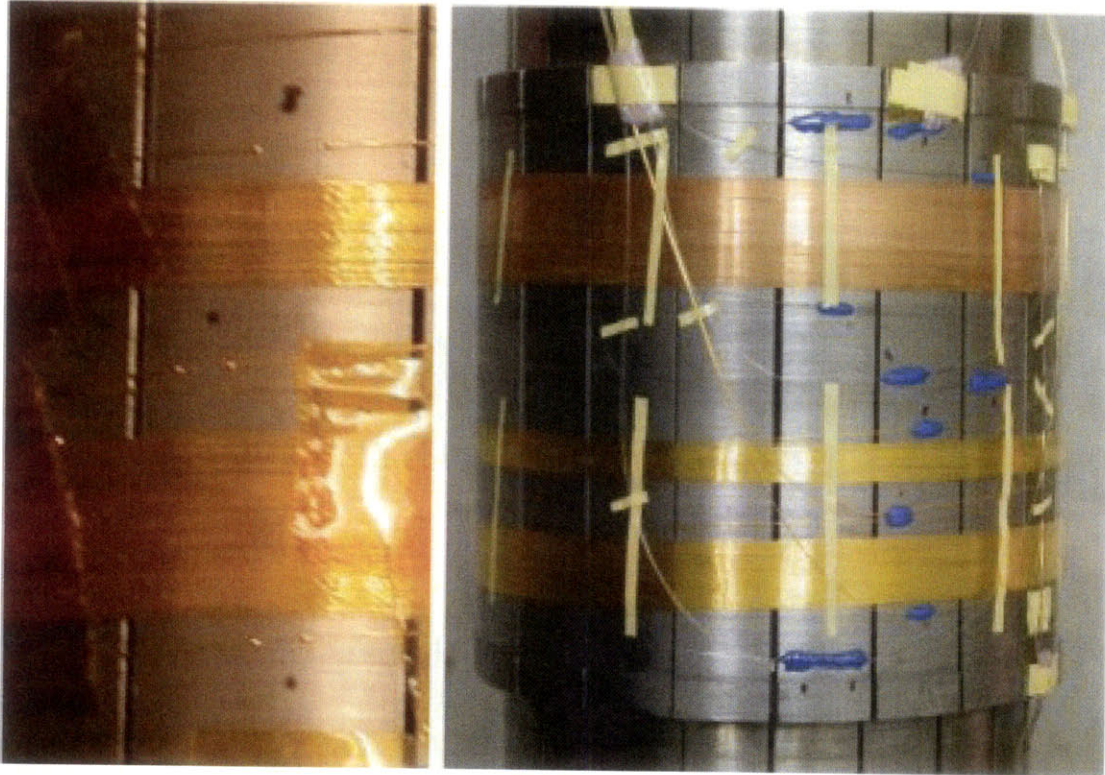
Figure F-6: Gold coating stripped off fibers where they will be epoxied (left), and the sample fiber epoxied into place (right).

Figure F-7 shows the top view of the probe. The three bars on the top were used to raise the threaded pull rod relative to the push rod. The bottom bar had a through-hole for the threaded rod, and was bolted to the push rod. The second rod was threaded, and as it was turned relative to the bottom bar, the threaded pull rod was lifted relative to the push rod. The top bar was designed to be a lock-nut; however, there was enough friction to hold the push-pull rods stationary relative to each other. Also seen in this figure are the sample fibers and the strain gage FBG fibers exiting through a hole at the top of the probe.

Figure F-8 is a picture of the probe cooling down as the liquid helium is transferred to the bottom of the cryostat. In the left side of the picture, some of the hardware can be seen including (clockwise from top right) the broadband laser source, the liquid helium level sensor, the thermostat used with the silicon diode and constantin heater wire, a power supply for a secondary heater, and an optical switch.

Figure F-9 is a picture of the top of the probe during the experiment.
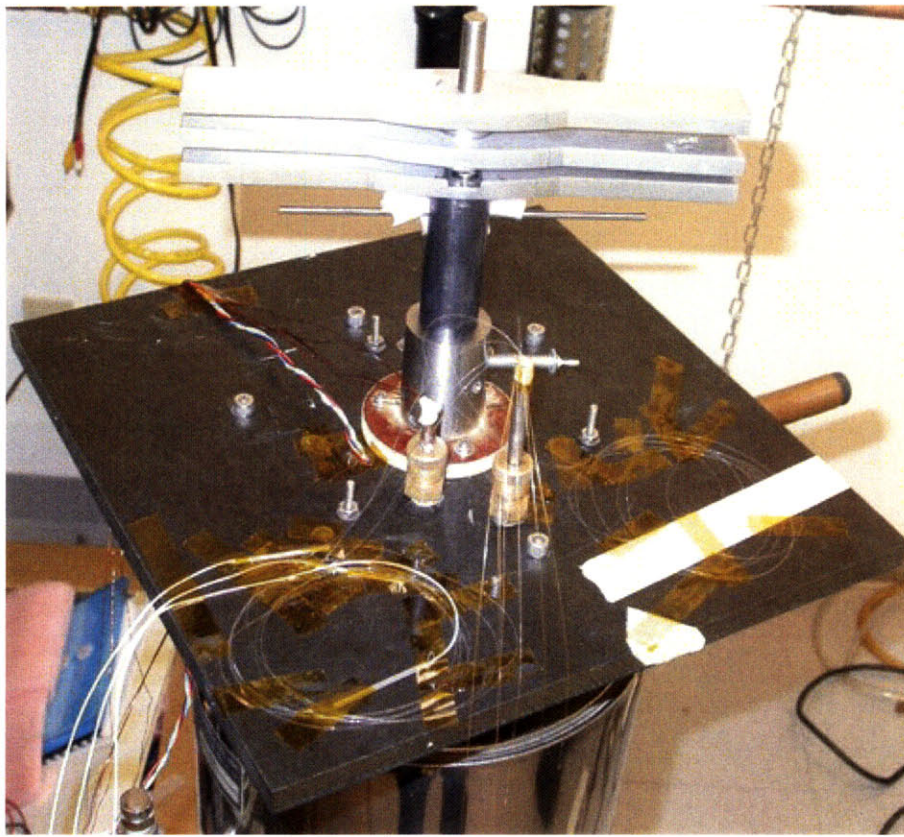
Figure F-7: Top view of the probe showing the threaded rod with the pulling mechanism.

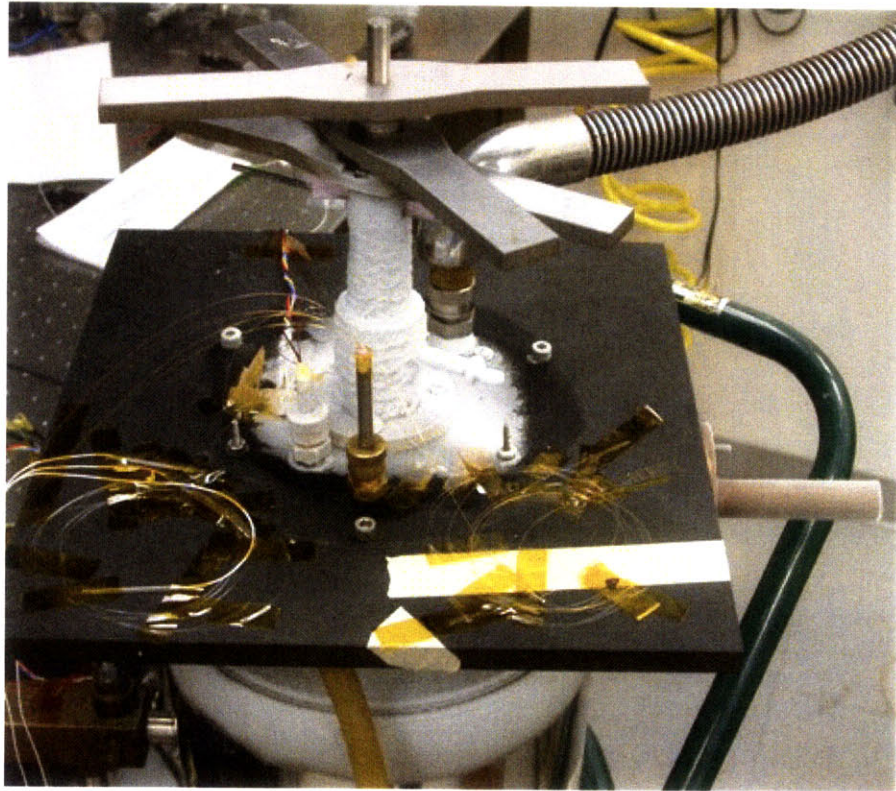

Figure F-8: Cooling down the probe with liquid helium.

Figure F-9: Top view during experiment.

Bibliography

[1] Website: http://www.jet.efda.org.

[2] Website: http://quench-analysis.web.cern.ch/quench-analysis/phd-fs-html/node45.html.

[3] Y. Iwasa. Case Studies in Superconducting Magnets. Plenum Publishing, New York, United States, 1994.

[4] S. Egorov. Fiber optic sensor for temperature measurements in the range of 4.2-100 K. ITER PF Insert Coil Design Progress Meeting; Naka Japan, 2001.

[5] M. Facchini W. Scandale M. Nikles P. Robert L. Thévenaz, A. Fellay. Brillouin optical fiber sensor for cryogenic thermometry. Proceedings of SPIE, 4694, 2002.

[6] J. P. Freidberg. Plasma Physics and Nuclear Fusion. Cambridge University Press, Cambridge, United Kingdom, 2007.

[7] J. Schultz. Superconducting magnets, quench protection. Wiley Encyclopedia of Electrical and Electronics Engineering, 21:1–27, 1999.

[8] X. Bao. Simultaneous strain and temperature measurements with polarization-maintaining fibers and their error analysis by use of a distributed Brillouin loss system. Optics Letters, 29, 2004.

[9] Website: http://www.iter.org.

[10] J. Wesson. Tokamaks. Oxford University Press, New York, United States, 2004.

[11] Y. Shimomura R. Aymar, P. Barabaschi. The ITER design. Plasma Physics and Controlled Fusion, 44:519–565, 2002.

[12] M. Wilson. Superconducting Magnets. Oxford University Press, New York, United States, 1983.

[13] F. Asner. High Field Superconducting Magnets. Oxford University Press, New York, United States, 1999.

[14] B. Seeber. Handbook of Applied Superconductivity, Vol.1. Institute of Physics Publishing, Philadelphia, United States, 1998.

[15] B. Montgomery M. Hoenig. Dense supercritical helium cooled superconductor for large high field stabilized magnets. IEEE Transactions in Magnetics, 11:569, 1974.

[16] A. Fuchs B. Heer C. Marinucci G. Vecsey Y. Takahashi K. Hamada H. Fujisaki S. Smith S. Pourrahimi A. Shajii J. Schultz M. Zhelamskij A. Klimchenko A. Lancetov A. Anghel, B. Blau. The QUench Experiment on Long Length - final report. CRPP, JAERI, SINTEZ, MIT Joint Report, 1997.

[17] L. Bottura. A numerical model for the simulation of quench in the ITER magnets. Journal of Computational Physics, 125:26–41, 1996.

[18] A. Shajii. Theory and modeling of quench in cable-in-conduit superconducting magnets. PFC/RR-94-5, 1994.

[19] J. Feng. A new thermohydraulic-quench code "SOLXPT3D-Q2,". ITER - USMIT - FENG - 122007 - 01, 2007.

[20] J. Schultz. Feasibility of the TPX voltage sensor quench detection system. MIT Plasma Science Fusion Center Report PSFC/RR-97-3, 1997.

[21] D. Sutter. Electrical protection of superconducting magnet systems. Fermi National Laboratory Technical Memorandum TM-559, 1975.

[22] T. Ogitsu. Quench observation using quench antennas on RHIC IR quadrupole magnets. IEEE Trans. Mag, 32:3098, 1996.

[23] J. Schultz J. Minervini S. Ezekiel A. Anghel G. Vecsey Y. Takahashi S. Pourrahimi, S. Smith. Performance of the US quench detection systems in the QUELL experiments. IEEE Transactions on Applied Superconductivity, 7:447–450, 1997.

[24] Miller. Pressure rise during the quench of a superconducting magnet using internally cooled conductors. Oak Ridge National Lab. Technical Report, 1980.

[25] L. Dresner. Parametric study of the stability margin of cable in conduit superconductors. IEEE Transactions on Magnetics, 17:753–756, 1981.

[26] S. Pourrahimi. US contributions to the development and calibration of quench detectors for the ITER QUELL. IEEE Transactions on Applied Superconductivity, 5:491–494, 1995.

[27] E. Hecht. Optics. Assison Wesley Longman, Reading, United States, 1998.

[28] G. Agrawal. Nonlinear Fiber Optics. Academic Press, San Diego, United States, 2001.

[29] D. Griffiths. Introduction to Electrodynamics. Prentics Hall, New Jersey, United States, 1999.

[30] D. Krohn. Fiber Optic Sensors. Instrument Society of America, North Carolina, United States, 1992.

[31] N. Harrick. Internal Reflection Spectroscopy. John Wiley and Sons, New York, United States, 1967.

[32] D. Krohn. Fiber optic sensors: A technology overview. Innovations, pages 11–13, 1982.

[33] H. Shaw B. Kim. Fiber optic gyroscopes. IEEE Spectrum, pages 54–60, 1986.

245

[34] S. Smith. Report on fiberoptic strain sensitivity reduction experiments at the francis bitter national magnet laboratory on 3/16/1995. TPX No:1314 - 950424 - MIT - SSmith - 01, 1995.

[35] G. Ghosh. Temperature dispersion of refractive indexes in some silicate fiber glasses. IEEE Photonics Technology Letters, 6:431–433, 1994.

[36] B. Soller. High resolution optical frequency domain reflectometry for characterization of components and assemblies. Optics Express, 13, 2005.

[37] B. Soller. Polarization resolved measurement of Rayleigh backscatter in fiber-optic components. OFC Technical Digest, 2005.

[38] 2006. Luna Technologies: Optical Backscatter Reflectometer Product Datasheet.

[39] J. von der Weid. On the characterization of optical fiber network components with optical frequency domain reflectometry. Journal of Lightwave Technology, 15, 1997.

[40] M. Froggatt. High-spatial-resolution strain measurement in optical fiber with Rayleigh scatter. Applied Optics, 37, 1998.

[41] D. Gifford. Distributed fiber-optic temperature sensing using Rayleigh backscatter. European Conference on Optical Communication, 3:511–512, 2005.

[42] S. Kreger M. Wolfe B. Soller M. Froggatt, D. Gifford. Distributed strain and temperature discrimination in unaltered polarization maintaining fiber. Presented at the Optical Fiber Sensors Conference, Cancun, Mexico, 2006.

[43] R. Boyd. Nonlinear Optics. Academic Press, San Diego, United States, 2003.

[44] T. Gogolla M. Farahani. Spontaneous Raman scattering in optical fibers with modulated probe light for distributed temperature Raman remote sensing. Journal of Lightwave Technology, 17, 1999.

[45] K. Brown. Combined Raman and Brillouin scattering sensor for simultaneous high-resolution measurement of temperature and strain. Proceedings of SPIE, 6167, 2006.

[46] A. Fellay. Brillouin-based temperature sensing in optical fibers down to 1 K. IEEE, 2002.

[47] K. Grattan. Optical Fiber Sensor Technology. Kluwer Academic Publishers, 2000.

[48] J. Smith. Simultaneous distributed strain and temperature measurement. Applied Optics, 38, 1999.

[49] S. Cho. Strain event detection using a double-pulse technique of a Brillouin scattering-based distributed optical fiber sensor. Optics Express, 12, 2004.

[50] S. Cho. Pulse width dependence of Brillouin frequency in single mode optical fibers. Optics Express, 13, 2005.

[51] Q. Yu L. Chen X. Bao, L. Zou. Development and application of the distributed temperature and strain sensors based on Brillouin scattering. IEEE, 2004.

[52] I. Fabelinskii. Molecular Scattering of Light. Plenum Press, New York, United States, 1968.

[53] P. Robert M. Nikles, L. Thévenaz. Brillouin gain spectrum characterization in single-mode optical fibers. Journal of Lightwave Technology, 15:1842–1851, 1997.

[54] T. Newson P. Wait. Landau placzek ratio applied to distributed fibre sensing. Opt. Commin, 122:141–146, 1996.

[55] R. Vacher. Behavior of phonons in amorphous media from 4 to 300 K. Physical Review, 14, 1976.

[56] C. Varma P. Anderson, B. Halperin. Anomalous low-temperature thermal properties of glasses and spin glasses. Philosophical Magazine, 1972.

[57] A. Pine. Brillouin scattering study of acoustic attenuation in fused quartz. Physical Review, 185, 1969.

[58] K. Dransfeld H Bommel. Excitation and attenuation of hypersonic waves in quartz. Physical Review, 117, 1960.

[59] H. Dardy J. Bucaro. High-temperature Brillouin scattering in fused quartz. Journal of Applied Physics, 45, 1974.

[60] O. Fukuda K. Inada T. Shiota, H. Hidaka. High-temperature effects of aluminum-coated fiber. Journal of Lightwave Technology, 4, 1986.

[61] T. Yoshino Y. Li, F. Zhang. Wide-range temperature dependence of Brillouin shift in a dispersion-shifted fiber and its annealing effect. Journal of Lightwave Technology , year = 2003, volume = 21,.

[62] Z. Wang J. Zong M. Blake S. Jiang [7] J. Geng, S. Staines. Highly stable low-noise Brillouin fiber laser with ultra-narrow spectral linewidth. IEE Photon Technology Letters, 18:1813–1815, 2006.

[63] M. Blake S. Jiang J. Geng, S. Staines. Distributed fiber temperature and strain sensor using coherent radio-frequency detection of spontaneous Brillouin scattering. Applied Optics, 46:5928–5932, 2007.

[64] J. Ekin. Experimental Techniques for Low Temperature Measurements. Oxford University Press, New York, United States, 2006.

[65] K. Hanby. Handbook on Materials for Superconducting Machinery. MCIC, Columbus, Ohio, United States, 1977.

[66] G. Recktenwald. Numerical Methods with MATLAB. Prentice Hall, New Jersey, United States, 2000.

[67] M Kitao K. Ogusu, H. Li. Brillouin-gain coefficients of chalcogenide glasses. Journal of Optical Society of America, 21, 2004.

[68] T. Newson M. Alahbabi, Y. Cho. 100 km distributed temperature sensor based on coherent detection of spontaneous Brillouin backscatter. Measurement Science and Technology, 15:1544–1547, 2004.

[69] Communications with Jihong Geng.

[70] J. Schultz. ITER central solenoid design description document, rev. 6. ITER - USMIT - SCHULTZ - 052404 - 01, 2004.

[71] R. Scott. Cryogenic Engineering. D. Van Nostrand Company, Inc, New Jersey, United States, 1959.

[72] STYCAST 2850 FT-FR data sheet. Website: http://www.emersoncuming .com/other/2850ft-fr.pdf.

[73] CuBall coated fiber data sheet. Website: http://www.oxford-electronics.com /CuBALL_Comparison_Data.htm.

[74] Communications with Joel Schultz, based on private communication with Keeman Kim.

[75] R. Tatam S. James. Optical fibre long-period grating sensors: characteristics and applications. Measurement Science and Technology, 14, 2003.

[76] A. Twin M. Morgan S. James, R. Tatam and P. Noonan. Strain response of fibre Bragg grating sensors at cryogenic temperatures. Measurement Science and Technology, 13, 2002.

[77] B. Zhang X. Zhang, Z. Wu. Strain dependence of fiber Bragg grating sensors at low temperature. Optical Engineering, 45, 2006.

[78] K. Hotate. Distributed fiber Brillouin strain sensing with 1-cm spatial resolution by correlation-based continuous-wave technique. IEEE Photonics Technology Letters, 14, 2002.

[79] K. Hotate. Fiber-optic distributed strain sensing system by Brillouin optical correlation domain analysis with a simple and accurate time-division pump-probe generation scheme. Japanese Journal of Applied Physics, 44, 2005.

[80] SAE Spring Committee. Spring Design Manual. Society of Automotive Engineers Inc. AE-21, 1996.

[81] H Carlson. Spring Designer's Handbook. Marcel Dekker Inc, 1978.

[82] R. Roark. Formulas for Stress and Strain. McGraw Hill, New York, United States, 1965.